INFORMATION TO USERS

This manuscript has been reproduced from the microfilm master. UMI films the text directly from the original or copy submitted. Thus, some thesis and dissertation copies are in typewriter face, while others may be from any type of computer printer.

The quality of this reproduction is dependent upon the quality of the copy submitted. Broken or indistinct print, colored or poor quality illustrations and photographs, print bleedthrough, substandard margins, and improper alignment can adversely affect reproduction.

In the unlikely event that the author did not send UMI a complete manuscript and there are missing pages, these will be noted. Also, if unauthorized copyright material had to be removed, a note will indicate the deletion.

Oversize materials (e.g., maps, drawings, charts) are reproduced by sectioning the original, beginning at the upper left-hand corner and continuing from left to right in equal sections with small overlaps. Each original is also photographed in one exposure and is included in reduced form at the back of the book.

Photographs included in the original manuscript have been reproduced xerographically in this copy. Higher quality 6" x 9" black and white photographic prints are available for any photographs or illustrations appearing in this copy for an additional charge. Contact UMI directly to order.

U·M·I

University Microfilms International
A Bell & Howell Information Company
300 North Zeeb Road, Ann Arbor, MI 48106-1346 USA
313/761-4700 800/521-0600

Order Number 9405518

Ultrafast physics behind the nonradiative relaxation process of chromium ions in forsterite crystals

Demos, Stavros Gregorios, Ph.D.

City University of New York, 1993

U·M·I
300 N. Zeeb Rd.
Ann Arbor, MI 48106

A

ULTRAFAST PHYSICS BEHIND THE NONRADIATIVE RELAXATION PROCESS OF CHROMIUM IONS IN FORSTERITE CRYSTALS.

By

Stavros G. Demos

A dissertation submitted to the Graduate Faculty in Physics in partial fulfillment of the requirements for the degree of the Doctor of Philosophy, the City University of New York.

1993

This manuscript has been read and accepted for the Graduate Faculty in Physics in satisfaction of the dissertation requirement for the degree of Doctor of Philosophy.

5/17/93
Date

Chairman of Examining Committee

Professor R. R. Alfano

5/18/93
Date

Executive Officer

Professor J. B. Krieger

Supervisory Committee

Professor J. L. Birman

Professor J. Gersten

Professor R. Dorsinville

Professor S. K. Gayen

Dr. R. Guenther

The City University of New York

ABSTRACT

ULTRAFAST PHYSICS BEHIND THE NONRADIATIVE RELAXATION PROCESS OF CHROMIUM IONS IN FORSTERITE CRYSTALS

By

Stavros G. Demos

Adviser: Professor Robert R. Alfano

The nonradiative relaxation following photoexcitation has been studied in Cr^{4+}-doped forsterite (Mg_2SiO_4) using picosecond laser excitation and ultrasensitive photon counting detection. The experimental techniques utilized were time resolved antiStokes Raman scattering and up-converted hot and ordinary luminescence.

The up-converted hot luminescence technique allowed the investigation of the upper state nonradiative relaxation of the excited state manifold of Cr^{4+}-doped forsterite. The excitation involves the absorption of two photons per photoexcited ion in a two-step absorption. Discrete peaks are observed in the hot up-converted luminescence spectrum and are attributed to the population of nonequilibrium vibronic levels during the deexcitation of the ions by phonon emission. This work reveals that the phonon modes participating in the initial steps of the nonradiative relaxation of the photoexcited ions have energies 218±20, 325±20, 365±20 and 513±12 cm^{-1}. The shape of the luminescence spectral envelope suggests two electronic bottlenecks at ≈2.1 and ≈2.45 eV associated with slower rates of vibrational relaxation at different parts of the excited state manifold. Time resolved measurements indicated that the average time for phonon emission is of the order of hundreds of fs.

Information on the nonequilibrium phonon dynamics of the 225, 335 and 370 cm^{-1} modes of forsterite has been obtained using time resolved Raman scattering. Laser pulses of 450 fs in duration and 590 nm in wavelength were used to excite the Cr ions 2.1 eV above the ground state. The probe pulses (obtained from the same laser) are monitoring the nonequilibrium phonon population through the intensity of the antiStokes Raman lines at various pump-probe delay times. Experiments were performed at room and liquid nitrogen temperatures. The observed nonequilibrium phonon populations are associated with the overall complex nonradiative decay following the excitation of the impurity Cr^{4+} ions. Using rate equations to describe the electron-lattice system, the nonradiative relaxation time and the phonon lifetimes were estimated by fitting to the experimental data. The nonradiative relaxation time is estimated to be in the order of few ps while the phonon lifetimes are of the order of 10 ps. Best fit suggests the presence of an electronic bottleneck immediately after photoexcitation with an estimated lifetime of 3 ps at room temperature.

This thesis is dedicated to

the memory of my wife and to my parents

Acknowledgments.

Many people have helped me for the completion of my thesis in various ways and I want to use the opportunity to acknowledge them. First of all, I would like to thank my family for their enormous support throughout this period. I wish to thank my thesis advisor, Professor Robert R. Alfano for galvanizing me in the field of experimental laser Physics. I feel that I owe him most that I know. I also want to express my appreciation to Prof. Alfano for his support that helped me continue my studies at a time of immense personal problems. I would like to thank my first advisor, Professor T. Boyer for his help when I started my graduate studies. I want to thank Dr. V. Petričević, Professor S. K. Gayen and Dr. J. M. Buchert for many helpful discussions on this thesis project as well as other areas of tunable solid state lasers. I also thank the faculty members of the Physics Departments at City College of New York and University of Ioannina for teaching me Physics. I want to thank Professors J. L. Birman, J. Gersten, R. Dorsinville, S. K. Gayen and Dr. R. Guenther for serving on my committee. Finally, I would like to thank everybody in IUSL for their cooperation and help.

This thesis work was supported by the Army Research Office.

Table of Contents.

List of Tables.

populated intermediate state (bottleneck at 2.1 eV), k^{-1}: nonradiative relaxation time of the electronic system (k:rate for energy transfer from the ion into the lattice), t_{phonon}: lifetime of the nonequilibrium phonon.

page: 204

List of Figures.

Chapter 3:

Chapter 4:

Chapter 5:

Chapter 6:

Chapter 7:

Chapter 1
Introduction

1.1 Background.

Tunable lasers have a wide range of scientific and technological applications in spectroscopy, photochemistry, remote sensing, communications and medicine. The most well known and used tunable lasers are based on organic dyes. Over the past decade, the increasing need for a more compact and durable laser sources has resulted in the development of tunable solid state lasers. There are three classes of tunable lasers using solid state host media: paramagnetic impurity ions, color centers and semiconductors. In this thesis, I have focused on the first class of tunable solid state lasers.

The first tunable solid state laser employed Ni^{2+} ions in MgF_2 (1963).[1] It took nearly twenty years for the first demonstration of tunable solid state laser operation at room temperature from Cr^{3+}:$BeAl_2O_4$ (alexandrite).[2] Since then, several other lasers have been demonstrated based on Cr^{3+} in various crystal hosts, such as, Cr^{3+}:$Be_3Al_2(SiO_3)_6$ (emerald)[3] and Cr^{3+}:GSGG.[4] New lasing ions[5,6], such as Ti^{3+} and Cr^{4+} have even pushed this technology further.

The rapid developments in the tunable solid state laser technology and search for new ions and hosts have made it imperative to understand and investigate the various loss mechanisms in ion-doped materials which obstruct or inhibit laser action. New diagnostic methods are needed to understand the physics involved in nonradiative processes. A detailed and quantitative understanding of the loss mechanisms is crucial for the selection and formulation of criteria for laser crystals. It is generally believed

that the main loss mechanism in lasers is the nonradiative relaxation. The energy is transferred from the excited ions into the lattice in the form of phonons. This reduces the quantum efficiency of the lasers and for some materials makes the lasing action impossible. Although the theory of nonradiative relaxation processes has evolved over the years, there is a need for experimental investigation of these processes in order to test and expand these theories.

A tunable solid-state laser crystal is composed of a host dielectric crystal doped with small concentrations of an impurity transition metal ion. Photoexcitation of the impurity ion is followed by nonradiative and radiative relaxation processes. The diagrams in figs. [1.1] and [1.2] show schematically the excitation and relaxation processes. The system initially consists of a photon and an ion in the ground state. After photoexcitation, the impurity ion reaches a higher vibrational level of the excited state. The excitation level is located above the lowest vibrational level of the excited state by an amount of energy V depending on the energy of the absorbed photon. The excess energy of the ion E_e, which is equal to V at t=0, is given into the lattice by phonon emission (see fig. [1.2]). Typically, within picoseconds after photoexcitation, the ion reaches the lowest vibrational level of the excited state which is the metastable level (storage level) of the system.[7-16] The phonons emitted during this process last for ≈10 ps which break down into low-energy large-wavevector acoustic phonons that have longer lifetimes and are responsible for the dissipation of the energy into the crystal (see fig. [1.1]).

The lasing property of the material is due to radiative transitions between a metastable level of the impurity ion to the ground state. Nonradiative relaxation involving phonon emission into the lattice is of

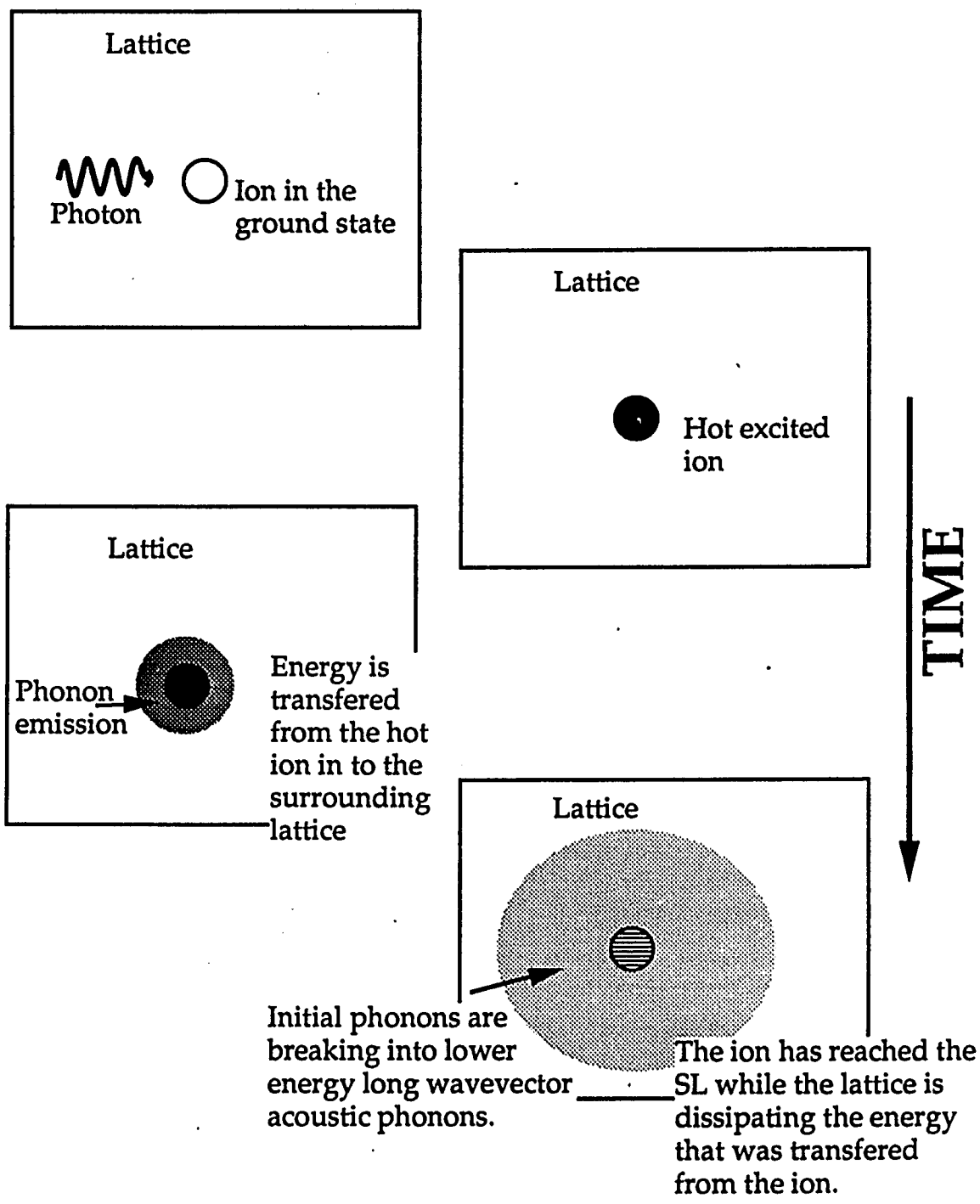

Figure 1.1: The processes taking place immediately after photoexcitation. The excited ion releases its excess energy into the surrounding lattice by the emission of high energy phonons until it reaches the storage level (SL). The initially generated phonons are breaking down to long wavevector acoustic phonons that dissipate the energy into the lattice.

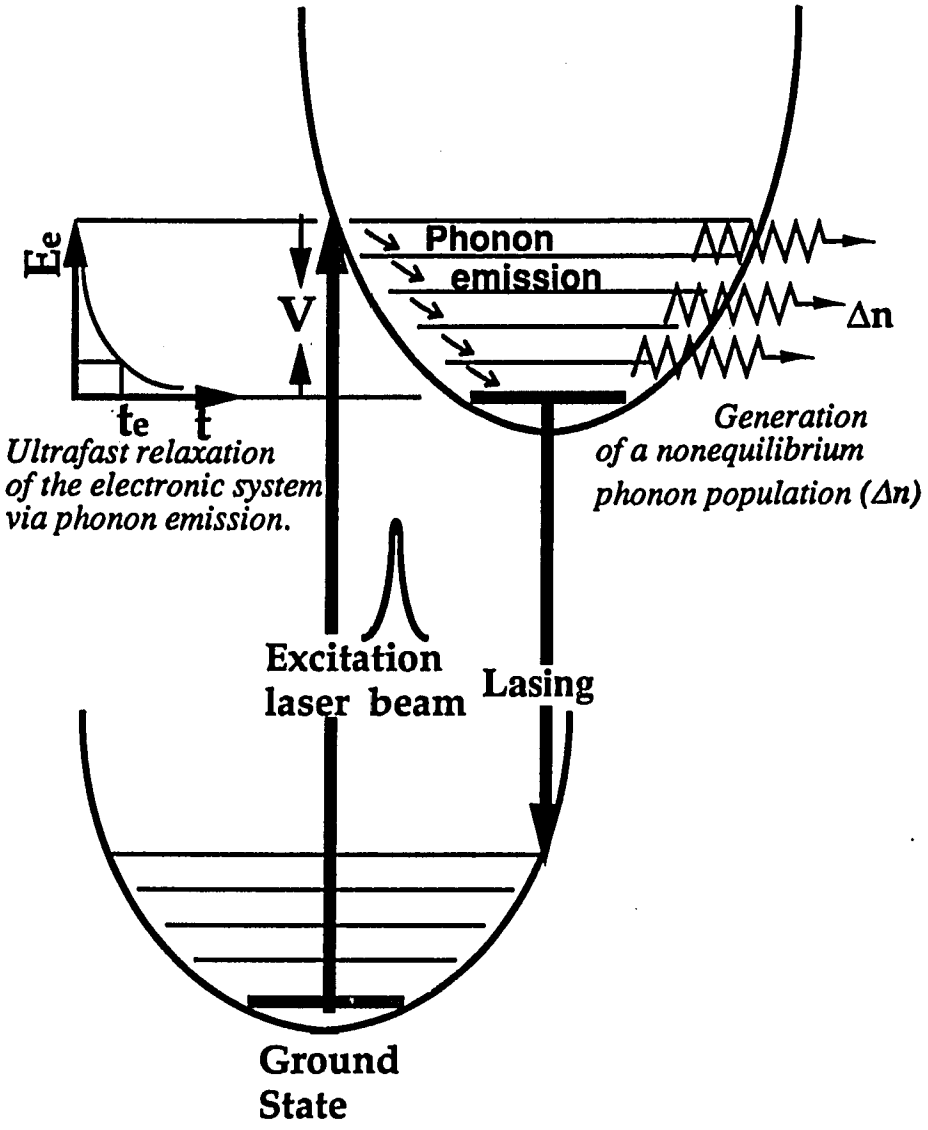

Figure 1.2: Typical energy diagram depicting the processes taking place in a tunable solid state laser crystal subsequently to photoexcitation.

crucial importance in laser materials because is an alternative radiationless relaxation channel from the excited state into the ground state and consequently, significantly affects the overall gain in the laser medium.

The key to a clearer understanding of the nonradiative relaxation is to determine the phonons involved in this process. The ultrafast nonradiative relaxation following photoexcitation of the impurity center provides the basis for time resolved investigation characteristics of the ion-lattice coupling. One may expect that strong coupling of the ion with many lattice modes will result into strong nonradiative relaxation. Up to this date, there is no theory that predicts which phonon modes are involved in the nonradiative relaxation. Experimental results showing which phonon modes are involved and their temporal dynamics will provide insight into the nonradiative relaxation processes and hopefully will help the theoreticians to improve the theory.

The basic principles of the experimental techniques used in this thesis research are illustrated in fig. [1.3]. An impurity ion absorbs a photon to reach an excitation energy level (EL). Following the photoexcitation, phonons are emitted and short-lived electronic-vibrational (vibronic) levels are populated which can give rise to hot luminescence during the ion relaxation. In order to investigate the nonradiative relaxation process, I have studied the nonequilibrium phonon population generated during the relaxation and the hot luminescence emission from the nonequilibrium upper electronic state vibronic levels.

The hot luminescence spectrum should contain peaks representing the populated vibronic levels during the vibrational relaxation. From the energy separation between the peaks we should be able to determine the

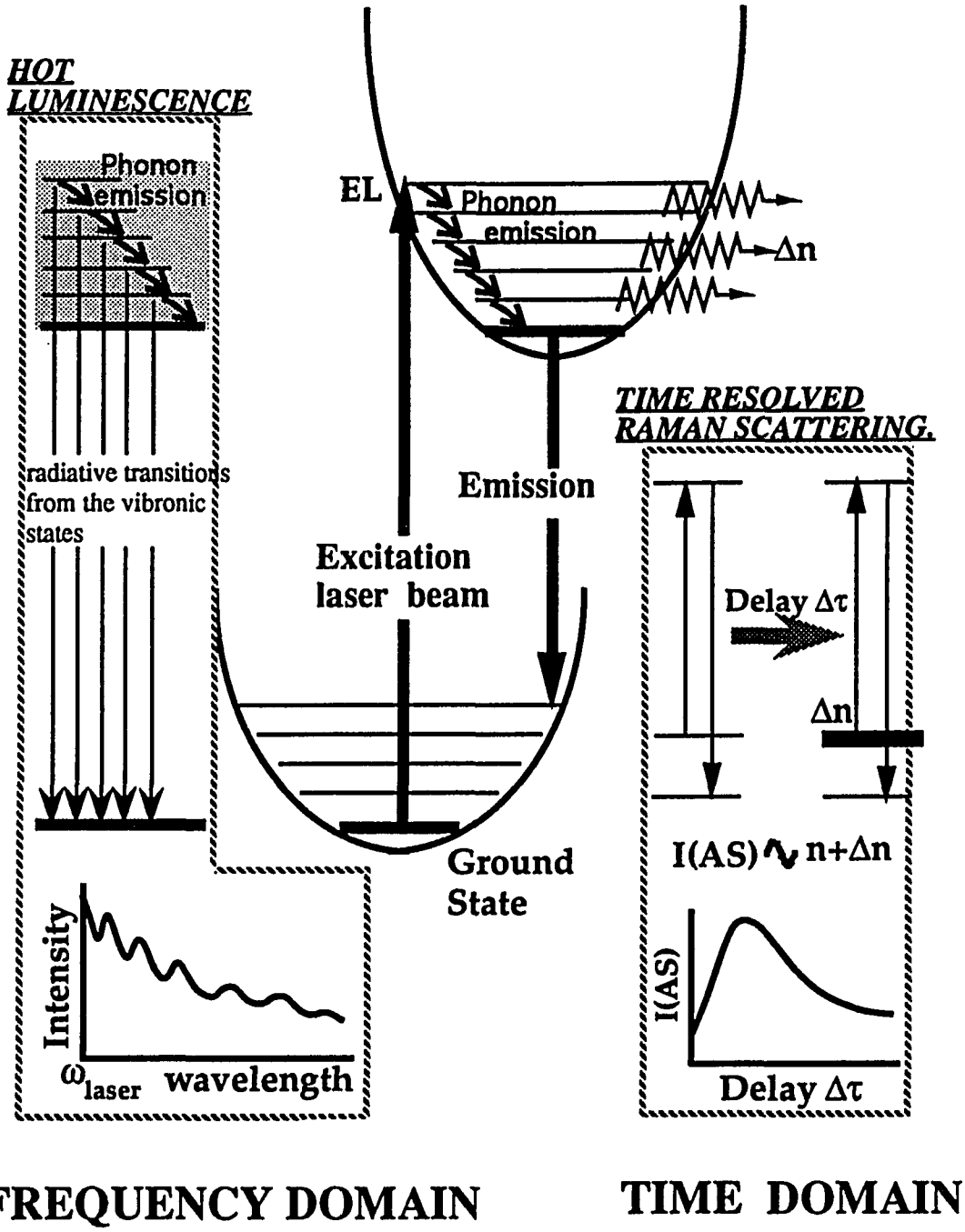

Figure 1.3: Schematic of the basic principles behind the experimental techniques used in this thesis. The hot luminescence arises from transitions from the vibronic states populated during the phonon emission. The generation of excess phonon population results in an increased antiStokes Raman signal from the participating phonon modes.

energy of the participating phonon modes. The lifetime of the hot luminescence emission allows for the measurement of the lifetime of the vibronic levels and consequently the nonradiative relaxation rates. Unfortunately, the hot luminescence emission overlaps with the Raman scattering component and possibly with the emission of other impurity centers or lattice defects, and the observation of peaks due to the vibronic levels in the overall emission spectrum is not possible. In order to avoid this problem, a new novel spectroscopic technique (**Up-converted hot luminescence**) was employed that allows for the observation of hot luminescence isolated from any of the other photoemission processes. This provides information on the relaxation of the photoexcited ions showing the phonon "steps" and the electronic bottlenecks of the excited state. Time resolved up-converted luminescence measurements reveal important information on the temporal behavior of the cascade relaxation via phonon emission process and on band structure information (electronic states and bottlenecks).

Direct measurement of the dynamics of nonequilibrium optical phonons emitted during the nonradiative relaxation can be investigated utilizing **time resolved antiStokes Raman scattering**. The non-equilibrium phonon populations generated during the nonradiative relaxation changes the average phonon occupation number of the participating modes. As a result, the intensity of the antiStokes Raman line of the participating mode changes proportionally to the change of the occupation number (see fig. [1.3]). The temporal behavior of the participating phonon population was measured using two laser pulses, one to excite the sample and generate phonons and a second, arriving at different delay times, as probe of the generated nonequilibrium phonon population. Analysis of the phonon

decay profiles provides the nonradiative relaxation time and the phonon lifetimes of the "accepting" phonon modes.

1.2 Thesis objectives.

This thesis addresses two fundamental questions associated with the nonradiative relaxation in the NIR tunable solid state laser crystal Cr^{4+}-doped forsterite: which optical phonon modes participate in the nonradiative decay and what is the ultrafast temporal dynamics of the coupled ion-lattice system following photoexcitation.

To investigate the radiationless relaxation processes, I have studied the nonradiative relaxation following photoexcitation in the NIR forsterite laser crystal. This work provides information on the ion-lattice coupling dynamics which should be applicable to the nonradiative relaxation process from the storage level into the ground state. The direct study of the nonradiative relaxation from the storage level to the ground state is very difficult to be achieved because of the slow nonradiative relaxation rates that do not allow the generation of a large nonequilibrium phonon population that can be discriminated from the thermal phonons in a time resolved experiment. For this reason, I have studied the ion-lattice dynamics through the nonradiative relaxation of the impurity ion following photoexcitation using the up-converted luminescence and time resolved Raman scattering techniques.

The up-converted emission process (shown in fig. [1.4a]) involves radiative transitions from: a) short lived vibronic levels (VL) having lifetimes of the order of 100 fs that are populated during the emission of phonons, b) electronic bottlenecks (BL) where the nonradiative relaxation slows down due to coupling with electronic states and the lifetime of the

respective vibronic levels is of the order of few ps and c) long lived (ns to ms) upper metastable levels (ML). The up-converted emission is observed at energies higher than the laser photon energy. The schematic in fig. [1.4c] depicts a typical up-converted luminescence spectrum. The spectral profile contains emission from vibronic levels, bottlenecks and metastable levels. Measuring the lifetime of different components of the up-converted emission we can determine which part of the emission is due to ordinary or hot luminescence. This also provides an estimation of the nonradiative relaxation rates of the excited state.

Fig. [1.4b] depicts the emission of phonons during the relaxation of the photoexcited impurity ion. The generated nonequilibrium phonon population reaches its maximum and then decays due to the finite lifetime of the phonons involved due to multiphonon process. The dynamics of the nonequilibrium phonons can be monitored by time resolved antiStokes Raman spectroscopy. The time dependent change of the intensity of the antiStokes Raman lines reflects the dynamics of the particular nonequilibrium phonon population. The nonradiative relaxation times and the phonon lifetimes are estimated from the temporal profile of the non-equilibrium phonon populations.

This thesis is organized into eight chapters. The experimental apparatus such as the laser and the photodetection systems are discussed in chapter 2. A rather detailed overview of the mode-locked Nd:YAG laser is presented where I explain how the laser system works and how to maintain optimum performance. The detection system is also described and I highlight the points of superiority of this detection system that have made this research possible.

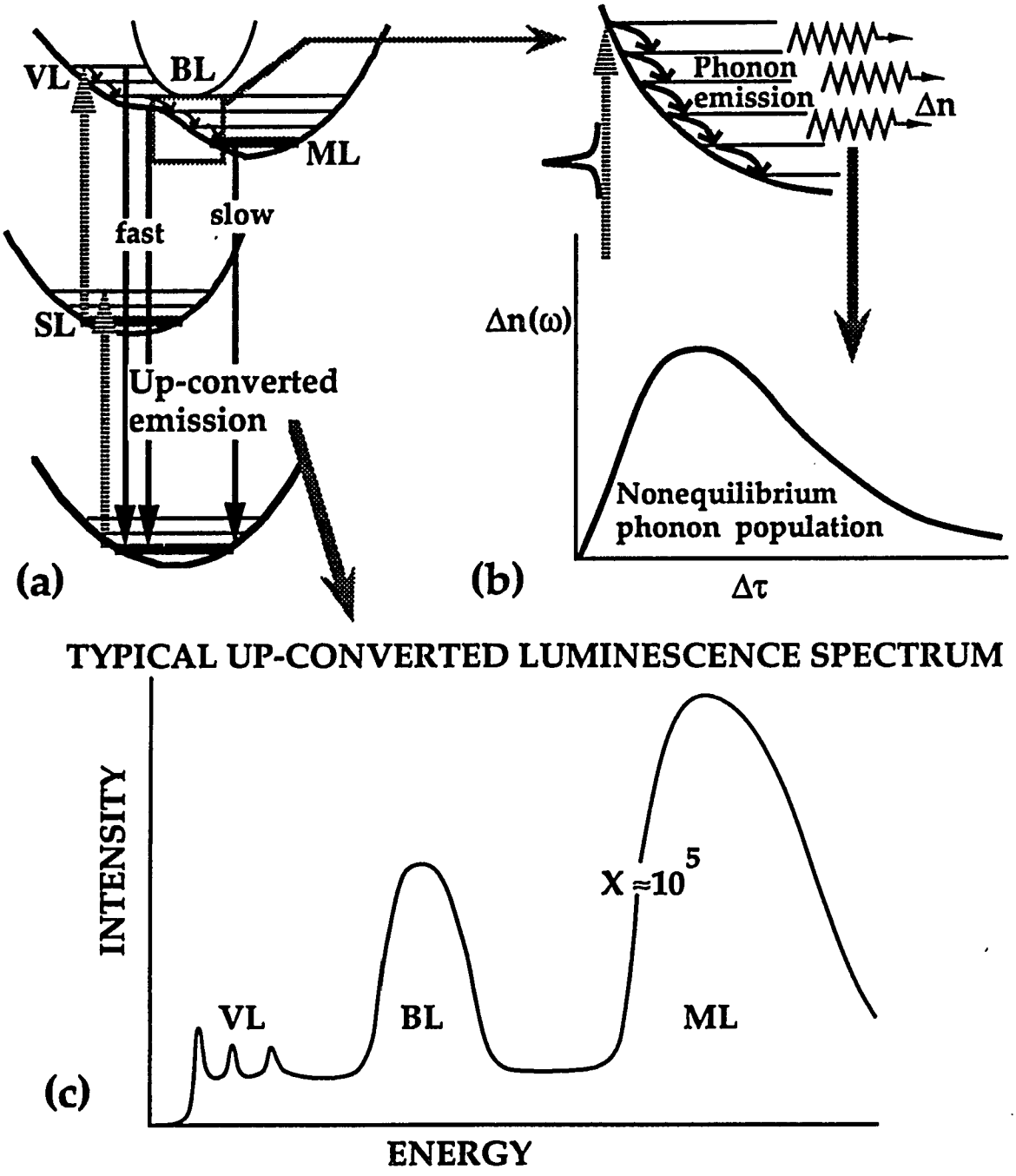

Figure 1.4: Schematic diagrams depicting a) The up-converted luminescence process (VL: vibronic levels, BL: bottleneck, ML: metastable level and SL: storage level), b) The generation of nonequilibrium phonon population ($\Delta n(\omega)$) during the nonradiative relaxation and c) The up-converted emission spectrum due to hot luminescence from vibronic levels (VL) and bottlenecks (BL) or ordinary luminescence due to upper metastable levels (ML).

In chapter 3, I will review some of the fundamental theoretical knowledge concerning the ion-lattice interaction, the theory of the radiative and nonradiative transitions in crystals and the basic theoretical concepts of the Raman scattering. The aim of this chapter is to provide the theoretical background required for the analysis of the experimental data.

The physical properties of forsterite crystal that are of importance for this research are described in chapter 4.

Chapter 5 contains the details of the up-converted hot and ordinary luminescence experiments. Experimental data under various laser excitation wavelengths provide details on the nonradiative relaxation at different parts of the excited state as well as details on the upper excited states electronic structure. Streak camera measurements of the up-converted emission provide important information on the nonradiative relaxation rates. A theoretical model explains the features of the up-converted emission observed in forsterite.

In chapter 6, I have measured the time evolution of nonequilibrium phonons generated subsequently to the absorption of light pulses by the Cr^{4+} ions in forsterite using time resolved antiStokes Raman scattering. A model based on rate equations explains the experimental data and allows the estimation of the nonradiative relaxation rates and the phonon lifetimes.

In chapter 7, I will compare the results obtained from the two experimental techniques and I will attempt to find some clues regarding the selection criteria for the phonons involved in the nonradiative relaxation. Finally, in chapter 8, I will express my opinion about the direction that future research should follow in order to achieve the better understanding of the nonradiative relaxation process and the potential uses of the bottlenecks.

1.3 References.

1. L. F. Johnson, R. E. Dietz and H. J. Guggenheim, Phys. Rev. Lett. **11**, 318 (1963).
2. J. C. Walling, O. G. Peterson, H. P. Jenssen, R. C. Morris, and E. W. O'Dell, IEEE J. Quantum Electr. **QE-16**, 1302 (1980).
3. M. L. Shand and J. C. Walling, IEEE J. Quantum Electr. **QE-18**, 1829 (1982) ; J. Buchert, A. Katz, and R. R. Alfano, IEEE J. Quantum Electr. **QE-19**, 1477 (1983).
4. B. Struve, G. Huber, V. V. Laptev, I. A. Shcherbakov and E. V. Zharikov, Appl. Phys. B. **30**, 117 (1983).
5. P. F. Moulton, J. Opt. Soc. Am. **B3**, 125 (1986).
6. V. Petricevic, S. K. Gayen, R. R. Alfano, K. Yamagishi, H. Anzai, and Y. Yamaguchi, Appl. Phys. Lett. **52**, 1040 (1988); Appl. Phys. Lett. **53**, 2590 (1988).
8. L. A. Riseberg and H. W. Moos, Phys. Rev. **174**, 429 (1968).
9. N. Robertson and L. Friedman, Philosophical Magazine **33**, 753 (1976).
10. C. W. Struck and W. H. Fonger, J. Lumin. **10**, 1 (1975).
11. J. M. Wiesenfeld, L. F. Mollenauer and Erich Ippen, Phys. Rev. Lett. **47**, 1668 (1981).
12. S. K. Gayen, W. B. Wang, V. Petricevic, R. Dorsinville, and R. R. Alfano, Appl. Phys. Lett. **47** (5) 455 (1985).
13. S. K. Gayen, W. B. Wang, V. Petricevic, and R. R. Alfano, Appl. Phys. Lett. **49** (8) 437 (1986).
14. S. K. Gayen, W. B. Wang, V. Petricevic, S. G. Demos, and R. R. Alfano, J. Lumin. **47**, 181 (1991).
15. A. M. Stoneham, Philosophical Magazine **36**, 983 (1977).

16. B. Henderson and G. F. Imbusch, "Optical Spectroscopy of inorganic solids", (1989), ch. 5 and 9, John Wiley & Sons, New York.

Chapter 2
Experimental Methods.

In this chapter, I will describe the major experimental systems used for my thesis: the laser and detection systems. The up-converted luminescence and time resolved Raman scattering experimental setups will be described in chapters 5 and 6 respectively.

2.1 The laser system.

The laser system utilized (shown in fig. [2.1]) is composed by a CW mode-locked[1-4] Nd:YAG laser, a pulse compressor,[3,4] and a synchronously pumped dye laser.[3,4] The mode-locked Nd:YAG laser (Spectra Physics, model 3000), produces 8 Watts of laser radiation at 1064 nm. The time duration of the output pulses is ≈80 ps and the repetition rate is 82 MHz. The output IR beam is introduced into a fiber-optic pulse compressor to produce a laser beam of 3.5 Watts average power at 1064 nm while the pulse duration is reduced to ≈6 ps. The frequency is doubled using a KTP crystal to produce ≈900 mW laser beam at 532 nm having pulse duration of ≈4 ps. The green beam is used to sync-pump the dye laser. Varying the dye solution and the mirrors in the dye laser cavity, 150-300 mW of tunable laser radiation is generated having pulse duration of ≈450 fs and spectral width of ≈58 cm^{-1}.

The pulsewidth of the pulse compressed 1064 nm beam has been measured using Kerr gate[5] where the IR pulses open the gate while the shorter pulses from the dye laser are monitoring the gate. The pulsewidth of the dye laser output is monitored using an autocorrelator. The optical

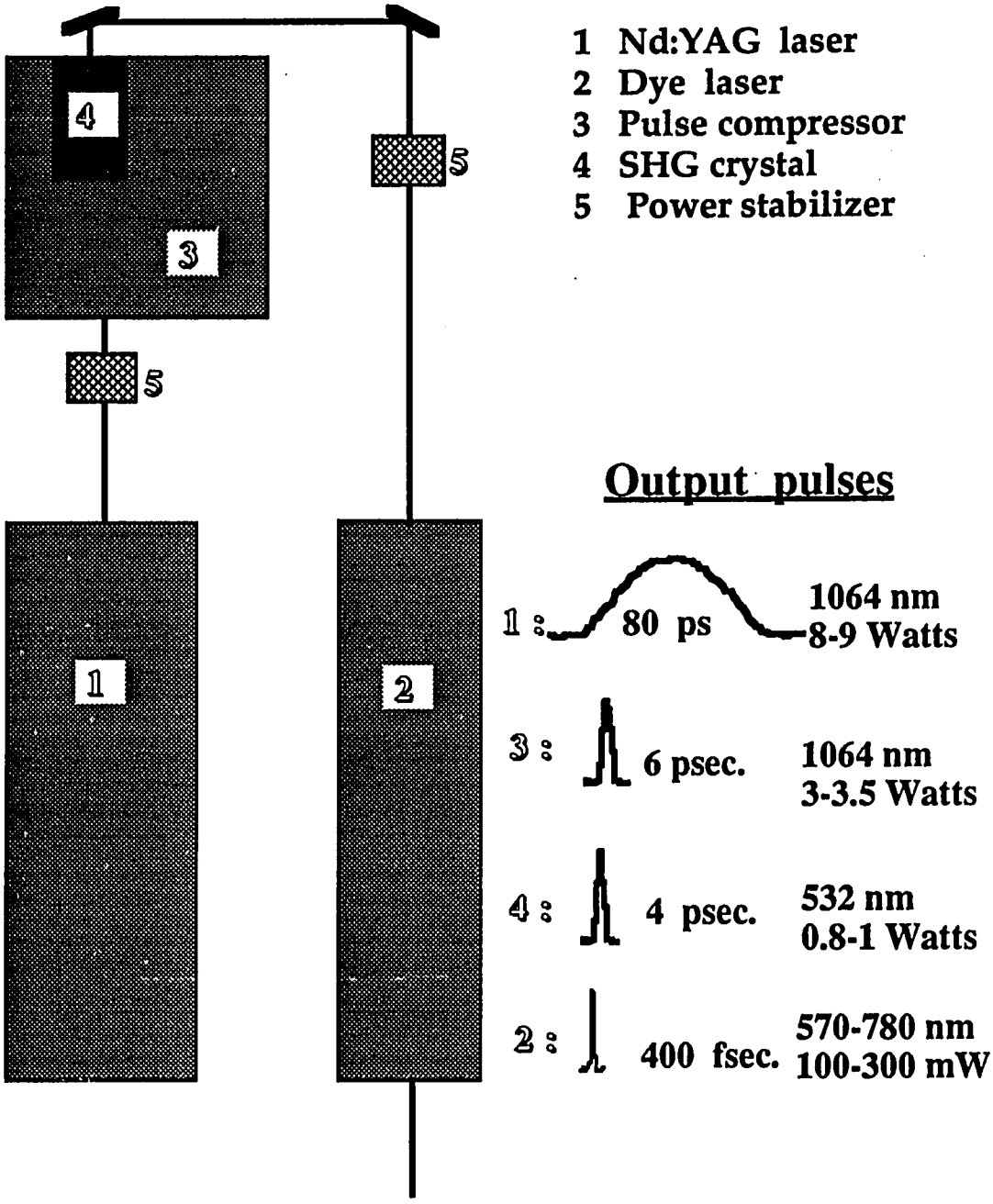

Figure 2.1: The laser system utilized for this research. The different components are listed in the upper left corner. The output pulse characteristics are provided in the lower left corner

configuration of the autocorrelator I have used is shown in fig. [2.2a]. The operation of the autocorrelator is based on splitting the pulsed laser beam into two equal in power beams that are recombined in a thin KDP crystal to observe the second harmonic of the two overlapping beams.[2,4] One of the two beams follows a path that is adjustable in length via a translation stage or a shaking mirror. The maximum intensity of the second harmonic is when the pulses of the recombined beams arrive at the same time. By varying the length of the second beam, the two pulses arrive on the KDP crystal at different times with respect to each other. From the intensity of the second harmonic at various delay times we can measure the pulsewidth of the laser pulse. Using the shaking mirror we can continuously monitor the pulses on the screen of an oscilloscope using a photomultiplier to measure the second harmonic. The oscilloscope trace of the 450 fs pulses from the dye laser is shown in fig. [2.2b]. In our autocorrelator, we can continuously monitor the pulses for pulsewidth shorter than 2 ps. When the pulses are longer, the translation stage can be used to measure pulses as long as hundreds of picoseconds.

The short pulses produced by the dye laser have the intrinsic disadvantage when used for spectroscopy that they posses a broad spectral width. The temporal profile of the dye laser pulses is partially controlled by adjusting the cavity length.[6] Practically, the pulsewidth can be tuned between 450 fs to ≈10 ps by adjusting the length of the dye laser cavity. For the up-converted luminescence measurements described in other chapters it was important to have the best possible spectral resolution while the pulse duration was not of importance. For this reason, the cavity length was adjusted for minimum spectral dispersion while the generated laser pulses were broader in the time domain (≈ 6 ps). For the time resolved Raman

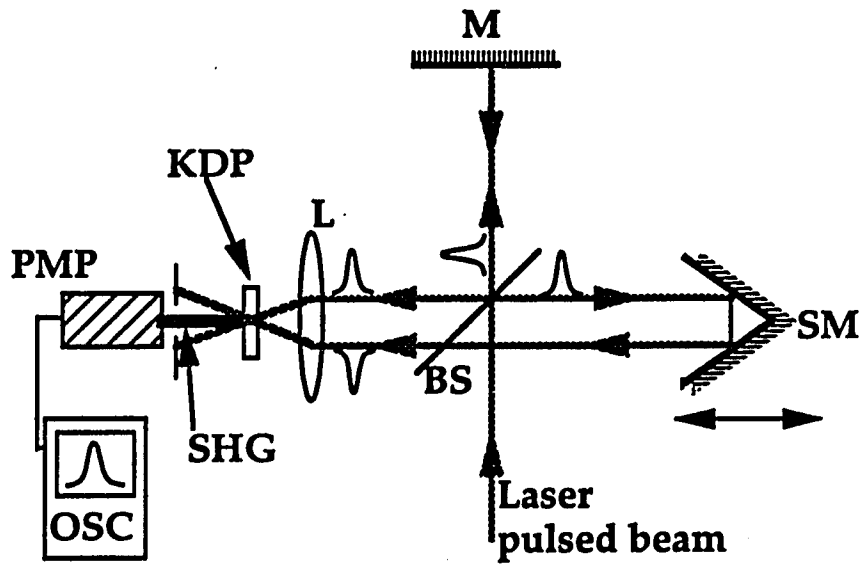

(a)

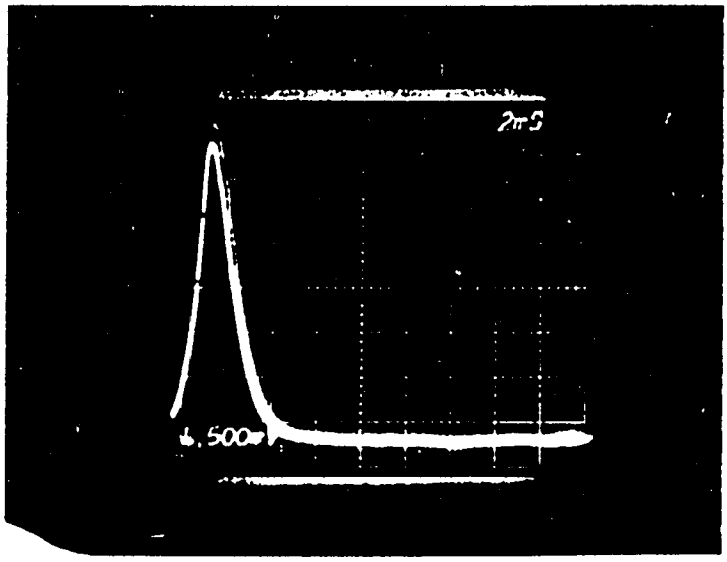

(b)

Figure 2.2. a) Schematic diagram showing the optical configuration of the autocorelator. BS: beam splitter, M: mirror, SM: shaking mirror, L: 5 cm focal length lens, KDP: thin KDP crystal, SHG: second harmonic of the two laser beams, PMP: photomultiplier, OSC: oscilloscope. b) oscilloscope trace of the 450 fs laser pulses of the R-6G dye laser.

scattering measurements in order to distinguish the different phonon modes in the antiStokes Raman spectrum it is important to have good spectral resolution but also the shortest possible pulses for best temporal resolution. For these experiments the 590 nm laser beam from the dye laser was used having 450 fs pulse duration and 58 cm^{-1} spectral width. The spectral width of 58 cm^{-1} from the dye laser makes the observation of the phonon modes in the Raman spectrum practically impossible. The transform limited spectral width to support 450 fs pulses having hyperbolic sech shape is given by the relation[3]

$$\Delta f.\Delta t \geq 0.3148 \qquad (2.1.1)$$

The above equation suggest that the transform limited spectral width is 23 cm^{-1} which is very different from the spectral width of the laser. To compensate for this problem, a narrow band interference filter at 590 nm having FWHM of 1.4 nm was used to reduce the bandwidth of the laser beam. That had as result the reduction of the spectral width down to 36 cm^{-1} with no detectable change in the pulse duration. The disadvantage of the use of the narrow band filter is that almost half of the laser power is lost during the pass of the laser beam through the filter but this was not a problem due to the superb performance of the detection system.

The laser system performs satisfactory when the alignment is optimum. I have found that this is not always easy and that it requires experience. In addition, in order to achieve the required optimum operational condition we had to make some modifications that allowed better performance. For these reasons I will explain briefly the laser system, how to achieve best performance and the modifications we have introduced.

The optical components in the cavity of the Nd:YAG laser are shown in fig. [2.3 a]. These are the back mirror (BM) positioned on a translation stage providing adjustability of the cavity length, the laser head (LH) that contains the laser rod (R) and the flashlamp (FL), the aperture (A), the polarizer (PL), the mode-locking crystal (MC) and the output mirror (OM). One problem on this laser was that in order to align the laser cavity the cover had to be removed. When the cover was put again in place, the extra weight on the structure was missaligning the laser. A possible solution was to use the laser without its cover. In this case we were experiencing problems because the optics inside the cavity need to be cleaned very often while the performance of the laser was deteriorating within days. To solve this problem we have opened a window in the cover of the laser from which we can have access to the components inside the cavity without removing the heavy cover. A second modification was the selection of the aperture (A in fig. [2.3 a]). The company had supplied us with a set of apertures that could be used. Reasonable performance was achieved using the 0.059 and 0.065 inches diameter apertures. However, using the 0.059" aperture, the laser power was low (less than 7 W) while the mode-locking was good. On the other hand, using the 0.065 " aperture the mode-locking was poor while the laser power was improved (≈ 8 W). For this reason I experimented with apertures having size between the two mentioned above. I achieved best performance using an aperture with diameter of 0.063 inches. The laser power was ≈ 8.4 W and the quality of the mode-locking adequate. The condition of mode-locking can be monitored to some extend by measuring the second harmonic output of the YAG laser. Using the 0.063" aperture we get ≈ 2.1 W of 532 nm beam while using the other apertures the output is less then 1.5 W. The third change we have

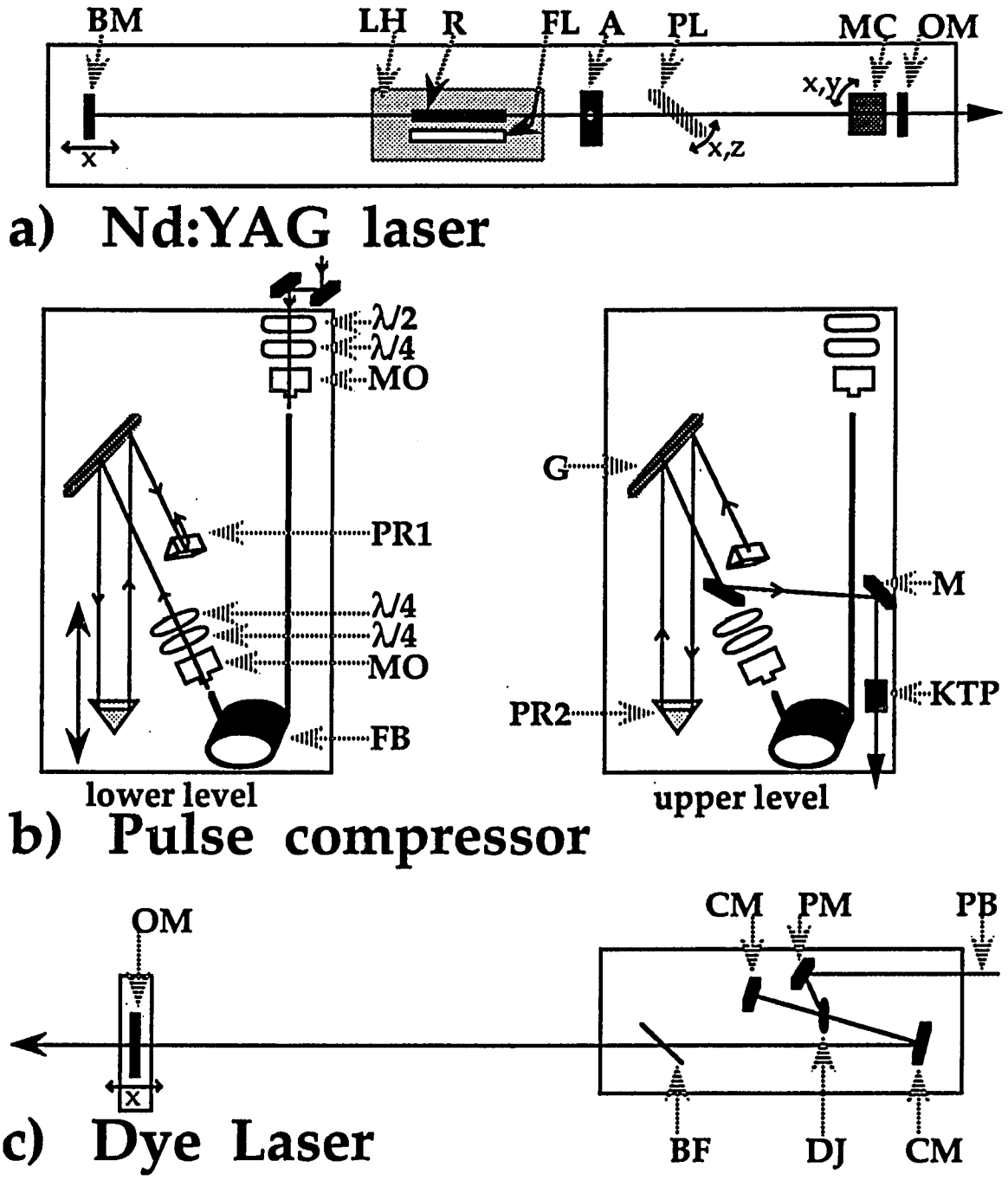

Figure 2.3: The three main components of the laser system. **a) The Nd: YAG mode-locked laser** (BM=back mirror, LH=laser head, R=laser rod, FL=flashlamp, A=aperture, PL=polarizer, MC=mode-locking crystal, OM=output mirror) **b)Pulse compressor** ($\lambda/2$ or $\lambda/4$= half or quarter wave plates, MO=microscope objective lens, FB=optical fiber, PR1= prism to raise the beam, PR2=prism on a translation stage, G=grating, M=mirror, KTP= second harmonic crystal) **c) Dye laser** (PB=532 nm pump beam, PM= mirror focusing the PB on the dye jet, CM=cavity mirror, DJ=dye jet nozzle, OM=output mirror, BF=birefrigent filter)

introduced is on the lamp current of the flashlamp (FL). The manufacturer suggests 17.5 A while we obtain best results using 18.2 A when the FL is new and increasing this current by 0.1 A for every ≈50 hours of operation. The lamp must be replaced after ≈ 300 hours of operation.

To mode-lock the laser it is very important to choose the correct frequency to drive the mode-locking crystal. Using the Mode Locker Driver (M 452) we change the frequency until the Servo Power on the Mode Locker Stabilizer (M 453) is at 80% maximum power and stability has been reached (see next section about alignment). The cavity length must be adjusted using the BM translation assembly to obtain maximum laser output power. Then, the position of the polarizer (which rotates in the x-z plane) must be adjusted for maximum power. Next, the BM, OM and A must be optimized. The last three steps should be repeated until no further improvement of the laser power is observed. At this stage, the laser power should be between 6.5 and 7.5 W. Fine alignment of the laser is required for optimum output power and mode locking conditions.

The fine alignment some times requires a lot of time of careful effort in order to be achieved. At this stage, it is necessary to monitor the laser output using a photodiode. Fig. [2.4] shows the trace in the oscilloscope when a) self-Q-switching is taking place indicating pure mode-locking and b) mode locking has achieved. The trace in the second case (mode-locked display) is smooth showing no spikes or burst of laser output which is the case when self-Q-switching is present. The steps to be followed for the fine alignment are the following:

1- Adjust PL.

2-Adjust cavity length using the BM translation assembly.

3- Adjust A, BM and OM for maximum power and best oscilloscope trace.

(a)

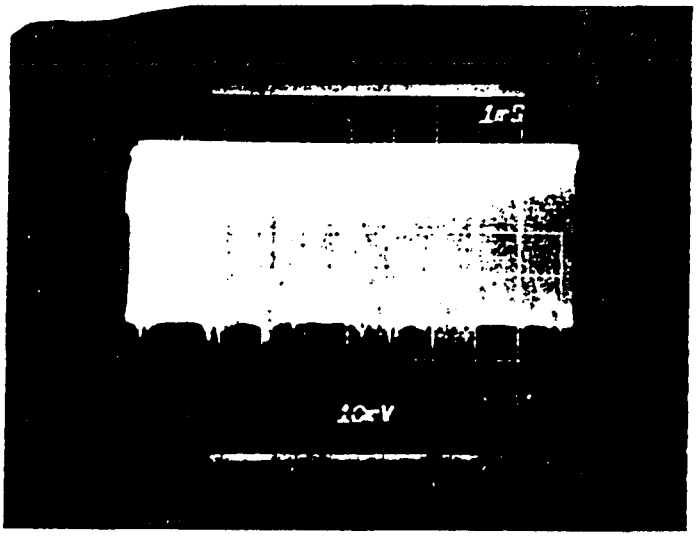

(b)

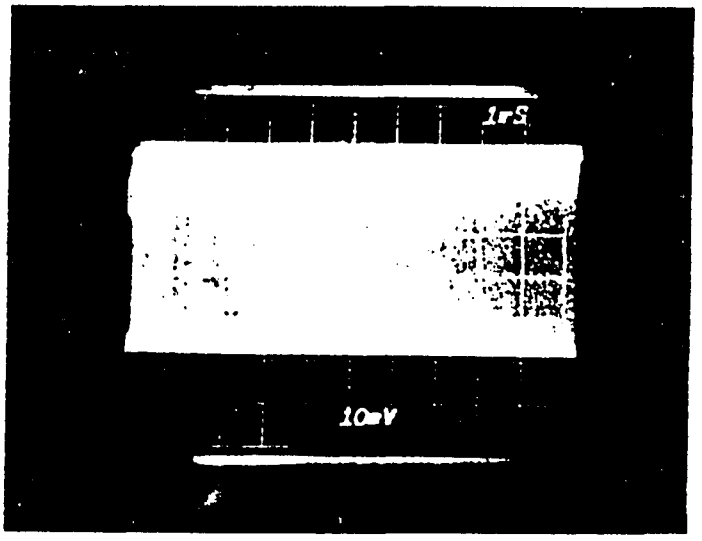

Figure 2.4: Oscilloscope trace from the photodiode at the output of the Nd:YAG laser when a) self-Q-switching is taking place and b) mode locking has achieved. The trace in the second case (mode-locked display) is smooth showing no spikes or burst of laser output which is the case when self-Q-switching is present.

4- Repeat step 3 until no further improvement is observed.

5- Repeat steps 1 to 4 until mode-locking is achieved.

The laser power now should be ≈7.6-8 W. If the oscilloscope trace indicates that the mode locking is still poor, turn off the mode locker (M 451) and start mode-locking the laser by increasing the frequency (using the appropriate procedure) until the previously designated optimum frequency is reached. If there is still a problem, start from the very beginning.

The final stage involves the alignment using the KTP crystal. It is imperative that no spikes, even very small, are present in the oscilloscope trace of the photodiode. That is because, if during the alignment the laser starts self-Q-switching, it is very likely that the KTP crystal will be damaged. For this reason, the alignment should be very careful and the operator very cautious.

6- Inset the frequency doubler unit and monitor the output power.

7- Adjust MC in the x-y plane for maximum power.

8- Adjust A and P for maximum power.

9-Repeat step 7 and 8 until no further improvement.

10- Remove the frequency doubler unit.

11- Adjust A, BM and OM for maximum power and best oscilloscope trace.

12- Repeat step 3 until no further improvement is observed.

13- Repeat steps 11 and 12 until maximum 1064 nm power and best mode-locking on the oscilloscope photodiode trace is achieved.

14- Repeat steps 6 through 14 until optimum performance has been reached.

The maintenance of the laser involves change of the flashlamp (FL) every 300 operational hours and adjustment of the lamp current with minor alignment of the PL, A, BM and OM. In addition, the polarizer (PL) must be cleaned every week while the laser rod (R) and mode locking crystal

(MC) need to be cleaned every three to six months. Dirty mirrors cause mainly difficulty in mode locking while dirty laser rod causes drop in the laser output. Some times reflections from outside the cavity (pulse compressor or other optics) cause self-Q-switching. This is happening because either the reflections are too strong and must be eliminated or the mode locking is poor (usually due to dirty intracavity optics) and small reflections that are always present trigger self-Q-switching.

The output pulses of the mode locked Nd:YAG laser undergo pulse compression in the fiber optic pulse compressor shown in the schematic of fig. [2.3 b]. The pulse compressor reduces the duration of the pulses from ≈ 80 ps (output of the YAG laser) to ≈6.5 ps. For minimum pulse duration and stability of the power of the pulse compressed beam, it is critical to have very good alignment. For this reason I will explain how I used to align this pulse compressor.

The schematic in fig. [2.3 b] shows all the adjustable elements of the pulse compressor. The input IR beam passes a half wave plate followed by a quarter wave plate ($\lambda/2$ and $\lambda/4$). The input energy on the compressor is adjusted by the $\lambda/2$ plate. A microscope objective lens (MO) focuses the beam into an optical fiber (FB). The output from the fiber is collimated by a second MO and passes through two $\lambda/4$ plates. The beam then is reflected by a grating (G) into a prism (PR2) where is reflected back into the grating. The prism (PR2) is on a translation stage and the distance between G and PR2 can be adjusted. The distance between the beams (in and out from the prism) is ≈ 2 cm. The beam is reflected again at the grating towards a second prism (PR1) that raises the height of the back scattered beam by ≈1 cm. All the above are depicted in the left schematic (lower level) of fig. [2.3 b]. The right schematic (upper level) of fig. [2.3 b] shows the path of the beam after

the prism PR1. The beam is reflected back at the grating, from there into the PR2 and returns for the final pass from the grating. The alignment between the PR1, PR2, G and direction of the output beam from the fiber should be such that the four beam-spots on G form a right parallelogram. The output beam from the prisms-grating delay line is exactly above the input beam. Two mirrors are directing the beam into the frequency doubler (KTP) that is consisted by a 3X3X5 mm^3 KTP crystal and two lenses (f=5 cm) to focus the IR beam into the crystal and to collimate the output 532 nm beam. For maximum output at 532 nm we must: a) Achieve good coupling between the input from the YAG beam into the fibber. b) Align the prisms-grating delay line and using the translation stage find the proper distance between G and PR2. c) Find the best relative position between the three $\lambda/4$ plates. d) Find the correct angle for the KTP crystal. The conditions (b), (c) and (d) can be achieved by trying different positions and monitoring the 532 nm output. Best coupling between the Nd:YAG laser beam and the fiber requires careful aligning.

The procedure is the following:

1- Make a nice cut (cleave) on the fiber tip using a single blade cleaver.

2- Using the $\lambda/2$ plate, allow only 1 W in the pulse compressor and place the power meter at the output of the fiber.

3-Use the fine adjustment on the holder of the fiber to get some laser light through the fiber. That can be seen using the IR viewer.

4-Use the fine adjustment on the holder of the microscope objective to maximize the output power.

5- Using the rotating adjustment on the fiber holder place the fiber tip on the focal point of the MO and maximize the output power.

6- Repeat steps 4 and 5 until maximum.

7-Using the vertical adjustment on the IR mirror outside the pulse compressor (see fig. 2.2 b) and the vertical adjustment on the MO, maximize the output power.

8- Repeat step 7 but using the horizontal adjustment.

9-Repeat step 5.

10- Allow full input power using the $\lambda/2$ plate.

11-Repeat step 5 very carefully not to cause any major misalignment that can burn the fiber. The output power should be 4.7-5 W.

Few important observations: a) When the cut of the fiber is not good, the output power usually is small (less than 4.2 W) and back reflection into the YAG laser can cause poor mode locking. b) If the distance between G and PR2 is not the best, the power of the green beam fluctuates significantly. c) The 532 nm output is very sensitive on the position of the $\lambda/4$ plates. There is a number of relative positions between the plates that give acceptable power. One should find the combination that gives the maximum power.

The laser system includes a power stabilizer as shown in fig [2.1]. A small unit containing a beam splitter and a photodetector is monitoring the green output of the pulse compressor. The photodetector signal is processed by the Driver electronics module (M 3270) which is driving an Acousto-optic modulator positioned between the YAG laser and the pulse compressor which is diffracting part of the IR beam in order to keep the 532 nm beam stable. Using the power stabilizer, the 900 mW at 532 nm beam is reduced to $\approx$ 650 mW. A signal output from the Driver electronics module allows the observation of the fluctuations of the 532 nm laser output on the oscilloscope. However, we have experienced difficulties using the stabilizer such as failure to stabilize the 532 nm output in many occasions and frequent burning of the input fiber-tip. The problem with the design of the

power stabilizer is that the fluctuation of the 532 nm laser output in mainly due to reasons other than the fluctuation of the YAG laser output and by modulating the IR input to the pulse compressor we can not solve the real problem. On the other hand, when the YAG laser and the pulse compressor are well aligned, the fluctuation of the 532 nm laser output following pulse compression is so small that no stabilization is needed. For this reason we aborted the use of the acousto-optic modulator of the IR laser power but we continued to use the photodetector unit of the 532 nm laser beam as a diagnostic tool of the status of the laser system. Oscilloscope traces are shown in fig. [2.5] when a) The mode locking is not good and the YAG laser is "slightly" self-Q-switching (the sharp spikes indicate self-Q-switching) b) The pulse compressor is not properly aligned and the output power fluctuates c) The operating condition is optimized and the oscilloscope trace is almost a straight line. Monitoring the output signal of the stabilizer is a valuable tool for optimizing the laser performance and especially the pulse compressor.

The synchronously pumped dye laser is shown in fig [2.3 c]. It is composed by the three cavity mirrors (CM and OM), the dye jet nozzle (DJ), a mirror (PM) that focuses the 532 nm pump laser beam into the dye jet and the birefringent filter (BF) that is used to tune the wavelength of the dye laser. The output mirror has a translation attachment that allows small changes in the cavity length. The cavity length of the dye laser should match the cavity length of the YAG laser for minimum pulsewidth. By adjusting the cavity length, the temporal profile of the output pulses is changing generating longer pulses.[6,7] We have utilized three different dyes for the completion of this work which are rhodamine-6G, DCM and Pyridine-1. For each dye a new set of cavity mirrors is required. More

(a)

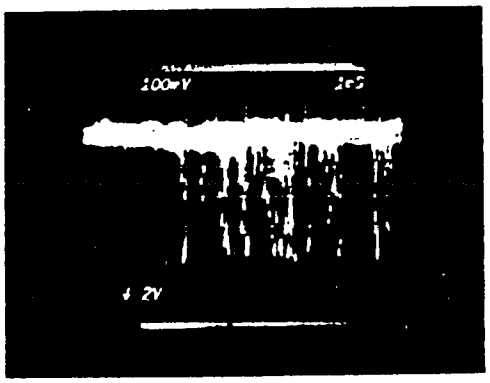

(b)

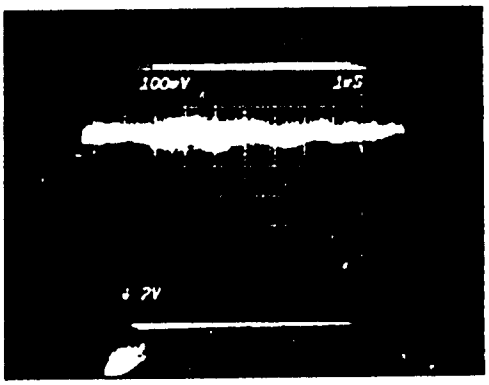

(c)

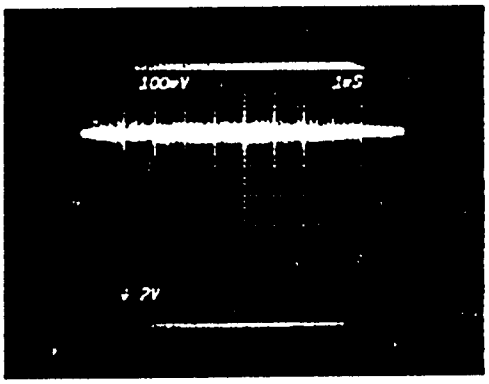

Figure 2.5: Oscilloscope traces from the output of the stabilizer when a) The mode locking is not good and the YAG laser is "slightly" self-Q-switching (the sharp spikes indicate self-Q-switching) b) The pulse compressor is not properly aligned and the output power fluctuates c) The operating condition is optimized and the oscilloscope trace is almost a straight line.

specifically, using rhodamine-6G as dye solution the dye laser is tunable in the 570-635 nm region. Using DCM dye, the tunability extends in the 620-720 region and finally, using Pyridine-1 dye solution the laser can be tuned in the 670-780 nm region. The dye mixing concentrations are a) 1.44 gr R-6G with 1.47 l of Ethylene Glycol and 30 ml Methanol b) 0.68 gr DCM with 900 ml of Ethylene Glycol and 600 ml Propylene Carbonate and c) 0.68 gr Pyridine-1 with 1.275 l of Ethylene Glycol and 225 ml Propylene Carbonate. The alignment of the dye laser is fairly easy. Using a power meter to monitor the output power and the external (horizontal and vertical) controls of the output mirror (OM) and of the mirror (PM) that focuses the pump beam on the dye jet we can carry out the basic alignment of the dye laser. For best output power there are few details that I found to be important which are

1-The direction of the pump beam (532 nm).

2-The divergence of the pump beam (adjusted by the second lens in the frequency doubler).

3- The dye jet should be at the focal point of the pump beam. There is internal mirror pivot that controls the distance between the pump mirror (PM) and dye jet.

4-Frequent cleaning the birefringent filter.

5-Cleaning of the cavity mirrors every few months.

6-The position of the two cavity mirrors noted as CM in fig. [2.3 c] with respect to the pump spot on the dye jet. There are three controls for each mirror (horizontal and vertical and a pivot). This is a rather difficult task but it is required only after major changes in the dye laser alignment. The output pulses are stable if the operating conditions of the laser system are

optimum. In addition, the temperature of the room should be stable, the humidity should be low and the laser must be on a floating optical table.

2.2 Detection system.

The detection system is composed by a SPEX triplemate spectrograph and a Photon-counting Image Acquisition System (PIAS, Hamamatsu, model C1815). Three holographic gratings are used in the spectrograph for best spectral resolution and low noise level. Each grating is located in a different compartment with a set of mirrors that are used to collimate the light before reaching the grating and then to focus the spectrally analyzed light in a slit of adjustable width. The size of the slit determines the spectral width of the light that passes the slit to enter the next compartment. The angle of the first grating is adjustable in order to allow the user to select the desirable spectral region to be farther analyzed (in combination with appropriate selection of the size of the slit). The second grating further purifies the selected spectral region before entering the last compartment. The two initial compartments are called "filter stage" while the last is the "spectrograph stage". The third grating (on the spectrograph stage) in positioned on a rotating base allowing for the selection of grating among three gratings having 600, 1200 and 1800 gr/mm. An external control panel allows the selection of "center" wavelength in the spectrograph stage. The spectral region recorded in the detector depends on the selection of grating. The 600 gr/mm grating has the minimum dispersion which means lower spectral resolution but the spectral width of the light reaching the array detector is larger (≈40 nm). One of these gratings is chosen depending on the specific need of each experiment. The overall transmission through the spectrograph is ≈10% of the input light in the visible. The detector is attached at the output of the spectrograph. For the Raman scattering experiments it is very important to choose the right combination of spectral

range in the filter stage and wavelength setting in the spectrograph stage. This is because we want to have minimum noise due to the laser beam light that "escapes" the filter stage and at the same time to be able to spectrally analyze phonon lines as close as possible to the laser wavelength. The filter stage spectral width should not contain the laser wavelength. However, there is always some laser light that reaches the spectrograph stage. This light can be much stronger than the intensity of the antiStokes Raman lines especially when the sample is at low temperatures. In most of the cases I have been using the 1200 gr/mm grating with the center wavelength at 578 nm (laser wavelength was at 590 nm) so that the laser light is just outside the photosensitive area of the detector. The slit after the first grating of the filter stage is chosen to allow light from the antiStokes Raman lines as close as 180 cm^{-1} from the laser wavelength. In the up-converted luminescence experiments there is no problem with the laser light because the observed luminescence is at higher wavelengths. For these measurements I have been using the 600 gr/mm grating in order to have the maximum detected spectral width.

The two dimensional photodetector PIAS is an extremely sensitive image measurement device that is capable of single photon detection and can detect signals as low as 10 $counts.sec^{-1}.cm^{-2}$. The PIAS is a measuring system that makes use of the photon counter to detect the input position of individual photons and accumulate them to create an image. The unique characteristics of PIAS are derived from its good quantum efficiency, single photon detection capability and its residual low noise level (≈6 counts/sec). The two dimensional image obtained, is composed by 512X512 pixels where each photon detected is recorded as a dot in the computer screen. The principals of operation of the PIAS detector are shown in fig. [2.6]. The

photons that reach the photocathode are converted to electrons (photoelectrons). The electrons are amplified 10^7 times by 3-stage MCP, then being accelerated, they impinge upon the PSD (position sensitive detector). The electron bombardment effect on the PSD causes the electrons to increase a further 10^2 times, resulting in a total electron gain of 10^9. The electric charge at the incident position on the PSD is collected by four electrodes. The current collected by an electrode is inversely proportional to the distance between the incident position and the electrode. The signals output of the PSD are fed through a pre-amp to a position analyzer. Here the individual input positions are detected by means of center of gravity arithmetic. Following this they undergo A/D conversion and are output as digital signals.

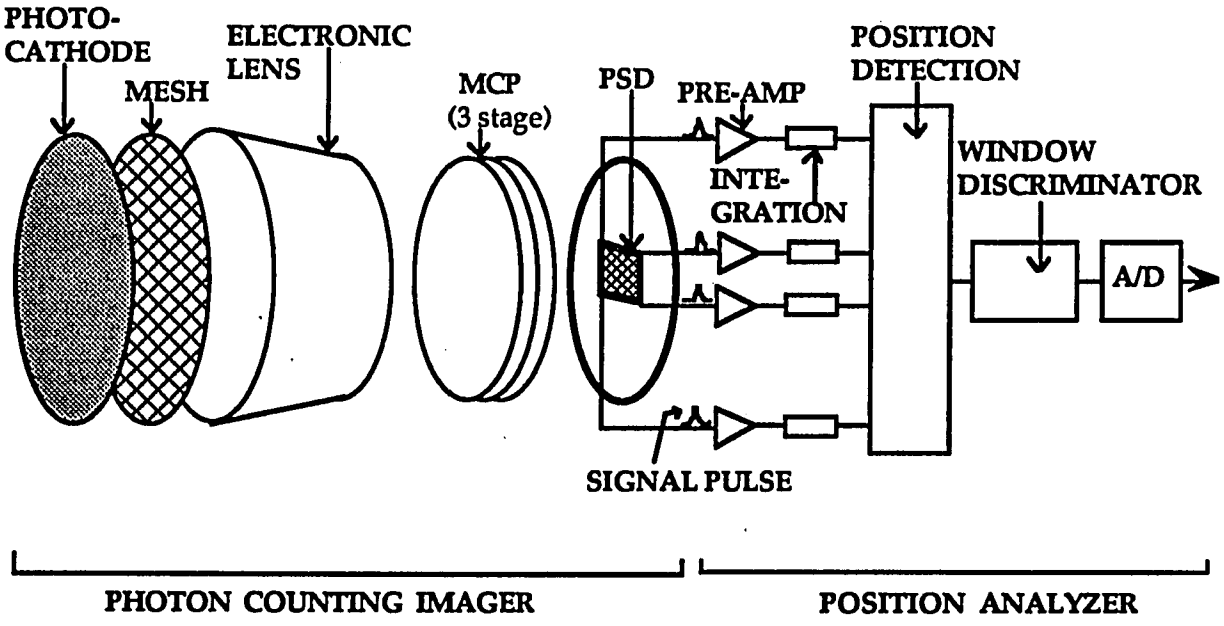

Figure 2.6 Schematic showing the principal of operation of the PIAS photon-counting detector

The sensitivity of PIAS extends in the 280-780 nm spectral region and its average quantum efficiency is ≈15%. The spectral response is given in fig. [2.7]. Energy discrimination is used to eliminate noise signal pulses (cosmic rays etc.) which are larger that the pulses gained from the photon as well as smaller pulses (thermions etc.), thus providing only the signal pulses. According to the manufacturer, the calculated signal/noise (S/N) ratio expresses the value when the noise is assumed to be the square root of the count number (signal). This means that the PIAS noise is composed of quantum noise of photons themselves, thus the theoretical limit in S/N ratio is obtained making it the most sensitive image measurement device currently available. This is due to the design of PIAS. A photon is generating a charge of the order of 10^{-19} C on the photocathode. But when this signal reaches the PSD is already amplified by 10^{-9} times providing a strong signal pulse (10^{-10} C) to the counting electronics that eliminates quantum noise due to the signal current. To compare PIAS with the CCD detector, the photocharge in CCD is not amplified (remains at the level of 10^{-19} C) before detection by the counting electronics introducing quantum noise due to the low charge. This is most important in very low photon counting levels where PIAS has a distinctive advantage. The dynamic ranges of different detectors are given in fig. [2.8] for comparison. It is clear that PIAS is the best available detector for low light intensity measurements. To give a practical example about the sensitivity of PIAS, I will give an example of one antiStokes Raman measurement at low temperature. After one hour of light collection I could observe a phonon line that its overall integrated intensity (in a 10X10 pixels area of the detector) was 30 counts above the noise level (≈15 counts). This means that the actual detected signal for each pixel was 0.3 counts/hour!

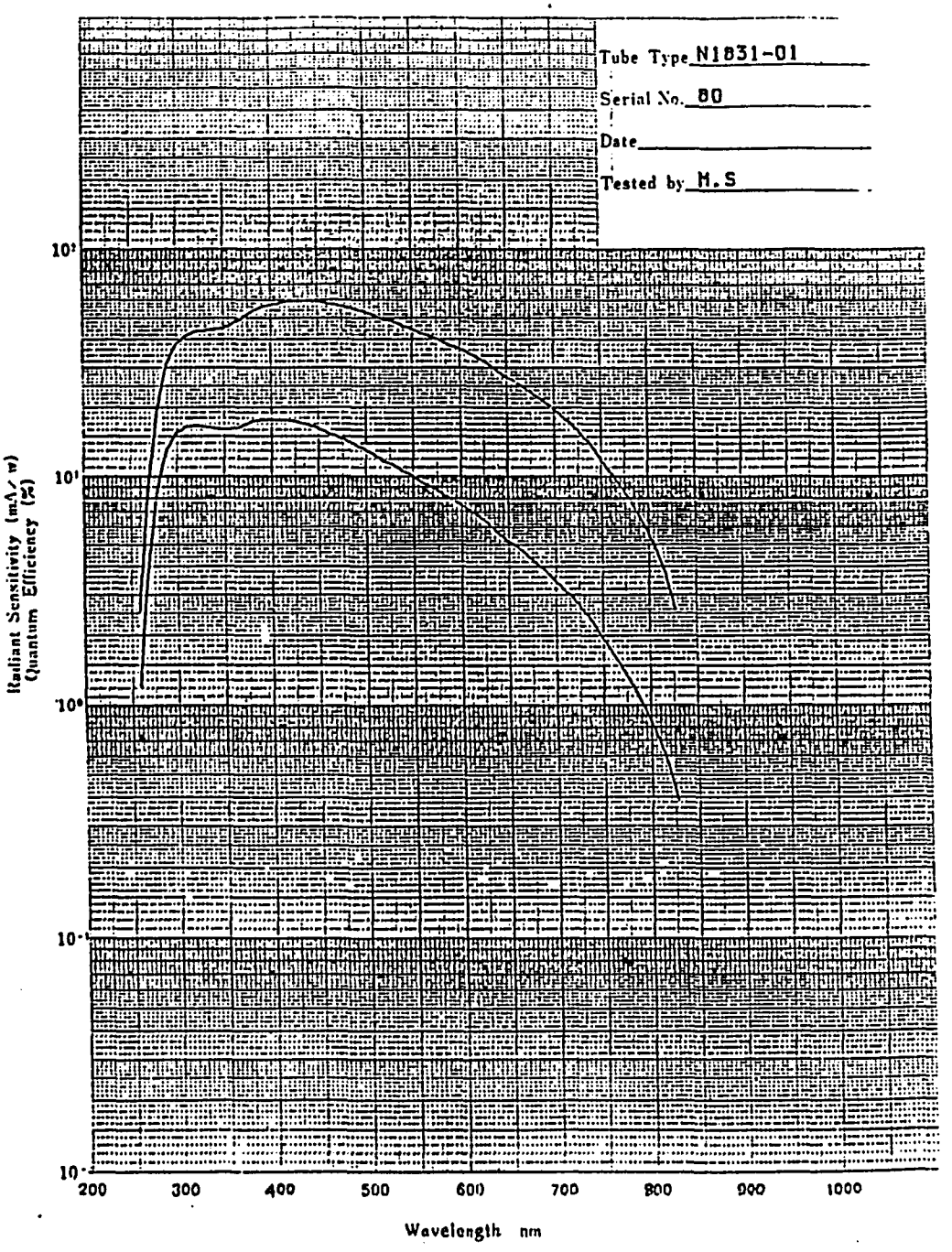

Figure 2.7: The spectral response curve of the PIAS detector. (Data obtained from Hamamatsu Photonics).

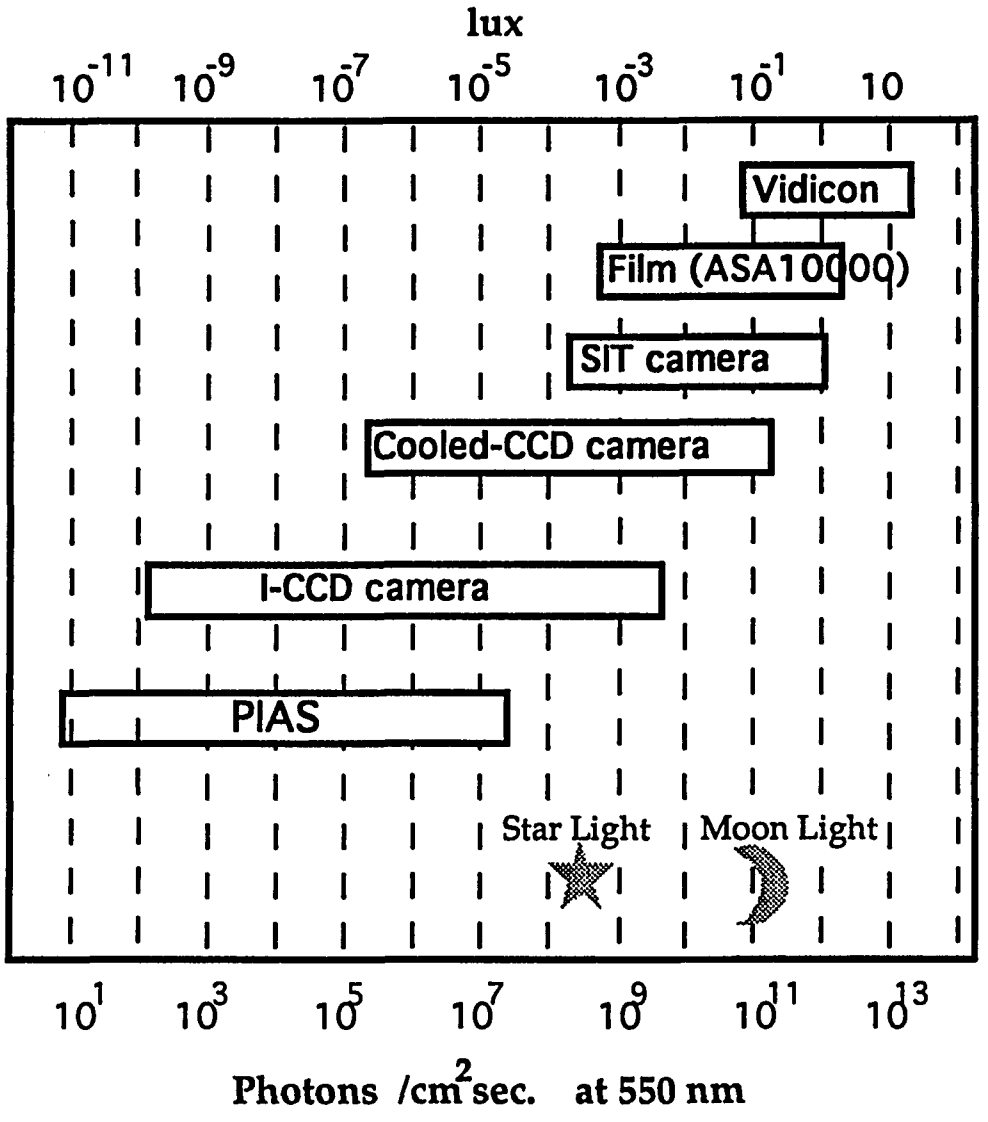

Figure 2.8: Dynamic ranges of different detectors. The PIAS detector is the most sensitive detector available but it operates only at low count signal levels. (Data obtained from Hamamatsu Photonics).

The design of PIAS that is so efficient at low counts creates problems when a relatively strong signal must be recorded. The PSD cannot distinguish as separate events signal pulses that arrive at times shorter than 10 μsec. If two photons arrive within 10 μsec, the electronics will detect only one event at a position which is the average of the original two. If the light level exceeds certain level (10000 count/ sec), the detector automatically shuts off. That means the PIAS detector can only be used with CW lasers or high repetition mode locked lasers where the generated signal per pulse is very low. PIAS cannot be used with lasers that have large energy per pulse that can generate many photons of the signal to be detected per laser pulse. For this reason, all my measurements were performed using the low in energy per pulse high repetition rate mode locked laser beam. The input signal level was always kept below 2000 count/sec in order to avoid the problems mentioned above.

The two dimensional image obtained by PIAS is transformed into a spectral profile calibrated in the desirable units using appropriate software that I have developed. There is a number of programs to perform different operations depending on the particular experiment. This software is provided in the appendix. For the room temperature Raman experiments the software integrates the counts in the vertical axis over a selectable window and displays the Raman spectral profile in cm^{-1}. Some of the options of this program are: smoothing, integration over the phonon peaks above the luminescence background, save the profile in ASCII, subtract prófiles of two spectral images etc. For the low temperature Raman measurements the program has the additional options of opening two windows, one that contains the image of the spectrum and a second that contains only background noise. By subtraction of the spectra contained in

these two windows we obtain the low T antiStokes Raman spectrum. Another option is to omit parts of the spectrum that are too strong in intensity and do not allow the observation of the fine structure of other parts of the spectrum as for example the high energy phonon modes. The program utilized for the up-converted luminescence measurements provides the selection of the units (eV, cm^{-1} or nm) we want to use in the calibration of the spectrum. The combination of PIAS and the holographic gratings of the spectrograph provides an overall very high sensitivity which is very important for the type of experimental work required in this research.

2.3 References.

1. "Ultrashort Pulse Measurements", D. J. Bradley and Geoffrey H. C. New, Proceedings of the IEEE, Vol. 62, No 3, (1974).

2. "Picosecond Laser Techniques and Design", A. G. Doukas, J. Buchert and R. R. Alfano, "Biological Events Probed by Ultrafast Laser Technology", Edited by R. R. Alfano, (1982).

3. "Ultrafast Laser Technology: The New Frontier in Optics", P. Delfeyett, S. K. Gayen and R.R. Alfano, Encyclopedia of Physical Science and Technology, Edited by R. A. Meyers, Academic Press, New York, (1987).

4. "Ultrafast Laser Technology", Roger Dorsinville, Proceedings of the IEEE, (1988).

5. "Picosecond laser Pulses", A. J. DeMaria, W.H. Glenn, M. J. Brienza and M. E. Mark, Proceedings of the IEEE, Vol. 57, No 1, (1969).

6. C. P. Ausschnitt, R. K. Jain and J. P. Heritage, IEEE J. Quantum Electron., Vol. QE-15, No 9, (1979).

Chapter 3
Theoretical Background.

3.1 Introduction.

In this thesis research I study the physics involved in the nonradiative relaxation of ion in crystals. The investigation involves the vibronic levels populated during the nonradiative relaxation and the nonequilibrium phonons generated. More specifically, studying the hot luminescence arising from the short-lived vibronic levels I have obtained information concerning the phonon modes involved in the vibrational relaxation and the relaxation dynamics. In addition, using time resolved Raman scattering, I have measured the kinetics of the nonequilibrium phonon modes associated with the relaxation of Cr ions in a forsterite crystal.

In chapters 5 and 6, I will present the experimental data and the theoretical models used to fit the data. Before that, it is appropriate to present in this chapter some formal quantum mechanical principals required to understand the fundamental concepts of the ion-lattice interaction and the interactions associated with radiative and nonradiative transitions as well as basic theoretical concepts of the Raman scattering process.

3.2 Ions in a lattice environment.

3.2.1 Fundamental interactions.

An impurity ion in a crystal participates in the vibrational motion of the host lattice, and this motion affects its optical properties. The Hamiltonian operator, H, describing the system is:

$$H=H_{FI}(\mathbf{r}_i)+H_c(\mathbf{r}_i,\mathbf{R}_l)+V_l(\mathbf{R}_l)+\sum_l \frac{\mathbf{P}_l^2}{2M_l} \tag{3.1}$$

where, $H_{FI}(\mathbf{r}_i)$ is the free ion Hamiltonian, $H_c(\mathbf{r}_i,\mathbf{R}_l)$ is the crystal field Hamiltonian, $V_l(\mathbf{R}_l)$ is the interior lattice potential energy, and the last term is the kinetic energy of the lattice ions. $(\mathbf{r}_i)$ is the position of the ith electron of the impurity ion while $(\mathbf{R}_l)$ and $(\mathbf{P}_l)$ are the position and momentum of the lth lattice ion.

The last two terms compose the lattice Hamiltonian ($H_{lattice}$) which is describing the lattice vibrations. If we neglect the anharmonic terms in the forces acting between the lattice ions, the vibrational modes are referred to as phonons. In this case, the lattice Hamiltonian becomes:

$$H_{lattice}=\sum_{\mathbf{k}} h\omega_{\mathbf{k}}(\alpha_{\mathbf{k}}^{+}\alpha_{\mathbf{k}}+\frac{1}{2})=\sum_{\mathbf{k}} h\omega_{\mathbf{k}}(n_{\mathbf{k}}+\frac{1}{2}) \tag{3.2}$$

where $\mathbf{k}$ refers to different lattice phonon modes of energy $h\omega_{\mathbf{k}}$ and $\alpha^{+}_{\mathbf{k}}$ ($\alpha_{\mathbf{k}}$) is the creation (annihilation) operator. The quanta of vibrational energy are the phonons. The definition of the operators $\alpha^{+}_{\mathbf{k}}$ and $\alpha_{\mathbf{k}}$ is given by:

$$\alpha_{\mathbf{k}}=\left(\frac{1}{2Mh\omega_{\mathbf{k}}}\right)^{\frac{1}{2}}(M\omega_{\mathbf{k}}\mathbf{Q}_{\mathbf{k}}^{+}+i\mathbf{P}_{\mathbf{k}}) \tag{3.3}$$

$$\alpha_{\mathbf{k}}^{+}=\left(\frac{1}{2Mh\omega_{\mathbf{k}}}\right)^{\frac{1}{2}}(M\omega_{\mathbf{k}}\mathbf{Q}_{\mathbf{k}}-i\mathbf{P}_{\mathbf{k}}^{+}) \tag{3.4}$$

where $\mathbf{Q}_{\mathbf{k}}$ and $\mathbf{P}_{\mathbf{k}}$ are the normal coordinates and momenta respectively. A phonon mode is a "vibration" of the normal coordinate $\mathbf{Q}_{\mathbf{k}}$ which is

composed of displacements of a group of lattice ions in specific directions and multiplied by appropriate phase factors.

The free ion Hamiltonian is:

$$H_{FI}=\sum_i \left(\frac{\mathbf{p}_i^2}{2m_i}+V'(\mathbf{r}_i)\right)+\sum_{i>j}\left(\frac{e^2}{4\pi\varepsilon_0 r_{ij}}\right)+\sum_i \zeta(\mathbf{r}_i)\,\mathbf{l}_i.\mathbf{s}_i \qquad (3.5)$$

where i refers only to the outer shell electrons. The first term describes the kinetic and potential energy of electrons, the second term is the interaction between the outer electrons and the third term is the spin-orbit interaction.

The crystal field Hamiltonian is

$$H_c(\mathbf{r}_i,\mathbf{R}_l)=\sum_i\sum_l H_{cl}(\mathbf{r}_i,\mathbf{R}_l) \qquad (3.6)$$

representing the Coulomb interaction of the outer shell electrons of the impurity ion with the neighboring lattice ions occupying positions $\mathbf{R}_l$.

The problem with the ion-lattice Hamiltonian H is the term $H_c(\mathbf{r}_i,\mathbf{R}_l)$, which contains the impurity ion electron coordinates ($\mathbf{r}_i$) and the lattice ions coordinates ($\mathbf{R}_l$). As a result, H_c couples the electronic motion with the vibrations of the lattice ions.

3.2.2 The Adiabatic approximation.

To achieve a solution for the ion-lattice Hamiltonian, the electronic and ionic variables must be decoupled. Let's first assume that the lattice is "frozen". In this case, we can omit the kinetic energy of the lattice ions in eq. 3.1. The lattice ions coordinates ($\mathbf{R}_l$) are regarded as parameters and the Hamiltonian H_o (eq. 3.1) in the static lattice approximation becomes:

$$H_o = H_{FI}(\mathbf{r}_i) + H_c(\mathbf{r}_i, \mathbf{R}_l) + V_l(\mathbf{R}_l)$$

$$= H_e(\mathbf{r}_i, \mathbf{R}_l) + V_l(\mathbf{R}_l) \qquad (3.7)$$

where $H_e(\mathbf{r}_i, \mathbf{R}_l)$ is the electronic part of the Hamiltonian. $V_l(\mathbf{R}_l)$ is included in H_o because the overall lattice potential energy depends on the coupling between the impurity ion and the rest of the lattice. Assuming the ion in the electronic state (a) described by the eigenfunction $\Psi_a(\mathbf{r}_i, \mathbf{R}_l)$ of the Hamiltonian H_o, the energy eigenvalue depends parametricaly on the sets of $\mathbf{R}_l$ values chosen and is given by:

$$E^a(\mathbf{R}_l) = \langle \Psi_a | H_e(\mathbf{r}_i, \mathbf{R}_l) | \Psi_a \rangle + \langle \Psi_a | V_l(\mathbf{R}_l) | \Psi_a \rangle \qquad (3.8)$$

$$= H_e^a(\mathbf{R}_l) + V_l^a(\mathbf{R}_l)$$

where $H_e^a(\mathbf{R}_l)$ is the electronic energy of the ion in the static field. The interionic energy $V_l^a(\mathbf{R}_l)$ depends on the electronic state (a) of the impurity ion.

Let's return to the dynamic lattice, seeking for eigenfunctions of the form $\{\Psi_a(\mathbf{r}_i, \mathbf{R}_l)\chi_a(\mathbf{R}_l)\}$ where Ψ_a is an eigenstate of H_o and $\chi_a(\mathbf{R}_l)$ is a function of the variables $\mathbf{R}_l$. The Schrödinger equation is

$$\left[H_0+\sum_l \frac{\mathbf{P}_l^2}{2M_l}\right]\Psi_a(\mathbf{r}_i,\mathbf{R}_l)\chi_a(\mathbf{R}_l)=E\Psi_a(\mathbf{r}_i,\mathbf{R}_l)\chi_a(\mathbf{R}_l) \tag{3.9}$$

Using $\mathbf{P}_l=-ih\nabla_l$ we obtain

$$\frac{\mathbf{P}_l^2}{2M_l}\Psi_a\chi_a=\frac{h^2}{2M_l}\{\chi_a\nabla_l^2\Psi_a+2(\nabla_l\chi_a)\cdot(\nabla_l\Psi_a)+\Psi_a\nabla_l^2\chi_a\} \tag{3.10}$$

If the dependence of Ψ_a on $\mathbf{R}_l$ is weak, the first two terms in eq. 3.10 may be neglected since they are small in comparison with the last term. This assumption imposes that the ion cannot change electronic state due to vibrations of the lattice ions but rather the electronic state is "adjusting" to the changes. Since the electronic motion is much faster than the lattice vibrations, the above approximation seems reasonable. This approximation is known as the **Born-Oppenheimer** or as the **adiabatic approximation**. The neglected terms are mixing different electronic states. If the energy separation between electronic states is large, the adiabatic approximation should be valid. Using the Born-Oppenheimer approximation, the Schrödinger equation becomes

$$[H_0\Psi_a(\mathbf{r}_i,\mathbf{R}_l)]\chi_a(\mathbf{R}_l)+\left[\frac{-h^2}{2M_l}\nabla_l^2\chi_a(\mathbf{R}_l)\right]\Psi_a(\mathbf{r}_i,\mathbf{R}_l)$$

$$=E\Psi_a(\mathbf{r}_i,\mathbf{R}_l)\chi_a(\mathbf{R}_l) \tag{3.11}$$

Ψ_a is an eigenfunction of H_o and eq. 3.11 reduces to

$$\left[\sum_l \frac{-h^2}{2M_l}\nabla_l^2+E^a(\mathbf{R}_l)\right]\chi_a(\mathbf{R}_l)=E\chi_a(\mathbf{R}_l) \tag{3.12}$$

The lattice ions oscillate about an average position that depends on the electronic state. We can write $\mathbf{R}_l$ as

$$\mathbf{R}_l=\mathbf{R}_l^a(0)+\mathbf{q}_l^a \tag{3.13}$$

The energy $E^a(\mathbf{R}_l)$ of the impurity ion becomes

$$E^a(\mathbf{R}_l) = H_e^a(0) + H_e^a(\mathbf{q}_l) + V_l^a(0) + V_l^a(\mathbf{q}_l)$$

$$= E^a(0) + V^a(\mathbf{q}_l^a) \tag{3.14}$$

The first term ($E^a(0)$) is the average energy while the second term ($V^a(\mathbf{q}_l^a)$) gives the effect of the lattice vibrations on the electronic energy and the interionic potential energy. The Schrödinger equation for the lattice (eq. 13) can now be written

$$\left[\sum_l \frac{\mathbf{P}_l^2}{2M_l} + V^a(\mathbf{q}_l^a)\right]\chi_a(\mathbf{q}_l^a) = \left(E - E^a(0)\right)\chi_a(\mathbf{q}_l^a) \tag{3.15}$$

Replacing the individual atoms displacement $\mathbf{q}_l$ with the normal coordinates Q_k we can write the lattice states as $\chi_a(Q_k)$. If $V^a(Q_k)$ is harmonic in the normal coordinates then the lattice eigenstates are

$$\chi_a = \prod_k |n_k\rangle \tag{3.16}$$

and the total energy is given by

$$E = E_0^a + \sum_k \hbar\omega_k^a\left(n_k + \frac{1}{2}\right) \tag{3.17}$$

n_k is the number of phonons in the kth mode. At temperature T, the average $\langle n_k\rangle$ is given by the Bose-Einstein factor $\langle n_k\rangle = (\exp(\hbar\omega/kT) - 1)^{-1}$

3.2.3 Single Configurational Coordinate model.

The electronic part of the $\Psi_a(\mathbf{r}_i, \mathbf{R}_l)\chi_a(\mathbf{R}_l)$ state is an eigenstate of H_0 (eq. 3.7) with energy $E^a(\mathbf{R}_l)$ given by eq. 3.8 and $\mathbf{R}_l$ is a set of parameters. In practice, a set of fixed parameters $\mathbf{R}_l(0)$ is used, and the ion-lattice system is described with the "crude Born-Oppenheimer states"

$\Psi_a(r_i, R_l(0))\chi_a(R_l)$. In the lattice states $\chi_a(Q_k)$, there are many vibrational modes to be taken into account making the analysis very difficult. For this reason, the simplification of one vibrational mode (breathing mode) has been adapted. The distance from the central impurity ion to the first shell of neighboring ions is labeled Q, and it is the variable configurational coordinate of the lattice state. Q is vibrating about its equilibrium value Q_0 and the crude Born-Oppenheimer wavefunction and potential energy can be written as

$$\Psi_a(r_i, Q_0^a)\chi_a(Q) \tag{3.18}$$

$$E^a(Q) = E^a(0) + V^a(Q) \tag{3.19}$$

This model is called the "single configurational coordinate model".

Fig. [3.1] shows the energy diagram based on the single configurational coordinate model. Two electronic states (a) and (b) are shown and their energy $E^a(Q)$ and $E^b(Q)$ is drawn as function of Q. The energy of the electronic state for rigid lattice is $E^a(0)$ and $E^b(0)$ respectively. The equilibrium positions are different and there is a shift ($Q_0^a - Q_0^b$) between the two energy minima. The solid curve is a Morse potential while the broken curve is the energy in the harmonic approximation. When the ion changes electronic state, it suddenly acquires a different equilibrium position and it start oscillating about its new equilibrium point. The diagram in fig. [3.1] is known as the configurational coordinate diagram.

3.2.4 Absorption and Emission transitions.

The radiative transitions between different electronic states (a) and (b) of an ion are possible by the absorption or emission of a photon. The process

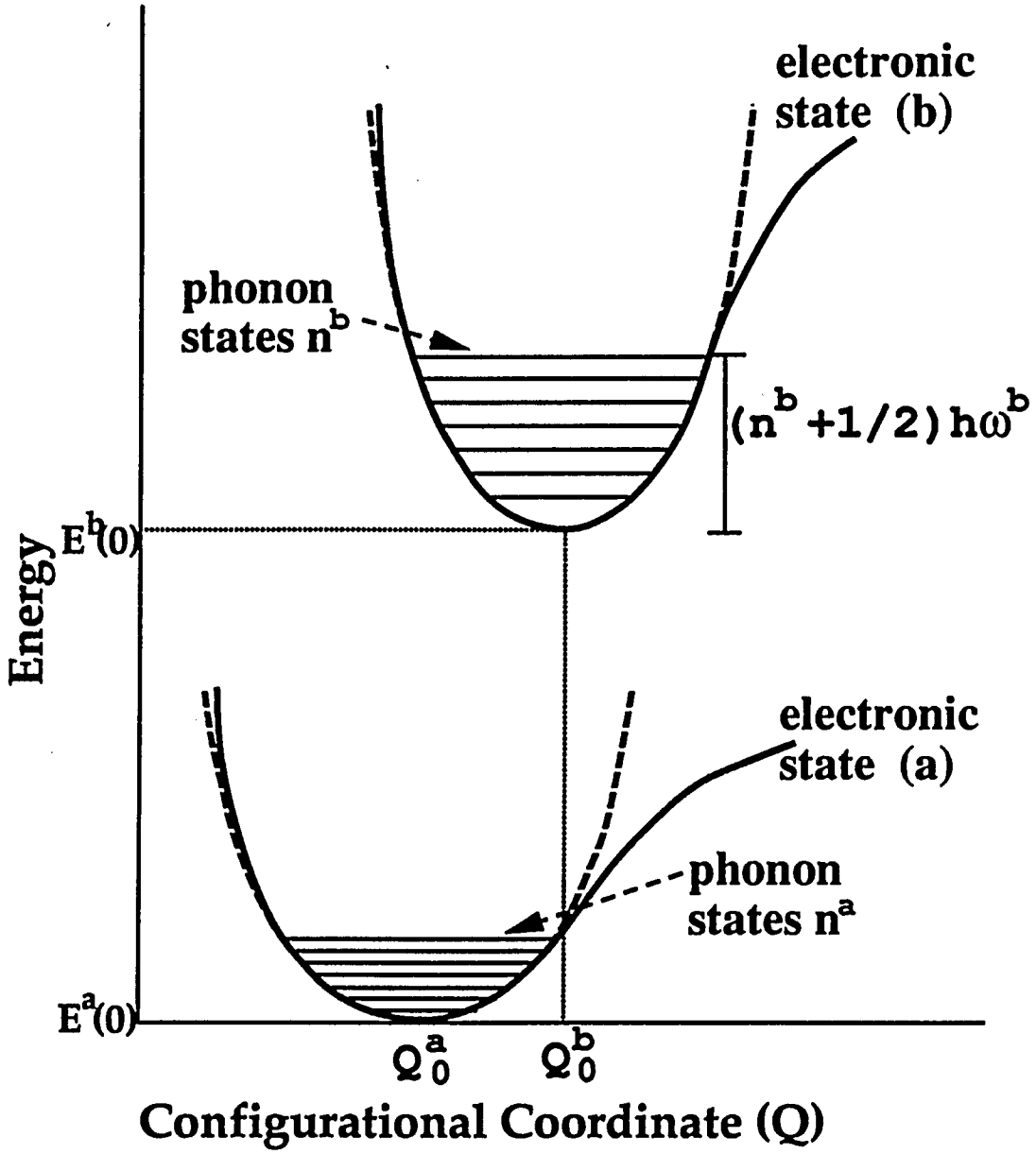

Figure 3.1. The ionic potential energy curves in the case of breathing-mode" vibrations when the electronic center is in states a and b. The broken curves are the approximate harmonic oscillator potentials.

is depicted in fig. [3.2] where the single configurational coordinate model in the harmonic approximation has been adapted.

For absorption, a photon with energy $h\omega_{ab}=E^b(Q_0^a)-E^a(0)$ is required. For the transition from the state (b) to the state (a), a photon with energy $h\omega_{ba}=E^b(Q_0^a)-E^a(0)$ is emitted. The difference between the energy of the ion following absorption and the minimum energy of the excited state (b) $E_{dis}=E^b(Q_0^a)-E^b(0)$ is going to be given into the lattice environment. In the present model, this energy is equal to the energy of S phonons of the breathing mode, that is, $E_{dis}=Sh\omega$. This means that when the S parameter is big, there is a large shift between the ground state and the excited state parabolas. For $S=0$, the two parabolas shown in fig. [3.1] are aligned in the Q-axis, that is $Q_0^a=Q_0^b$. The parameter S is called Huang-Rhys parameter. The S parameter characterizes the difference in electron lattice coupling between electronic states.

The transition probability W_{if} is defined as the probability of a transition from a state $|i\rangle$ to a state $|f\rangle$ per unit time and is given by Fermi's Golden Rule

$$W_{if}=\frac{2\pi}{h^2}|V_{fi}|^2\rho(E_f-E_i) \tag{3.20}$$

where V_{fi} is the matrix element of the interaction causing the transition and ρ is the density of states. The interaction making the transition possible can be either electric dipole (ED), magnetic dipole (MD) or electric quadruple (EQ). The relative strengths of the three allowed transitions are in the approximate ratio of ED:MD:EQ$\approx$1:10^{-5}:10^{-6}. Depending on the selection rules, one of the above interactions becomes dominant. For example, if there is inversion symmetry, ED transitions are not allowed and the MD

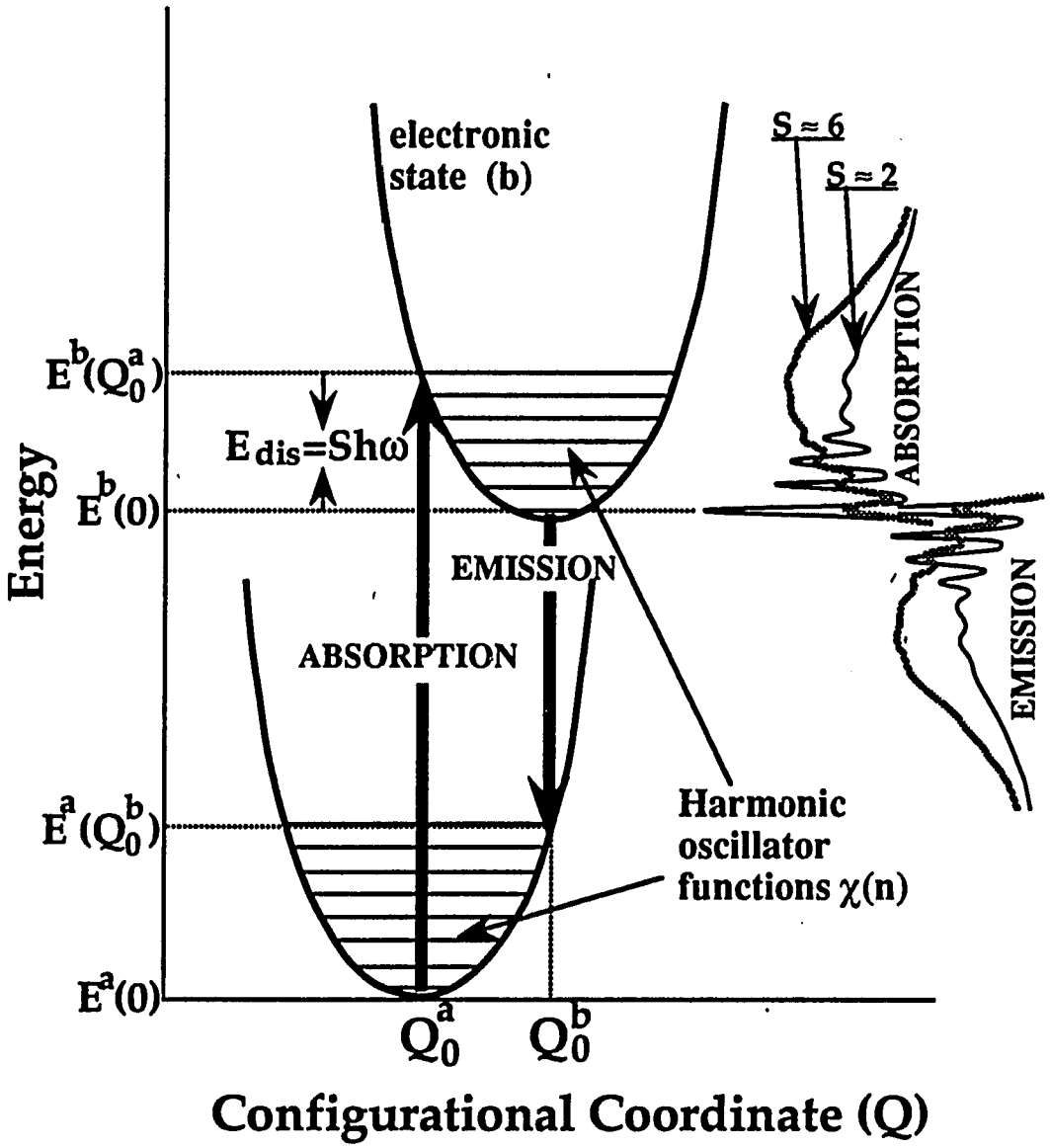

Figure 3.2. Configurational coordinate diagram in the harmonic approximation for electronic states a and b. The shape of the absorption and emission band depends on the configurational coordinate displacement between the ground state and the excited state parabolas.

transitions will contribute the most in the overall absorption or emission spectrum.

The probability for transition from an electronic-vibrational (vibronic) state (a,n) to a vibronic state (b,m) is proportional to the square of the matrix element

$$\langle \Psi_b(r_i, Q)\chi_b(m) \mid \mu \mid \Psi_a(r_i, Q)\chi_a(n) \rangle \tag{3.21}$$

where the integration is over the electronic and vibrational coordinates and μ is the appropriate electronic dipole operator. At very low temperatures, the ions occupy the lowest vibronic level of the electronic state. In this case, we can replace in eq. 3.21 the variable Q with the value of Q_0^a. Expansion of this assumption for $n \neq 0$ is known as the Gordon approximation where the matrix element of eq. 3.21 is given approximately by

$$\langle \Psi_b(r_i, Q_0^a) \mid \mu \mid \Psi_a(r_i, Q_0^a) \rangle \langle \chi_b(m) \mid \chi_a(n) \rangle \tag{3.22}$$

The first term is the contribution of the electronic state and represents the electronic transition probability while the second term is the contribution of the vibrational part of the ion-lattice wavefunctions. Notice, the first term is independent from the vibrational wavefunction. The transition probability can be written as

$$W_{an\text{-}bm} = P_{ab} \mid \langle \chi_b(m) \mid \chi_a(n) \rangle \mid^2 \tag{3.23}$$

where P_{ab} is the purely electronic transition probability. The overall shape of the absorption spectrum from the state (a, n) to the state (b) is given by

$$I_{an\text{-}b}(E) = I_0 R_n \sum_m \mid \langle \chi_b(m) \mid \chi_a(n) \rangle \mid^2 \delta(E_{b,m} - E_{a,n} - E) \tag{3.24}$$

where R_n is the thermal average over the initial vibrational states $|n>$ and I_o the intensity of light available for absorption. The shape of the emission spectrum from the state (a, n) to the state (b) is given by

$$I_{an-b}(E)=R_n'\sum_m |<\chi_b(m)|\chi_a(n)>|^2\delta(E_{b,m}-E_{a,n}-E) \tag{3.25}$$

where R_n' is the average population of the initial vibrational states $|n>$. In both cases (eqs. 3.24 and 3.25), $\chi_b(m)$ and $\chi_a(n)$ are harmonic oscillator functions but are defined with respect to deferent zeros in the Q-axis, thus

$$<\chi_b(m)|\chi_a(n)>=\exp(\frac{-A^2}{4})(\frac{n!}{m!})^{1/2}(\frac{-A}{\sqrt{2}})^{m-n}L_n^{m-n}(\frac{A^2}{2}) \tag{3.26}$$

where L_n^{m-n} are the associated Laguerre polynomials of which $L_0^{m-n}(x)=1$ and $A=(M\omega/h)^{1/2}(Q_0^b-Q_0^a)$. At T=0, only the lowest vibrational level of the state (a) is occupied and eq. 3.26 becomes

$$|<\chi_b(m)|\chi_a(0)>|^2=\frac{\exp(-S)S^m}{m!} \tag{3.27}$$

The transition band shape at T=0 becomes

$$I_{a-b}(E)=I_0\sum_m\frac{\exp(-S)S^m}{m!}\delta(E^b(0)-E^a(0)+mh\omega-E) \tag{3.28}$$

The above band shape is composed by a series of delta-function lines at energies differing by $h\omega_{phonon}$ having different intensities. The relative intensity of the lines depends on the S parameter. The features of eq. 3.28 are depicted in fig. [3.3]. For S=0, only the first line is different from zero. For increasing S, the intensity of the first line decreases while the other phonon lines increase their intensity creating a sideband. In reality, the lines shown in fig. [3.3] are replaced with peaks in a continuous spectrum. For small S parameter, there is a number of peaks followed by a continuous spectrum

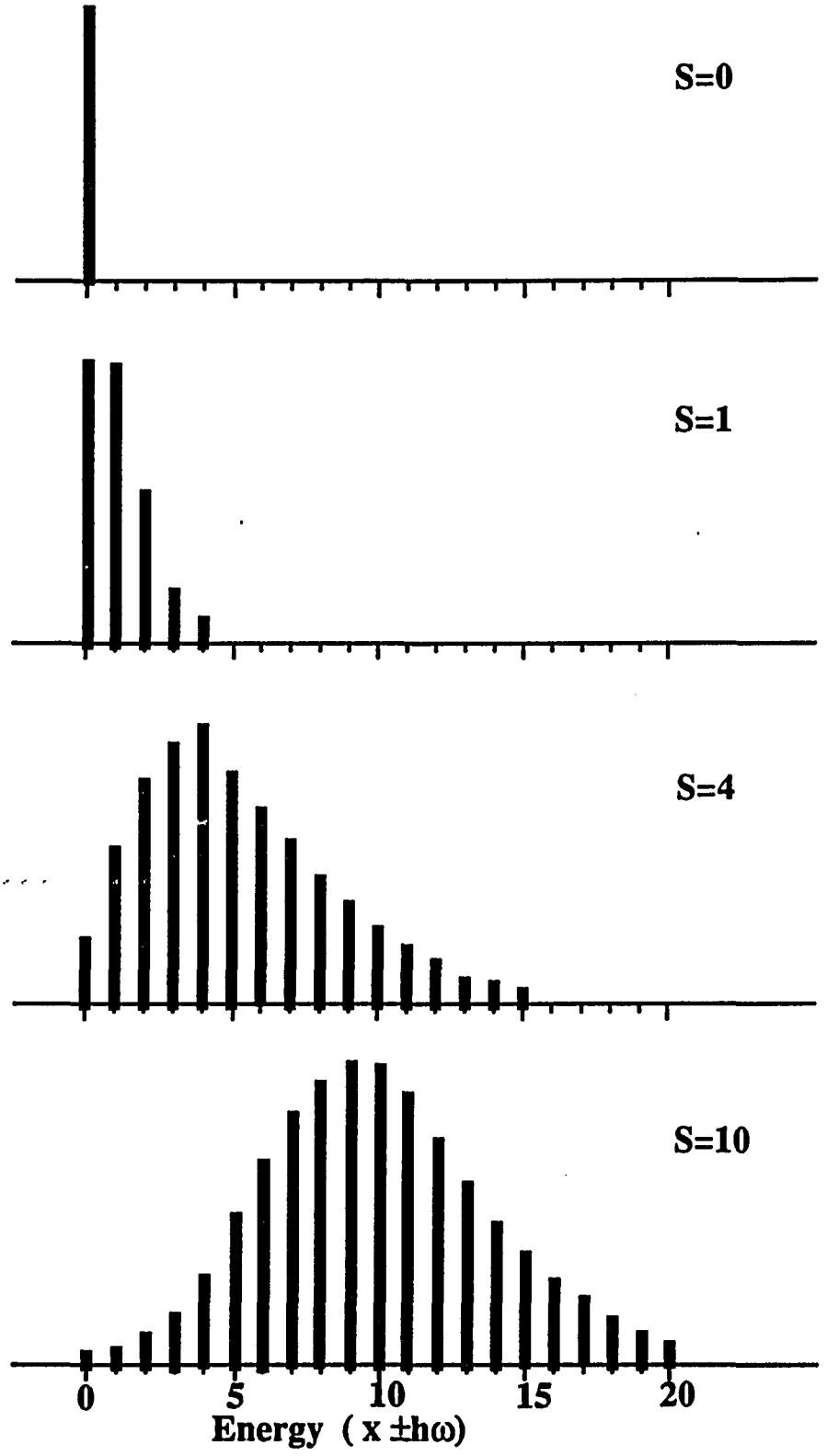

Figure 3.3. The relative intensities of the different vibrational peaks in the absorption or emission spectrum (+hω or -hω in the energy axis respectively) as function of the Huang-Rhys parameter. The envelope of the individual intensities gives the predicted band shapes.

(see fig. [3.2]). The relative intensity of the peaks can be explained by eq. 3.28. In the case of large S, the phonon peak structure is smeared out into a continuous broadband spectrum.

Interesting conclusion can be reached from eqs. 3.24 and 3.25 if we take into account that $\sum_m |\langle\chi_b(m)|\chi_a(n)\rangle|^2=1$. We can see that the overall intensity is independent from the value of S and temperature and depends only on the average population of the initial states. For $S\neq0$ or $T\neq0$, intensity from the zero phonon transition is transferred into the sideband but the integrated intensity remains the same. In the emission spectrum (eq. 3.25), the dependence only on R_n' plays an important role in the shape of the overall hot luminescence spectrum arising from nonequilibrium vibronic levels of the same excited electronic state. The contribution from each vibronic level is proportional to its average population which in turn is proportional to its lifetime. I will discuss in detail the hot luminescence emission characteristics in chapter 5.

The adoption of one mode for the representation of the sideband is an unrealistic description. In reality, the sideband when S<1 shows a number of different modes. For large S, the sideband phonon details are smeared out in to a continuous spectrum and the configurational coordinate model gives a reasonably good description of the smoothed sideband. Another problem with the configurational coordinate model arises in cases where the transition between two states is electric dipole not-allowed. For example, if the ion occupy a site with inversion symmetry, electric dipole moment transitions are not allowed. In this case, the transition occurs via magnetic dipole process which is a much weaker process ($\approx10^{-4}$ of electric dipole). However, odd symmetry distortion of the

lattice can destroy the inversion symmetry and increase the electric dipole moment transition probability. Due to the fact that the electric dipole transitions are much stronger than magnetic dipole transitions, the overall transition spectrum may be shared by both types of emission. Because the electric dipole moment transitions require a vibration of odd symmetry, the electric dipole moment transitions appear only in the sideband and the single configurational description fails to describe the relative intensity of the sideband with respect to the zero phonon line. Additional problems arise from the terms left out in the adiabatic approximation (eq. 3.10) and especially the $2\,(\nabla_1\chi_a)\,.\,(\nabla_1\Psi_a)$ term which has the stronger dependence in R_1. Let's assume the initial and final states possess even parity. This term can mix odd parity with even parity electronic states add make electric dipole moment transition possible resulting to an increased sideband intensity.

3.2.5 Nonradiative relaxation.

Up to this point we have examined only the radiative transitions between two electronic states. During this process, energy is released by the excited ion in the form of a photon. In addition to radiative relaxation of an excited ion there are nonradiative mechanisms where no photon emission is involved but the energy is absorbed by the lattice in the form of phonons. The nonradiative relaxation is always the process that enables the excited ions to reach their lowest electronic level. It is also a competing mechanism with the radiative relaxation between two electronic states. The coupling strength between the excited ion and the lattice phonon modes plays a key role in the nonradiative relaxation. Some theoretical work has been carried out by different theoreticians but due to the complexity of the problem

many simplifications were adapted with most common the assumption of only one lattice phonon mode. In this research, we have measured phonon modes involved in the nonradiative relaxation of forsterite. We have also studied the dynamics of the nonradiative relaxation and the temporal behavior of the nonequilibrium phonons involved. In this section I will present the fundamental quantum mechanics involved in the nonradiative relaxation of an excited ion in a lattice environment.

The absorption of a photon by an optically active ion is depicted in fig. [3.2]. Following the photoexcitation, an amount of energy $E_{dis}=E^{b}(Q_0^{a})-E^{b}(0)$ is going to be given nonradiatively into the lattice in the form of phonons. The interaction of the impurity ion with the lattice is due to the modulation of the crystal field by the lattice vibrations. This is conceived as the displacement of the impurity ion with respect to the lattice environment about its equilibrium position. Expanding the crystal field in a Taylor's series in terms of the normal coordinates Q_i we can write the crystal field Hamiltonian as

$$H_c(Q_k)=H_{st}+\sum_{i}{}'H_iQ_i+\sum_{i,j}{}'H_{ij}Q_iQ_j+\ldots\ldots \tag{3.29}$$

where the zero order term in the expansion (H_{st}) is the static crystal field. The expansion coefficients are the partial derivatives of the crystal field given by

$$H_i=\frac{\partial H_c}{\partial Q_i},\quad H_{ij}=\frac{\partial^2 H_c}{\partial Q_i\partial Q_j},\ldots\ldots \tag{3.30}$$

The normal coordinates Q_i can be expressed in terms of the creation and annihilation operators (see eqs. 3.3 and 3.4). Therefore, a given term in the Hamiltonian (eq. 3.29) is a product of two terms, one operating on the atomic system ($H_{i\ldots j}$), and one on the lattice vibrations ($Q_{i\ldots j}$). Let's

consider a nonradiative transition between two states with the emission of k phonons. This can be accounted for by a) considering the first order term in eq. 3.29 and carrying this to the kth order of perturbation theory b) considering the kth order term in eq. 3.29 in the first order perturbation theory and c) all the intermediate terms (for example, the (k/2)th term in second order perturbation). The expression for the nonradiative transition rate is then given by

$$W^{k}=\frac{2\pi}{h}\sum_{i\ldots j,\,a_1\ldots a_{k-1}} |\langle n_i+1|Q_i|n_i\rangle|^2\ldots|\langle n_j+1|Q_j|n_j\rangle|^2$$

$$X\frac{|\langle\Psi_{a_k}|H_i|\Psi_{a_{k-1}}\rangle|^2+\ldots+|\langle\Psi_{a_1}|H_j|\Psi_{a_0}\rangle|^2}{(E_{a_{k-1}}+h\omega_j+\ldots+h\omega_{i-1}-E_{a_0})^2\ldots(E_{a_1}+h\omega_j-E_{a_0})^2}$$

$$Xg(\omega_i)\ldots g(\omega_j)\,\delta(E_{a_k}+h\omega_i+\ldots+h\omega_j-E_{a_0})$$

$$+ \text{ intermediate terms } +$$

$$\frac{2\pi}{h}\sum_{i\ldots j}\left(\frac{1}{k!}\right)^2|\langle\Psi_{a_k}|H_{i\ldots j}|\Psi_{a_0}\rangle|^2|\langle n_i+1|Q_i|n_i\rangle|^2\ldots|\langle n_j+1|Q_j|n_j\rangle|^2$$

$$Xg(\omega_i)\ldots g(\omega_j)\,\delta(E_{a_k}+h\omega_i+\ldots+h\omega_j-E_{a_0}) \qquad (3.31)$$

where $n_i\ldots n_j$ are the phonon occupation numbers of the participating phonon modes $i\ldots j$, $\Psi_{a_1}\ldots\Psi_{a_{k-1}}$ are the intermediate virtual states and $g(\omega_i)\ldots g(\omega_j)$ are the densities of phonon states. The expansions in eq. 3.30 are extremely difficult for all but for the simplest crystals. In addition, theoretical solution of eq. 3.31 is almost impossible except for very rough order of magnitude estimates. However, because of the very large number of interacting phonon modes and intermediate states, it is likely that any precise features of the phonon modes and vibronic levels will statistically averaged out for these high order processes. Therefore, symmetry properties

of the participating phonon modes and vibronic states should be relatively unimportant. In any case, the creation of k phonons will be accomplished by these terms that contain k phonon creation operators $a_1^+.a_2^+.....a_k^+$, where the subscripts represent the phonon modes created. The matrix element of the transition is in the following form

$$\langle n_1+1|a_1^+|n_1\rangle\langle n_2+1|a_2^+|n_2\rangle\ldots\langle n_k+1|a_k^+|n_k\rangle$$

$$=\sqrt{1+n_1}\sqrt{1+n_2}\ldots\sqrt{1+n_k} \qquad (3.32)$$

From eq. 3.32 we obtain the temperature dependent multiphonon transition rate

$$W^k(T)=W_0^k(n_1+1)\,(n_2+1)\ldots(n_k+1) \qquad (3.33)$$

where W_0^k is the transition rate at $T=0$. Assuming only one phonon mode involved in the process, eq. 3.33 becomes

$$W^k(T)=W_0^k(n_1+1)^k \qquad (3.34)$$

The problem of nonradiative transitions has been of experimental and theoretical interest for some time. The largest portion of this work is dealing with the nonradiative relaxation from the lowest excited state to the ground state, a competing mechanism with the radiative relaxation. The reciprocal fluorescence lifetime is the sum of the nonradiative and radiative decay rates. The latter can be measured experimentally from the integrated absorption in a sample of known concentration and the observed ratio of the total emission rate. The earliest work on this subject concerned the absorption of radiation by F-centers.[1,2] Similar calculation have been made for the relaxation processes of rare-earth ions in crystals where the modulation of the electric crystalline field by the vibrating lattice provides the coupling.[3,4] In this work, the single phonon configurational coordinate

model described in this thesis was utilized and eq. (3.34) was obtained. The transition probability given by eq. (3.34) was also obtained by other workers[5-7] that utilized similar approaches of the single phonon model. The relation (3.34) has been used over the years to explain the temperature dependence of the nonradiative transition rate between two electronic states. Best fitting to experimental data provides an estimation for (k) and therefore the effective phonon energy. These measurements have indicated that the nonradiative relaxation is accompanied with the emission of high energy optical phonons that undertake the task of carrying the energy from the excited ion into the lattice. The assumption of the one participating phonon mode model has no base and is just a simplification. This problem has been addressed to some extent by taking the continuous nature of the phonon spectrum into account by using an effective phonon spectrum.[8,9] This leads to expressions of the nonradiative relaxation rate which in some cases provide better fitting to the experimental data.[10] Nonradiative multiphonon transitions are also discussed by other groups within the context of the configurational coordinate description.[11-19] From the experimental point of view, the investigation of the nonradiative relaxation rate between the lowest excited state and the ground state is very common. The relation (3.34) provides a good fitting in most of the cases and an estimation of the effective phonon mode. The introduction of ultrafast laser pulses have made possible measurements of the nonradiative relaxation times associated with the transfer of energy from an optically active center in to the lattice environment following photoexcitation.[20-23] This relaxation involves the transfer of the excess energy (the energy between excitation level and storage level) into the lattice by the emission of phonons. A detailed temperature dependence of the nonradiative relaxation for the

F_A(II) center in KCl:Li was performed in ref. [20]. To fit their experimental data they utilized an expression of the temperature dependence of the nonradiative relaxation similar to eq. 3.34 given by[15,16]

$$W^k(T)=W_0^k\, e^{An_1}\, (n_1+1)^k \tag{3.35}$$

where A is a coupling strength factor and is much less than 2. Best fitting to the experimental data was obtained for A=0 which leads to eq. 3.34.

Lattice modes may play two distinct roles in the nonradiative relaxation. These leads to the description as "promoting" and "accepting" modes.[24,25] To avoid possible confusion, it should be stressed that any one mode may belong to both classes, to one of them , or even to neither. There is a real physical basis behind this distinction. The accepting modes are involved in the energy conservation and act as sources and sinks for energy during the nonradiative process. The promoting modes, however, matter because they make a transition an allowed one through the matrix elements involved in the transition. In this research we have experimental evidence on the participating accepting phonon modes, and we will try to fit eq. 3.33 into our experimental data.

The lifetime of the nonequilibrium optical phonon in solids is of the order of 10 ps.[26-29] Due to the anharmonicity of the lattice forces, an optical mode can interchange energy with other lattice modes. Through this process, thermal equilibrium is achieved in the lattice and the energy released by the excited ion is dissipating. The principal anharmonic interaction is due to the cubic anharmonicities resulting in to the splitting of an optical phonon into two new phonons of opposite momentum. This process was estimated[30] from second order perturbation theory. Assume an optical phonon at k≈0 of frequency ω_0 that splits into two phonons of

frequency ω_1 and ω_2 and wavevector $\mathbf{k}_1$ and $\mathbf{k}_2$, respectively. Conservation of energy and momentum requires

$$\omega_0=\omega_1+\omega_2 \tag{3.36}$$

and

$$\mathbf{k}=\mathbf{k}_1+\mathbf{k}_2\approx 0 \tag{3.37}$$

The new phonons generated will also split into lower energy acoustic phonons. In the last stage, low in energy long wavevector acoustic phonons are generated possessing long lifetimes[31-37] (tens of ns to few μs) that can travel inside the crystal carrying with them the energy released by the impurity ion. The lifetime $\tau(T)$ of the optical phonons as a function of temperature is given by the following expression[30]

$$\tau(T)=\tau(T=0)\left(1+N_1+N_2\right)^{-1} \tag{3.38}$$

where N_1 and N_2 are the equilibrium occupation numbers of the modes $\mathbf{k}_1$ and $\mathbf{k}_2$ interacting with optical mode. We will attempt to use eq. 3.38 in order to extract information on how the optical modes observed to participate in the nonradiative relaxation break down in to lower energy phonons.

3.3 Raman scattering.

3.3.1 General considerations.

Raman scattering provides a direct way to measure the lattice vibrations through the interaction of light with the lattice. Using short laser pulses, time resolved experiments have been used since 1971 to monitor the temporal evolution of nonequilibrium phonons. In this section, I will present the theoretical background of this technique and point out the most important concepts utilized in this research.

Consider an experiment where a laser beam of light is incident on a crystal. The spread of frequencies in the incident laser light is very small, and can be regarded as monochromatic with a single angular frequency ω_I and wavevector $\mathbf{k}_I$. Depending on the nature of the crystal, part of the incident light will be absorbed, another portion will pass through the crystal and a portion of light (10^{-6}-$10^{-9} \times I_0$) will interact with the lattice vibrations (phonons) to produce a scattering signal with a spectrum having wavevector $\mathbf{k}_S$ and frequency ω_S. Momentum and energy conservation requires that the wavevector $\mathbf{k}$ and frequency ω_k of the phonons involved, satisfy the following relations (see figure)

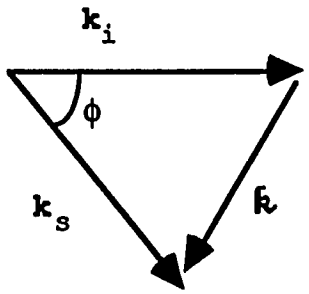

$$\mathbf{k}_S = \mathbf{k}_I \pm \mathbf{k} \qquad (3.39)$$

$$\omega_S = \omega_I \pm \omega_k \qquad (3.40)$$

In eqs. 3.39 and 3.40 the plus sign corresponds to destruction of a phonon (antiStokes scattering) and the minus sign to the creation of a phonon (Stokes scattering) by the incident photon. The photon wavevectors are related to their frequencies by

$$\mathbf{k}_I c = \eta_I \omega_I \qquad (3.41)$$

$$\mathbf{k}_S c = \eta_S \omega_S \tag{3.42}$$

where η_I and η_S are the refractive indices of the medium for the incident and scattered light.

The phonon frequencies are approximately 100 times smaller than the photon frequencies therefore, the amplitude of the incident light wavevector ($|\mathbf{k}_I|$) and scattered light wavevector ($|\mathbf{k}_S|$) are approximately equal and, for visible light, in the order of 2×10^5 cm^{-1}. Eq. 3.39 implies that the phonon wavevector should be in the same order of magnitude with the photon wavevector. Since the phonon wavevector near the edges of the Brillouin zone is typically of the order of 1×10^8 cm^{-1} ($=2\pi$/lattice constant) we see that the optical phonons involved in the Raman scattering process are near the $k=0$ portion of the entire Brillouin zone.

Measurement of the scattered light spectrum for a fixed scattering angle determines the function

$$\frac{d^2\sigma}{d\Omega d\omega_S} \equiv \text{spectral differential cross section} \tag{3.43}$$

This is defined as the rate of removal of energy from the incident beam as a result of its scattering in volume V into a solid-angle element $d\Omega$ with a scattered frequency between ω_S and $\omega_S + d\omega_S$, divided by the product of $d\Omega d\omega_S$ with the incident beam intensity. The spectral differential cross section has the dimensions of area divided by frequency. It is used to determine the amount of light scattered in a specific direction and can be experimentally measured.

3.3.2 Normal modes of lattice vibrations.

The absorption of energy by the lattice during the nonradiative relaxation is achieved through the generation of vibrational lattice modes (phonons). The relaxation of the ion involves the creation of a number of phonons of various frequencies. The problem we are facing is the following; An impurity ion releases energy in to its lattice environment via the emission of phonons. It reasonable to expect two types of phonons, the pure lattice phonons and the phonons associated with the impurity ions. It is obvious that in the selection rules governing which are the participating modes, the kind of vibration introduced into the lattice is a very important factor. In an effort to understand the experimental data, I will present in this section a standard treatment of the vibrations within the lattice and then I will expand the discussion for the case of impurity ions in a crystal.

Let's assume that the electronic state of the lattice ions do not correlate with the lattice vibrations and that the interaction between the ions can be described by a potential energy function $V\{\mathbf{R}_k\}$ which depends on the position of all lattice ions $\{\mathbf{R}_k\}$. Let $q\binom{l}{k}$ be the displacement from the equilibrium position of the k-th type of ion in the l-th unit cell from its equilibrium position. Expanding $V\{\mathbf{R}_k\}$ in powers of $q\binom{l}{k}$ we can write

$$V\{\mathbf{R}_k\}-V\{\mathbf{R}_k(0)\}=\sum_{k,l,\alpha} V_\alpha\binom{l}{k}\cdot q_\alpha\binom{l}{k} + \frac{1}{2}\sum_{k,k',l,l',\alpha,\beta} V_{\alpha\beta}\binom{ll'}{kk'}\cdot q_\alpha\binom{l}{k}\cdot q_\beta\binom{l'}{k'}+\cdots \quad (3.44)$$

where

$$V_\alpha\binom{l}{k}=\left.\frac{\partial V}{\partial q_\alpha\binom{l}{k}}\right|_{\{\mathbf{R}_k(0)\}} \quad (3.45)$$

$$V_{\alpha\beta}\binom{ll'}{kk'}=\left.\frac{\partial^2 V}{\partial q_\alpha\binom{l}{k}\,\partial q_\beta\binom{l'}{k'}}\right|_{\{\mathbf{R}_k(0)\}} \quad (3.46)$$

In the harmonic approximation, the higher order terms in eq. 6 are neglected. Since the lattice is vibrating about its equilibrium position, the first term in eq. 3.44 is zero ($V_\alpha\binom{l}{k}=0$). Furthermore, the forces between different lattice ions depend on the distance between the ions and not on the position of the ions in the lattice. Therefore,

$$V_{\alpha\beta}\binom{ll'}{kk'} = V_{\alpha\beta}\binom{l-l'}{kk'} \tag{3.47}$$

Under these assumptions, the lattice Hamiltonian can be written as

$$H=\frac{1}{2}\sum_{k,l,\alpha} M_k \dot{q}^2_\alpha\binom{l}{k} + \frac{1}{2}\sum_{k,k',l,l',\alpha,\beta} V_{\alpha\beta}\binom{l-l'}{kk'}\, q_\alpha\binom{l}{k}\, q_\beta\binom{l'}{k'} \tag{3.48}$$

where M_k is the mass of the k-th lattice ion. The equation of motion becomes

$$M_k \ddot{q}^2_\alpha\binom{l}{k} = -\sum_{k',l',\alpha,\beta} V_{\alpha\beta}\binom{l-l'}{kk'}\, q_\beta\binom{l'}{k'} \tag{3.49}$$

Let's assume solution in the form

$$q_\alpha\binom{l}{k}=\frac{1}{\sqrt{M_k}} q_\alpha(k)\ \exp[i(\mathbf{k}.\mathbf{x}(l)-\omega t)] \tag{3.50}$$

where $\mathbf{x}(l)$ is the position of the l-th unit cell. Substituting in eq. 3.49 we obtain

$$\omega^2(\mathbf{k})\, q_\alpha(k)=\sum_{k',\beta} D_{\alpha\beta}\binom{\mathbf{k}}{kk'}\, q_\beta(k') \tag{3.51}$$

where

$$D_{\alpha\beta}\binom{\mathbf{k}}{kk'}=\frac{1}{\sqrt{M_k M_{k'}}}\sum_{l} V_{\alpha\beta}\binom{l}{kk'}\exp[i\mathbf{k}.\mathbf{x}(l)] \tag{3.52}$$

If there are n ions per unit cell, eq. 3.51 represents 3n equations. The eigenfrequancies of the lattice vibrations (normal modes) are obtained from

$$\left| D_{\alpha\beta}\left(\begin{smallmatrix}k\\ kk'\end{smallmatrix}\right) - \omega^2(k)\,\delta_{\alpha\beta}\delta_{kk'} \right| = 0 \qquad (3.53)$$

The above equation has 3n real roots $\omega_i(k)$; i=1,2,3,...,3n. For each value of k, there are 3n normal modes. The frequencies $\omega_i(k)$ are all functions of **k**, with the periodicity of the reciprocal lattice. Plane waves whose wavevectors **k** differ by reciprocal lattice vectors **G** describe identical lattice waves. Plotting the frequency $\omega_i(k)$ against the wavevector **k** forms a curve known as a dispersion curve (see fig. [3.5]). The 3n different curves are referred to as branches. The eigenvectors $e_\alpha\left(k\middle|\begin{smallmatrix}k\\ i\end{smallmatrix}\right)$ are obtained by replacing $\omega_i(k)$ in eq. 3.51 and they form a set of orthogonal vectors. The displacement $q\left(\begin{smallmatrix}l\\ k\end{smallmatrix}\right)$ can be expanded in terms of these eigenvectors

$$q_\alpha\left(\begin{smallmatrix}l\\ k\end{smallmatrix}\right) = \frac{1}{\sqrt{NVM_k}} \sum_{k,i} Q\left(\begin{smallmatrix}k\\ i\end{smallmatrix}\right) e_\alpha\left(k\middle|\begin{smallmatrix}k\\ i\end{smallmatrix}\right) \exp\left[i\,(k\,.\,x(l))\right] \qquad (3.54)$$

where N is the number of unit cells per unit volume and V is the volume of the crystal. The expansion coefficients $Q\left(\begin{smallmatrix}k\\ i\end{smallmatrix}\right)$ are called "normal coordinates". In terms of the normal coordinates, the lattice Hamiltonian becomes

$$H = \frac{1}{2} \sum_{k,i} \left\{ \dot{Q}^*\left(\begin{smallmatrix}k\\ i\end{smallmatrix}\right) \dot{Q}\left(\begin{smallmatrix}k\\ i\end{smallmatrix}\right) + \omega_i^2(k)\, Q^*\left(\begin{smallmatrix}k\\ i\end{smallmatrix}\right) Q\left(\begin{smallmatrix}k\\ i\end{smallmatrix}\right) \right\} \qquad (3.55)$$

and the equation of motion is

$$\ddot{Q}\left(\begin{smallmatrix}k\\ i\end{smallmatrix}\right) + \omega_i^2(k)\, Q\left(\begin{smallmatrix}k\\ i\end{smallmatrix}\right) = 0 \qquad (3.56)$$

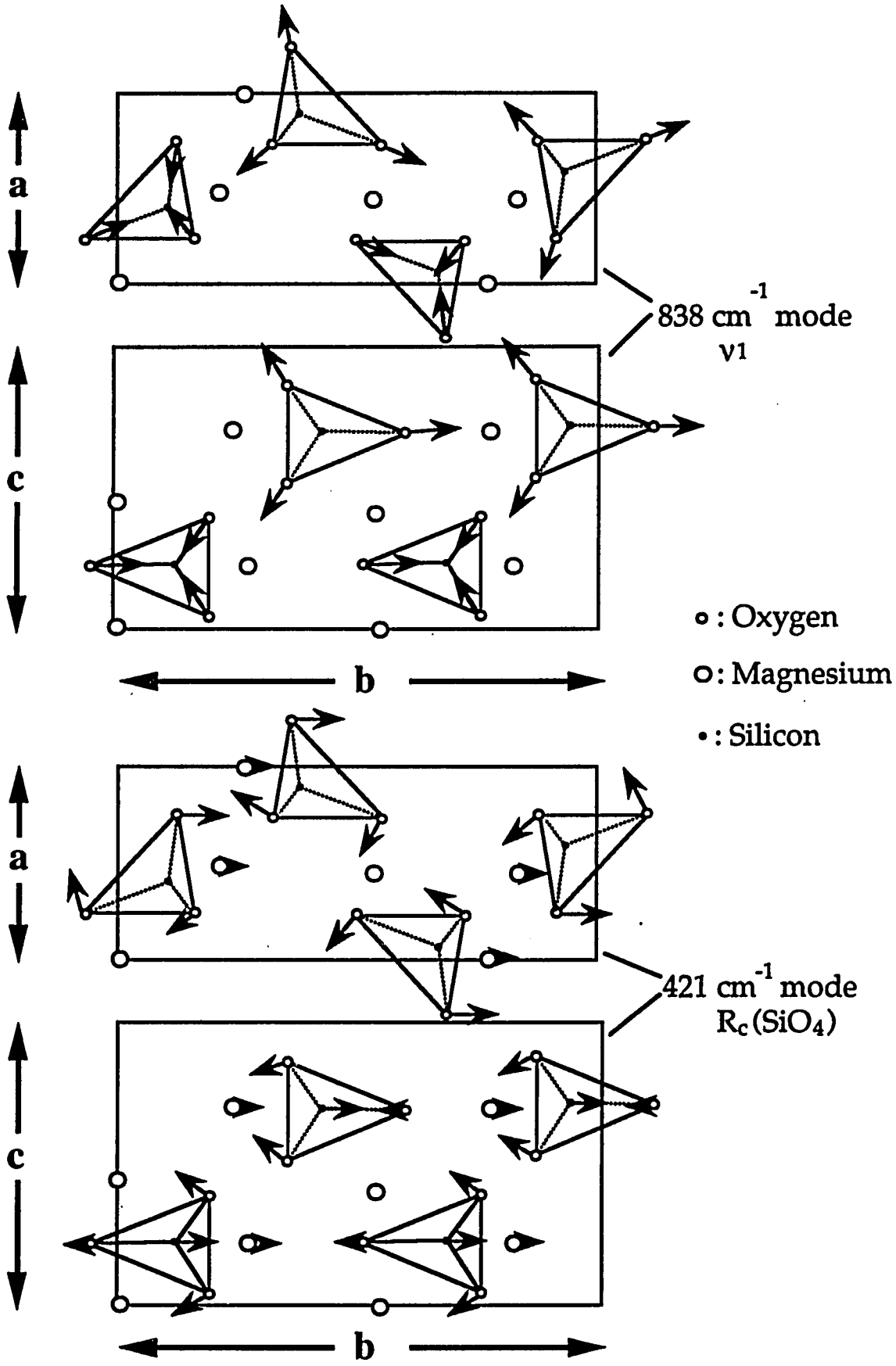

Figure 3.4. Theoretical vibrational modes of B_{2u} (TO) symmetry (From ref. 38)

Eqs. 3.55 and 3.56 indicate that each lattice vibrational frequency $\omega_i(k)$ is associated with the "vibration" of a normal coordinate $Q(\vec{k}_i)$. On the other hand, eq. 3.54 indicates that a normal coordinate is described as the displacement of the lattice ions in specific directions. Therefore, each vibrational mode is composed by the vibration of a group of lattice ions in certain directions with specific phase difference with respect to each other. These concepts are demonstrated in fig. [3.4], where two vibrational modes of forsterite are depicted.[38] In table [4.4], the kind of lattice motion is given for all vibrational modes of forsterite.

In terms of quantum mechanics, $Q(\vec{k}_i)$ becomes an operator and can be written as a linear combination of creation and destruction operators in the second quantization scheme

$$Q(\vec{k}_i)=\left(\frac{h}{2\omega_i(\vec{k})}\right)^{\frac{1}{2}}(\alpha^{+}_{\vec{k}i}+\alpha_{\vec{k}i}) \qquad (3.57)$$

where $\alpha^{+}_{\vec{k}i}$ and $\alpha_{\vec{k}i}$ satisfy the usual boson operator commutation relations. The quantized excitations are called phonons, and they possess energy $h\omega_i(k)$ and momentum $h\vec{k}$. The average occupation number $\langle n_{\vec{k}i}\rangle$ of the $(\vec{k}_i)$ phonon mode at temperature T is given by the Bose-Einstein factor

$$\langle n_{\vec{k}i}\rangle=\left[\exp\left(\frac{h\omega_i(\vec{k})}{k_BT}\right)-1\right]^{-1} \qquad (3.58)$$

where k_B is the Boltzmann constant.

For $\vec{k}=0$, three of the normal modes correspond to rigid translations in three orthogonal directions. These three modes are called acoustic modes and the corresponding branches are known as "acoustic branchs" (see fig. [3.5]. The remaining 3n-3 modes are called "optical modes" ("optical

branches"). For $\vec{k} \approx 0$, the frequencies $\omega_i(\vec{k})$ of the optical branches are typically 50 to 1500 cm^{-1}. Raman scattering involves inelastic scattering of photons by optical phonons.

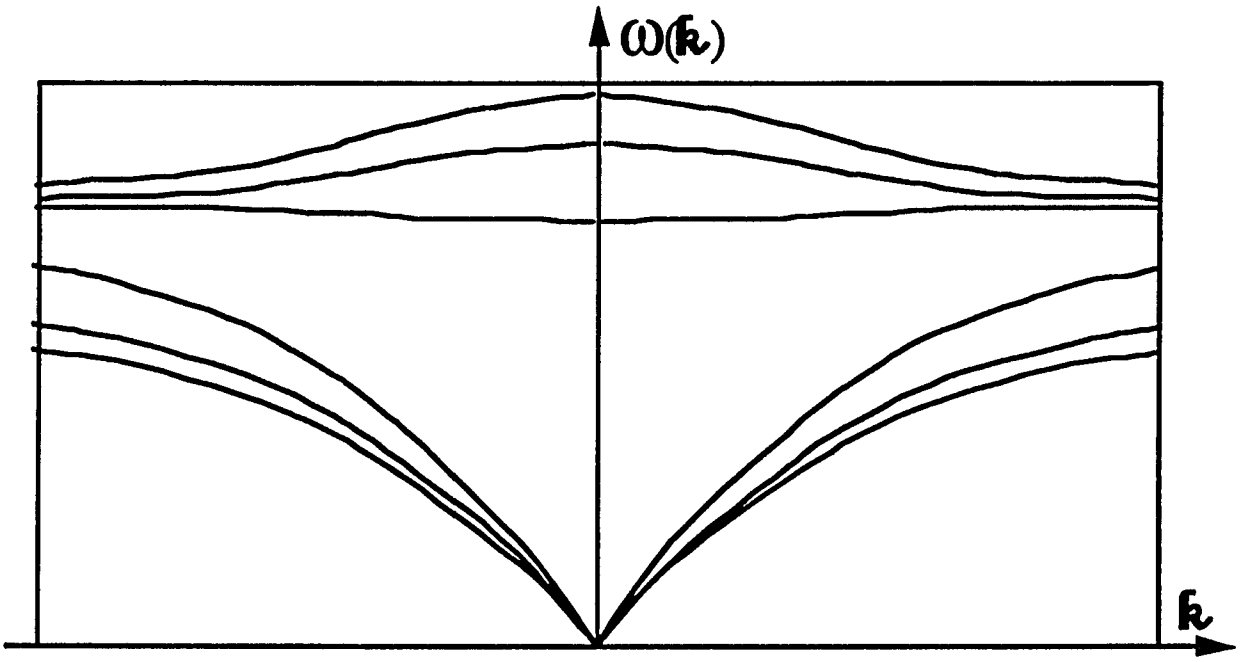

Figure 3.5: Typical dispersion curves along a general direction in k-space for a lattice with a two-ion basis. The three lower curves are the acoustic branches and are linear in k for small $\vec{k}$. The three upper curves are the optical branches.

As we can see from eq. 3.49 and 3.54, the frequencies of vibration of different modes for the same $\vec{k}$ depend on the forces between the neighboring ions and the masses of the ions involved in the vibrational mode. When an impurity ion is replacing a lattice ion we should expect that the vibrations involving the impurity ion have different frequencies since the masses are different and possibly the forces. As a result, new phonon lines should appear in the Raman spectrum that are due to the impurity

ions. For low impurity ion concentration, these new modes will only appear under resonant excitation condition which I will discuss in section 3.3.5.

In the case of Cr^{4+} doped forsterite (details follow in chapter 4), the Cr ions substitute for Si ions in the crystal in tetrahedrally coordinated sites. There are two type of lattice vibration, the internal modes of the tetrahedral involving motion of the Si ion with the four neighboring O ions and the external modes of vibration where the SiO_4 tetrahedral vibrates as one unit. The Cr ions having atomic mass 52 are heavier than the Si ions (atomic mass =28) that they substitute and therefore the vibrations involving the Cr ions have different frequencies that the lattice vibrations. More specifically, the modes of vibration of the heavier Cr ions should have lower frequency than the same type of lattice vibration. The difference in frequency should be larger for the internal modes of vibration because the number of ions involved in these modes is smaller and the presence of the Cr ion will give a bigger effect. On the other hand, the external modes of vibrations involve more atoms while the SiO_4 (or CrO_4) tetrahedral vibrates as unit and as a result the presence of the Cr ions will not have as big effect in the frequency of vibration as for the internal modes. As we will see in chapter 6, under resonant excitation conditions we were able to observe Cr-ion associated modes in the antiStokes Raman spectrum. The observed modes are internal modes of vibration of the CrO_4 tetrahedral and are clearly separable from the lattice modes.

Following photoexcitation, the Cr ions are in a high vibrational level of the excited state. The excess energy is going to be given in to the lattice in the form of lattice phonons. The generated phonons are in the immediate neighborhood of the Cr ions and as a result their frequency may be slightly lower than the pure lattice modes due tot the presence of the heavier Cr

ions. A possible selection rule on which are the lattice modes involved in the nonradiative relaxation could be some kind of resonance between the lattice modes of vibration and the Cr-ion associated modes. It is reasonable to think that when a lattice mode has the same frequency with a Cr-ion mode (not necessarily of the same type), the transfer of energy from the hot ion into the lattice is more likely to take place through the resonant lattice mode. If this is true, we should expect in forsterite the external modes of vibration to play the dominant role in the nonradiative relaxation because the frequency of the internal modes is more affected by the presence of the heavier Cr ions and therefore, resonance is less likely. I will return to this discussion after I will present the experimental data.

3.3.3 Modulation of the electric susceptibility by lattice vibrations.

The vibrational excitation of the lattice modulates the wavefunctions and energy levels of the medium. The effect in the changes of these quantities is represented macroscopically by an additional contribution to the susceptibility. Raman scattering occurs through the modulation of the electric susceptibility χ_{ij} by the lattice phonons. A normal mode that modulates the electric susceptibility χ_{ij} can produce Raman scattering and its associated phonon branch is called "Raman active".

In order to see how a lattice mode modulates the electric susceptibility, we expand χ_{ij} in the atomic displacement coordinates about its equilibrium value as follows:

$$\chi_{ij}(\mathbf{x}(l),t)=\chi_{ij}^{0}+\sum_{k,\alpha}\frac{\partial\chi_{ij}}{\partial q_{\alpha}\binom{l}{k}}\cdot q_{\alpha}\binom{l}{k}+$$

$$+\frac{1}{2}\sum_{k,k',l',\alpha,\beta}\frac{\partial^2\chi_{ij}}{\partial q_\alpha\binom{l}{k}\,\partial q_\beta\binom{l'}{k'}}\cdot q_\alpha\binom{l}{k}\cdot q_\beta\binom{l'}{k'}+\ldots$$

$$=\chi^0_{ij}+\chi^1_{ij}+\chi^2_{ij}+\ldots \tag{3.59}$$

The first term is responsible for the elastic scattering of light. The second term which is first order in displacement produces the first order Raman scattering. The next term is responsible for the second order Raman scattering and so forth.

In terms of the normal coordinates, using eq. 3.51 the first order term of the electric susceptibility for the n-th mode can be written as:

$$\chi^1_{ij}(n,\mathbf{x}(l),t)=\sum_{k,\alpha}\frac{\partial\chi_{ij}}{\partial q_\alpha\binom{l}{k}}\cdot q_\alpha\binom{l}{k}$$

$$=\sum_{\mathbf{k}}Q\binom{\mathbf{k}}{n}\exp[i(\mathbf{k}\cdot\mathbf{x}(l)-\omega t)]\sum_{k,\alpha}\frac{\partial\chi_{ij}}{\partial q_\alpha\binom{l}{k}}e_\alpha\left(k\middle|\binom{\mathbf{k}}{i}\right)\frac{1}{\sqrt{NVM_k}}$$

$$=\sum_{\mathbf{k}}\chi^1_{ij}(\mathbf{k})\exp[i(\mathbf{k}\cdot\mathbf{x}(l)-\omega t)] \tag{3.60}$$

where

$$\chi^1_{ij}(\mathbf{k})=\sum_{k,\alpha}Q\binom{\mathbf{k}}{n}\frac{\partial\chi_{ij}}{\partial q_\alpha\binom{l}{k}}e_\alpha\left(k\middle|\binom{\mathbf{k}}{i}\right)\frac{1}{\sqrt{NVM_k}} \tag{3.61}$$

The expression in eq. 3.60 describes the modulation of the electric susceptibility due to the n-th normal mode. A more descriptive way of expressing the modulation of the susceptibility is to assume an excitation $X(\mathbf{r},t)$ of the medium that is responsible for the inelastic scattering characterized by space and time dependent amplitude

$$X(\mathbf{r},t)=\sum_{\mathbf{k}}\{X(\mathbf{k},t)\exp(i\mathbf{k}\cdot\mathbf{r})+X^*(\mathbf{k},t)\exp(-i\mathbf{k}\cdot\mathbf{r})\} \tag{3.62}$$

The electric susceptibility can now be written as

$$\chi_{ij} = \chi^0_{ij}(\omega_I) + \chi^1_{ij}(\omega_I,\omega)\, X(\mathbf{r},t) + \ldots \tag{3.63}$$

where ω_I is the frequency of the incident light and ω is the lattice modulation frequency. The second term in eq. 3.63 is responsible for Raman scattering and the first order electric susceptibility $\chi^1_{ij}(\omega_I,\omega)$ depends on ω_I and ω.

When a laser light beam is incident into the medium, the j-th Cartesian component of the electric field at position ($\mathbf{r}$) and time (t) can be written as

$$E^j_I(\mathbf{r},t) = E^j_I \exp(i\mathbf{k}_I.\mathbf{r} - i\omega_I t) + E^{j*}_I \exp(-i\mathbf{k}_I.\mathbf{r} + i\omega_I t) \tag{3.64}$$

The induced polarization is then given by

$$P^j_I(\mathbf{r},t) = \chi_{ij} E^j_I = \chi^0_{ij}(\omega_I) E^j_I(\mathbf{r},t) + \chi^1_{ij}(\omega_I,\omega)\, X(\mathbf{r},t) E^j_I(\mathbf{r},t) + \ldots \tag{3.65}$$

and it can be separated into two components, the Stokes $P^j_S(\mathbf{r},t)$ and the antiStokes $P^j_{AS}(\mathbf{r},t)$,

$$P^j_S(\mathbf{r},t) = \sum_{\mathbf{k}_S} \{P^j_S(\mathbf{k}_S,t) \exp(i\mathbf{k}_S.\mathbf{r}) + P^{j*}_S(\mathbf{k}_S,t) \exp(-i\mathbf{k}_S.\mathbf{r})\} \tag{3.66}$$

$$P^j_{AS}(\mathbf{r},t) = \sum_{\mathbf{k}_{AS}} \{P^j_{AS}(\mathbf{k}_{AS},t) \exp(i\mathbf{k}_{AS}.\mathbf{r}) + P^{j*}_{AS}(\mathbf{k}_{AS},t) \exp(-i\mathbf{k}_{AS}.\mathbf{r})\} \tag{3.67}$$

In order to introduce the frequency (ω) in our equations, the crystal modulation and polarization is expressed in terms of their Fourier transform with respect to the time

$$X(\mathbf{k},t) = \int X(\mathbf{k},\omega) \exp(-i\omega t)\, d\omega \tag{3.68}$$

$$P^j_{S,AS}(\mathbf{k}_{S,AS},t) = \int P^j_{S,AS}(\mathbf{k}_{S,AS},\omega_{S,AS}) \exp(-i\omega_{S,AS} t)\, d\omega_{S,AS} \tag{3.69}$$

Substituting in the second term of eq. 3.65 the expressions for E_I, X, P_S and P_{AS} from eqs. 3.64, 3.66, 3.67, 3.68 and 3.69 leads on comparison of terms with common time dependence to

$$P_S^j(\mathbf{k}_S, \omega_S) = \chi^1_{ji}(\omega_I, -\omega)\, X^*(\mathbf{k}, \omega)\, E_I^i \tag{3.70}$$

$$P_{AS}^j(\mathbf{k}_S, \omega_S) = \chi^1_{ji}(\omega_I, \omega)\, X(\mathbf{k}, \omega)\, E_I^i \tag{3.71}$$

where the frequencies are related by eq. 2.

3.3.4 Semi-classical approach of Raman scattering.

3.3.4.a Theory.

The lattice constant of a crystal is typically of the order of 1×10^{-8} cm while the visible light wavelength is $\approx5\times10^{-5}$ cm. Under these conditions, the crystal can be considered as a continuous medium. This fact insures the validity of the semi-classical approach where both the incident and scattered radiation are treated classically as electromagnetic waves and the lattice vibrations semi-classically as optical phonons which create fluctuations of the electric susceptibility of the medium. The incident radiation creates inside the scattering medium oscillating dipoles (polarization) whose frequency is modulated by the optical phonons. The intensity of the inelastically scattered light is estimated by calculating the power radiated by the oscillating dipoles.

The characteristics of the scattered light is determined by the radiation fields generated by the polarization. We consider the radiation by a single component of the Stokes polarization

$$\mathbf{P}_S \exp(-i\omega_S t + i\mathbf{k}_S \cdot \mathbf{r}) \tag{3.72}$$

The electric field generated by the Stokes polarization has frequency ω_S, and the spatial dependence of its amplitude $\mathbf{E}$ is determined from Maxwell's equations using eqs. 3.64 and 3.72,

$$\nabla\times\nabla\times\mathbf{E}-\frac{\eta_S^2\omega_S^2}{c^2}\mathbf{E} = \frac{\omega_S^2}{c^2}\mathbf{P}_S\exp(i\mathbf{k}_S.\mathbf{r}) \tag{3.73}$$

The solution has two parts;

$$\mathbf{E}=\mathbf{E}_h\exp(i\mathbf{k}_S.\mathbf{r})+\mathbf{E}_i\exp(i\mathbf{k}_S.\mathbf{r}) \tag{3.74}$$

The homogeneous part ($\mathbf{E}_h$) is obtained by substituting zero on the right-hand side of eq. 3.73 and corresponds physically to free electromagnetic waves in the absence of any Stokes polarization (elastic scattering). The inhomogeneous part ($\mathbf{E}_i$) corresponds physically to an electromagnetic wave driven by the Stokes polarization and is responsible for the Stokes Raman scattering. Substituting the second term of the right of eq. 3.74 into eq. 3.73 and using $\nabla\times\nabla\times\mathbf{E}=\nabla(\nabla.\mathbf{E})-\nabla^2\mathbf{E}$ and the Maxwell equation

$$\nabla.\mathbf{D}=i\mathbf{k}_S.(\varepsilon_0\eta_S^2\mathbf{E}_i+\mathbf{P}_S)=0 \tag{3.75}$$

we obtain the solution

$$\mathbf{E}_i=\frac{k_S^2\mathbf{P}_S-(\mathbf{k}_S.\mathbf{P}_S)\mathbf{k}_S}{\eta_S^2(\mathbf{k}_S^2-k_S^2)} \tag{3.76}$$

We assume for simplicity that the illuminated region by the laser beam focused into to the crystal is a slab, of thickness L and volume V. Scattered light is emitted in all directions from the illuminated region but let's

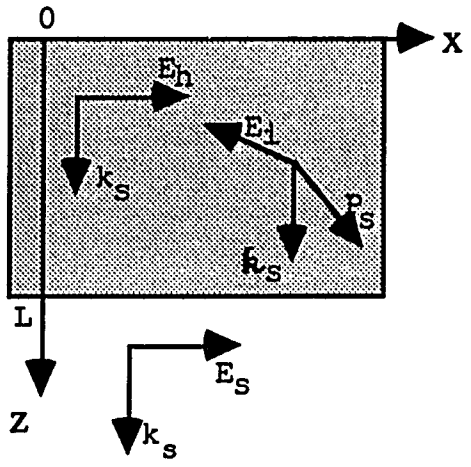

concentrate to the contribution of scattering perpendicular to the slab in the two dimensional arrangement shown in the figure. Scattered light is emitted in all directions but we ignore all contributions except that for which k_s is oriented in the positive z-direction. This component is not zero for $0<z<L$. For $z>L$ the scattering polarization is zero and the field determined by eq. 3.73 has the form

$$\mathbf{E}_S \exp(i\mathbf{k}_S.\mathbf{r}) \tag{3.77}$$

The tangential boundary conditions at z=0 and z=L give respectively

$$E_h^x + E_i^x = 0 \tag{3.78}$$

$$E_h^x \exp(ik_S.L) + E_i^x \exp(i\mathbf{k}_S.L) = E_S^x \exp(ik_S.L) \tag{3.79}$$

From eqs. 3.76, 3.78 and 3.79 we obtain the scattered light electric field

$$\mathbf{E}_S = \frac{k_S^2 \boldsymbol{\varepsilon}_S.\mathbf{P}_S}{\eta_S^2 (\mathbf{k}_S^2 - k_S^2)} \left(\exp\left(i(\mathbf{k}_S - k_S)L\right) - 1 \right) \tag{3.80}$$

where $\boldsymbol{\varepsilon}_S$ is the unit vector parallel to $\mathbf{E}_S$.

The cross sectional area of the scattered beam is V/L. The instantaneous energy flow from the scattered beam is VI_S/L where I_S is the scattered light intensity. For each photon of energy $h\omega_I$ that is scattered, a photon of energy $h\omega_S$ arises and consequently, there is an energy loss due to the different photon energies. In accordance with the definition that follows eq. 4a, the spectral differential cross section is

$$\frac{d^2\sigma}{d\Omega d\omega_S} = \frac{\omega_I V}{\omega_S L} \frac{d^2 \langle I_S \rangle}{d\Omega d\omega_S} \frac{1}{\langle I_I \rangle} \tag{3.81}$$

where $\langle I_I \rangle$ and $\langle I_S \rangle$ are the average incident beam and scattered light intensities. The cycle-averaged intensity of the incident beam is

$$\langle I_I \rangle = 2\varepsilon_0 \eta_I |\mathbf{E}_I|^2 \tag{3.82}$$

The average total intensity of the scattered light is obtained by integration of the scattered field over the frequency spectrum ω_S and summation of the intensity contributions over all the wavevectors $\mathbf{k}_S$ present in the Stokes polarization (eq. 3.69)

$$\langle I_S \rangle = 2\varepsilon_0 \eta_S \sum_{\mathbf{k}_s} \int d\omega_S \mathbf{E}_S^* \mathbf{E}_S \tag{3.83}$$

Substituting eq. 3.80 in eq. 3.83 we obtain

$$\langle I_S \rangle = \int d\omega_S \int d\Omega \omega_S^4 V \eta_S \frac{\langle \varepsilon_S . \mathbf{P}_S^*(\mathbf{k}_S)\, \varepsilon_S . \mathbf{P}_S(\mathbf{k}_S) \rangle_{\omega_S} L}{8\pi^2 \varepsilon_0 c^3} \tag{3.84}$$

where the ε_S is the scattered light polarization while the wavevector summation is converted to an integration as

$$\sum_{\mathbf{k}_s} \Rightarrow \frac{V}{(2\pi)^3} \int d\Omega \int d\mathbf{k}_S \mathbf{k}_S^2 \tag{3.85}$$

where V is the volume of the crystal. Using eqs. 3.70, the power spectrum of the polarization fluctuations in eq. 3.84 can be written

$$\langle \varepsilon_S . \mathbf{P}_S^*(\mathbf{k}_S)\, \varepsilon_S . \mathbf{P}_S(\mathbf{k}_S) \rangle_{\omega_S} = |\varepsilon_0 \varepsilon_S^i \chi_{ji}^1 (\omega_{I'} - \omega) E_I^j|^2 \langle X(\mathbf{k}) X^*(\mathbf{k}) \rangle_\omega \tag{3.86}$$

The Stokes scattering cross section (eq. 3.81) thus becomes

$$\frac{d^2\sigma}{d\Omega d\omega_S}(\text{Stokes}) = \frac{\omega_I \omega_S^3 V \eta_S |\varepsilon_0 \varepsilon_S^i \varepsilon_I^j \chi_{ji}^1 (\omega_{I'} - \omega)|^2}{(4\pi\varepsilon_0)^2 c^4 \eta_I} \langle X(\mathbf{k}) X^*(\mathbf{k}) \rangle_\omega \tag{3.87}$$

There are two important factors in eq. 3.87. The $|\varepsilon_0 \varepsilon_S^i \varepsilon_I^j \chi_{ji}^1 (\omega_{I'} - \omega)|^2$ factor contains the information about polarization selection rules. The second factor, $\langle X(\mathbf{k}) X^*(\mathbf{k}) \rangle_{\omega'}$ is called power spectrum, and contains information

about the shape of the scattered spectrum. It can be shown that the power spectrum for the Stokes Raman scattering can be written as

$$\langle X(\mathbf{k})\, X^{*}(\mathbf{k})\rangle_{\omega} = [n(\omega)+1]\, G(\omega) \tag{3.88}$$

where $n(\omega)$ is the average phonon population given in eq. 3.58 and $G(\omega)$ contains the spectral information.. Combining eqs. 3.87 and 3.88, the Stokes Raman scattering cross section becomes

$$\frac{d^2\sigma}{d\Omega d\omega_S}(\text{Stokes}) = \frac{\omega_I \omega_S^3 V^2 \eta_S \left|\varepsilon_0 \varepsilon_S^i \varepsilon_I^j G(\omega)\, \chi_{ji}^1(\omega_I, -\omega)\right|^2}{(4\pi\varepsilon_0)^2 c^4 \eta_I}\, [n(\omega)+1] \tag{3.89a}$$

Similarly, the cross section for the antiStokes Raman scattering is given by a similar expression

$$\frac{d^2\sigma}{d\Omega d\omega_{AS}}(\text{antiStokes}) = \frac{\omega_I \omega_{AS}^3 V^2 \eta_{AS} \left|\varepsilon_0 \varepsilon_{AS}^i \varepsilon_I^j G(\omega)\, \chi_{ji}^1(\omega_I, \omega)\right|^2}{(4\pi\varepsilon_0)^2 c^4 \eta_I}\, n(\omega) \tag{3.89b}$$

The subscripts (I) and (S, AS) stand for incident and scattered light (Stokes, antiStokes) respectively.

3.3.4.b Detection of nonequilibrium phonons.

From the point of view of time resolved experimental techniques, the most important factor in eqs. 3.89 is the last term which is associated with the average phonon population. For Stokes scattering this factor is $[n(\omega)+1]$ while for antiStokes scattering is $[n(\omega)]$.This implies that the Stokes (I_S) and antiStokes (I_{AS}) scattered light intensities are given by

$$I_S = A_1\, [n(\omega)+1] \tag{3.90a}$$

$$I_{AS} = A_2\, [n(\omega)] \tag{3.90b}$$

while $n(\omega) = (\exp(h\omega/K_B T) - 1)^{-1}$.

From a practical point of view, $n(\omega)$ gives the probability that a phonon mode is "vibrating" at a given moment. At room temperature, the value of $n(\omega)$ for optical phonon modes is between 0.01 [$n(1000\ cm^{-1})$] and 1 [$n(150\ cm^{-1})$] depending on the phonon mode frequency. A 10% chance on the effective occupation number of a specific mode will generate an equal change in the antiStokes Raman line arising from this mode but a much smaller change in the Stokes Raman line. For example, the antiStokes Raman line of the 225 cm^{-1} mode of forsterite at room temperature exhibits a ≈10% change in intensity at 8 ps delay time. The thermal phonon occupation number at room temperature is $n(225)=0.50$. According to eq. 3.90, a 10% change in the intensity of the Raman line suggests a 10% change on the average phonon occupation number, which means that the effective phonon occupation number at 8 ps delay time is $n_{eff.}(225)=0.55$. The Stokes Raman line intensity is proportional to $[n(225)+1]=1.5$ and at 8 ps delay time is proportional to $[n_{eff}(225)+1]=1.55$. This means the overall change in the intensity of the Stokes Raman line is only 3% while in the antiStokes line is 10%. This example demonstrates that in a time resolved experiment it is easier and more sensible to detect changes in the phonon population by monitoring the antiStokes Raman lines than the Stokes Raman lines.

In time resolved experiments, two pulses are used, one (pump pulse) to photoexcite the sample resulting to subsequent nonequilibrium phonon generation and a second (probe) to detect the changes in the phonon population by monitoring the intensity of the antiStokes Raman line of the phonon mode. From eq. 3.90 we see that the intensity of the antiStokes

Raman lines due to the probe beam [$I_{AS}(\Delta\tau)$] as function of the delay time between pump and probe $\Delta\tau$ is

$$I_{AS}(\Delta\tau) \sim n(\omega) = n_{thermal}(\omega) + n_{noneq.}(\omega) \tag{3.91}$$

where $n_{thermal}(\omega)$ are the equilibrium lattice phonons and $n_{noneq.}(\omega)$ are the nonequilibrium phonon population generated by the pump pulse. The change of the intensity $\Delta I_{AS}(\Delta\tau)$ between a positive delay time and a negative delay time used as reference (the probe pulse arrives before the pump pulse and therefore no nonequilibrium phonon population is present) is given by

$$\Delta I_{AS}(\Delta\tau) = I_{AS}(\Delta\tau) - I_{AS}(\Delta\tau<0) \sim n_{noneq.}(\omega) \tag{3.92}$$

From the above relation we see that by monitoring the changes of the intensity of the antiStokes Raman line we can obtain the temporal evolution of the nonequilibrium phonon population. Therefore, in time resolved experiments involving the generation of nonequilibrium phonons, the antiStokes Raman scattering component is most important for the investigation of the temporal behavior of the phonon population. In chapter 6, I will use the concepts of this paragraph in order to estimate the number of phonons of each mode participating in the nonradiative relaxation.

3.3.5 Quantum Mechanics of Raman scattering.

The quantum mechanical Hamiltonian of the interacting crystalline medium and radiation field can be written as

$$H = H_R + H_L + H_{ER} \tag{3.93}$$

where H_R is the radiation field Hamiltonian, H_L is the total crystal Hamiltonian and H_{ER} is the interaction Hamiltonian of the radiation field with the electrons of the lattice ions.

The radiation field is expressed in terms of n_I incident photons and n_S scattered photons where

$$H_R|n_I, n_S\rangle = (n_I h\omega_I + n_S h\omega_S)\,|n_I, n_S\rangle \tag{3.94}$$

Quantization of the radiation field leads to the vector potential and electric field operators which in the Schrödinger representation are given by

$$\mathbf{A}(\mathbf{r}) = \sum_k \left(\frac{h}{2\varepsilon_0 \eta^2 V \omega_k}\right)^{1/2} \varepsilon_k \left(\mathbf{a}_k \exp(i\mathbf{k}.\mathbf{r}) + \mathbf{a}_k^+ \exp(-i\mathbf{k}.\mathbf{r})\right) \tag{3.95}$$

$$\mathbf{E}(\mathbf{r}) = i\sum_k \left(\frac{h\omega_k}{2\varepsilon_0 \eta^2 V}\right)^{1/2} \varepsilon_k \left(\mathbf{a}_k \exp(i\mathbf{k}.\mathbf{r}) - \mathbf{a}_k^+ \exp(-i\mathbf{k}.\mathbf{r})\right) \tag{3.96}$$

where $\mathbf{a}_k$ and $\mathbf{a}_k^+$ are the creation and destruction operators for a photon of wavevector $\mathbf{k}$, frequency ω_k and polarization ε_k. The radiation field is included in the electronic Hamiltonian by making the replacement

$$\mathbf{p}_j \rightarrow \mathbf{p}_j + e\mathbf{A}(\mathbf{r}_j) \tag{3.97}$$

and the resulting electron-radiation Hamiltonian is

$$H_{ER} = \frac{e^2}{2m}\sum_j \mathbf{A}(\mathbf{r}_j).\mathbf{A}(\mathbf{r}_j) + \frac{e}{m}\sum_j \mathbf{A}(\mathbf{r}_j).\mathbf{p}_j = H'_{ER} + H''_{ER} \tag{3.98}$$

These two contributions are referred to as the A^2 and $\mathbf{A}.\mathbf{p}$ parts.

The crystal Hamiltonian H_{eL} was discussed elsewhere and it contains the interaction between the lattice phonons and the lattice ions. We will express this interaction as

$$H_{eL} = Q_{m,k}\,\Xi^{Q_{m,k}} \tag{3.99}$$

where $\Xi^{Q_{m,k}}$ is called "deformation potential" and $Q_{m,k}$ is the normal coordinate operator

$$Q_{m,k}=i\left(\frac{h}{2N\omega_m(k)}\right)^{1/2}\left(\beta_{km}\exp(ik.x)-\beta^{+}_{km}\exp(-ik.x)\right) \tag{3.100}$$

where β^{+}_{km} and β_{km} are creation and destruction operators for the phonon of branch m and wavevector k.

The Raman scattering process is considered, in quantum mechanic terms, as a third-order light scattering process depicted in the schematic. A photon ($h\omega_I$) is absorbed, causing an atomic transition from the state $|g>$ to a virtual state $|j_1>$. The interaction involved is the $A.p$ part (H''_{ER}) of eq. 3.98 because it contains the electronic momenta that allow scattering in which the initial and final electronic states are different. From the state $|j_1>$ through the electron lattice (H_{eL}) interaction there is an emission (for Stokes scattering) of a phonon and transition to the atomic state $|j_2>$. Finally, through H''_{ER}, the scattered photon ($h\omega_S$) is emitted and the ion returns to its initial atomic state $|g>$. The matrix element involved in the first interaction is given by

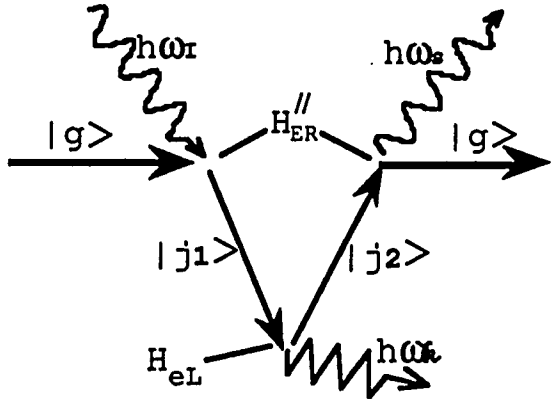

$$<j_1,n_I-1|H''_{ER}|g,n_I>=\frac{e}{m}\left(\frac{hn_I}{2\varepsilon_0\eta_I^2V\omega_I}\right)^{\frac{1}{2}}<j_1|\sum_j\exp(ik.r_j)\varepsilon_I.p_j|g> \tag{3.101}$$

The electronic wavefunction of an atom typically extends over the order of the Bohr radius a_0, and the exponentials in the matrix element can be

expanded in power series since $a_0 k_I$ is small. Retention only of the zero-order term gives

$$\langle j_1, n_I-1 \mid H''_{ER} \mid g, n_I \rangle = \frac{e}{m}\left(\frac{h}{2\varepsilon_0 \eta_I^2 V \omega_I}\right)^{\frac{1}{2}} (n_I)^{1/2} \varepsilon_I \cdot \mathbf{P}_{j_1 g} \tag{3.102}$$

where $\mathbf{P}_{j_1 g}$ is the matrix element of the total electron momentum. Similarly, the matrix element of the second interaction is

$$\langle j_2, n(\omega_{m,k})+1 \mid H_{eL} \mid j_1, n(\omega_{m,k}) \rangle = i\frac{h}{2N\omega_{m,k}}^{\frac{1}{2}} \left(n(\omega_{m,k})+1\right)^{1/2} \Xi^{\Omega_{m,k}}_{j_2 j_1} \tag{3.103}$$

and the third matrix element is

$$\langle g, n_S+1 \mid H''_{ER} \mid j_2, n_S \rangle = \frac{e}{m}\left(\frac{h}{2\varepsilon_0 \eta_S^2 V \omega_S}\right)^{\frac{1}{2}} (n_S+1)^{1/2} \varepsilon_S \cdot \mathbf{P}_{g j_2} \tag{3.104}$$

The three interactions can happen in any possible time ordering giving rise to six possible combinations. The overall transition rate is then given by

$$W = \frac{4\pi^3 e^4 n_I (n_S+1)\left(n(\omega_{m,k})+1\right)}{h^3 m^4 N \varepsilon_0^2 \eta_I^2 \eta_S^2 V \omega_I \omega_S \omega_{m,k}} \left| R(-\omega_I, \omega_S, \omega_{m,k}) \right|^2 \delta(\omega_I - \omega_S - \omega_{m,k}) \delta(k_I - k_S - k) \tag{3.105}$$

where

$$\begin{aligned} R(-\omega_I, \omega_S, \omega_{m,k}) = \sum_{j_1, j_2} \Bigg\{ & \frac{P^S_{g j_2} \Xi^{\Omega_{m,k}}_{j_2 j_1} P^I_{j_1 g}}{(\omega_{j_1} - \omega_I)(\omega_{j_2} + \omega_{m,k} - \omega_I)} + \frac{\Xi^{\Omega_{m,k}}_{g j_2} P^S_{g j_2 j_1} P^I_{j_1 g}}{(\omega_{j_1} - \omega_I)(\omega_{j_2} + \omega_S - \omega_I)} \\ & + \frac{\Xi^{\Omega_{m,k}}_{g j_2} P^I_{g j_2 j_1} P^S_{j_1 g}}{(\omega_{j_1} - \omega_S)(\omega_{j_2} + \omega_S - \omega_I)} + \frac{P^I_{g j_2} \Xi^{\Omega_{m,k}}_{j_2 j_1} P^S_{j_1 g}}{(\omega_{j_2} - \omega_S)(\omega_{j_2} + \omega_S + \omega_{m,k})} \\ & + \frac{P^S_{g j_2} P^I_{j_2 j_1} \Xi^{\Omega_{m,k}}_{j_1 g}}{(\omega_{j_1} + \omega_{m,k})(\omega_{j_2} + \omega_{m,k} - \omega_I)} + \frac{P^I_{g j_2} P^S_{j_2 j_1} \Xi^{\Omega_{m,k}}_{j_1 g}}{(\omega_{j_1} + \omega_{m,k})(\omega_{j_2} + \omega_{m,k} + \omega_S)} \Bigg\} \end{aligned} \tag{3.106}$$

The rate in eq. 3.105 for a transition between an initial state $|n_I, n_S\rangle$ and a final state $|n_I-1, n_S+1\rangle$ accompanied by the emission of a phonon, includes a factor $(n_S+1)n_I$. The two contributions to the cross section $n_S n_I$ and n_I describe, respectively, stimulated and spontaneous scattering. In this thesis we are dealing with spontaneous Raman scattering and we will only consider the spontaneous contribution. Therefore, the transition rates for Stokes and antiStokes Raman scattering are

$$W_{STOKES} = \frac{4\pi^3 e^4 \, n_I\left(n(\omega_{m,k})+1\right)}{h^3 m^4 N \varepsilon_0^2 \eta_I^2 \eta_S^2 V \omega_I \omega_S \omega_{m,k}} \left|R\left(-\omega_I, \omega_S, \omega_{m,k}\right)\right|^2 \tag{3.107}$$

$$W_{ANTISTOKES} = \frac{4\pi^3 e^4 \, n_I n(\omega_{m,k})}{h^3 m^4 N \varepsilon_0^2 \eta_I^2 \eta_S^2 V \omega_I \omega_S \omega_{m,k}} \left|R\left(-\omega_I, \omega_S, -\omega_{m,k}\right)\right|^2 \tag{3.108}$$

The notation is such that a negative (positive) frequency denotes destruction (creation) of the corresponding photon or phonon.

It is clear from eq. 3.106 that the transition rate becomes large in conditions of resonance between the incident and scattered frequencies and the electronic transition frequencies. The large resonance scattering rates are experimentally useful for excitations whose light scattering would have been otherwise unobservably weak. This is a feature of great importance for this research.

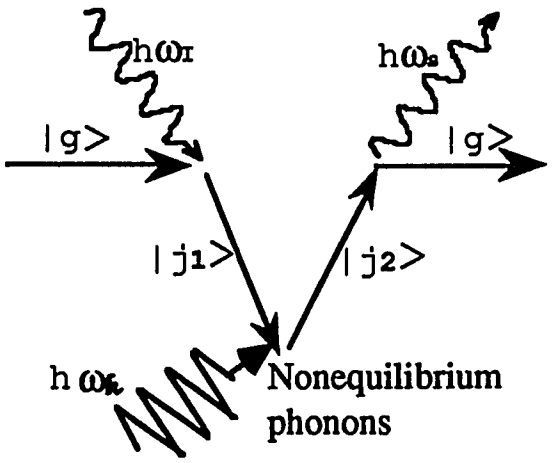

In our time resolved antiStokes Raman scattering experiments, the quantum mechanical process of most importance is shown in the schematic on the right. A nonequilibrium phonon is interacting with a photon from

the probe beam to generate a scattered photon with energy equal to the sum of the energies of the incident photon and the nonequilibrium phonon. Using eqs. 3.106 and 3.108 the rate for this process becomes

$$W = \frac{4\pi^3 e^4 \, n_I n(\omega_{m,k})}{h^3 m^4 N \varepsilon_0^2 \eta_I^2 \eta_S^2 v \omega_I \omega_S \omega_{m,k}} \left| \frac{P^S_{gj_2} \Xi^{Q_{m,k}}_{j_2 j_1} P^I_{j_1 g}}{(\omega_{j_1} - \omega_I)(\omega_{j_2} - \omega_{m,k} - \omega_I)} \right|^2 \qquad (3.109)$$

When ω_{j_1} coincides with an electronic state and $\omega_I \approx \omega_{j_1}$, the denominator in eq. 3.109 becomes very small and the rate for antiStokes Raman scattering W becomes very large. In our experiments, the laser wavelength is tuned to an absorption band of the Cr ions fulfilling the resonant conditions described above. The nonequilibrium phonons generated during the relaxation of the excited Cr ions are obviously coupled with the Cr ions and their contribution to the Raman scattering is enhanced due to the resonant conditions. On the other hand, Raman scattering due to lattice phonons not coupled with the Cr ions is not resonantly enhanced. The generated antiStokes Raman scattering from the nonequilibrium phonons is responsible for the changes in the intensity in the corresponding lines as a function of delay time. The validity of this model is further enhanced by the observation of Cr-ion associated modes under resonant excitation. More specifically, when pumping with E//a-axis of the crystal, the antiStokes Raman spectrum contains lines that appear only for laser wavelengths such that the Raman lines overlap with the absorption peak for E//a (see fig. [6.11]). Details on the experiments are given in chapter 6. These lines are due to Cr-ion vibrational modes and appear only under resonant conditions as it is described by eq. 3.109. The observation of these lines show that Cr-ion associated Raman lines are resonantly enhanced and therefore the

nonequilibrium phonons (which are coupled with the Cr ions) can be observed using a time resolved Raman scattering experiment. The enhancement of the Raman signal arising from the nonequilibrium phonon population makes possible the observation time dependent changes which is one of the main objectives of this thesis.

3.4 References

1. K. Huang and A. Rhys, Proc. R. Soc., **204**, 406, (1951).

2. R. C. O'Rourke, Phys. Rev., **91**, 265, (1953).

3. L. A. Riseberg and H. W. Moos, Phys. Rev., **147**, 429, (1968).

4. H. W. Moos, J. Lumin., **1**, 106, (1970).

5. N. Robertson and L. Friedman, Philosophical Magazine **33**, 753 (1976).

6. N. Robertson and L. Friedman, Philosophical Magazine **36**, 1013 (1977).

7. C. W. Struck and W. H. Fonger, J. Lumin. **10**, 1 (1975).

8. H. Gummel and M. Lax, Ann. Phys. (N.Y.) **2**, 28 (1957).

9. H. L. Pryce, Phonons, edited by R. W. Stevenson (Plenum, New York, 1966), p. 403.

10. M. D. Sturge, Phys. Rev. B, **8**, 6, (1973).

11. G. Rickayzen, Proc. R. Soc., **241**, 480, (1957).

12. R. Englman and J. Jortner, Mol. Phys. **18**, 379, (1969).

13. P. T. Landsberg, Phys. Status Solidi, **41**, 457 (1970).

14. P. T. Landsberg, Phys. Status Solidi, **41**, 457 (1970).

15. F. K. Fong, S. L. Naberhuis and M. M. Miller, J. Chem. Phys. **56**, 4020, (1972).

16. J. Jortner, Mol. Phys. **32**, 379, (1976).

17. A. M. Stoneham, Philosophical Magazine **36**, 983 (1977).

18. For a general reviw and references, see R. Englman, Nonradiative decay of ions and Molecules in Solids, (North-Holland, Amstrerdam, 1979).

19. M. Lax, H. J. Carmichael and W. J. Shugard, Phys. Rev. B, **26**, 3547, (1982).

20. J.M. Wiesenfeld, Linn F. Mollenauer and Erich Ippen, Phys. Rev. Lett., **47**, 1668 (1981).

21. S. K. Gayen, W. B. Wang, V. Petricevic, R. Dorsinville, and R. R. Alfano, Appl. Phys. Lett. 47 (5) 455 (1985).

22. S. K. Gayen, W. B. Wang, V. Petricevic, and R. R. Alfano, Appl. Phys. Lett. 49 (8) 437 (1986).

23. S. K. Gayen, W. B. Wang, V. Petricevic, S. G. Demos, and R. R. Alfano, J. Lumin. 47, 181 (1991).

24. A. M. Stoneham, Philosophical Magazine 36, 983 (1977).

25. B. Henderson and G. F. Imbusch, "Optical Spectroscopy of inorganic solids", (1989), ch. 5 and 9, John Wiley & Sons, New York.

26. A. Laubereau,D.von der Linde and W. Kaiser, Phys. Rev. Lett., 27, 802 (1971).

27. D.von der Linde, J.Kuhl and H.Klingenberg, Phys. Rev. Lett., 44 1505 (1980)

28. J.A.Kash, J.C.Tsang and J.M.Hvam, Phys. Rev. Lett., 54 2151 (1985)

29. K. T. Tsen, R. P. Joshi, D, K. Ferry and H. Morkoc,Phys. Rev. B, 39, 2, 1446 (1973).

30. P. G. Klemens, Phys. Rev., 148, 845 (1966).

31. R. G. Vebrich, V. Narayanamutri, and M. A. Chin, Phys. Rev. Lett., 45, 1432 (1980)

32. P. Hu, V. Narayanamutri, and M. A. Chin, Phys. Rev. Lett., 46, 192 (1981)

33. R. S. Meltzer, J. E. Rives and G. S. Dixon, Phys. Rev. B, 28, 4786 (1983)

34. R. J. G. Goossens, J. I. Dijkhuis, and H. W. de Wijn, Phys. Rev. B, 32, 5163 (1985)

35. M. J. Van Dort, C. R. de Kok, J. I. Dijkhuis, and H. W. de Wijn, J. Lumin. 45, 150 (1990)

36. D. M. Boye, J. E. Rives and R. S. Meltzer, J. Lumin. 45, 147 (1990)

37. W. A. Tolbert, W. M. Dennis, and W. M. Yen, Phys. Rev. Lett., **65**, 607 (1990)

38. Kazuaki Iishi, American Mineral., **63**, 1198-1208 (1978)

Chapter 4
Properties of Forsterite.

4.1 Background.

The chromium-doped forsterite ($Cr:Mg_2SiO_4$) has become an important solid state laser because it is tunable between 1150-1350 nm.[1-5] The unique spectroscopic property of chromium-doped forsterite is that the tetravalent chromium (Cr^{4+}) substituting for tetrahedrally coordinated Si was identified as the lasing center.[2,3,6-10] This has lead to a search for new Cr^{4+} based crystals such as Cr^{4+}:YAG. The electronic structure of forsterite has been studied by absorption and emission measurements[6-9] as well as electron paramagnetic resonance.[10-12] These measurements clearly demonstrate the presence of both Cr^{3+} and Cr^{4+} ions in forsterite.

Forsterite (Mg_2SiO_4), is a member of the olivine family. It has an orthorhombic structure with space group P_{bnm}[13,14] and it is a naturally occurring gem. The orthorhombic structure of forsterite crystal is shown in fig. [4.1] in schematic form. It contains four formula units per unit cell, i.e. 28 atoms. The unit cell dimensions are a=4.76 Å, b=10.22 Å, c=5.99 Å. Laser action occurs along the b-axis. The Mg atoms occupy octahedral sites while the Si atoms occupy tetrahedral sites. The Mg atoms are in two crystalographically distinct position, which have inversion and mirror point symmetry. The four equivalent SiO_4 groups (as well as four of the Mg ions) are situated on mirror planes perpendicular to the b-axis atoms and they have mirror point symmetry. All the polyhedra are extremely distorted. Cr-doped forsterite exhibits dichroic properties. To the eyes it

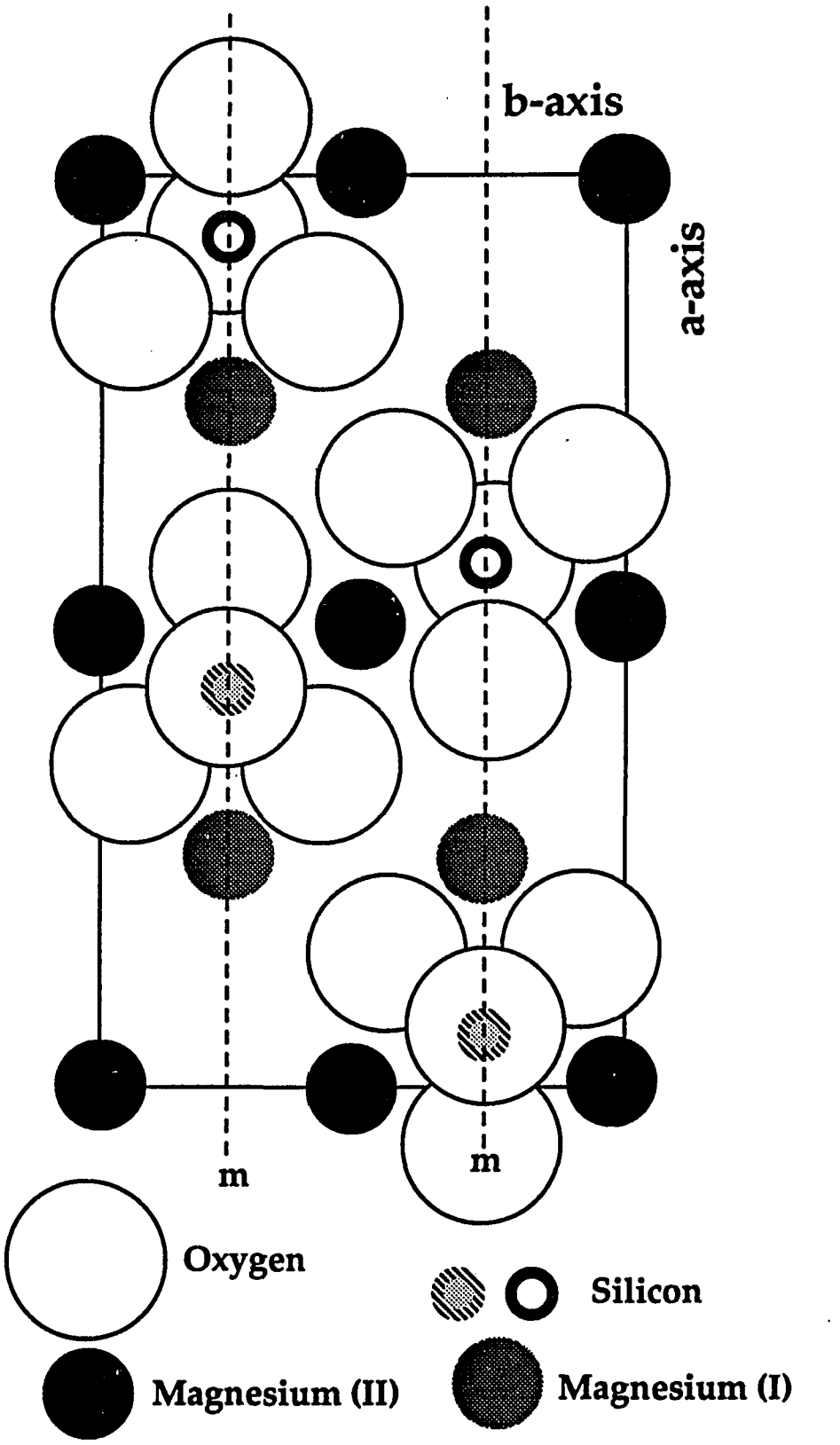

Figure 4.1: Unit cell of forsterite viewed along the c-axis. m represents mirror planes perpenticular to the b-axis.

appears greenish, bluish and reddish when looking through the a, b, and c-axis respectively.

Single crystals of chromium doped forsterite have been grown successfully using the Czochralski method,[15] as well as the laser-heated pedestal growth (LHPG) technique.[3] The general features of the absorption and emission spectra of Cr:doped forsterite grown by the two methods are similar. Cr^{3+} and Cr^{4+} coexist in forsterite crystals and their relative concentration depends on the growth atmosphere. By growing the crystal in a reducing atmosphere the concentration in Cr^{3+} increases while by employing pure O_2 the Cr^{4+} concentration increases. The tetravalent chromium replaces Si in the Mg_2SiO_4 host in tetrahedral sites. The trivalent chromium substitutes for the octahedrally coordinated Mg ions and therefore some of the Cr^{3+} ions have inversion [Cr^{3+}(I)] symmetry while the others have mirror symmetry [Cr^{3+}(II)]. Trivalent chromium enters the mirror and the inversion site in a ratio 3:2. The existence of Cr3+ ions in the two sites in the ratio given above has been verified by EPR and ENDOR measurements.[10-12] The metastable level of Cr^{3+}(I) is the ^2E state. In contrast to Cr^{3+}(I), Cr^{3+}(II) is a low field site, in which the $^4T_2$ state is the metastable state and is below the ^2E state. This is because the Mg(II) octahedron is larger than the Mg(I) octahedron. The Tanabe-Sugano energy level diagrams of Cr^{3+} in octahedral field and Cr^{4+} in tetrahedral field is given in fig. [4.2]. The absorption spectra are given in fig. [4.3]. The absorption and emission characteristics can be summarized in the tables [4.1] and [4.2].

The modes of vibration of Mg_2SiO_4 are separated into internal (SiO_4) and external (lattice) modes.[13,14,16,17] In table [4.3], all the modes observed in the Raman scattering spectra and in the infrared absorption measurements

are provided as they have been given in the literature. The 1050-800 cm^{-1} region corresponds to various stretching vibrations of the SiO_4 tetrahedron; The symmetric stretch modes are denoted as (ν_1) while the antisymmetric stretch modes are denoted as (ν_3). The 650-475 cm^{-1} region corresponds to bending vibrations of the SiO_4; Two-fold and three-fold degenerate deformation modes exist in this spectral region and are denoted as (ν_2) and (ν_4) respectively. Below 475 cm^{-1} are the external modes of vibration, which are described as translations of the Mg ions or of the SiO_4 along a crystal axis [T_i(Mg) or $T_i(SiO_4)$], or rotations of the SiO_4 [$R_i(SiO_4)$]. In the backscattering geometry utilized in the time resolved Raman scattering experiments, the modes observed have A_g and B_{2g} symmetry.

In this research we have concentrated our effort on the investigation of the nonradiative relaxation of the Cr^{4+} ions in forsterite. For this reason, I will extent the presentation of general background only for the Cr^{4+} ions in forsterite.

TABLE 4.1: (From ref. 6)
Energy levels of Cr^{4+}:Mg_2SiO_4

Transition	Energy (cm^{-1})
$^3A_2 \rightarrow {}^3T_2$	9,150
$^3A_2 \rightarrow {}^3T_1$	15,430
$^3A_2 \rightarrow {}^1E$	15,875
$^3A_2 \rightarrow {}^3T_1$	26,810
$^3A_2 \rightarrow {}^1T_1$	28,735
$^3T_2 \rightarrow {}^3A_2$	8,750*

* : zero phonon line

TABLE 4.2: (From ref. 6)
Energy levels of Cr^{3+}:Mg_2SiO_4

Transition	Energy (cm^{-1})
$^4A_2 \rightarrow {}^4T_2$	15,100
$^4A_2 \rightarrow {}^2E$	14,450
$^4A_2 \rightarrow {}^2T_1$	15,380
$^4A_2 \rightarrow {}^2T_2$	21,050
$^4A_2 \rightarrow {}^4T_{1a}$	21,500
$^4A_2 \rightarrow {}^4T_{1b}$	33,780
$^4T_2 \rightarrow {}^4A_2$	11,100*
$^2E \rightarrow {}^4A_2$	14,437**

* :zero phonon line at 13,566 cm^{-1}

** : R line

(a)

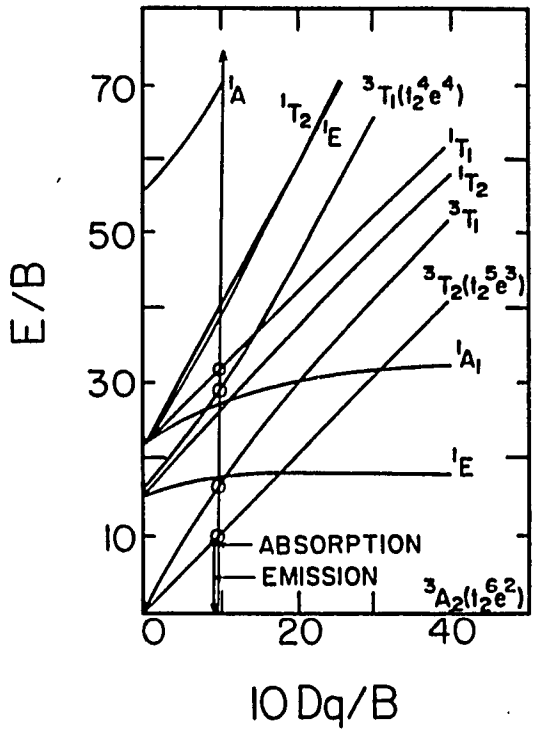

(b)

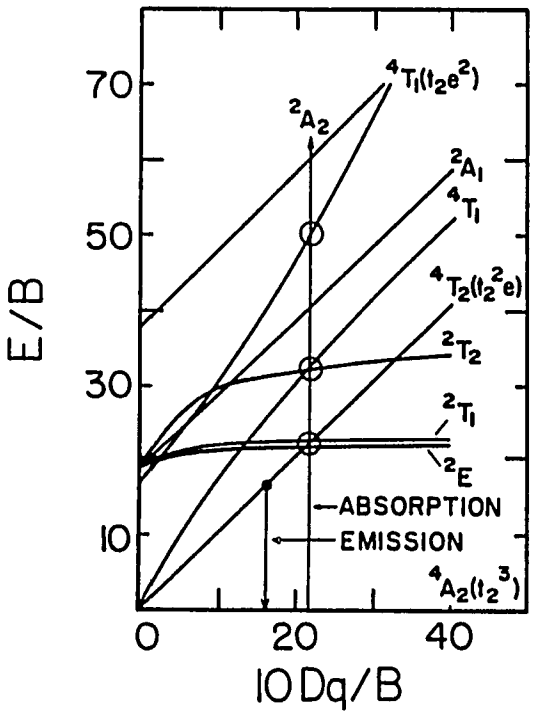

Figure 4.2: Tanabe-Sugano diagram for a) Cr^{4+} in tetrahedral coordination (upper diagram) and b) Cr^{3+} in octahedral coordination. (lower diagram).

(a)

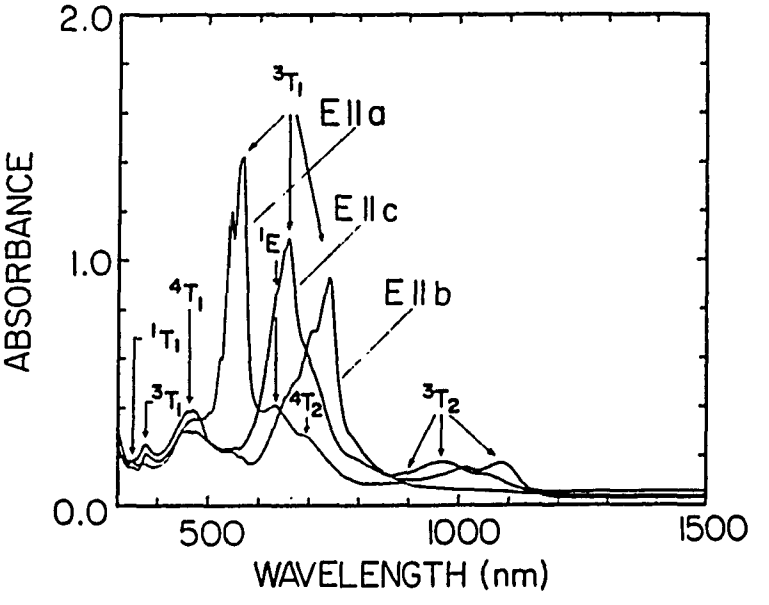

(b)

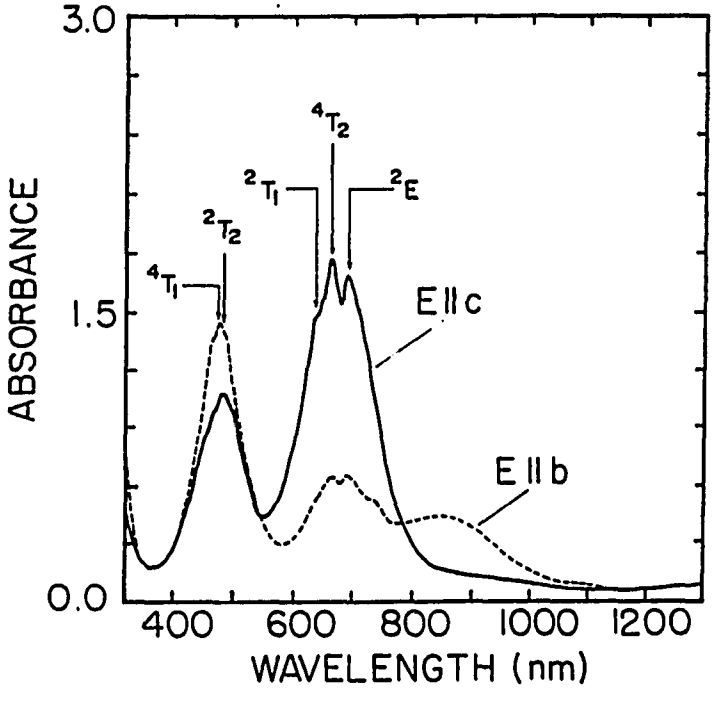

Figure 4.3: Room temperature absorption spectrum of Cr:Mg_2SiO_4 grown a) in oxidized atmosphere (upper spectra) and b) in a reducing atmosphere (lower spectra) for different crystal orientations. (From ref. 6).

symmetry	Experiment	Assignment
A_g	966	ν_3
	856	ν_3
Raman	826	ν_1
active	609	ν_4
	546	ν_4
	424	ν_2
	340	$R_c(SiO_4)$
	329	T_b(MgII)
	305	T_a(MgII, SiO_4)
	227	T_b(SiO_4, MgII)
	183	T_a(MgII, SiO_4)
B_{2g}	884	ν_3
	588	ν_4
Raman	441	ν_2
active	368	$R_b(SiO_4)$
	324	$R_a(SiO_4)$
	244	$T_c(SiO_4)$
	142	T_c(MgII)
B_{1g}	976	ν_3
	866	ν_3
Raman	839	ν_1
active	632	ν_4
	583	ν_4
	434	ν_2
	418	$R_c(SiO_4)$
	318	T_b(MgII)
	260	T_a(MgII, SiO_4)
	224	T_a(MgII, SiO_4)
	192	T_b(SiO_4, MgII)
B_{3g}	922	ν_3
	595	ν_4
Raman	412	ν_2
active	376	$R_c(SiO_4)$
	318	$R_b(SiO_4)$
	272	T_c(MgII)
	226	$T_c(SiO_4)$

symmetry	Exper.(TO/LO)	Assignment
B_{1u}	885/994	ν_3
	502/585	ν_4
IR	483/489	ν_2
active	423/459	$R_c(SiO_4)$
	296/318	T_c(MgI)
	274/278	T_b(MgII)+T_c(MgI)
	224/--	T_a(MgI)
	201/--	$T_{b,c}$(MgI)
B_{2u}	987/993	ν_3
	882/979	ν_3
IR	838/843	ν_1
active	537/597	ν_4
	510/516	ν_4
	465/493	ν_2
	421/446	$R_c(SiO_4)$
	400/412	T_c(MgI)
	352/376	$T_{b,c}$(MgII)
	294/313	$T_{a,c}$(MgI)+T_b(MgII)
	280/283	T_b(MgI)
	224/--	T_a(MgII)
	201/--	T_a(MgI,SiO_4)
B_{3u}	980/1086	ν_3
	957/963	ν_3
IR	838/845	ν_1
active	601/645	ν_4
	562/566	ν_4
	498/544	ν_2
	403/469	$R_a(SiO_4)$
	378/386	T_c(MgI)
	320/323	$T_{b,c}$(MgI)
	293/298	$T_{a,c}$(MgI)
	274/276	T_a(MgI)+T_b(MgII)
	224/--	$T_{a,b}$(MgII)
	201/--	T_b(MgI,SiO_4)

Table 4.3: Observed frequencies in Raman scattering and infrared absorption spectra and their assignment for Mg_2SiO_4 (From Ref. 14).

4.2 Cr^{4+} -doped forsterite.

Cr^{4+} ions in forsterite possess a $3d^2$ electronic configuration. The Tanabe-Sugano diagram of $3d^2$ in a tetrahedron is shown in fig. [4.2]. In a tetrahedral field, the ground state of the free ion, ^3F, splits into $^3A_2$, $^3T_2$ and $^3T_1(^3F)$. The lowest in energy of the above is the $^3A_2$, which is the new ground state. One of the excited states of the free ion, ^3P, transforms into $^3T_1(^3P)$. The transitions $^3A_2 \rightarrow {}^3T_1$ are electric dipole allowed while the $^3A_2 \rightarrow {}^3T_2$ is forbidden. However, the tetrahedron has an orthorhombic distortion and the transition becomes electric dipole allowed. The only emission reported up to this work that is due to the Cr^{4+} ions, is the NIR fluorescence associated with the $^3T_2 \rightarrow {}^3A_2$ transition. The $^3T_2$ state is the lowest excited electronic state, and is the lasing level in forsterite. In the low temperature spectrum shown in fig. [4.4], the zero phonon peak of this emission is at ≈1093 nm. The spectrum also contains a series of phonon satellites at longer wavelengths with the first and stronger positioned 148 cm^{-1} from the zero phonon peak. The lifetime of this emission is 27 μs at T=77 K and decreases to 3 μs at room temperature.

The polarized site-selective excitation spectrum at T=10 K is shown in fig. [4.5]. The three absorption bands observed are due to the splitting of the $^3T_1(^3F)$ electronic state due to the orthorhombic distortion. Under C_{2u}-orthorhombic field, $^3T_1$ splits into $^3A_2$, $^3B_1$, and $^3B_2$ which are the cause of the absorption bands for E ∥ c, E ∥ b and E ∥ a respectively. Furthermore, under spin-orbit interaction, the spin-triplet degeneracy of each orthorhombic field component is split in to three spin singlets. This splitting is also seen in the absorption spectrum. For example, in fig. [4.5] and for E ∥ a, three peaks due to spin orbit interaction appear at 572, 567 and

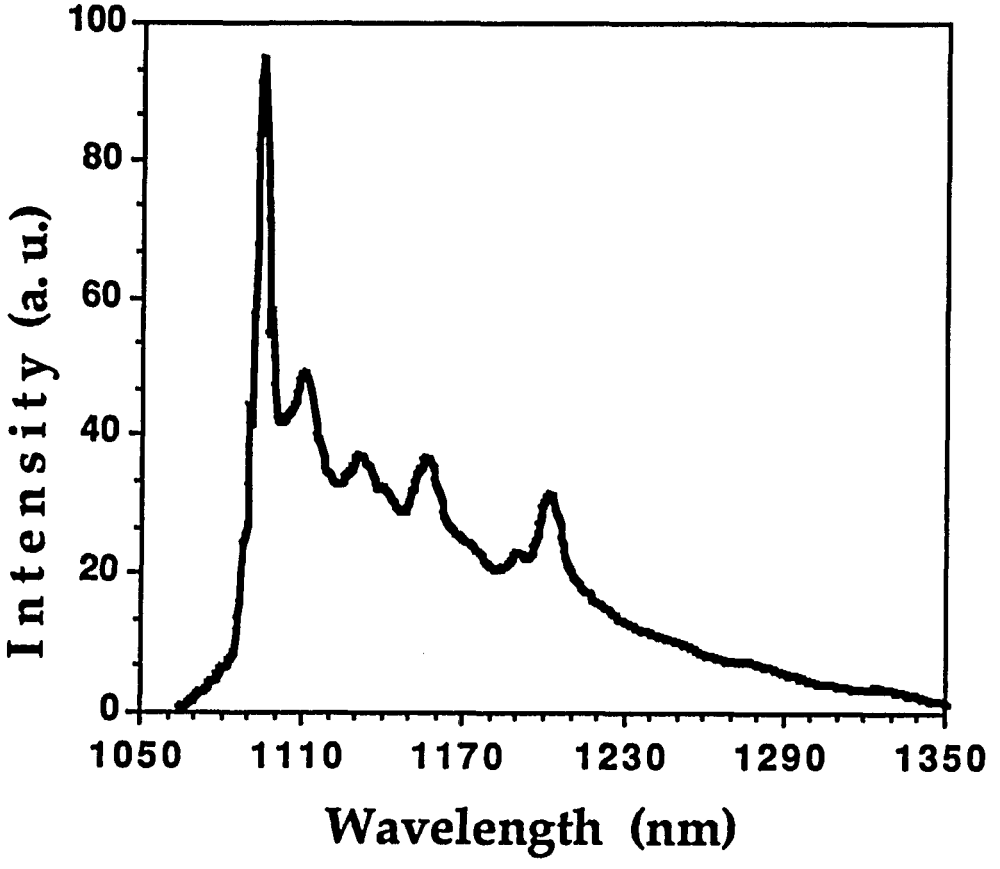

Figure 4.4: The NIR emission due to the $^3T_2 \rightarrow {}^3A_2$ transition in forsterite at T=80 K under 1064 nm excitation. (From Ref. 6)

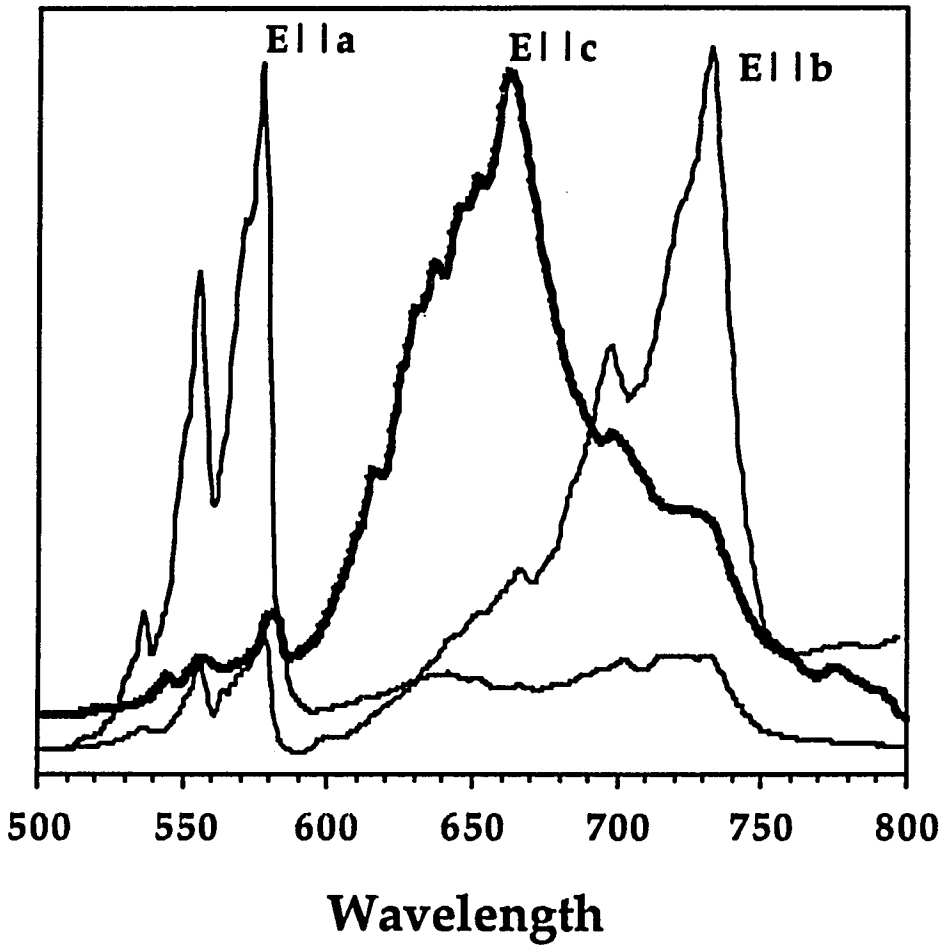

Figure 4.5: The site-selective excitation spectra of Cr $^{4+}$ ions in forsterite at 10 K. Absorption is due to the transition $^3A_2 \rightarrow {}^3T_1$ while the monitored wavelength is 1094 nm. (From Ref. 8)

560 nm. The other two bands are the first and second orders phonon sidebands of the zero-phonon transitions. The average phonon energy was found to be ≈740 cm^{-1} which is likely a localized stretching mode of the tetrahedron,[8,18] as this frequency is not a normal mode of forsterite. The spectra in other polarizations have similar splitting but are not resolvable as well as for E ∥ a. Low temperature absorption shows that the $^3T_2$ state is also split into nine spinors. All the above are summarized in Table [4.4].

For the completion of this research, a number of forsterite crystals were available. Two of these crystal (2X10X10 and 8X10X10 mm^3) contain mostly Cr^{4+} ions and they have been used for the investigation of nonradiative relaxation of Cr^{4+} ions in forsterite. The Cr^{4+} ion concentration was estimated[19] to be 3.71X10^{18} ions/cm^3 for the 2X10X10 mm^3 sample and 2.74X10^{18} for the 8X10X10 mm^3 sample. One crystal (30X5X5 mm^3) contains mostly Cr^{3+} ions and has been used for comparison with measurements associated with the relaxation of Cr^{4+} ions . In addition, a pure Mg_2SiO_4 crystal (5X17X13 mm^3) that was free of any impurity Cr ions was at hand.

Tetrahedral		Orthorhombic		Spin-orbital coupling	
$^3A_2$	0	$^3A_2$	0	$^3A_2$	0
				B_1	9139 / (1094)
		$^3A_1$	9150	B_2	9152 / (1093)
				A_2	9169 / (1091)
				A_2	9812 / (1019)
$^3T_2$	10140	$^3B_1$	9820	A_1	9824 / (1018)
				B_2	9836 / (1017)
				B_1	11455 / (873)
		$^3B_2$	11470	A_1	11472 / (872)
				A_2	11489 / (871)
				A_1	13684 / (733)
		$^3A_2$	13850	B_2	13812 / (724)
				B_1	14045 / (712)
				B_2	15050 / (665)
$^3T_1$	15610	$^3B_1$	15300	A_1	15340 / (652)
				A_2	15500 / (645)
				A_2	17470 / (572)
		$^3B_2$	17670	A_1	17680 / (567)
				B_1	17857 / (560)

Table 4.4: The energy levels of Cr^{4+} ions in forsterite after taking into account the orthorhombic distortion and spin-orbit interaction. The energy is given in cm^{-1} (nm) and was obtained from low temperature absorption measurements (From Ref. 8).

4.3 References

1. V. Petričević, S. K. Gayen, R. R. Alfano, K. Yamagishi, H. Anzai, and Y. Yamaguchi, Appl. Phys. Lett. **52**, 1040 (1988).
2. V. Petričević, S. K. Gayen, and R. R. Alfano, Appl. Phys. Lett. **53**, 2590 (1988).
3. H. R. Verdun, L. M. Thomas, D. M. Andrauskas, T. McCollum, and A. Pinto, Appl. Phys. Lett. **53**, 2593 (1988)
4. V. G. Barishevskii, M. V. Korzhik, A. E. Kimaev, M. G. Livshitz, V. B. Pavlenko, M. L. Meilman, and B. I. Minkov, Zh. Prikl. Spectrosk. (Moscow) **53**, 7 (1990).
5. A. Seas, V. Petričević, and R. R. Alfano, Opt. Lett. **16**, 937 (1992).
6. V. Petričević, S. K. Gayen, and R. R. Alfano, in *Tunable Solid-State Lasers*, Vol. 5 of the OSA Proceeding Series, M. L. Shand and H. P. Jenssen, eds. (Optical Society of America, Washington, D.C., 1989), pp. 77-84.
7. H. R. Verdun, L. M. Thomas, D. M. Andrauskas, T. McCollum, and A. Pinto, OSA Proceedings of the Advanced Solid-State Lasers, eds. M. L. Shand and H. P. Jenssen, Vol. 5, 85, (1989).
8. W. Jia, H. Liu, S. Jaffe, and W. M. Yen, Phys. Rev. B **43**, 5234 (1991).
9. R. Moncorge, G. Cormier, D. J. Simkin and J. A. Capobianco, J. Quantum Electr. **27**, 114 (1991).
10. K. R. Hoffman, J. Casas-Gonzales, S. M. Jacobsen, and W. M. Yen, Phys. Rev. B **44**, 125289 (1991).
11. H. Rager, Phys. Chem. Minerals **1**, 371 (1977).

12. L. V. Bershov, J. M. Gaite, S. S. Hafner, and H. Rager, Phys. Chem. Mineral **9**, 95 (1983).

13. V. Devarajan and E. Funck, J. Chem. Phys., **62**, No 9, 3406, (1975).

14. Kazuaki Iishi, American Mineral., **63**, 1198-1208 (1978).

15. N. Nishide, Y. Segewa, P. H. Kim, S. Namba, and A. Masuyama, Reza Kagaku Kenkyu **7**, 89 (1985).

16. M. Th. Paques-Ledent and P. Tarte, Spectroch. Acta **29A**, 1007, (1973).

17. A. Chopelas, American Mineral., **76**, 1101 (1991).

18. H. Rager and G. Weiser, Bull. Mineral. **104**, 603 (1981).

19. V. Petričević, unpublished data.

Chapter 5

Up-converted Luminescence.

5.1 Introduction.

The photoexcitation of an impurity ion in a crystal is followed by ultrafast nonradiative relaxation via phonon emission.[1-5] This process allows for the transfer of the excess energy of the ion (the difference between excitation energy level and storage level) into the surrounding lattice . During this process, nonequilibrium vibronic levels are populated with energy separation equal to the energy of the emitted phonons. From these short-lived vibronic levels there is a probability for radiative relaxation to the ground state[6,7] resulting in a weak luminescence called hot luminescence (HL). Hot luminescence has been observed in various dielectric crystals.[8,9] The observed weak signal of HL occurs at frequencies lower than the excitation frequency and typically overlaps with the Stokes Raman scattering components. The overlapping of the HL with the peaks of the Raman scattering emission prevents the observation of the fine structure in the HL spectrum. The HL fine structure is a signature of the initial steps of the cascade process directly showing which phonon modes are involved in the vibrational relaxation. In semiconductors, the presence of an acceptor level discriminates the HL signal from the Raman signal.[10,11] The HL emission is due to the recombination of electrons with neutral acceptors and consequently this emission occurs at energies lower than the Raman lines. The recombination of unrelaxed carriers with neutral acceptors has been observed in GaAs showing a series of peaks from the

energy loss of hot electrons by LO phonon emission.[10-14] The first peak in the HL spectra of GaAs arises from the transition from the excitation level (no phonon emitted) to the acceptor level. In dielectric crystals, phonon peaks involving the lowest states of the molecular anharmonic oscillator[15,16] have been observed in F centers with substitutional molecular defects.

In transition metal-doped materials, ordinary luminescence (OL) occurs from the long-lived storage levels or nearby thermally populated electronic states. In some crystal systems, conversion of long-wave into short-wave radiation is possible by multiphoton absorption. This mechanism is called up-conversion. Green up-converted OL has been observed in $MgF_2:Ni^{2+}$ under photoexcitation by deep red 752.5 nm[17] radiation. This emission arises from a higher metastable level populated by excited state absorption (ESA). Up-conversion processes have been extensively studied in rare earth ion-doped crystals[18]. In 1987 the first laser action upon up-conversion was reported[19] in $YAlO_3:Er^{3+}$ crystal, demonstrating that ESA can be a very efficient way to populate higher lying electronic states.

In this chapter, I will deal with hot luminescence following ESA from the SL in Cr^{4+}-doped forsterite. The excitation level is higher than the photon energy by an amount of energy equal to the energy of the storage level. Therefore, hot luminescence from the excitation level and the vibronic levels underneath that are populated during the vibrational relaxation is blue-shifted with respect to the laser wavelength. The observed up-converted HL spectrum is thus isolated from any of the other photoemission processes. The use of a two-step photoexcitation technique

allows the observation of fine vibrational structure in the up-converted hot luminescence emission associated with the nonequilibrium vibronic levels.

The schematic diagram depicting the up-converted two step hot luminescence process is shown in fig. [5.1]. Absorption of the laser light by the ions quickly produces a highly populated storage level. In the case of excited state absorption the center absorbs a photon while it is temporally relaxing at the storage level (SL) and reaches an excitation level (EL) at energy:

$$E_{EL}=E_{SL}+ h\omega_{laser} \qquad (5.1)$$

This process requires two steps and in the case of low-energy ultrashort pulses the photons originate from different pulses. The time separation between two pulses should be smaller than the lifetime of the storage level because a populated SL should be available when the second pulse arrives.

The up-converted HL spectrum involves downward radiative transitions from the manifold of nonequilibrium electronic-vibrational states populated during the vibrational relaxation of the ions. The overall up-converted emission spectrum is an assemble of the radiative transitions from each nonequilibrium vibronic level of the excited state to the ground state vibronic levels. A detailed discussion of this emission is presented is section 5.4 where I show that the initial vibronic levels have most of their radiative emission directed to the zero vibronic level of the ground state. This gives rise to peaks in the up-converted hot luminescence that are separated by energy equal to the energy separation of the vibronic levels. Typical spectra of up-converted hot luminescence emission under various laser excitation wavelengths are shown in fig. [5.5]. This allows for the determination of the phonon modes involved in the initial steps of the nonradiative relaxation.

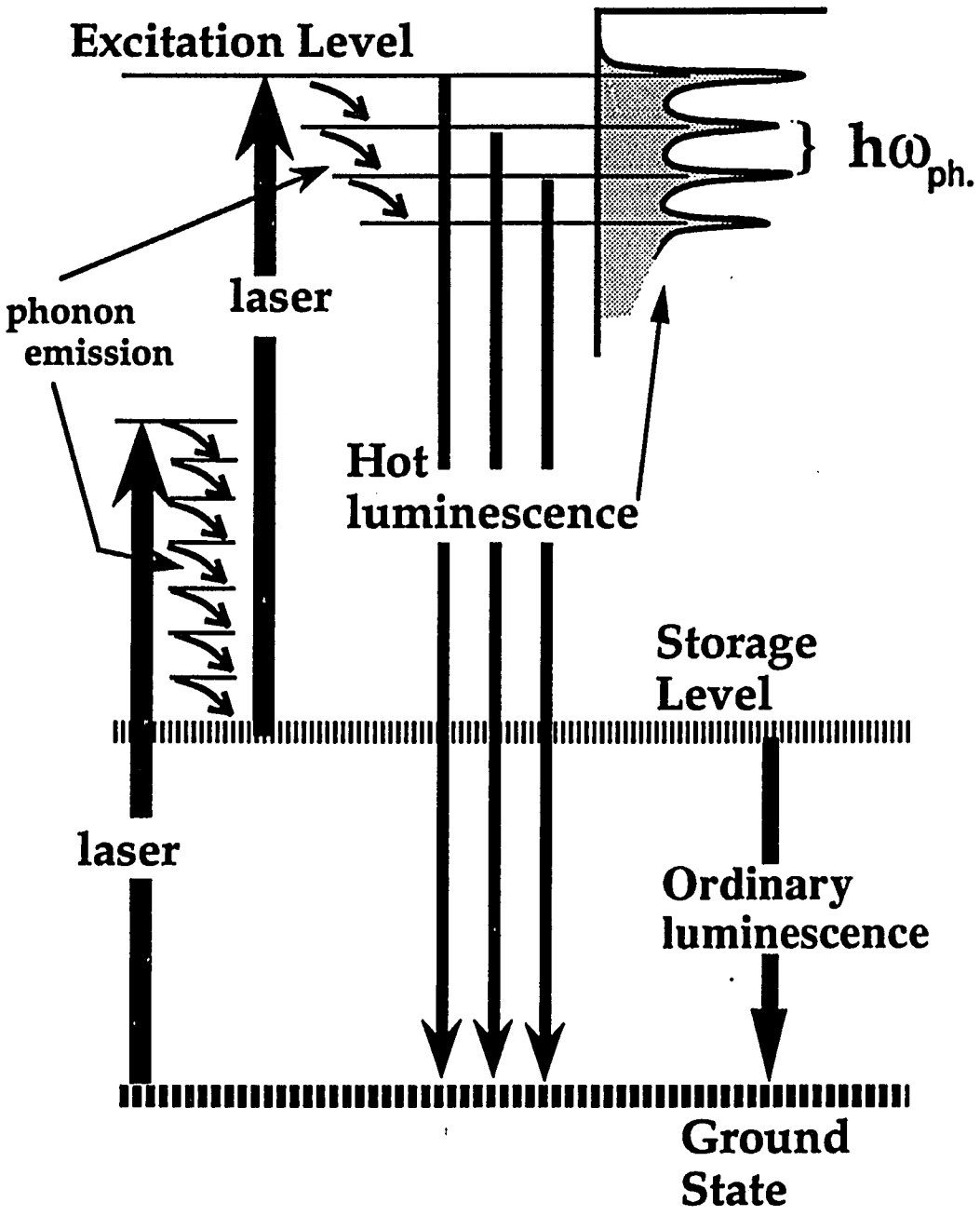

Figure 5.1: Schematic diagram showing the up-converted hot luminescence and ordinary luminescence processes in Cr doped forsterite.

5.2 Experimental setup.

The 1064 and 532 nm laser output after pulse compression and the tunable output of the dye laser (570 nm to 780 nm) were the excitation sources. The laser power utilized for spectroscopy was 200 to 400 mW and the pulse duration 4 to 6 ps depending on the particular laser wavelength. The sample is the forsterite crystal of 10X10X8 mm^3 in dimension Using two-step photoexcitation the higher lying vibrational levels of the $^3T_1$ electronic state were populated. The experimental set-up is shown in fig. [5.2]. The laser beam is focused into the sample using a 90 mm focal length lens while the fluorescence light is collected and focused into the spectrograph by an 85 mm camera lens. Two scattering geometries were utilized shown in fig. [5.2], the backscattering (BS) configuration (arrangement A) and the 90° scattering geometry (PS) configuration (arrangement B). In the BS geometry, a 3 mm in diameter mirror in front of the camera lens directs the focused laser beam into the sample. In the PS scattering geometry, the direction of the laser beam is perpendicular to the direction of scattered light collection while the sample is placed at 45° with respect to excitation beam. PIAS was the detector used to spectrally analyze the up-converted HL signal. An optical cryostat was used for the low temperature experiments. The experiments were performed at room and liquid nitrogen temperatures. ESA was possible since the time interval between consecutive pulses is 12 ns while the lifetime of the SL is 3-25 μs depending on the temperature.

The up-converted HL is observable throughout the energy spectrum determined by the two-photon-step excitation level and the laser photon energy. The emission shows phonon peaks and areas of enhanced emission.

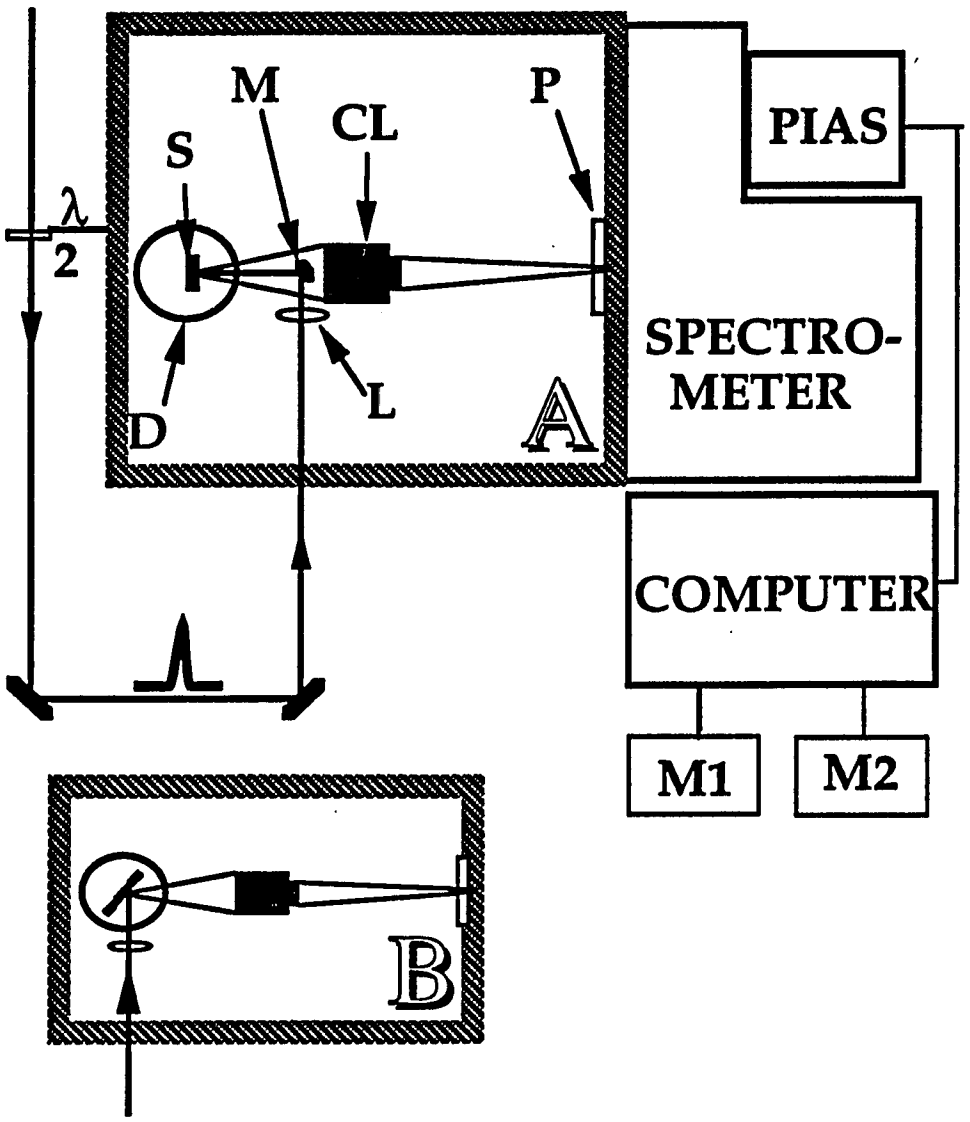

Figure 5.2: Experimental setup showing the optical configuration for A) backscattering geometry and B) for 90° scattering geometry (S: sample, CL: 85 mm camera lens, L: 90 mm focal length lens, M: 2 mm diameter mirror, P: polarizer, D: optical cryostat, M1 and M2: computer monitors 1 and 2.

The peaks are associated with the phonon "steps" in the vibrational relaxation (see fig. [5.1]) while the enhanced emission can be attributed to electronic states or bottlenecks. The use of a Streak camera allowed an accurate characterization of the observed emission. The decay time should be of the order of few ps for HL emission from electronic bottlenecks. Emission from electronic levels should be significantly longer. The experimental layout for the time resolved experiments using streak camera is shown in fig. [5.3]. The laser excitation beam utilized was obtained from the Nd:YAG laser after pulse compression. For 1064 nm excitation, 2 W average power was used while the pulse duration was ≈6 ps. For 532 nm excitation, 1 W average power was available while the pulse duration was ≈4 ps. The sample used for the streak camera experiments is the forsterite crystal of 10X10X2 mm^3 in dimension. The emitted light is collected and collimated in the forward direction by a 105 mm camera lens and focused into a double grating spectrograph by a 300 mm focal length achromatic lens. The forward direction and a thin sample were chosen in order to avoid temporal broadening of the signal due to the thickness of the sample or from the induced time delay when the excitation pulses travel in one direction and the collection optics is in the opposite direction. The streak camera is attached to the output of the spectrograph. The time resolution of the streak camera is 10 ps and therefore, signals shorter than 10 ps were not time resolved. Using the Streak camera system we discriminated the hot luminescence emission from the emissions from a metastable level and obtained information on the decay dynamics.

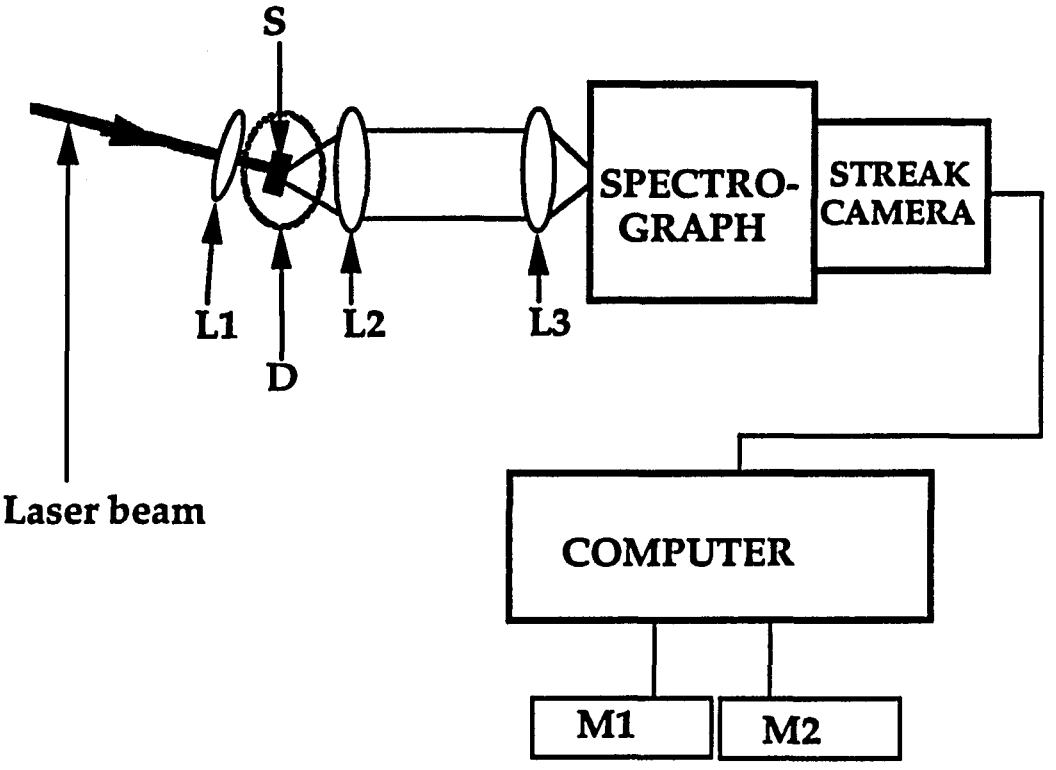

Figure 5.3: Experimental setup showing the optical configuration for experiments using the streak camera. (S: sample, L1: 40 mm focal length lens, L2: 105 mm camera lens, L3: 300 mm focal length achromatic lens, D: optical cryostat, M1 and M2: computer monitors 1 and 2.

5.3 Experimental results on up-converted hot luminescence.

In Cr^{4+} forsterite, the storage level (SL) is located at 1.135 eV. Ions at the SL absorb a photon to reach an excitation level at energy given by the sum of the energies of the SL and the photon absorbed (see fig. [5.1]). HL spectra for different excitation wavelengths are shown in fig. [5.4]. Ions in the SL (1.137 eV, $^3T_2$ state) absorb a photon to reach a higher lying vibrational level (EL) of the $^3T_1$ state within the ESA process. Using 617 nm (2.01 eV) pulses for excitation, the energy of the excitation level is E_{EL}=3.145 eV (=1.135+2.01). Fig. [5.4a] shows the emission spectrum measured at T=80 K in BS geometry. The polarization of the excitation beam (P_e) and the polarizer in the collection path (P_s) were parallel to the c-axis of the crystal. This luminescence signal shows a series of peaks with the highest energy peak positioned at exactly the excitation level E_{EL}=3.145 eV. Fig. [5.4b] displays spectra taken using pump wavelengths at 626 nm to reach E_{EL}=3.116 eV and 614 nm to reach E_{EL}=3.155 eV. Notice, the spectral profiles are similar while the highest energy peak shifts proportionally to the laser frequency shift as it is anticipated from eq. 5.1 ($E_{EL}=E_{SL}+\hbar\omega_{laser}$). In these cases, the first peak appears at the excitation level energy. The spacing between the remaining peaks is 513±12 cm^{-1} and 325±12 cm^{-1}. This behavior indicates that the signal indeed arises from hot luminescence since in these cases it is expected that the spectral profiles are independent of small pumping wavelength shifts.[20]

Up-converted HL for a wider set of laser wavelengths is shown in fig. [5.5]. The lower profile was obtained under 617 nm. Pumping with 650 and 690 nm laser light the second and third spectral profiles were obtained. The energy of the excitation levels are at 3.043 eV and 2.932 eV, respectively in

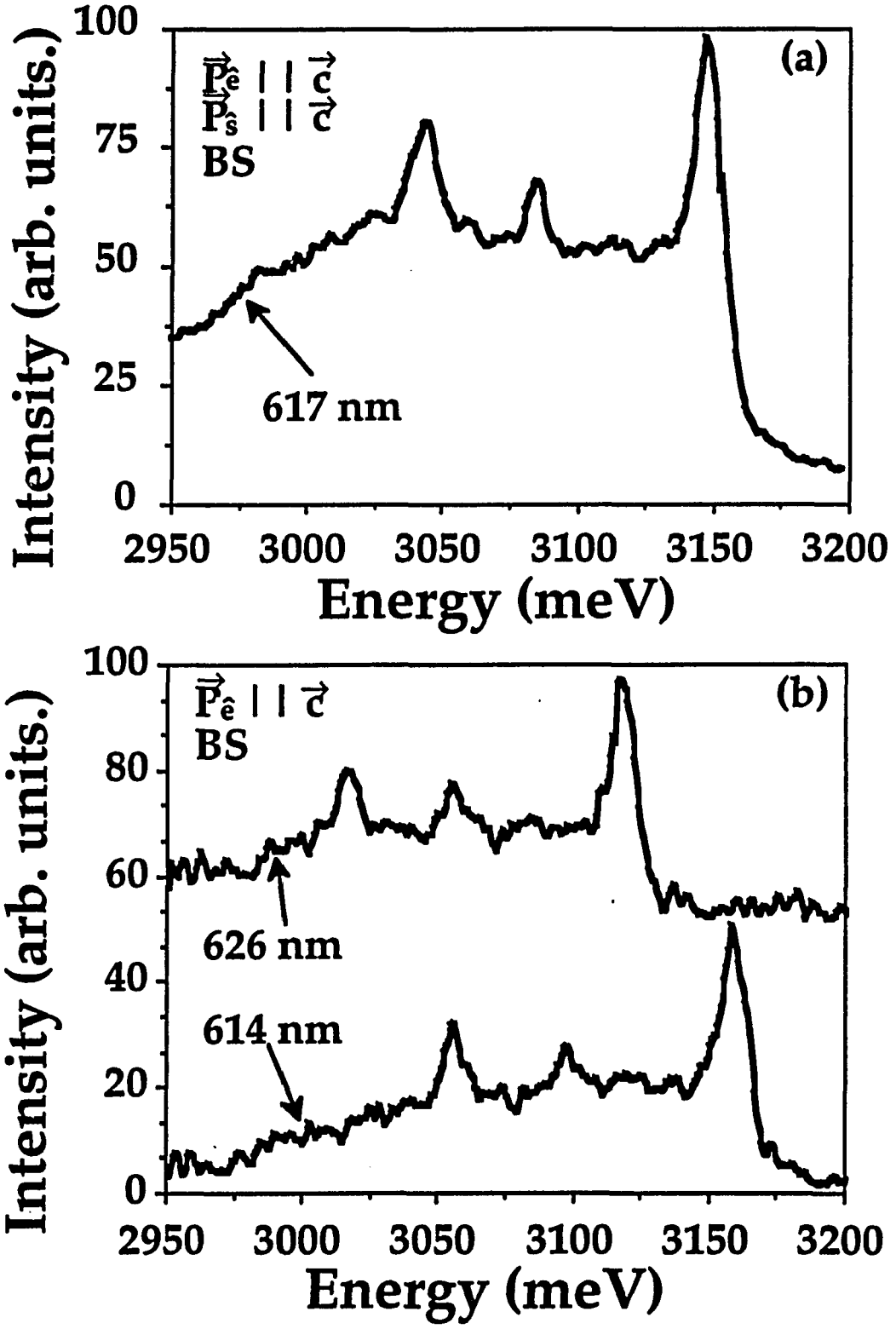

Figure 5.4: Hot luminescence spectra following excited state absorption under a) 617 nm excitation and b) 614 nm (upper profile) and 626 nm excitation (lower profile) at liquid nitrogen temperature

consistence with eq. 5.1. Up-converted HL for 740 nm excitation to reach the 2.811 eV level is shown in the upper profile of fig. [5.5]. In all spectra shown in figs. [5.4] and [5.5], three main peaks appear with the highest energy peak positioned at the exactly the two-step excitation energy. These peaks reveal the dominant phonon modes involved in the vibronic relaxation. The energy of the phonons is given by the difference in energy between successive peaks in the HL emission. The measured energy of these modes is 513±12 cm^{-1} and 325±12 cm^{-1}. At lower energies, a continuous emission is observed. These features are observed in all up-converted HL spectra obtained under excitations from 600 nm to 780 nm (excitation levels from 3.20 eV to 2.72 eV). Up-converted HL profiles obtained under 640 to 670 nm excitation have two additional smaller peaks positioned at ≈325 and ≈690 cm^{-1} from the highest energy peak. The size of these small peaks is always similar as shown in the profile under 650 nm excitation of fig. [5.5] (noted by arrows). This indicates that in the 3.07 to 2.98 eV part of the excited state there is an alternative relaxation channel associated with the emission of a 325±20 cm^{-1} followed by a 365±20 cm^{-1} phonons instead of the emission of 513 cm^{-1} and 325 cm^{-1} phonons. An additional characteristic of all spectra shown in fig. [5.5] is the increase in the HL emission intensity at energies below ≈2.7 eV.

Pumping with 1064 nm (1.165 eV) laser light, the first HL peak following ESA appears at 2.300 eV (1.135+1.165). Fig. [5.6] displays the HL spectra under 1064 nm excitation for the BS geometry and for P_e//b-axis at liquid nitrogen temperature. Figs. [5.6a] and [5.6b] show HL spectra taken with P_s//b-axis and P_s//c-axis of the crystal, respectively. Using excitation polarization P_e//c-axis the spectra are practically identical to the spectra taken with P_e//b-axis showing that the HL spectral profiles are independent

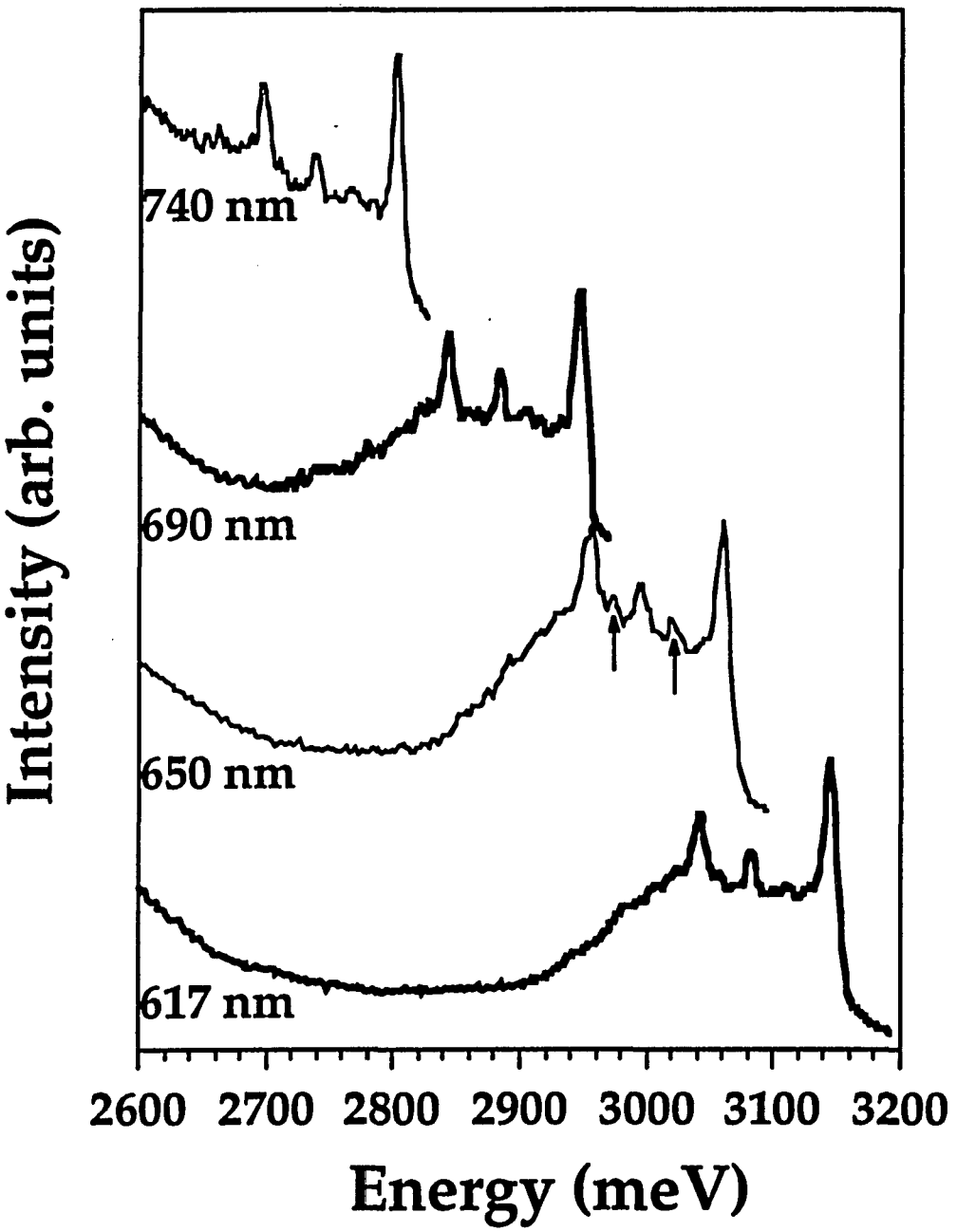

Figure 5.5: Up converted hot luminescence spectra following excited state absorption under: 617 nm excitation (lower profile), 650 nm excitation, 690 nm excitation and 740 nm excitation (upper profile) at liquid nitrogen temperature.

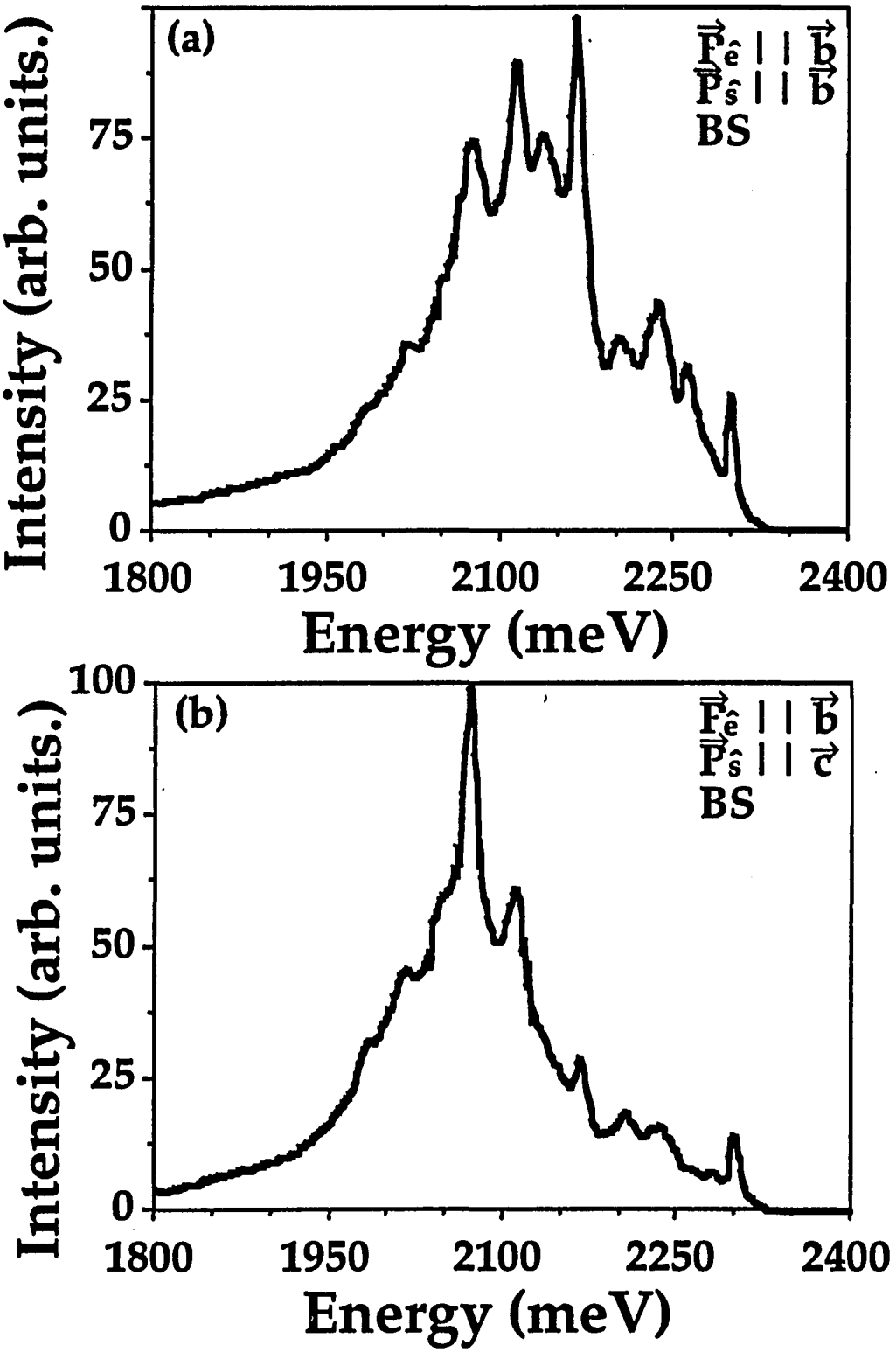

Figure 5.6: Up-converted hot luminescence under 1064 nm excitation. The laser polarization (Pe) is parallel to the b-axis and the emission polarization (Ps) is a) Ps//b and b) Ps//c-axis of the crystal at backscattering geometry (BS). The sample was at liquid nitrogen temperature.

of the polarization of the excitation laser beam. However, the HL intensity is reduced by a factor of ≈4. Figs. [5.7a] and [5.7b] show HL spectra for the PS geometry. Although the relative intensity of the peaks change, their energies remain the same. The intensities of the peaks in all spectra strongly depend on the luminescence polarization. The location of the peaks in energy is the same in all spectra under 1064 nm excitation. The spacing between the peaks are different occurring at ≈323 cm^{-1} and ≈218 cm^{-1}. The room temperature HL spectra displayed in figs. [5.8a] and [5.8b] show no well defined peak structure but the overall spectral envelope has a similar shape to the low temperature spectra. All spectra shown in figs. [5.6], [5.7] and [5.8] exhibit a characteristic increase of intensity at ≈2.1 eV. The HL tail at energies lower than 1.8 eV is observable but not shown in our figures since it does not carry any new information. The intensity of the lower energy emission tail is approximately equal to the HL intensity exhibited at 1.85 eV and shown in our figures. The integrated intensity at 2.1 eV is about 10 times larger than at 1.85 eV.

The peak structure in the up-converted HL spectrum is due to emission from the higher lying vibronic levels of the $^3T_1$ state. These vibronic levels are populated during the transfer of energy from the ion to the lattice environment by phonon emission. We can now study which are the phonons involved in this process by measuring the energy separation of the peaks observed in the up-converted HL spectrum. The measured differences in energy between successive peaks are shown in Table 5.1 for 617 nm, 650 nm and 1064 nm excitation wavelengths. Under 600 to 780 nm laser excitation, two peaks appear following the highest energy zero-phonon peak. The energy separation is 510±15 cm^{-1} and 320±15 cm^{-1}, indicating the phonon modes participating in the relaxation process of the excited state

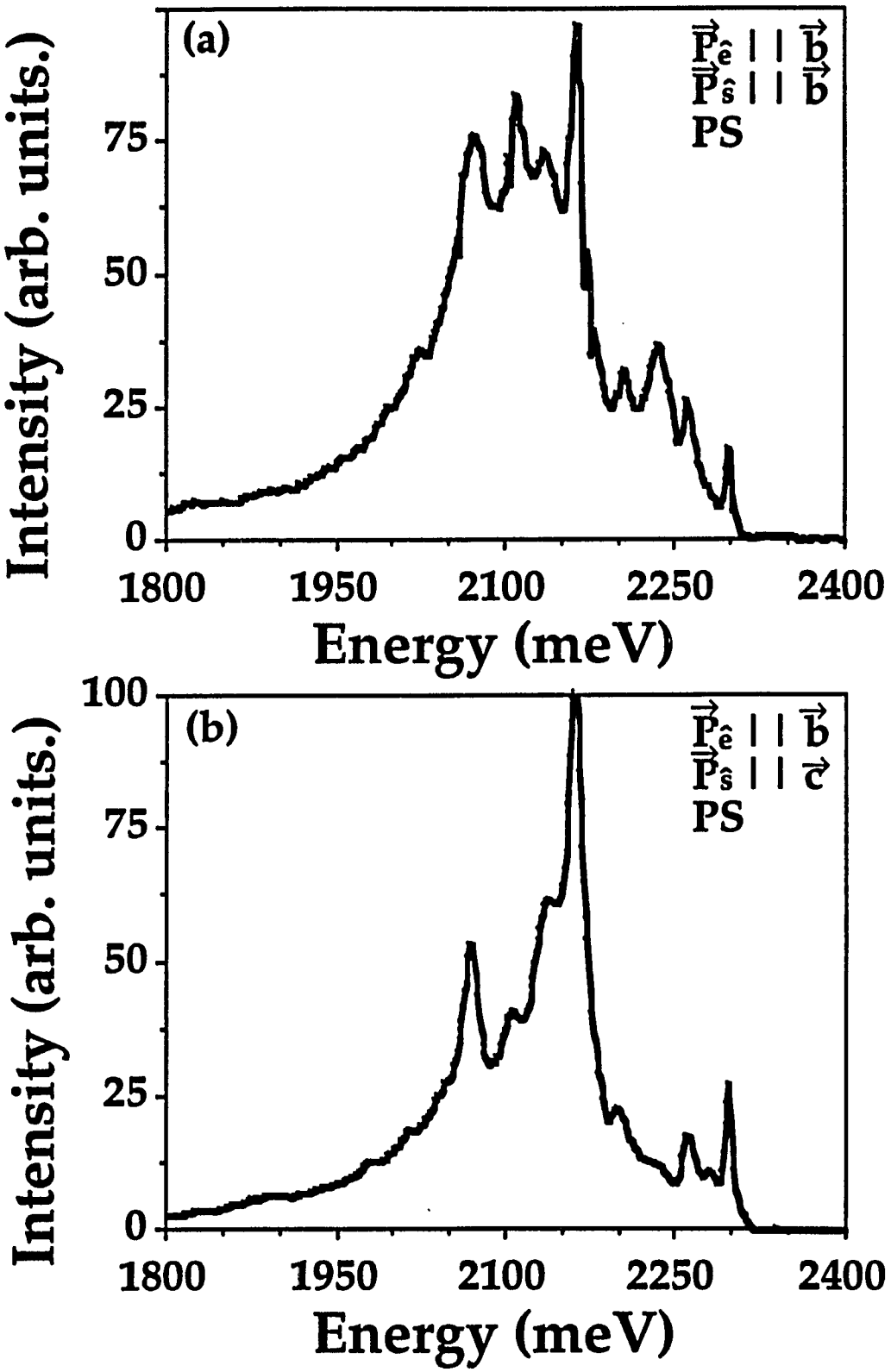

Figure 5.7: Up-converted hot luminescence under 1064 nm excitation. Pe//b-axis and a) Ps//b or b) Ps//c-axis of the crystal. The experimental conditions are 90° scattering geometry (PS) with the sample at liquid nitrogen temperature.

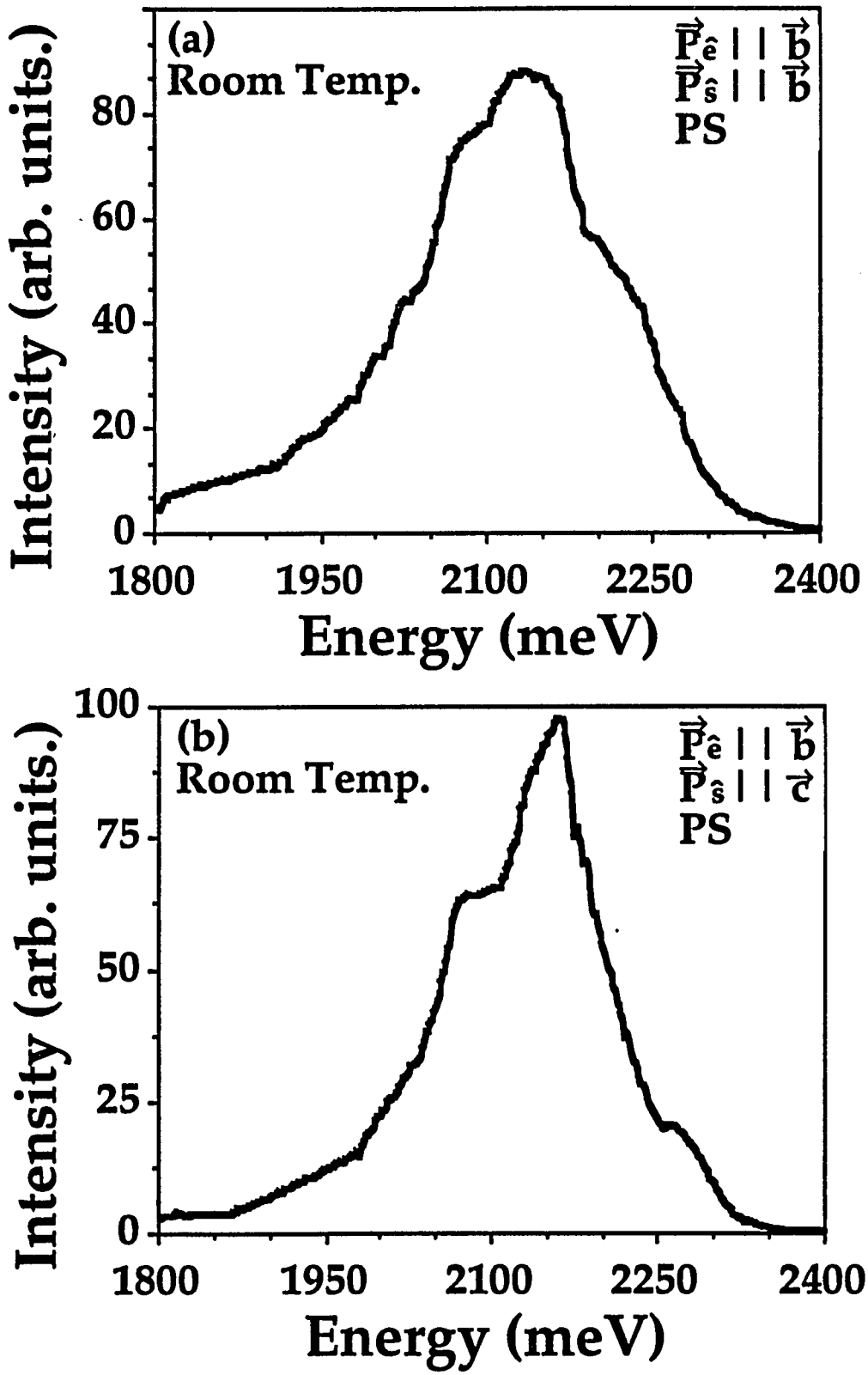

Figure 5.8: HL under 1064 nm excitation. Experimental conditions are Pe//b-axis, a) Ps//b and b) Ps//c-axis of the crystal. The scattering geometry is PS and the sample is at room temperature.

excitation wavelength	phonon peak	Energy difference between successive phonon peaks (cm^{-1})	
617 nm	1	$513 \pm 12\ cm^{-1}$	
	2	$325 \pm 12\ cm^{-1}$	
650 nm	1	$515 \pm 15\ cm^{-1}$	$325 \pm 20\ cm^{-1}$
	2	$315 \pm 20\ cm^{-1}$	$365 \pm 20\ cm^{-1}$
1064 nm	1	$323 \pm 20\ cm^{-1}$	
	2	$218 \pm 20\ cm^{-1}$	
	3	$226 \pm 20\ cm^{-1}$	
	4	$323 \pm 20\ cm^{-1}$	
	5	$218 \pm 20\ cm^{-1}$	
	6	$210 \pm 20\ cm^{-1}$	
	7	$323 \pm 20\ cm^{-1}$	

Table 5.1: The energy separation between successive peaks provides the energy of the phonons involved in the vibrational relaxation. In this table, the measured phonons are given for three different excitation wavelengths at 617, 650 and 1064 nm.

located at 3.15 eV. However, under 640 to 670 nm laser excitation two additional small peaks appear indicating an alternative relaxation route via the emission of a 325±20 cm^{-1} phonon followed by a 365±20 cm^{-1} phonon. Excitation of the sample with 1064 nm allows the observation of the phonon modes participating in the vibronic relaxation of the part of the excited state located at 2.3 eV above the ground state. The energy separation of these peaks is given in Table 5.1 indicating that there are two accepting phonon modes centered at 323 cm^{-1} and 218 cm^{-1}.

The up-converted HL is observable throughout the energy spectrum determined by the two-photon-step excitation level and the laser photon energy. This emission is shown in fig. [5.9] under 710 nm excitation. The emission starts at 2.881 eV which is the excitation energy for this laser wavelength. The phonon peaks described above (sector A) are followed by an increase of the signal that peaks at ≈2.43 eV (sector B). Another region of stronger emission is observed at lower energies centered at ≈2.05 eV (sector C). The overall spectrum appears as two band emission on top of a background. Besides the three phonon peaks (sector A) observed just below the excitation level, there are three sharp peaks in each strong emission band. The overall two band structure (sectors B and C) and the peaks on them are independent of the excitation wavelength. Varying the laser wavelength, the initial HL structure follows the shift in the laser photon energy (as shown in fig. [5.5]) but the two bands with their peaks remain at the same position. The peaks within the lower energy band in fig. [5.9] (sector C) are located at 2.075 eV, 2.11 eV and 2.17 eV while in the higher energy band (sector B) the peaks are at 2.486 eV, 2.494 eV and 2.542 eV.

Fig. [5.9] demonstrate that the rate of nonradiative relaxation is different at various parts of the excited state. The regions of stronger

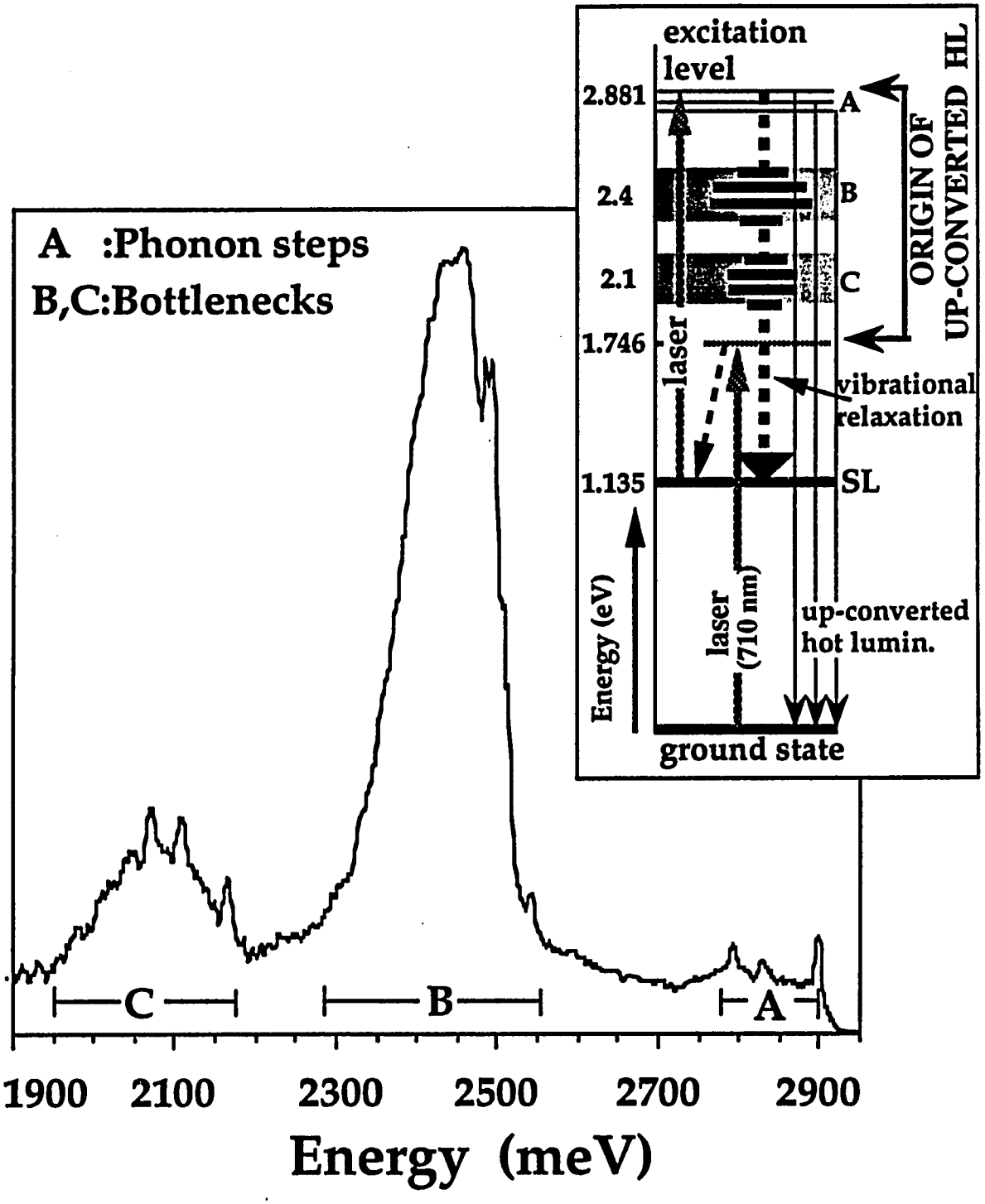

Figure 5.9: Up-converted HL under 710 nm laser excitation. The dynamics of the process is depicted in the insert at the right. The details are described in the text. The size of the bars in the vibrational relaxation indicates slowing through bottleneck. Sector A is the part of the emission occupied by the phonon steps while sectors B and C represent the two electronic bottlenecks.

emission can only be associated with the excited state electronic structure since it remains independent from the excitation wavelength. In these parts of the excited state the nonradiative relaxation slows down and the lifetime of the vibronic levels populated during this process increases. This case is depicted in the insert in fig. [5.9]. The shaded areas noted as B and C represent the two regions of stronger emission. It is characteristic that under 1064 nm excitation (figs. [5.6], [5.7] and [5.8]) the up-converted HL emission in the 2.1 eV region (that corresponds to sector C in fig. [5.9]) exhibits also a similar increase in intensity. A more detailed approach to this phenomenon is discussed in the next section where we attribute the increase in intensity in sectors B and C to the presence of electronic bottlenecks.

Up-converted HL from the 2.35 to 1.95 eV region of the excited state is shown in fig. [5.10] under 1064 nm excitation (thick line) and 710 nm excitation (thin line) for comparison. It is apparent that the two profiles are similar. The profiles exhibit an increase with maximum at approximately 2.1 eV in both cases. The three peaks appearing at 2.075 eV, 2.11 eV and 2.17 eV under 710 nm excitation are also present in the spectrum under 1064 nm excitation. Notice that pumping with 1064 nm laser only the sector C of fig. [5.9] can be reached by ESA. The resulting HL spectrum shown in fig. [5.10] is a combination of phonon peaks analogous to sector A of fig. [5.9] and the emission of sector C.

A streak camera was used to determine the lifetime of the emission under 1064 nm excitation. The 2 mm forsterite crystal was pumped with 1064 nm laser pulses having 5 ps pulse duration and average beam power of 3 Watts. The sample was kept at room temperature. The scattered light was collected in the forward direction and focused into a single-grating spectrograph. The spectrally analyzed signal is recorded by a streak camera

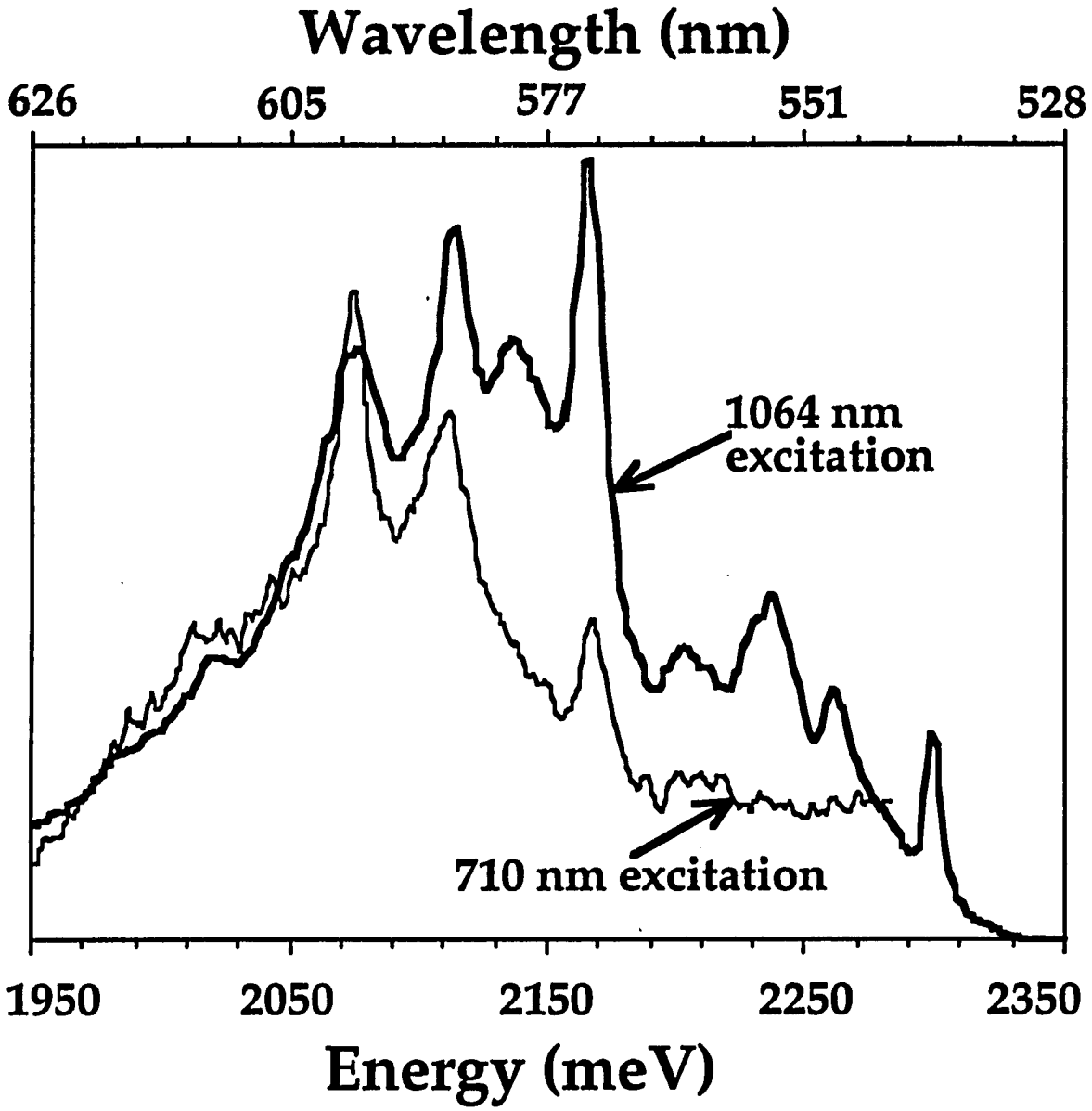

Figure 5.10: Up-converted hot luminescence under 1064 nm excitation (thick line) and 710 nm excitation (thin line). The sample was at liquid nitrogen temperature.

and a three dimensional profile is obtained. This time-spectrum-intensity profile from the 2.1 eV band is shown in fig. [5.11]. We see that the spectral profile is the same as in fig. [5.9] while the temporal profile is in the order of picoseconds. The configuration of the optical elements of the spectrometer introduces a temporal broadening of the light signal that is analyzing and in order to avoid this problem, interference and color filters were used to isolate the ≈2.1 eV HL emission instead of the spectrograph. The result is shown in fig. [5.12] with broken line. The laser pulse which was simultaneously recorded by the streak camera is shown in the same figure with a thin line. The profiles are practically identical with FWHM ≈10 ps. The resolution of the streak camera is 10 ps and therefore the detected signal is resolution limited. Nevertheless, the lifetime of the observed signal is smaller than 10 ps showing the ultrashort character of this emission. We repeated the measurement of the lifetime with the sample kept at T=78 K. The emission is stronger in this case but the recorded trace in the computer monitor is similar to the room temperature measurement indicating that the emission lifetime is still shorter than 10 ps.

The intensity of the emission shown in figs. [5.4] through [5.10] changes as the square of the average laser power. Change of the laser pulsewidth (by detuning the cavity length of the dye laser) while the average power remains the same has no effect on the intensity of the signal. This suggests that the emission is due to ESA. The very short lifetime of the emission reconfirms that the signal is due to hot luminescence from very short live vibronic levels. These levels are populated during the nonradiative relaxation of the ions that experienced ESA. The overall emission from these levels is proportional to the time that the ions "spent" on them.

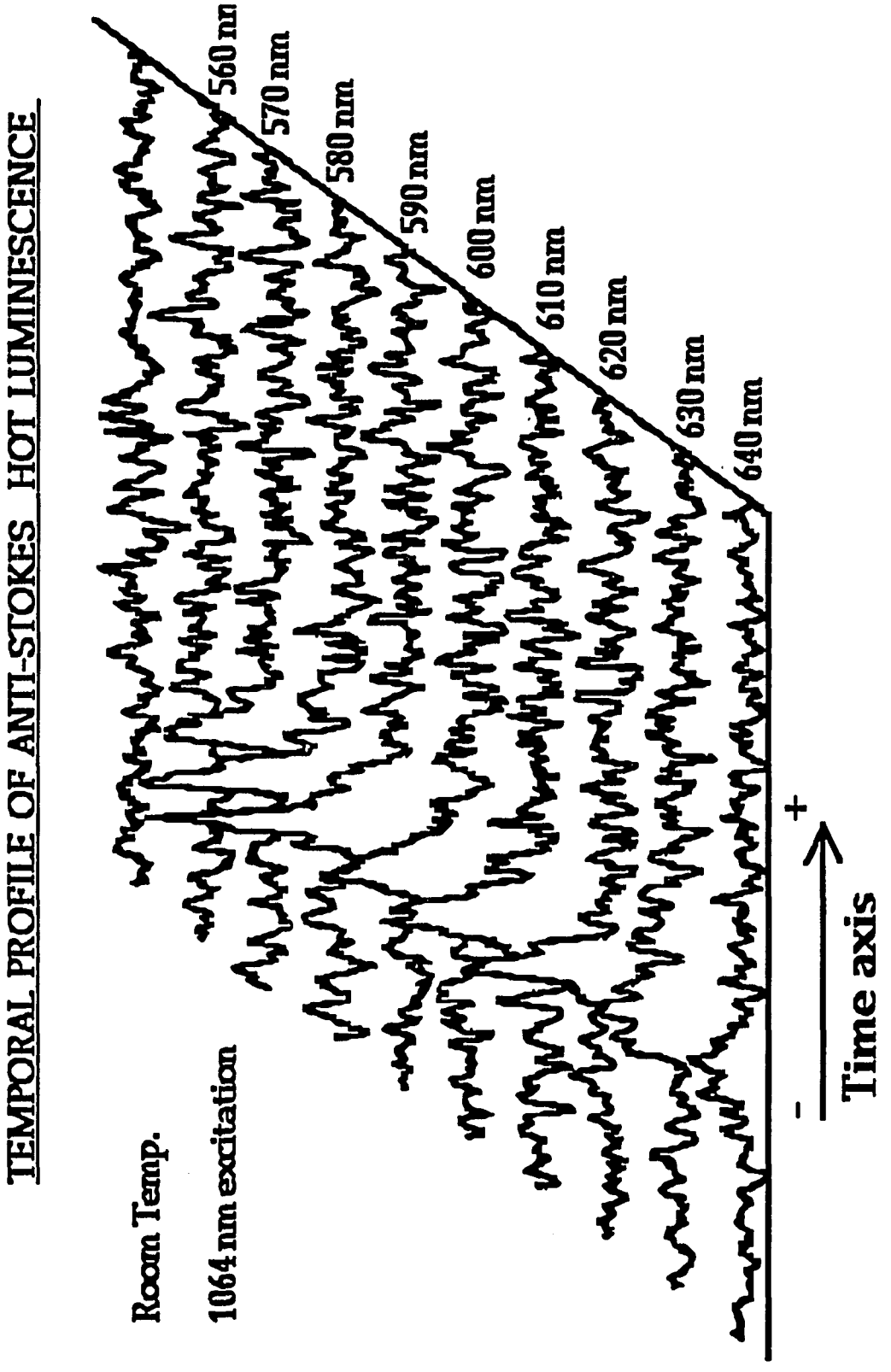

Figure 5.11: Streak camera time-spectrum profile of the up-converted hot luminescence under 3 W - 6 ps - 1064 nm laser excitation. The length of the time axis is ≈550 ps.

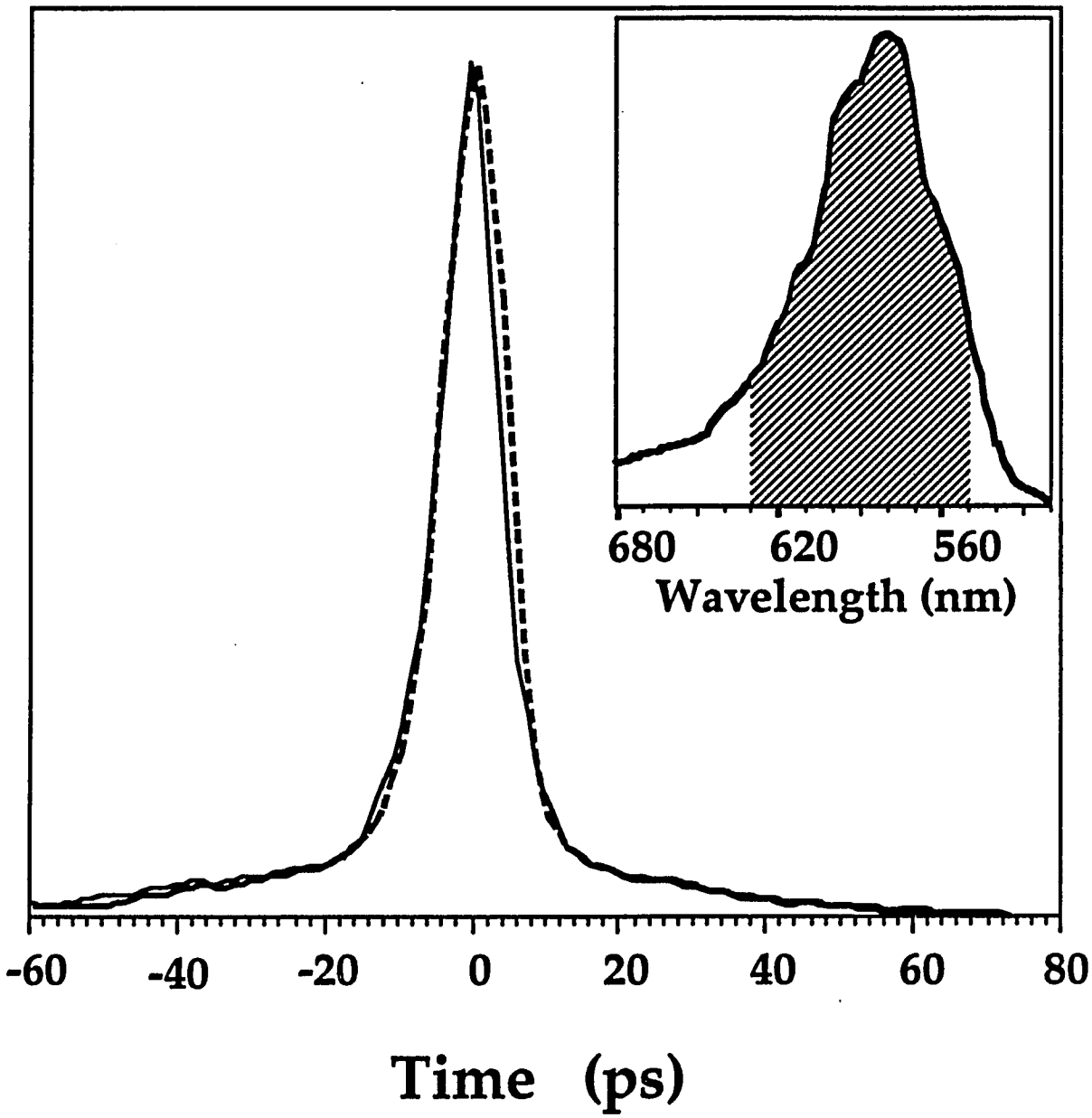

Figure 5.12: Streak camera temporal profile of a) The up-converted HL emission under 3 Watts, 5 ps 1064 nm laser excitation (broken line) and b) the laser pulse (thin line). Insert shows the spectral profile of the room temperature emission with the part detected by the streak camera.

5.4 Theoretical Model.

5.4.1 Hot luminescence.

To explain the observed salient spectral features described above, the following model is presented. Using eqs. 3.20, 3.21 and 3.22, the probability for radiative transition from the n-th vibrational level of the excited state (T) to the m-th vibrational level of the ground state (g) is given by the expression:

$$W_{Tn-gm} \sim \frac{2\pi}{h^2} \left| \langle \Psi_g(r_i,Q) \,|\, \vec{\mu}.\hat{\varepsilon} \,|\, \Psi_T(r_i,Q) \rangle |\vec{E}| \langle \chi_g(m) \,|\, \chi_g(m) \rangle \right|^2 \qquad (5.2)$$

where the integration is over the electron and vibrational coordinates, $\vec{\mu}$ is the appropriate electronic dipole operator and $\hat{\varepsilon}$ the unit polarization vector of the electric field intensity ($\vec{E}=\hat{\varepsilon}|\vec{E}|$). The relative values of W_{Tn-gm} depend on the squares of the vibrational overlap integrals. The vibrational wave functions $\chi_T(n)$ and $\chi_g(m)$ are each a similar set of harmonic oscillator functions but are defined with respect to different zeros of the configurational coordinate Q.

The shape and intensity of the emission spectra arising from radiative transitions from the n-th vibrational level of the excited state to any of the vibrational levels of the ground state is given (using eq. 3.25) by:

$$I_{T,n}(E) = I_0 R_{T,n} \sum_m P_{Tn-gm} \left| \langle \chi_g(m) \,|\, \chi_g(m) \rangle \right|^2 \delta(E_{T,n}-E_{g,m}-E) \qquad (5.3)$$

where P_{Tn-gm} is the purely electronic transition probability between the excited state and the ground state and $R_{T,n}$ indicates the average excited state population in the n-th vibronic level of the excited state. When the point of maximum amplitude of $\chi_T(n)$ is aligned with the middle of the ground state

parabola Q_0 (maximum amplitude of $\chi_g(0)$), the transition $\chi_T(n) \rightarrow \chi_g(0)$ will be dominant leading to a strong zero phonon peak followed by weak sidebands. The reason is that the vibrational integral $|\langle\chi_g(0)|\chi_T(n)\rangle|$ is larger than other combinations of $\chi_T(n)$ with $\chi_g(m\neq0)$. This is similar with the case described by eqs. 3.26, 3.27, 3.28 and fig. [3.3] for S=0. The emission of a phonon will lead to a vibrational wavefunction $\chi_T(n-1)$ which will have its maximum amplitude at a point shifted with respect to Q_0. The photoemission spectrum from this vibrational level will be characterized by a strong peak arising from the $\chi_T(n-1) \rightarrow \chi_g(0)$ transition but the relative intensity of the sideband will increase. The difference in energy between the zero phonon peaks [$\chi_T(n) \rightarrow \chi_g(0)$ and $\chi_T(n-1) \rightarrow \chi_g(0)$] will be equal to the energy of the emitted phonon. After the emission of a sufficient number of phonons (i), the point of maximum amplitude of $\chi_T(n-i)$ will be very different from Q_0 producing a spectrum having a broad band with no peaks. The shape of the overall hot luminescence spectrum $I_T(E)$ will be given by the sum of the different components $I_{T,n}(E)$ representing the superposition of the spectral profiles due to each vibrational level.

$$I_T(E) = \sum_n I_{Tn} \tag{5.4}$$

The zero-phonon peaks [$\chi_T(n-i) \rightarrow \chi_g(0)$] should be positioned on top of a broadband background coming from the superposition of the vibrational sidebands. The intensity of the peaks should diminish after the emission of a number of phonons and the rest of the HL signal should be observable throughout the excited state band until the beginning of the ordinary luminescence. These features should dominate in the low temperature spectrum where SL is well defined.

Crossings between electronic levels in the configurational diagram will deform the potential energy curve causing lower vibronic relaxation rates of the ionic system. Lifetimes on the order of picoseconds are expected from these "trapping" states depending on the coupling strengths. Since the excited ions relax passing through the same nonequilibrium excited state vibronic levels, the average occupation number of each level (parameter $R_{T,n}$ in eq. 5.3) is proportional to its lifetime. I have discussed in section 3.2.4 (following eq. 3.28) that the contribution of each vibronic level to the overall HL emission depends only on the average population of the vibronic state. As a result, the HL emission from the vibronic levels within this electronic bottleneck will be more intense because the excited ions are occupying these levels for longer period of time resulting in an increased average population and overall probability for radiative transition to the ground state. The ratio of the total integrated intensities of the HL emission from the different vibronic levels should be approximately equal to the ratio of their lifetimes.

5.4.2 Up-converted hot luminescence in forsterite.

In the previous section I discussed the case of HL emission following direct excitation. However, what we are studying in this research is up-converted HL which differs from the ordinary HL in only one aspect which is that the excitation involves two steps. In order to use the above model to explain the observed up-converted HL spectra in forsterite we take into account that at low temperature only the zero vibrational levels [$\chi_g(0)$] of the ground state ($^3A_2$) and [$\chi_{SL}(0)$] of the SL ($^3T_2$) are populated. The position of the maximum amplitudes of the vibrational wavefunctions $\chi_{SL}(0)$ and $\chi_g(0)$ are slightly shifted with respect to each other due to the

small Huang-Rhys factor S≤0.4 in forsterite.[21] A Cr^{4+} ion in the $\chi_{SL}(0)$ state absorbs a photon to reach a higher excited state having vibrational wavefunction $\chi_T(s)$ at the point Q_0 of the excited state configurational coordinates parabola. This process is depicted in fig. [5.13]. In the photoemission spectrum from $\chi_T(s)$, the transition leading to zero vibrational level $\chi_g(0)$ [$\chi_T(s) \rightarrow \chi_g(0)$] of the ground state will be dominant (see right hand side of fig. [5.13]). This transition appears as the highest energy peak in the overall up-converted emission. As the excited Cr^{4+} ions relax down the ladder of the electronic manifold emitting phonons, the position of maximum amplitude of $\chi_T(n)$ shifts and the intensity of the zero phonon transition decreases while the intensity of the vibrational sideband increases. Further emission of phonons leads to a continuous broadband spectrum associated with the radiative transitions from $\chi_T(n)$. The overall up-converted HL spectral profile is a superposition of all these components and appears as a sharp line at exactly the excitation level followed by other peaks on top of a background and at decreasing energy ending in a broadband emission with no structure. At high temperatures, the thermal population of many vibrational levels of the metastable level will produce a broad storage level. The ESA from the broad SL produces also broad vibronic levels that overlap resulting in the loss of the fine structure in the HL spectrum. The overall profile remains the same, reflecting the excited state band characteristics. HL spectra taken under 600 to 780 nm excitation (see figs. [5.4] and [5.5]) have all of the above characteristics. On the other hand, the spectra shown in Figs. [5.6], [5.7], [5.8], [5.9] and [5.10] taken under 1064 and 710 nm excitation exhibit the additional feature of the enhancement of the HL emission at ≈2.43 and ≈2.1 eV. This enhancement

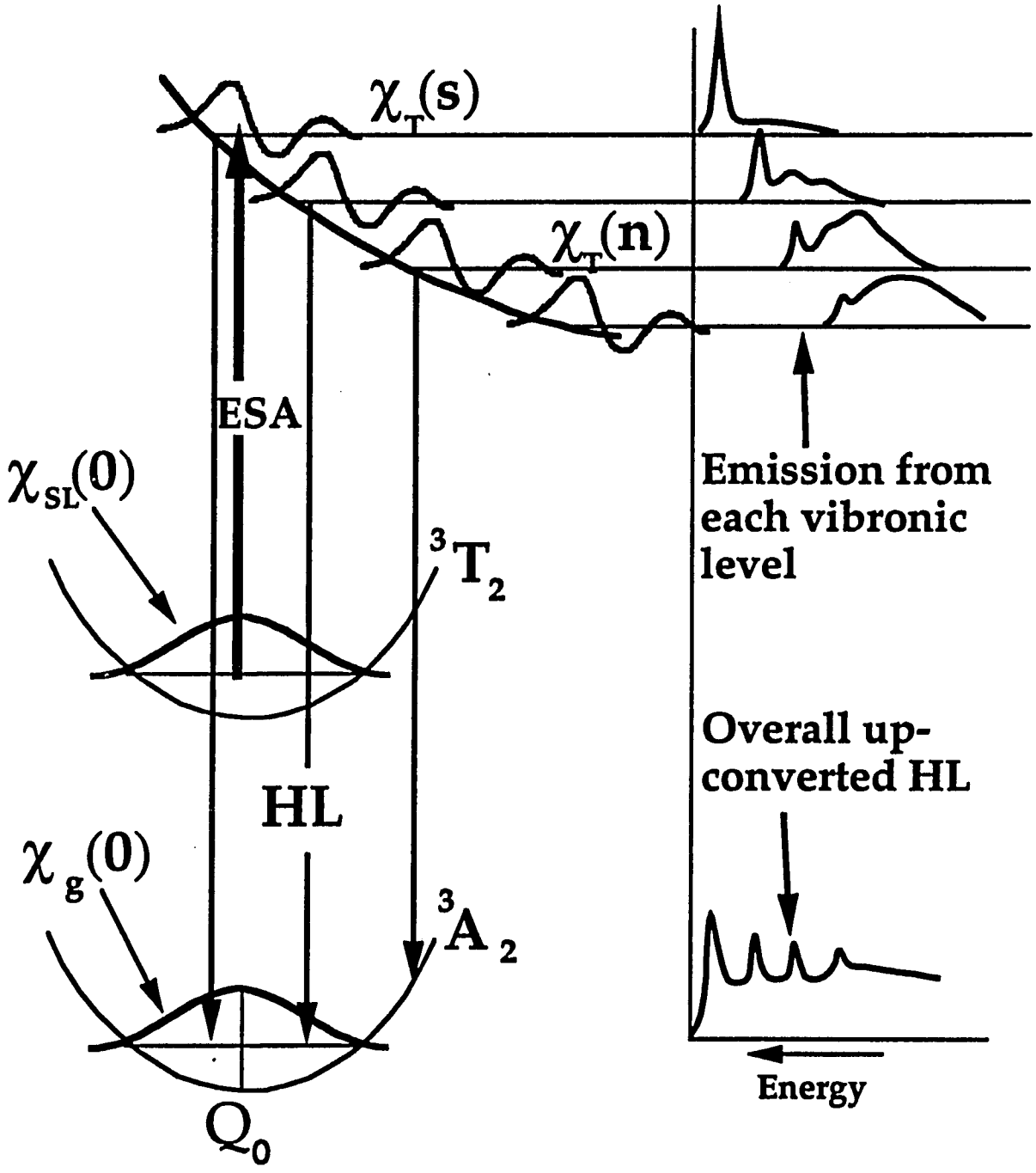

Figure 5.13: Schematic diagram showing the relation between the vibrational wavefunctions $\chi(m)$ and up-converted HL in forsterite. The emission from each vibronic level is depicted (on the upper right side) as well as the overall up-converted hot luminescence (on the lower right side) which is the superposition of the HL emissions from each vibronic level.

can be explained in terms of a slowing down of the nonradiative relaxation in this region due to crossing between electronic states which I will discuss in section 5.6.

5.5 Up-converted ordinary luminescence and metastable levels.

There are two types of emission associated with radiative transitions from the upper excited states. These are the ordinary luminescence (OL) and the hot luminescence (HL). The OL emission arises from transitions between metastable levels and the ground state while HL is due to radiative transitions from the manifold of nonequilibrium vibronic states populated during the nonradiative decay. The fundamental difference between OL and HL is that OL is independent of the pumping wavelength since it depends only on the position of the metastable energy level. HL on the other hand, occurs immediately after photoexcitation with the emission starting from the excitation energy. In the case of up-converted luminescence, both types of emission are possible.

Subsequently to the two step photoexcitation, the metastable levels located below the excitation level will be populated through nonradiative relaxation of the ions. This process is depicted in fig. [5.14]. Three metastable levels are displayed and the two-step photoexcitation process is depicted for three different laser wavelengths. Photoexcitation of the Cr^{4+} ions populates the lower lying metastable levels. Excited state absorption from these levels leads to the population of the higher lying metastable level. Up-converted OL occurs from the radiative transitions between the metastable levels populated by ESA and the ground state. Varying the laser wavelength and monitoring the up-converted luminescence, information was obtained on the position of the metastable levels. Details regarding fig. [5.14] are described below.

Up-converted ordinary luminescence is shown in fig. [5.15] for 532 nm laser excitation. The emission is characterized by a narrow peak due to

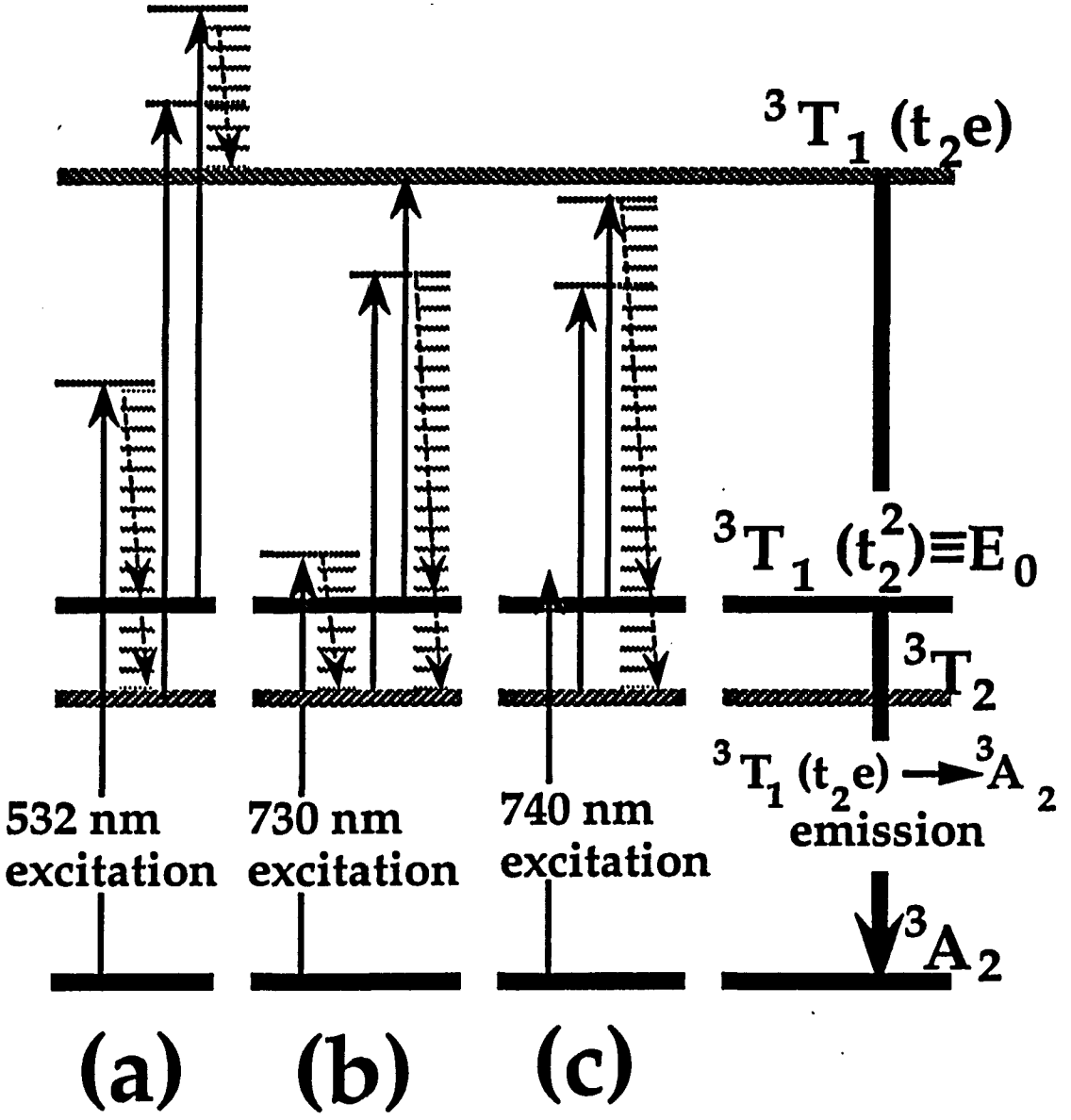

Figure 5.14: Schematic diagram showing the up-converted ordinary luminescence process in Cr4+ forsterite under a) 532 nm, b) 730 nm, and c) 740 nm excitations. Solid arrows are photon transitions and dashed arrows are vibrational transitions.

the zero-phonon line at 26,450 cm^{-1} followed by a broad vibrational side band peaking at ≈25,800 cm^{-1}. Attempts to fit this low-temperature emission spectra using Pekarian bandshape curve yielded values of the Huang-Rhys parameter between 1<S<2 and phonon energy of ~295 cm^{-1}. The 370 nm absorption band shown in Refs. 22 and 23 and its assignment using the Tanabe-Sugano energy diagram of Cr^{4+}-doped forsterite suggests[22-24] that this emission originates from the $^3T_1(t_2e)$ electronic state. The narrow peak at 3.28 eV (26,450 cm^{-1}), corresponding to the zero-phonon transition provides the exact position of this electronic state with respect to the ground state. This emission remains the same for laser excitations with wavelengths shorter than 575 nm which is the cut-off wavelength for the $^3T_2 \rightarrow {}^3T_1(t_2e)$ transition (see fig. [5.14a]). Using a streak camera and excitation pulses of 55 ps in duration at 532 nm, the lifetime of the $^3T_2 \rightarrow {}^3T_1(t_2e)$ emission was measured to be 395 ± 9 ps (see insert in fig. [5.15])

Using the same excitation (532 nm) but with increased spectral resolution (using a grating with 1800 gr/mm) it was determined that the peak at ~26,450 cm^{-1} actually consists of a zero-phonon line at 26,424 cm^{-1} with two satellites at 26,529 cm^{-1} and 26,625 cm^{-1}. The relative intensities of the three peaks were measured at several temperatures and were shown to obey the Boltzman distribution, indicating that they correspond to the same center. These three lines are assigned to spin-orbit split $^3T_1(t_2e)$ state of the tetrahedral Cr^{4+} ion. The emission spectra in the 26,200 - 26,800 cm^{-1} range at two different temperatures are shown in fig. [5.16].

The two-step photoexcitation process was used to measure the excited-state excitation spectrum of the Cr^{4+} ion in the violet and near ultraviolet spectral region. In this case, the integrated luminescence intensity over the 370 - 410-nm range was measured as the excitation

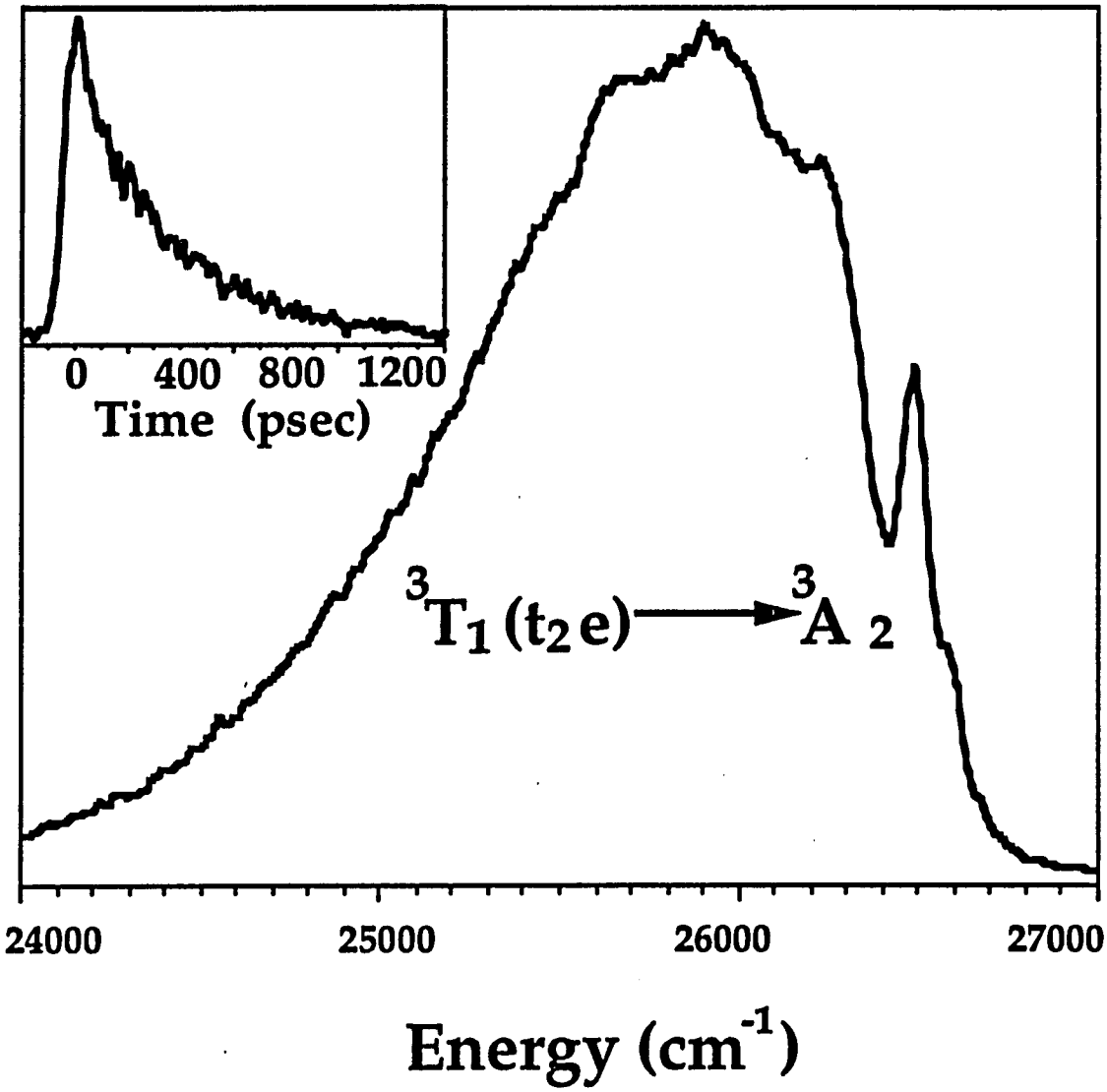

Figure 5.15: Up-converted ordinary luminescence under 532 nm laser excitation. This emission arises from the $^3T_1(t_2e)$ state following excited state absorption. Insert shows the temporal profile of this emission.

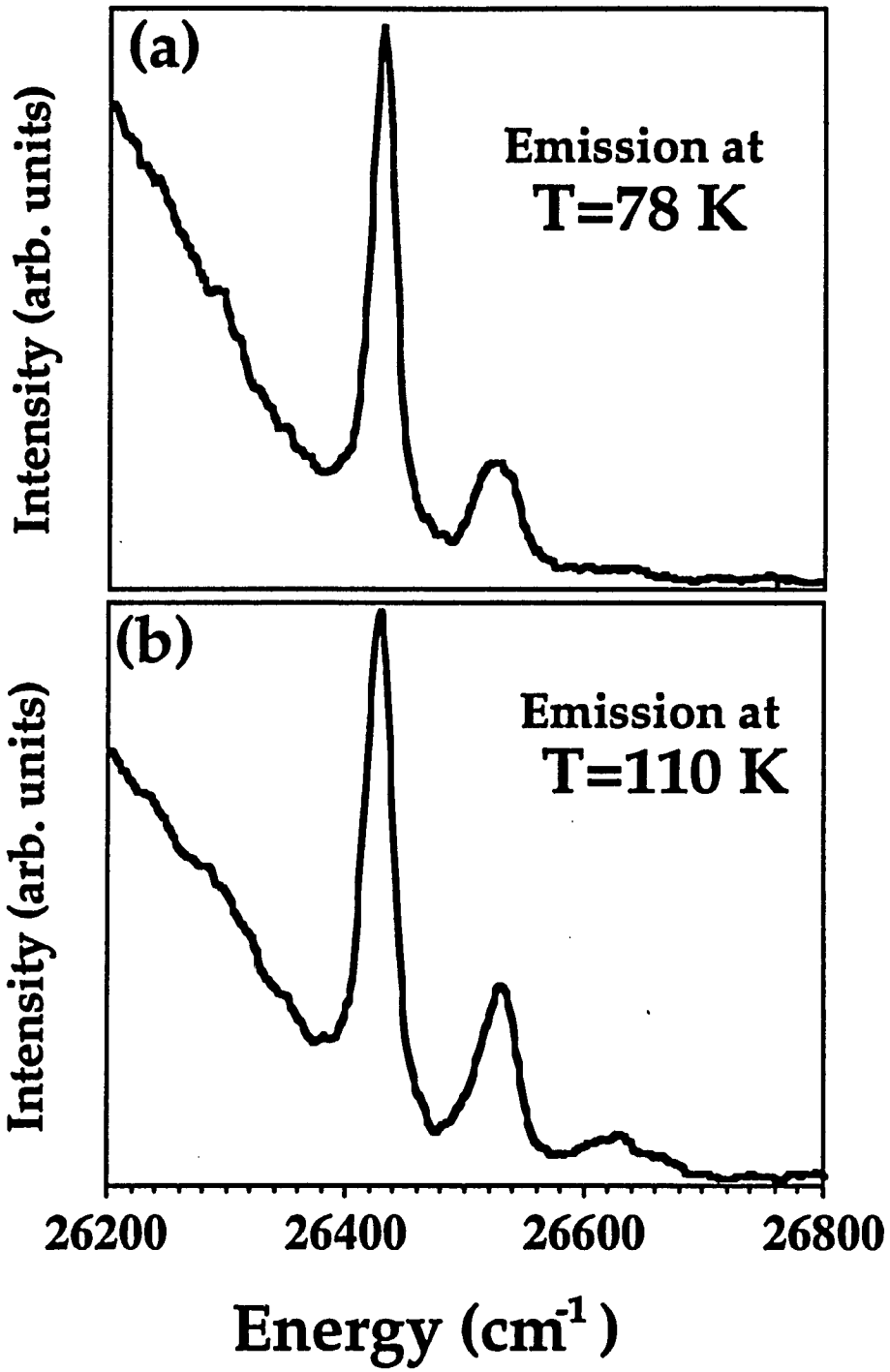

Figure 5.16: High resolution up-converted luminescence spectra for (a) sample temperature T=78 K, and (b) T=110 K. The three peaks correspond to the spin-orbit splitting of the $^3T_1(t_2e)$ state. The relative intensities of the three peaks obey the Boltzman distribution.

wavelength was changed from 572.7 - 594.5 nm, which, assuming a two-step process, resulted in effective excitation from 25,970 - 26,610 cm^{-1}. This method enabled us to determine with relatively high resolution the structure of the absorption spectrum of the Cr^{4+} ion in the spectral range where there is an overlap of features of both the Cr^{3+} and Cr^{4+} ions, that could not be easily resolved by standard absorption measurements. The excited-state excitation spectrum is shown in fig. [5.17]. The integrated luminescence intensity over the 370 - 410-nm range is plotted as a function of the effective excitation energy. The spectrum is characterized by two peaks, one at 26,425±10 cm^{-1} and another at 26,525±10 cm^{-1}. These two energies are the same as those of the two peaks observed in the up-converted luminescence spectrum. Since the pump wavelength was changed from 572.7 - 594.5 nm, and assuming a two-step process, the effective excitation energy was determined by adding ~9150 cm^{-1} to the energy of the excitation light covering effectively the 25,970 - 26,610 cm^{-1} range. The third peak that could be expected at 26,625 cm^{-1} was not observed because that energy was not available due to limited tuning range of the pump laser with a lower limit of 572.7 nm or, through an up-conversion process 26,610 cm^{-1}. The excited-state absorption originates from the spin-orbit split $^3T_2$ state, where the energies of the three levels are 9137 cm^{-1}, 9151 cm^{-1} and 9169 cm^{-1}, as determined by Jia et al.[24] Since the splitting is relatively small and since the Boltzman distribution for T=78 K predicts that the relative populations of the three levels are reasonably close, an average of 9150 cm^{-1} was used to calculate the effective excitation energy. The effect of the ~30-cm^{-1} splitting of the SL was seen as broadening of the features observed in the excited-state excitation spectrum. Nevertheless, the slightly broader structures observed in the excitation spectrum coincide with the

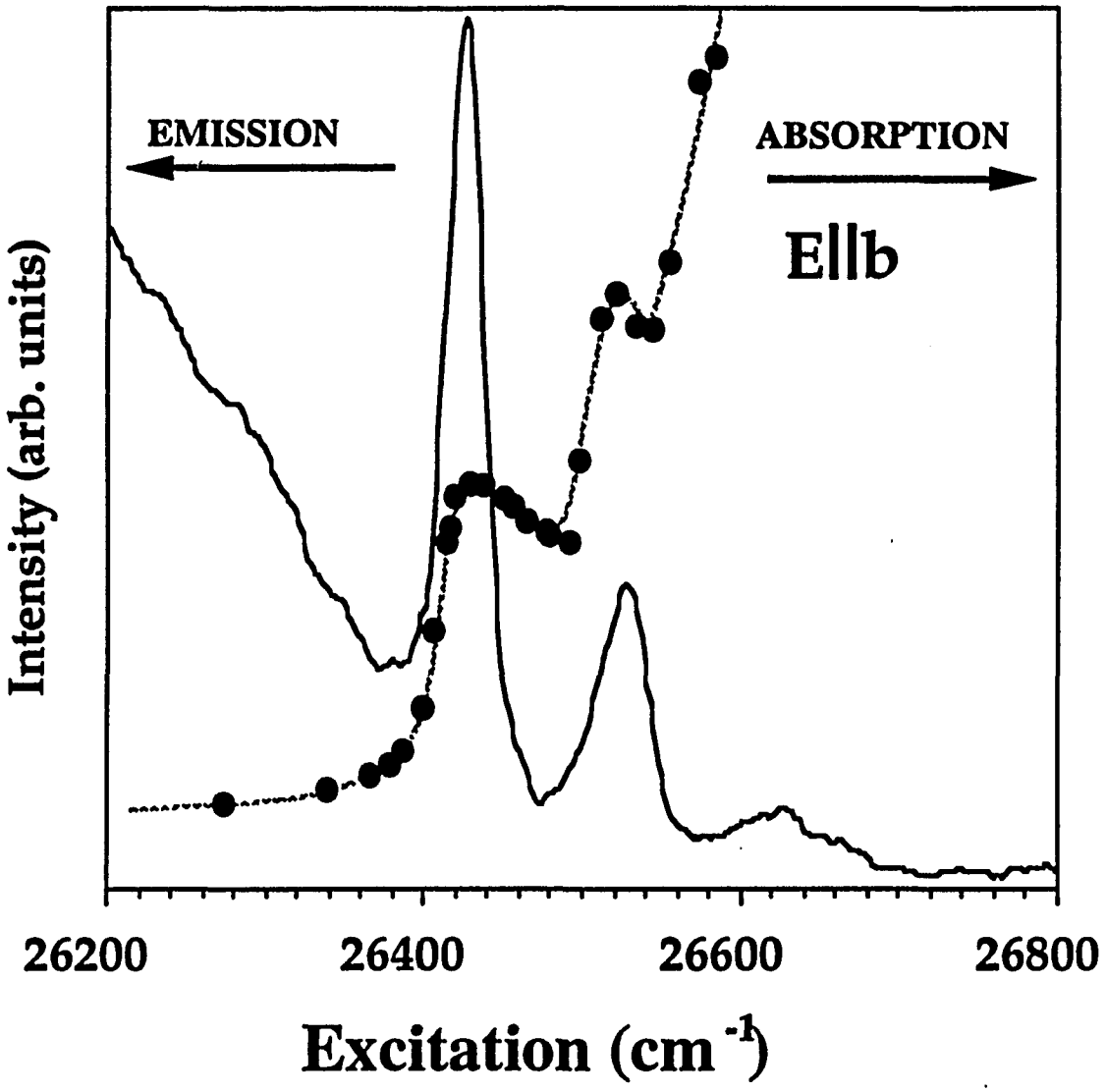

Figure 5.17: Excited-state excitation spectrum: The integrated emission in the 378 - 414-nm spectral range is shown as function of the effective excitation.

sharp structures observed in the up-converted luminescence spectra and unambiguously confirm that they correspond to transitions involving the same triplet excited state.

For photon energies lower than the energy (2.145 eV = 578 nm) required for the excited ion in the SL ($^3T_2$) to reach the $^3T_1(t_2e)$ electronic state through the ESA process, the up-converted HL emission is observed (see figs. [5.4] and [5.5]). For laser wavelengths longer than 600 nm there is not enough photon energy for the excited ions in the $^3T_2$ state to reach the $^3T_1(t_2e)$ metastable level by ESA. However, as shown in fig. [5.18], the $^3T_1(t_2e) \rightarrow {}^3A_2$ emission is still present under 642 nm excitation. The narrow peak at 26,450 cm^{-1} and the broad sideband centered at 25,800 cm^{-1} are identical to the features of the emission under 532 nm excitation shown in fig. [5.15]. Another narrow peak at 3.067 eV (24,740 cm^{-1}) is the highest energy peak in the up-converted HL spectrum ($E_{ph} + E_{SL}$). This $^3T_1(t_2e) \rightarrow {}^3A_2$ emission persists for laser wavelengths up to 730 nm. Fig. [5.19] shows that this emission disappears under 740 nm excitation which indicates that another metastable level exists such that ESA absorption from this level leads to population of the $^3T_1(t_2e)$ metastable level. This process is depicted in figs. [5.14b] and [5.14c], respectively. The lifetime of this level should be longer than 12 ns since ESA is possible under our excitation levels. The fact that the emission disappears under 740 nm excitation indicates that the energy gap between the new metastable level and the $^3T_1(t_2e)$ state is slightly larger than the energy of the 740 nm photons. The cut-off wavelength of 735±5 nm can be used to estimate the energy (E_0) of this level (see fig. [5.14]):

$$E(^3T_1(t_2e))) = E_0 + E(735\pm5\ nm) \quad , \qquad (5.5)$$

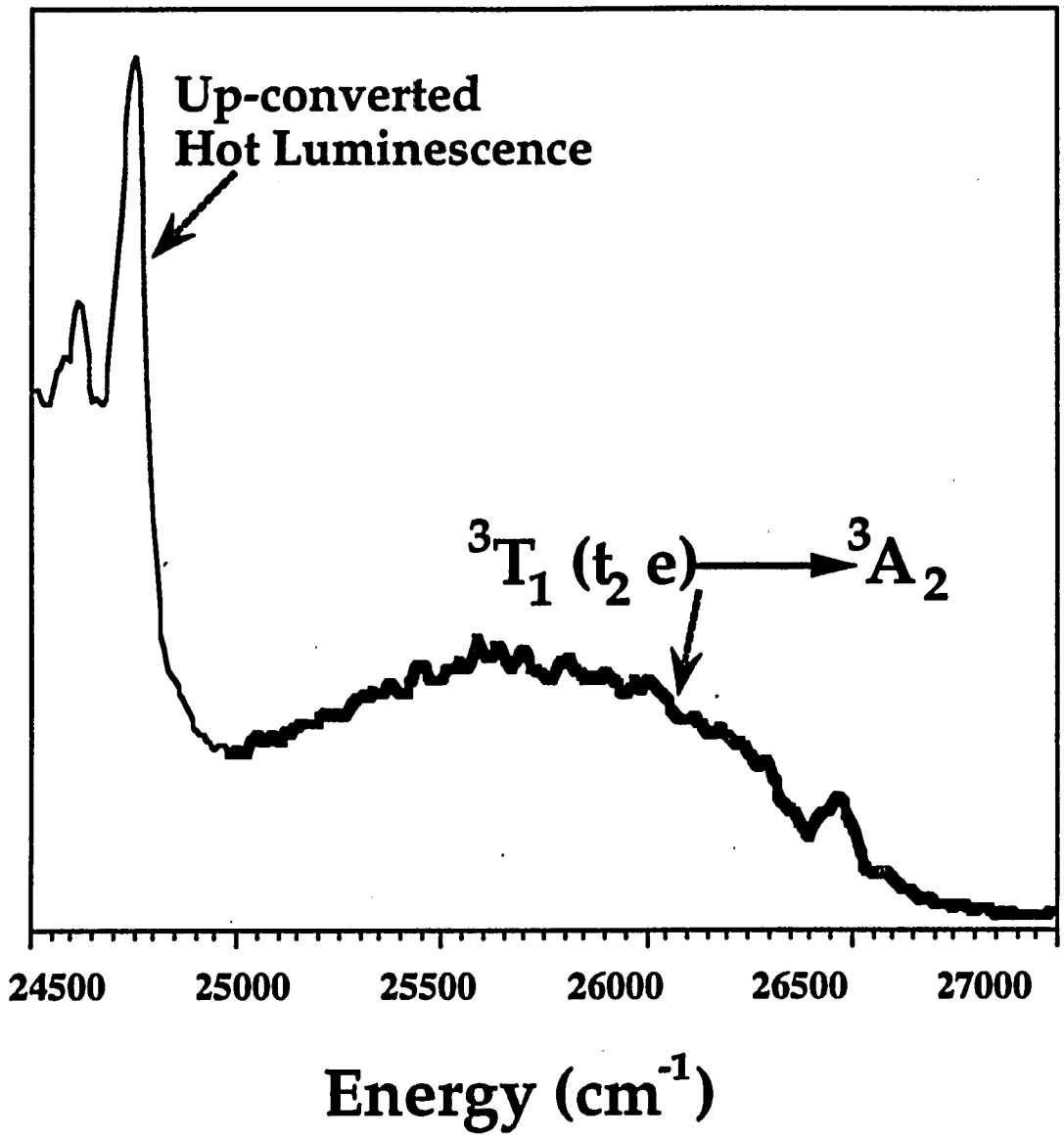

Figure 5.18: Up-converted luminescence under 642 nm laser excitation. The higher energy part (thick line) is due to the $^3T_1(t_2e) \rightarrow {}^3A_2$ emission following ESA from the $^3T_1(t_2^2)$ state. The lower energy part (thin line) is due to up-converted hot luminescence following ESA from the $^3T_2$ state.

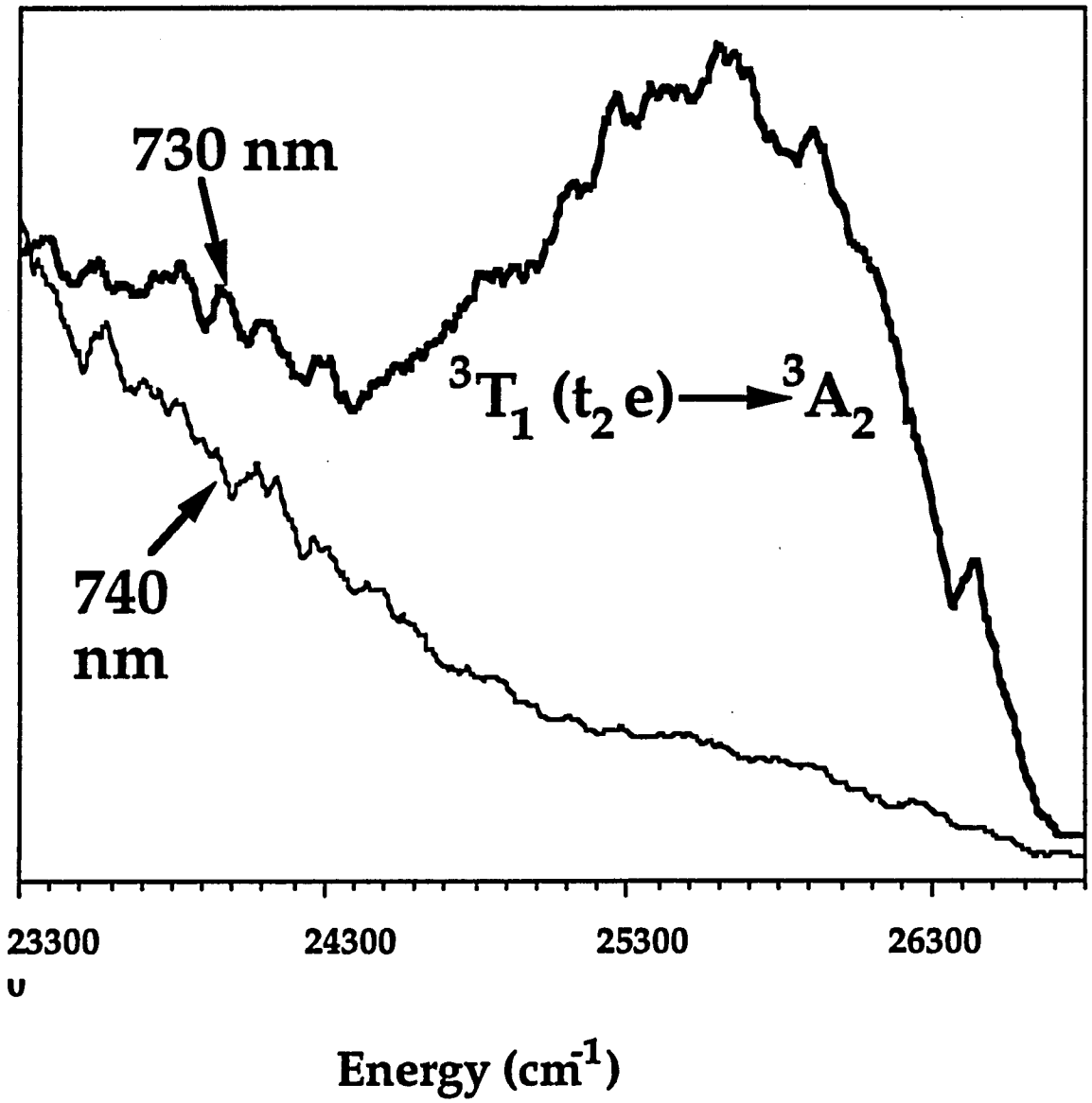

Figure 5.19: The $^3T_1(t_2e)\rightarrow{}^3A_2$ emission under 730 nm and 740 nm excitation. This emission disappears under 740 nm laser excitation.

yields $E_0 = 1.593 \pm 0.012$ eV (=12,847± 90 cm^{-1}) .

According to the Tanabe-Sugano energy level diagram (see fig. [4.2a]), this new metastable state at E_0 is assigned to the $^3T_1(t_2^2)$ electronic state. More specifically, taking into account the splitting of the $^3T_1(t_2^2)$ state due to orthorhombic distortion of the tetrahedra containing the Cr^{4+} ion, this level is the lowest vibronic level of the $^3A_2(^3T_1)$ state (see table [4.4]).

The ratio of the intensities of the $^3T_1(t_2e) \rightarrow {}^3A_2$ transition after ESA originating from the $^3T_2$ SL (laser wavelength shorter than 570 nm) over the intensity of the emission following ESA from the $^3T_1(t_2^2)$ state (laser wavelength longer than 600 nm) is of the order of 100 fold. This means that the average population of the $^3T_1(t_2^2)$ state is approximately 10^{-2} the population of the $^3T_2$ SL, assuming the same cross sections. Therefore, the lifetime of the $^3T_1(t_2^2)$ state should be of the order of hundreds of nanoseconds. The $^3T_1(t_2^2)$ state exhibits strong absorption in all crystal orientations. Ordinary luminescence from the $^3T_1(t_2^2)$ state (beginning at 780 nm and longer according to eq. 5.5) has not been detected because of the presence of Cr^{3+} ions in forsterite that emit very strongly in the same spectral region. Another reason could be the relatively weak emission intensity due to the short lifetime of $^3T_1(t_2^2)$ state. An attempt was made to observe the $^3T_1(t_2e) \rightarrow {}^3T_2$ transition. This emission is expected to have a similar spectral profile with the $^3T_1(t_2e) \rightarrow {}^3A_2$ emission due to the very small offset between the ground state ($^3A_2$) and the $^3T_2$ state as indicated by the Huang-Rhys parameter S<1. The zero-phonon peak is expected at ≈ 570 nm. Using 532 nm laser excitation, the 570 nm spectral region is occupied by the Raman signal which is much stronger. Pumping with 457.9 nm from an argon-ion laser to avoid the Raman signal, the emission observed at 570 nm

spectral region was approximately 50 times stronger than the observed $^3T_1(t_2e) \rightarrow {}^3A_2$ transition and no structure with the expected characteristics was detected.

Fig. [5.20] displays the up-converted luminescence under 532 nm laser excitation in the 24,000 to 28,000 cm^{-1} spectral region. The overall emission can be divided into two sectors (A and B in fig. [5.20]) of very different intensity. The sector B is due to the $^3T_1(t_2e) \rightarrow {}^3A_2$ transition that is also shown in fig. [5.15]. Sector A is due to up-converted hot luminescence from the very short lived vibronic levels populated during the relaxation of the photoexcited ions by phonon emission. The first narrow peak in the up-converted hot luminescence spectrum is located at 27,956 cm^{-1} (3.466 eV = $h\omega_{532\ nm} + E_{SL}$). Since the lifetime of the $^3T_1(t_2e) \rightarrow {}^3A_2$ emission is known (≈395 ps), the ratio of the intensities of the up-converted OL over the intensity of the up-converted HL can provide an estimate of the lifetime of the nonequilibrium vibronic levels. I will discuss this aspect in the next section.

The same experiments were attempted on a forsterite crystal grown in reducing atmosphere (favoring Cr^{3+} substitution), but none of the above emission spectra was observed. This indicates that the observed up-converted emission is due to the Cr^{4+} ions.

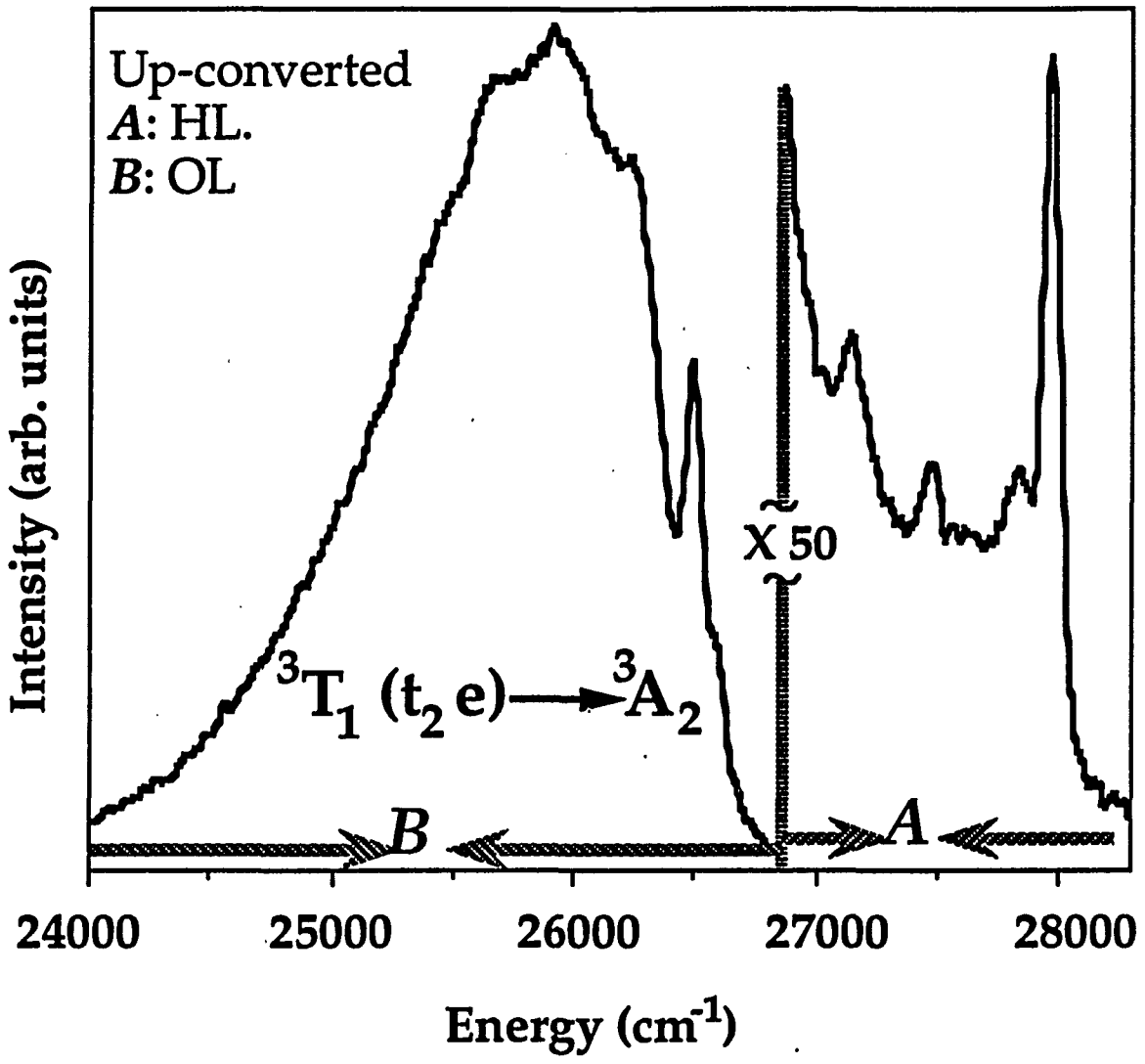

Figure 5.20: Up-converted luminescence under 532 nm excitation. Sector A is due to up-converted hot luminescence. Sector B is due to ordinary luminescence from the $^3T_1(t_2e)$ electronic state. The sample was held at liquid nitrogen temperature.

5.6 Discussion.

The up-converted hot luminescence that we are dealing with is due to two-step photon absorption and is blue-shifted with respect to the excitation source preventing any overlapping with the Raman signal or luminescence from other impurity centers (which are red-shifted processes). This selective isolation of the HL signal allows the observation of the peak structure in the HL profile and subsequently the determination of which phonon modes are involved in the nonradiative decay. In semiconductors, hot luminescence characterized by discrete peaks separated by energy equal to the energy of the LO phonon involved in the nonradiative relaxation has also been observed.[11-13,20] This emission arises from radiative transitions of hot electrons in the Γ-valley to an acceptor level located above the valence band. The highest energy peak appears at energy equal to the difference between the excitation level and the acceptor level and by changing the laser wavelength the position of the highest energy peak shifts. Due to the presence of the acceptor level above the valence band, the observed hot luminescence emission in semiconductors is red-shifted with respect to the laser wavelength and for this reason it does not spectrally overlap with the Raman scattering emission allowing the clear observation of the details contained in the emission. Comparison of the HL observed in semiconductors with the up-converted HL in forsterite shows a significant difference in the spectral profile; that is the number of peaks observed at energies lower of the highest energy peak. In semiconductors, peaks are observed until the ordinary luminescence takes over (the hot electrons have reached the bottom of the Γ-valley). On the other hand, in forsterite only few peaks are observed from the vibronic levels near the excitation

level while at lower energies a continuous with no peaks spectrum is observed. To explain this difference we have to consider the energy diagrams in both cases. In semiconductors the HL emission is due to transition from a parabola (Γ-valley) to a level (acceptor level) while in forsterite the emission is due to transitions between two parabolas (in the configurational coordinate model). Therefore, in semiconductors all the peaks can be observed while in forsterite, according to the model presented in the previous section, only the initial vibronic levels will generate discrete peaks.

The HL spectra from the 3.2 to 2.6 eV levels reached after pumping with 600 to 780 nm and ESA show the emission of two phonons, one ≈513 cm^{-1} followed by a ≈325 cm^{-1} phonon. An additional decay channel is revealed under 640 to 670 nm excitation involving a ≈325 cm^{-1} phonon followed by a ≈365 cm^{-1} phonon. Pumping with 1064 nm leads to HL from levels below 2.3 eV. The separation between the peaks in the latter spectra is ≈218 cm^{-1} and ≈323 cm^{-1} indicating the phonons emitted during the vibronic relaxation below 2.3 eV. This shows the different nonradiative relaxation dynamics associated with various parts of the excited state. From table [4.3] we see that the 513 cm^{-1} mode is an internal mode of the tetrahedral (SiO_4) while the 218, 323 and 365 cm^{-1} modes can be assigned either to translational modes of the Mg ion or external modes of the (-SiO_4).[25,26] Although more than one phonon modes are involved in the vibrational relaxation, the peaks in the up-converted HL spectra are well defined. This suggests that the sequence of phonon emission is predetermined by the ion-lattice interaction dynamics.

From fig. [5.9] it is clear that the intensity of the up-converted HL is different at various parts of the excited state. The two bands of stronger

emission located at 2.43 ± .15 eV (sector B) and 2.05 ± .12 eV (sector C) indicate the presence of electronic bottlenecks. The nonradiative relaxation slows down in these parts of the excited state resulting to a stronger HL emission. The slowdown of the nonradiative relaxation arises from the energy level structure of the excited ions. Following photoexcitation, the ions are involved in a cascade process of phonon emission while they slide down the electronic manifold. During this energy transfer from the ions into the lattice, the ions are crossing higher lying electronic states. The process slows down in regions of electronic state crossing and halts when the ions reach a metastable level. The vibronic levels close to a crossing point have longer lifetimes.

From the Tanabe-Sugano energy-level diagram of forsterite the upper ^1E and $^3T_1$ electronic states are predicted to be at about 2.01 eV. A small peak on the absorption spectra is located at 1.97 eV and has been assigned to the ^1E state. The absorption bands of the ^1E and the $^3T_1$ electronic states overlap in this region. The crossing of the ^1E with the $^3T_1$ state as shown in fig. [5.21] produces an electronic bottleneck trap that delays the nonradiative decay of the excited electron-lattice system. This bottleneck is apparent in all HL spectra obtained under 1064 and 710 nm excitation (fig. [5.10]) as an enhancement of the signal arising from levels with energy 2.1±0.2 eV. The relative intensity of the average HL signal under 1064 nm excitation at 2.1 eV over the signal at 1.85 eV is over 10 fold which means that the ratio of the lifetimes of these levels is of the same order. These results indicate that a significant slowing down of the nonradiative relaxation process is taking place at about 2.1 eV due to the crossing of the $^3T_1$ and ^1E electronic states. Typical lifetimes of the vibrational levels are of the order of 100 fs. Therefore, from the intensity ratio, the lifetime of the states inside the

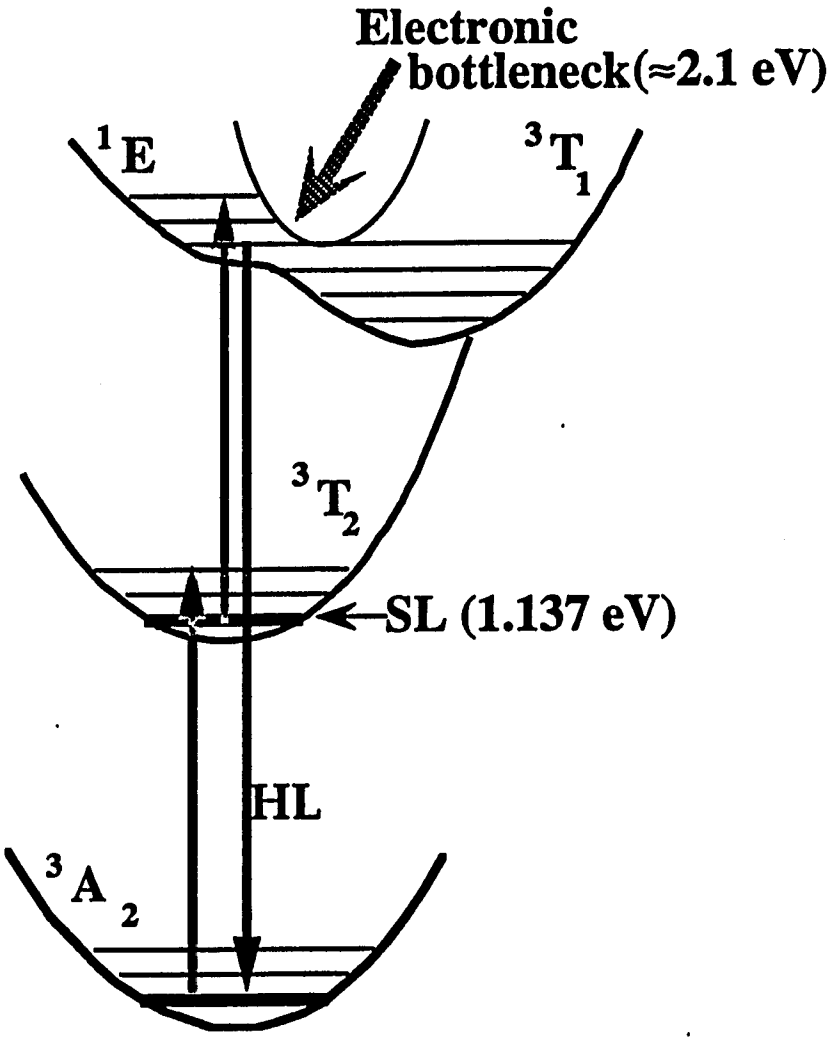

Figure 5.21: Energy diagram of Cr^{4+} in forsterite. The ^1E electronic state is crossing the $^3T_1$ state causing an electronic bottleneck.

bottleneck should be of the order of 1 ps (at peak position) or less. The up-converted HL spectra under 1064 nm excitation shows that the electronic bottleneck extends from ≈ 2.30 eV to 1.95 eV containing approximately 12 vibronic levels. Therefore, the expected overall time that the excited ions need to cross the electronic bottleneck states is on the order of 10 ps or less. This was confirmed by the streak camera measurement of this emission (see fig. [5.12]) which provides an upper limit for the decay time of 10 ps for the HL originated in this electronic bottleneck.

The absorption spectrum in Cr^{4+} forsterite revels that there is an absorption band starting at ≈2.36 eV due to the $^3B_2(^3T_1)$ state. The observed bottleneck in the 2.55 to 2.27 eV region can be assigned to the $^3B_2(^3T_1)$ state. The sharp peaks (three in each bottleneck band) of the up-converted HL energy profile shown in fig. [5.6], contain information on the details of the electronic structure of the bottlenecks. The electronic bottleneck at 2.1 eV clearly observed in the up-converted HL spectra, is very difficult to detect using direct pumping. Only a strong emission on top of the antiStokes room temperature Raman spectrum that appears when the laser photon energy is less than 2.1 eV is an indication of the presence of this electronic bottleneck. This is due to anti-Stokes HL emission following the population of vibronic states within the bottleneck via absorption of light by thermally excited ions in the ground state.

The experiments also demonstrate the dependence of the up-converted HL on the emission polarization (figs. [5.6] and [5.7]). This dependence is expected since it is a common characteristic in the OL emission spectra in transition metal-doped materials and it has been reported in forsterite. Furthermore, it has been shown that the up-converted HL spectrum does not depend on the excitation polarization. The

spectral profiles remain the same for the different laser polarizations. This indicates that the ions immediately after excitation "forget" how they were excited.

ESA under 1064 nm excitation will excite Cr ions to a level 2.302 eV above the ground state. This level can also be reached by direct absorption of 539 nm photons where forsterite absorbs strongly. Therefore, a strong two-step absorption is expected under 1064 nm excitation, resulting in a significant HL signal. On the other hand, two-step excitation with 620 nm photons is equivalent to absorption of one 395 nm photon for which the sample exhibits very little absorption. This explains why the HL signal under 620 nm excitation is ≈ 100 times weaker than spectra taken under 1064 nm excitation.

Using 532 nm laser excitation, the lifetime of the $^3T_1(t_2e)$ electronic state was measured to be 395 ps. The integrated intensity of $^3T_1(t_2e) \rightarrow {}^3A_2$ emission (B-sector in fig. [5.20]) is estimated to be ≈ 600 times stronger than the emission from the highest energy vibronic level (first narrow peak in up-converted HL emission in A-sector) under the same 532 nm laser excitation. The ratio of the intensities due to emission from different levels of the same electronic state should be equal to the ratio of their lifetimes. Therefore, the lifetime of the highest energy vibronic level is estimated to be ≈ 660 femtoseconds (395 ps / 600). Since the depletion of the population of a nonequilibrium vibronic state is due to the emission of phonons during the vibrational relaxation of the excited ions, this time can also be considered as the time between successive phonon emission in this part of the excited state manifold.

Using the 10 ps upper limit of the emission from the 2.1 eV bottleneck and the low temperature up-converted HL spectrum for

calibration (the intensity of the lines is proportional to the lifetime of the vibronic level they originate) we can estimate the upper limits of the lifetime of different vibronic levels. More specifically, using fig. [5.6a] or [5.7a] we estimate an upper limit of 400 fs for the lifetime of the highest energy vibronic level located at 2.3 eV while inside the bottleneck the maximum upper limit for the lifetime of the vibronic level located at the peak of the emission is 2 ps. Using fig. [5.6b] and [5.7b] for calibration we estimate the lifetime of the 2.3 eV level to be less than 400 fs from fig. [5.6b] and 650 fs from fig. [5.7b] while the maximum upper limit in both spectra is 3.2 ps for the vibronic level inside the bottleneck that has maximum intensity.

The profile shown in fig. [5.9] is directly associated with the relaxation pathway of Cr^{4+} ions in forsterite in the 2.9 eV to 1.9 eV region. Assuming that the average phonon mode involved in the nonradiative relaxation is 300 cm^{-1} and that the time for each phonon step is 300 fs then the distance of 1 eV will be covered in 8 ps. However, if we normalize the nonradiative relaxation rate of 300 fs per phonon with respect to the profile shown in fig. [5.9] in such way that stronger emission means proportionally slower rate, then we estimate that at liquid nitrogen temperature the ions need ≈32 ps to cross the 2.9 to 1.9 eV part of the excited state in forsterite. The presence of the bottlenecks in the nonradiative relaxation provide an explanation on the different nonradiative relaxation times that have been measured in different crystals.[1-4] For example, under similar excitation conditions, the nonradiative relaxation time was measured to be less than 5 ps in ruby [Cr^{3+}:Al_2O_3], 17 ps in Alexandrite [Cr^{3+}:$BeAl_2O_4$] and 23 ps in Emerald [Cr^{3+}:$Be_3Al_2(SiO_3)_6$].

The experiments were repeated on a forsterite crystal that is doped mostly with Cr^{3+} ions under the same excitation conditions but no up-converted emission was detected. This indicates that the reported emissions are due to Cr^{4+} ions. The intensity of all up-converted luminescence emissions changes as the square of the average laser excitation power. However, no change in the intensity was observed when the pulsewidth was varied keeping the average power constant. This intensity dependence is consistent with radiative transitions following excited state absorption.

The up-converted two-step HL technique allows the study of the relaxation dynamics of the upper excited states. In addition, information concerning the potential surfaces and electronic bottlenecks can be extracted. In the case of tunable solid state crystals, in order the phonon "steps" to be observable in the up-converted HL emission as peaks there is a condition to be satisfied; That is, the positions of minimum energy of the lowest excited electronic state (storage level) and the ground state in the configurational coordinate energy diagram representation should be very close. In this case, following ESA from the SL the ions will reach an excitation level having maximum amplitude of its vibrational wavefunction above the middle of the $\chi_g(0)$ vibrational wavefunction of the ground state. This is the case in forsterite and is depicted in fig. [5.13]. Thus, the phonon peaks can be observed as we have already discussed for the case of forsterite. If there is a large shift between the ground state and the lowest excited state parabolas, radiative transitions from the initially populated vibronic levels following ESA will involve many vibrational levels of the ground state making the observation of discrete peaks in the up-converted HL spectrum impossible. The emission will start at the excitation level energy from where it gradually increases in intensity while the overall up-converted HL

spectrum will be a smooth with no peak structure. When the position of minimum energy of the ground state end the first excited state (SL) is small and consequently the condition for peaks to exist in the up-converted HL spectrum is satisfied, the ordinary luminescence emission from the storage level should have a strong zero-phonon peak. Therefore, we can assume that when photoluminescence from the storage level exhibits a strong zero-phonon peak, up-converted HL following ESA should have peaks showing the phonon modes involved in the vibrational relaxation.

From our work, several questions need to be addressed by physicists such as:

a) Why some modes participate in the nonradiative relaxation and other don't.

b) Which are the selection criteria for the participating phonon modes and how this affects the nonradiative relaxation.

c) How exactly the energy is transferred from the impurity ion into the lattice and what is the role of the local modes.

e) What exactly is the origin of the electronic bottlenecks and how the presence of a bottleneck affects the electron phonon coupling and the nonradiative relaxation.

f) Is it possible to design a crystal in which there are no nonradiative relaxation processes.

The technique presented here can be used in a variety of systems in order to study the characteristics of the upper excited states and the nonradiative processes.

5.7 Up-converted luminescence in Ruby and Ni^{2+}:MgO.

I have tested the up-conversion technique in Cr^{3+}-doped forsterite, Ruby and Ni^{2+}-doped MgO. As I have mentioned before, using a Cr^{3+} doped forsterite we could not observe any up-converted luminescence.

In **Ruby**, up-converted luminescence was observed but it has the characteristics of up-converted OL not HL. Fig. [5.22] shows the up-converted emission in Ruby under various laser excitations. The absorption spectrum in Ruby exhibits a sharp absorption line at 691 nm followed by a broad absorption band that starts at ≈ 660 nm. The storage level in Ruby is at 1.786 eV. Consequently, the lowest in energy excitation level can be reached by ESA with 692 nm laser excitation (just enough energy per photon to populate the SL) which is at 3.571 eV (346 nm). Our detector is sensitive at wavelengths higher that 280 nm and as a result, using single laser beam excitation, only a small portion of the excited state can be investigated.

Fig. [5.22a] shows the emission under 650 nm laser excitation but this emission remains the same for any excitation wavelength lower than 660 nm. The spectral profile shows a phonon peak located at 3.658 eV that should be associated with zero phonon transition from an electronic state at 3.658 eV to the ground state. Pumping with 691 nm laser light there is not enough energy per photon available to the Cr^{3+} ions in Ruby to reach the 3.658 eV state by ESA. Indeed, as we can see in fig. [5.22b] this emission is completely missing but two new lines appear that seem to originate from two electronic levels located at 3.587 eV and 3.478 eV. Changing the laser wavelength to 690 nm the spectral profile remains unchanged which means that this emission is OL from an upper state and not HL. Using excitation wavelengths between 532 and 691 nm, I could not detect any HL features in

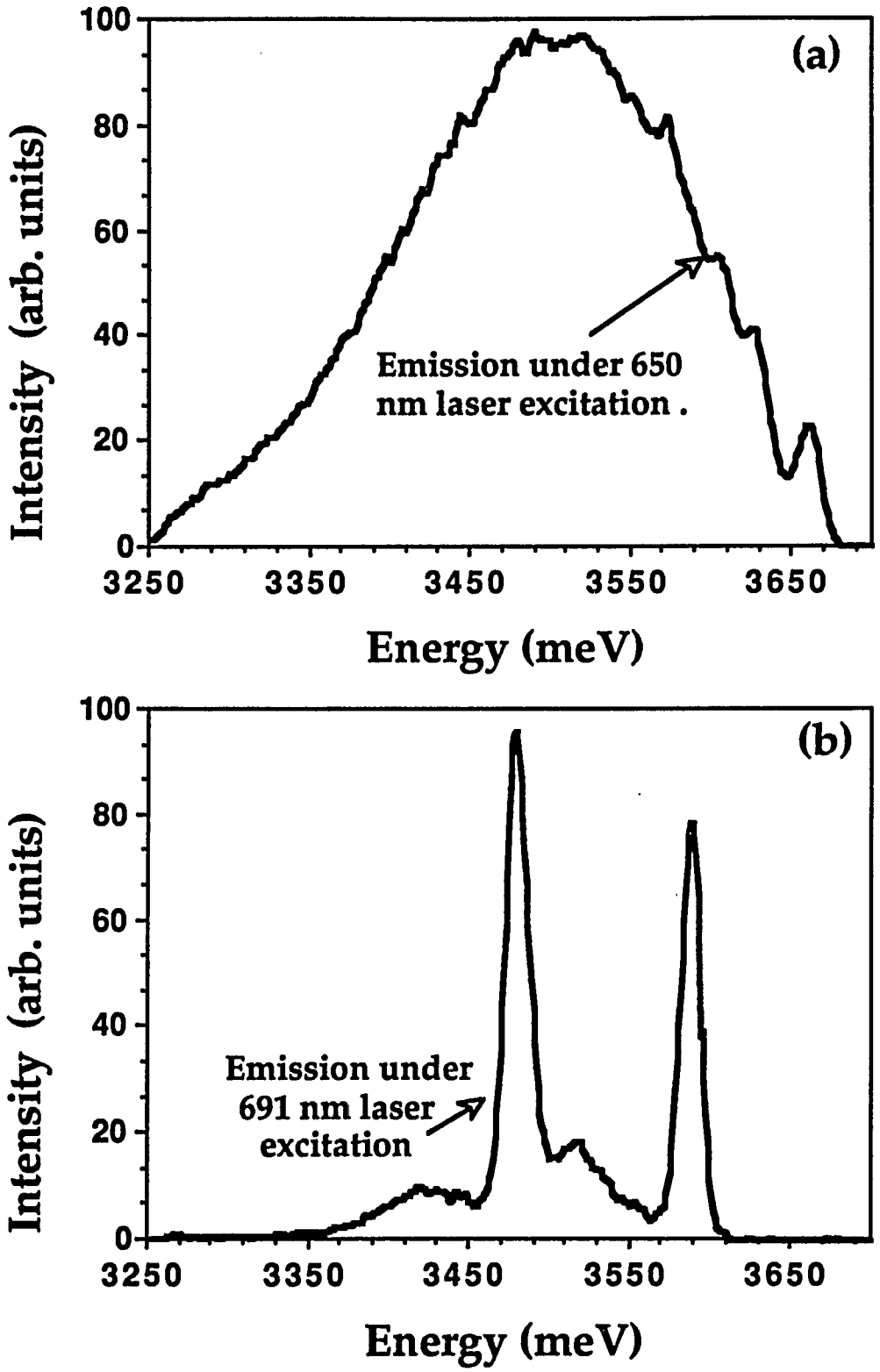

Figure 5.22: Up-converted luminescence in Ruby under different laser excitation. a) The excitation wavelength is 650 nm but this spectrum remains the same for laser wavelengths lower than 660 nm. b) The up-converted emission under 691 nm excitation.

the up-converted luminescence spectra in Ruby. The fact that only a small portion of the excited state of Ruby can be investigated using a single laser beam for two step excitation may be a frequent problem since many ions have their storage level at high energies. To overcome this difficulty, two-beam excitation of different wavelength is required. The first should carry enough energy per photon to excite the ions into the SL (691 nm). The second beam should have longer wavelength (longer than 691 nm) and will be used for the observation of up-converted HL.

In Ni^{2+}:MgO, the SL is located at 0.992 eV (8002 cm^{-1}) and a strong zero-phonon peak is present in the emission spectrum from the SL to the ground state (see fig. [5.23]). Therefore, Ni^{2+}:MgO is ideal for testing the concept of the up-converted luminescence technique. The divalent Ni^{2+} ion has a $3d^8$ electron configuration.[27-29] The Ni in MgO occupies an octahedral site with inversion symmetry and its Tanabe-Sugano energy diagram is identical to the Cr^{4+} ions in forsterite. Due to the inversion symmetry, only vibrationally induced electric-dipole transitions are possible while the primary transitions are magnetic dipole.

Fig. [5.24] shows up-converted luminescence under 609 and 617 nm laser excitation. In both cases, the higher energy peaks (marked as a1) appear at the excitation energy level as it is described by eq. 5.1 ($E_{EL}=E_{SL}+\hbar\omega_{laser}$). The first peak (at EL) shifts when the excitation wavelength changes indicating that this emission is due to up-converted hot luminescence. A second peak (marked as a2) follows with energy separation from the first peak of 390 cm^{-1} indicating the phonon mode involved in the nonradiative relaxation of Ni^{2+} ions in MgO. At lower energies there is an emission that is

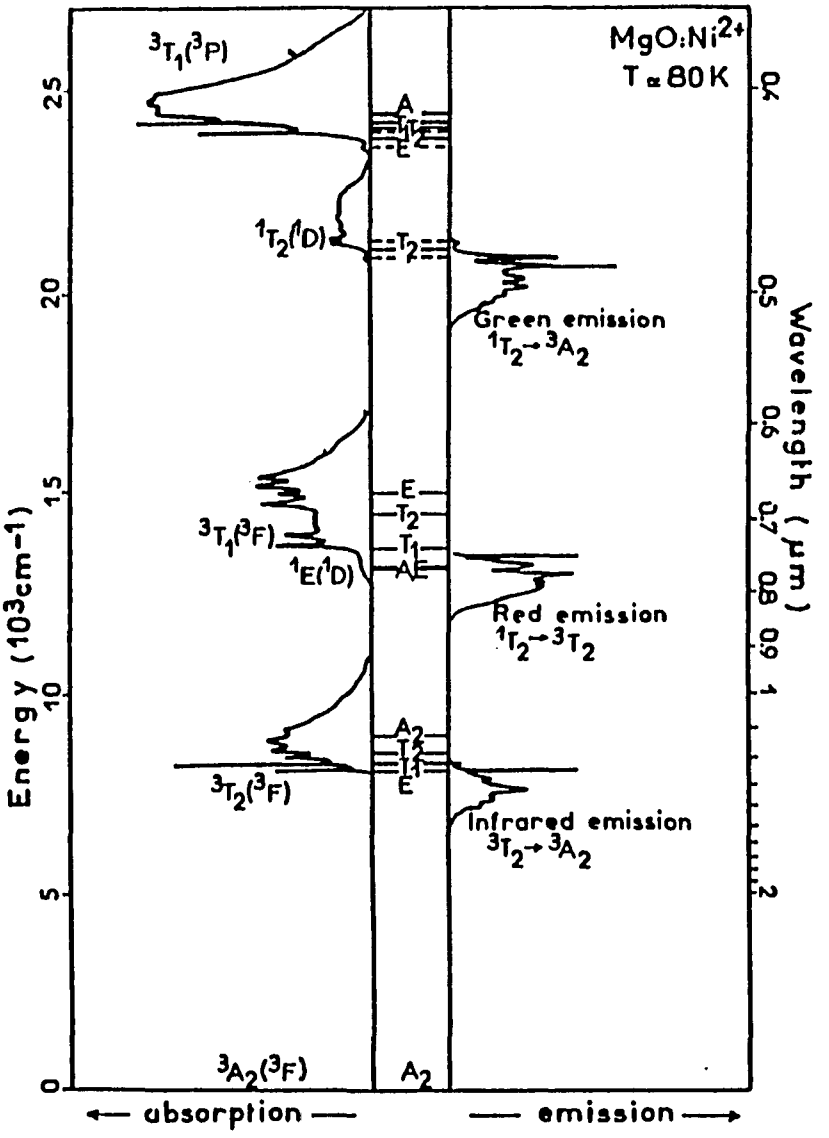

Figure 5.23: Absorption and emission spectra in Ni^{2+}:MgO showing its electronic structure. (From Ref. 17)

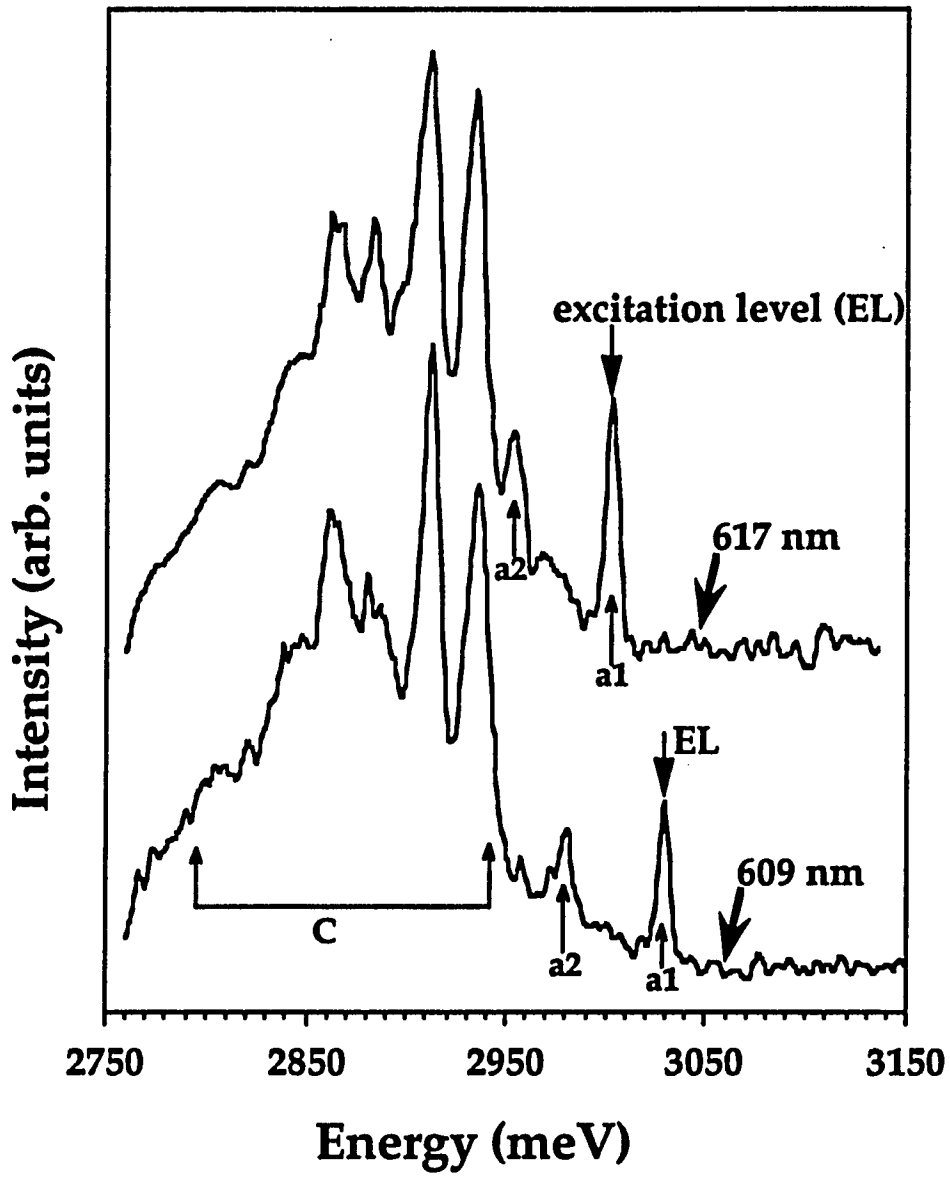

Figure 5.24: Up-converted luminescence in Ni:MgO under 609 and 617 nm laser excitation. Details on the assignment of the peaks are given in the text.

independent of the excitation wavelength indicating the presence of an electronic bottleneck (sector C in fig. [5.24].

Fig. [5.25a] shows the up-converted luminescence spectrum under 1064 nm excitation. The most intense peak (a1) appears at the two-step excitation level (2.157 eV). The (a1) peak is followed by another intense peak (a2) with energy lower by 390 cm^{-1} indicating the phonon mode involved in the nonradiative relaxation in this part of the excited state. The interesting feature of this spectrum is the peak (b1) which appears at energy higher that the two step excitation level. The difference in energy between (b1) and (a1) is 169 cm^{-1}. This peak could be due to an electronic transition from EL assisted by the annihilation of a phonon. Smaller peaks marked as (e) in fig. [5.25a] are due the vibrational sidebands of the (a1) and (a2) peaks.

The 390 cm^{-1} separation between the peak (a1) at the excitation level and the second peak (a2) was also observed under 532 nm laser pumping. The up-converted luminescence spectrum under 532 nm excitation is shown in fig. [5.25b]. In this case, there is again a peak at energy higher than the excitation level marked as (b2). The difference in energy between (a1) and (b2) is 694 cm^{-1}. The origin of the peak (b2) should be the same as with the peak (b1) observed under 1064 nm excitation. At lower energies, there is an area of stronger emission with peak structure centered at 2.87 eV (sector C) which is in the same energy region with the electronic bottleneck observed under 609 and 617 nm excitation (sector C in fig. [5.24]). Apparently, sector C in figs. [5.24] and [5.25b] is due to the same electronic bottleneck located at ≈2.87 eV.

These results demonstrate that the up-conversion luminescence technique is a powerful tool for the investigation of the vibrational

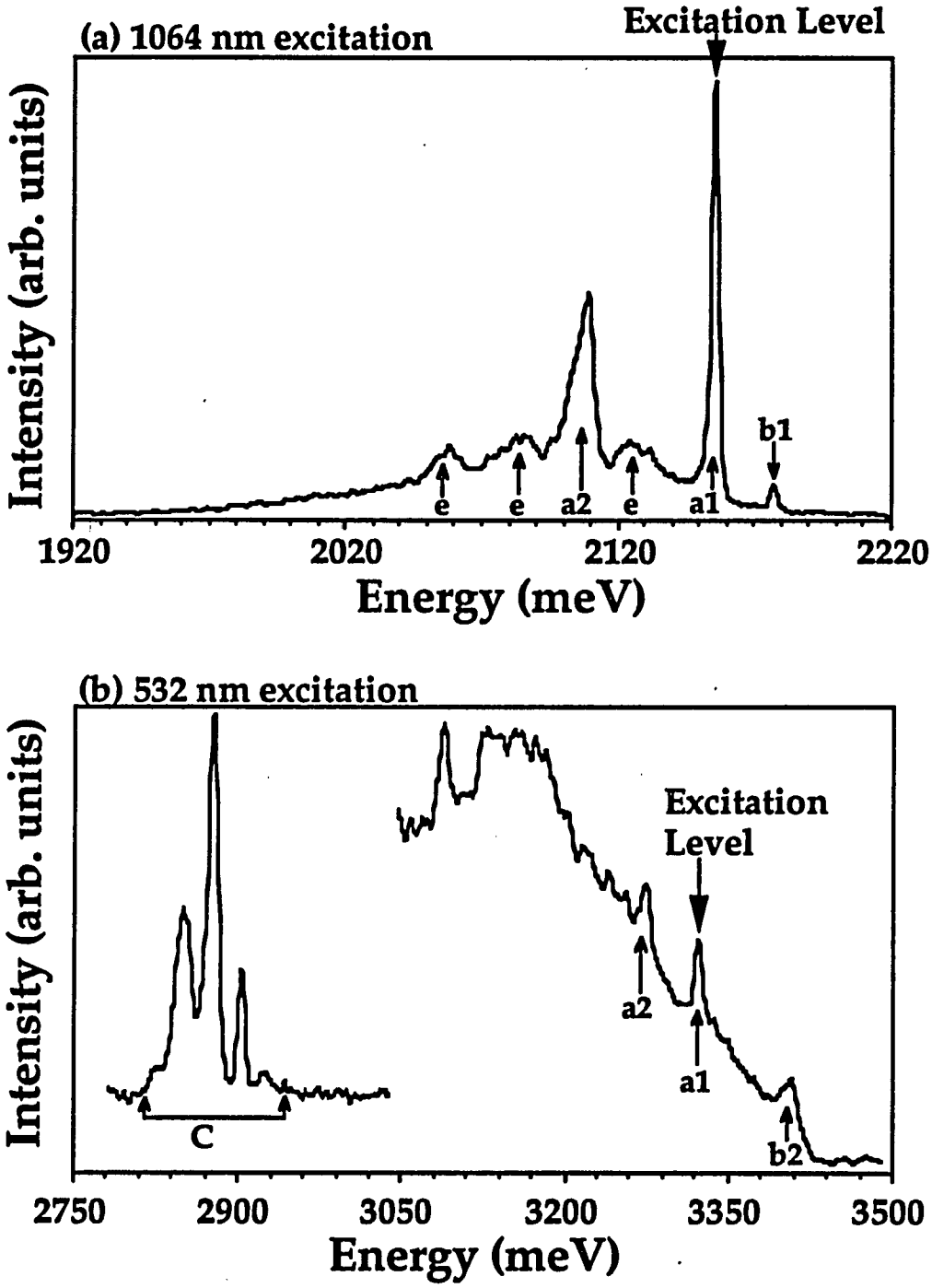

Figure 5.25: Up-converted luminescence in Ni:MgO under 1064 and 532 nm excitation. See the text for more details

relaxation of impurity ions in dielectric crystals. This technique can also be used in any other system that has a relatively long-lived storage level.

5.7 References.

1. J. M. Wiesenfeld, Linn F. Mollenauer and Erich Ippen, Phys. Rev. Lett. **47**, 1668 (1981).

2. S. K. Gayen, W. B. Wang, V. Petricevic, R. Dorsinville, and R. R. Alfano, Appl. Phys. Lett. **47** (5) 455 (1985).

3. S. K. Gayen, W. B. Wang, V. Petricevic, and R. R. Alfano, Appl. Phys. Lett. **49** (8) 437 (1986).

4. S. K. Gayen, W. B. Wang, V. Petricevic, S. G. Demos, and R. R. Alfano, J. Lumin. **47**, 181 (1991).

5. A. M. Stoneham, Philosophical Magazine **36**, 983 (1977).

6. K. Peuker and E. D. Trifonov, Phys. Stat. Solidi **30**, 479 (1968).

7. V. Hizhnyakov and I. Tehver, Phys. Stat. Solidi **39**, 67 (1970).

8. Yuzo Mori, Ryo Hattori and Hiroshi Ohkura, J. Phys, Soc. Jap., **51**, 2713, (1982).

9. Y. Kondo, T. Noto, S. Sato and M. Hirai, J. Lumin., **38**, 164, (1987).

10. B. P Zacharchenya, V. D. Dymnikov, I. Ya. Karlik, D. N. Mirlin, L. P. Nikitin, V.I. Perel, and I.I. Reshina, J. Phys. Soc. Jap., **49**, Suppl. A., 573, (1980).

11. D. N. Mirlin, I. Ya. Karlik, L. P. Nikitin, I.I. Reshina, and V. F. Sapega, Solid State Comm., **37**, 757, (1981).

12. B. P Zacharchenya, J. Lumin., **24/25**, 669, (1981).

13. G. Fasol and H. P. Hughes, Phys. Rev.B, **33**, 2953, (1986).

14. C. L. Petersen and S. A. Lyon, Phys. Rev. Lett., **65**, 760 , (1990).

15. P. Saari and K. Rebane, Solid State Comm., **7**, 887, (1969).

16. Yihong Yang, Wolf von der Osten, and Fritz Luty, Phys. Rev. B, **32**, 2724, (1985).

17. R. Moncorge, F. Auzel, and J. M. Breteau, Philosophical Magazine B **51**, 489 (1985); R. Moncorge and T. Benyattou, Phys. Rev. B **37**, 9186 (1988).

18. E. W. J. L. Oomen, J. Lumin., **50**, 317, (1992).

19. A. Silversmith, W. Lenth and R. M. Macfarlane, Appl. Phys. Lett. **54**, 2301, (1989).

20. G. Fasol, W. Hackenberg, H. P. Hughes, K. Ploog, E. Bauser, and H. Kano, Phys. Rev. B., **41**, 1461, (1990)

21. K. R. Hoffman, S. M. Jacobsen, J. Casas-Gonzalez and W. M. Yen, Proceedings of the Advanced Solid-State Lasers Topical meting, Hilton Head, S.C., March 18-20, 1991

22. V. Petričević, S. K. Gayen, and R. R. Alfano, in *Tunable Solid-State Lasers*, Vol. 5 of the OSA Proceeding Series, M. L. Shand and H. P. Jenssen, eds. (Optical Society of America, Washington, D.C., 1989), pp. 77-84.

23. H. R. Verdun, L. M. Thomas, D. M. Andrauskas, T. McCollum, and A. Pinto, OSA Proceedings of the Advanced Solid-State Lasers, eds. M. L. Shand and H. P. Jenssen, Vol. 5, 85, (1989).

24. W. Jia, H. Liu, S. Jaffe, and W. M. Yen, Phys. Rev. B **43**, 5234 (1991).

25. V. Devarajan and E. Funck, J. Chem. Phys., **62**, No 9, 3406, (1975).

26. Kazuaki Iishi, American Mineral., **63**, 1198-1208 (1978).

27. R. Pappalardo, D. L. Wood, and R. C. Linares, J. Chem. Phys., **35**, No 4, 1460, (1961).

28. M. V. Iverson, J. C. Windscheif, and W. A. Sibley, Appl. Phys. Lett. **36**, 183, (1971).

29. W. E. Vehse, K. H. Lee, S. I. Yun and W. A. Sibley, J. Lumin., **10**, 163, (1975).

Chapter 6

Time Resolved Raman Scattering.

6.1 Introduction.

The time resolved experimental research is presented in this section showing the first direct measurements of the kinetics of nonequilibrium optical phonons associated with the nonradiative relaxation of an impurity ion in a dielectric crystal. The dynamics of different phonon modes was investigated at room and liquid nitrogen temperatures. Most importantly, phonon modes involved in the nonradiative relaxation of a photoexcited ion in a crystal are directly identified for the first time. Our work is an attempt to understand the underlying nonradiative processes in the NIR tunable solid state laser crystal Cr-doped forsterite.

The growth and decay dynamics of the optical phonons involved in the nonradiative relaxation of an excited ion is the key to the understanding of the electron-phonon coupling and radiationless decay processes in solid state materials. The first work in this direction to directly investigate the optical phonon relaxation in condensed matter was pioneered in the early 1970s (refs. 1-4) when time resolved Raman methods were used to measure the nonequilibrium optical phonons generated in solids by stimulated Raman scattering or photoexcitation of carriers. In semiconductors, hot carriers relax via emission of small wavevector optical phonons.[5] The lifetime of these phonons is of the order of few ps[3,4] and they decay into near-zone-boundary acoustic phonons[6,7] with long lifetimes (3 μs in GaAs) . In a dielectric crystal where many vibrational modes are present, our

knowledge of which modes participate in the initial steps of the nonradiative decay ("promoting" and "accepting" modes[8]) of an excited impurity ion is not well documented experimentally . However, a significant amount of work has been done over the last 10 years investigating the dynamics of large wavevector, low frequency phonons[9-13] showing lifetimes in the order of 10 ns.

In a previous chapter we discussed the properties of forsterite and we mentioned that forsterite contains Cr^{3+} and Cr^{4+} ions. The sample used for these experiments was grown in atmosphere favoring Cr^{4+} substitution. Using this sample, the intensity of the antiStokes Raman lines of the 225, 335 and 370 cm^{-1} lattice modes exhibited detectable changes at various pump-probe delay times indicating the presence of nonequilibrium phonons. A sample containing mostly Cr^{3+} ions was used for comparison but no changes on the above Raman lines were observed. Consequently, the observed changes in the intensity of the Raman lines should be attributed to the nonequilibrium phonon population generated during the nonradiative relaxation of the Cr^{4+} ions in forsterite.

In this chapter, I will present the experimental results obtained using the time resolved antiStokes Raman scattering technique to determine phonon modes active in the nonradiative decay. A model based on rate equations will allow an estimation of the key relaxation parameters. These results provide information on phonon modes involved in the nonradiative relaxation of the Cr^{4+} ions in forsterite and the decay rates.

6.2 Time resolved Raman scattering experiment.

The synchronously pumped R-6G dye laser was used to photoexcite Cr ions in the forsterite crystal ($Cr:Mg_2SiO_4$) into the upper electronic band. A problem I have experienced was the strong antiStokes luminescence that appears when the temperature of the sample is higher than T≈200 K and does not allow the observation of the antiStokes Raman lines. This emission appears when the excitation wavelength was longer than ≈595 nm. This emission is due to the presence of an electronic bottleneck at 2.1 eV. I have selected as best laser excitation wavelength the 590 nm in order to be as close as possible to the maximum of the absorption peak due to the $^3T_1$ electronic state (located at ≈640 nm) and have a level of antiStokes luminescence that is low enough to clearly observe the Raman phonon lines.

The optical configuration is shown in fig. [6.1]. The laser pulsewidth was 450 fs and it was continuously monitored by an autocorrelator. The laser beam is divided in two parts: one serving as probe which goes through an adjustable delay line and the other serves as pump beam with its polarization rotated by 90 degrees. Zero delay at the sample is determined to within ± 150 fs by observance of the second harmonic in a thin KDP crystal after the mixing of the pump with the probe beam. The PIAS detector attached at the SPEX triplemate spectrograph was used to detect the spontaneous Raman signal. The pump and probe excitation beams are focused and the backscattered light is collected by a (10X) microscope objective lens. The effective focal length of this lens is ≈ 1 cm and therefore, the spot diameter of the beam is estimated to be in the range of 10 μm. The

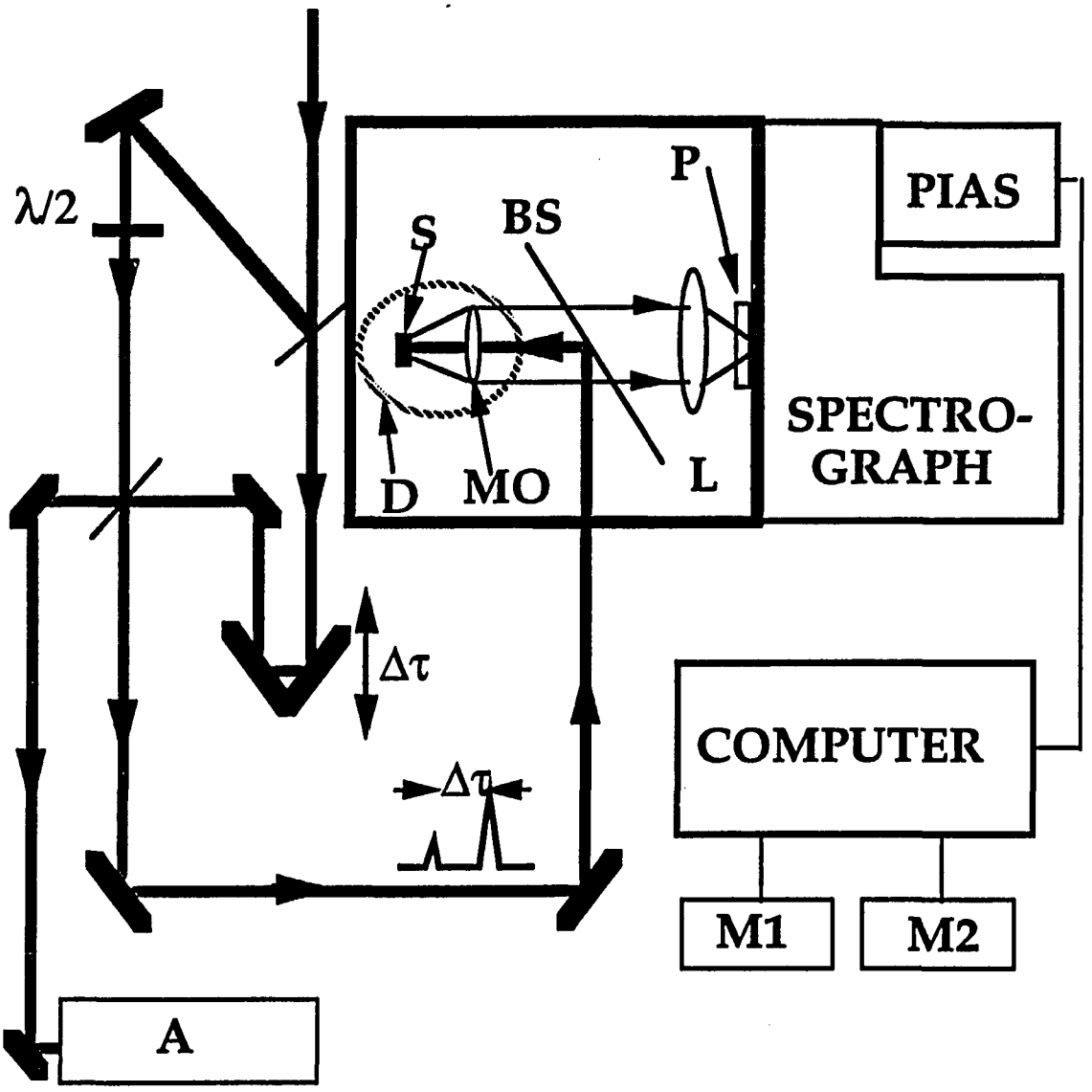

Figure 6.1: Time resolved photon counting Raman experimental setup ($\Delta\tau$: delay time, A: autocorrelator, S: sample, MO: microscope objective, BS: beam-splitter, L: lens, P: polarizer, M1 and M2: computer monitors 1 and 2, D: optical cryostat.

polarizations of the excitation pump beam and the probe beam are perpendicular.

Due to different selection rules for the cross polarized pump and probe beams, different phonon Raman lines are observed from each beam. The intensity of the lines due to the pump beam are independent of the pump-probe delay time and its intensity depends only on the average laser beam power under the condition that the pump pulses precede the arrival of the probe pulses. On the other hand, the lines arising from the probe beam are expected to carry the Raman signal from the nonequilibrium phonon population generated by the nonradiative decay following the photoexcitation of the Cr ions by the pump pulse. For negative delay times, where the probe pulse arrives before the pump pulse, nonequilibrium phonons can be generated by the probe pulse that can cause an increase of the intensity of the pump Raman lines. Therefore, the pump Raman lines can be used as a reference indicating the average laser beam output only for positive delay times.

The two dimensional image obtained by PIAS was transformed into a spectrum calibrated in the appropriate units. Software to calculate integrated intensities of the Raman peaks and also to discriminate low signals from strong background was required. Using the pump Raman lines as reference, the change in the phonon population is estimated from the ratio of the intensities of the probe associated Raman lines over the reference Raman line of the pump. The ratio is obtained using the integrated peak intensities (over a spectral width of 26 cm^{-1}) after subtraction of the luminescence background in this spectral region. This method is particularly efficient when small changes must be observed while the laser output power is fluctuating in time. The ratio of the pump and

probe beam intensities remains the same and therefore, changes in the relative intensity of the Raman lines is independent from the fluctuations of the laser power reflecting only changes in the phonon population.

The experiments were performed for three different pump-probe-scattered light polarization configurations with respect to the crystal axis. These configurations covered most of the Raman phonon modes observed in the backscattering geometry. In the first configuration, the pump beam polarization (P_{pump}) is parallel to the c-axis, the probe beam polarization (P_{probe}) parallel to the b-axis and the collected backscattered light polarization ($P_{scatt.}$) parallel to the b-axis of the crystal. In this case, the 225, 335, 545, and 835 cm^{-1} Raman lines are due to the probe beam and can be investigated for possible time dependent changes in intensity. The second configuration is $P_{pump}//c$, $P_{probe}//b$ and $P_{scatt.}//c$ axis of the crystal. The Raman lines due to the probe beam are at 370, 590, and 870 cm^{-1}. The third configuration is $P_{pump}//c$, $P_{probe}//a$, and $P_{scatt.}//a$ axis. The probe beam Raman lines to be examined are the 300, 490, 605, and 770 cm^{-1} modes.

Excitation with laser polarization parallel to the c-axis of the crystal was preferable due to the stronger absorption exhibited by the Cr^{4+} ions at the 590 nm excitation wavelength. The power of the pump and probe laser beams utilized for each polarization configuration was chosen to generate Raman lines from the pump (reference lines) and probe beam of the same intensity. For this reason, the ratio of the pump beam power over the probe beam power for the first and third configuration was chosen to be 3/1. For the second configuration, the ratio of the beam powers was approximately 1/1.

From the Raman active modes that we investigated, the 225, 335 and 370 cm^{-1} modes exhibited detectable changes in intensity at various pump-

probe delay times. The temporal behavior of the 225 and 335 cm^{-1} modes was also measured at liquid nitrogen temperature. For the low temperature measurements the microscope objective was positioned inside an optical cryostat on a holder attached on the shield of the cold figure of the dewar. The microscope objective lens is composed by two groups of lenses and each group has two lenses. The two lenses of a group are attached to each other and in between them there is an index matching material. At low temperatures, the index matching material brakes into very small pieces and the lens loses its transparency. For this reason the lens was modified to withstand the very low temperatures. More specifically, the lenses were taken apart and the index matching material was cleaned using acetone. Then the lens was put together again for safe use at liquid nitrogen temperature. The modified lens is backscattering a portion of the incident laser beam. This causes increased background noise in our measurements and as result, the error bar for these measurements is increased.

6.3 Experimental results

The pump and probe beams are cross polarized with respect to different crystal axis, resulting in a different set of phonon lines in the antiStokes Raman spectra from each beam. This is demonstrated in fig. [6.2], where the Raman spectrum for the pump (thin line) and the probe (thick line) scattering configurations is shown. The pump-probe-scattered light polarization configurations is, $P_{pump}//c$, $P_{probe}//b$ and $P_{scatt.}//b$ axis of the crystal. The excitation source was the 590 nm output of the R-6G dye laser but, for best spectral resolution, the pulsewidth was tuned to ≈10 ps. The spectrograph grating was 600 $^{gr}/_{mm}$ in order to include all antiStokes Raman lines in one spectrograph setting. We can see that the Raman lines are different and therefore in the time resolved experiment where both beams overlap we will be able to distinguish the pump beam Raman lines from the probe beam Raman lines. Applying different polarization of the pump-probe and scattered light with respect to the crystal axis, we investigated most of the Raman active phonon modes of forsterite in the backscattering configuration.

Fig. [6.3] displays typical antiStokes Raman spectra over the 150 to 500 cm^{-1} spectral region at two pump-probe delay times for the $P_{pump}//c$, $P_{probe}//b$ and $P_{scatt.}//b$ axis scattering configuration. In comparison with the spectra shown in fig. [6.2], the 1200 $^{gr}/_{mm}$ grating was used for best spectral resolution. In addition, due to the short pulsewidth (450 fs) the laser line bandwidth is larger and as a result, the bandwidth of the Raman lines is larger. The intensities of the 225 and 335 cm^{-1} modes exhibit delay time dependent changes with respect to the intensity of the 370 cm^{-1} mode. The 370 cm^{-1} line is due to the pump beam and therefore, its intensity is

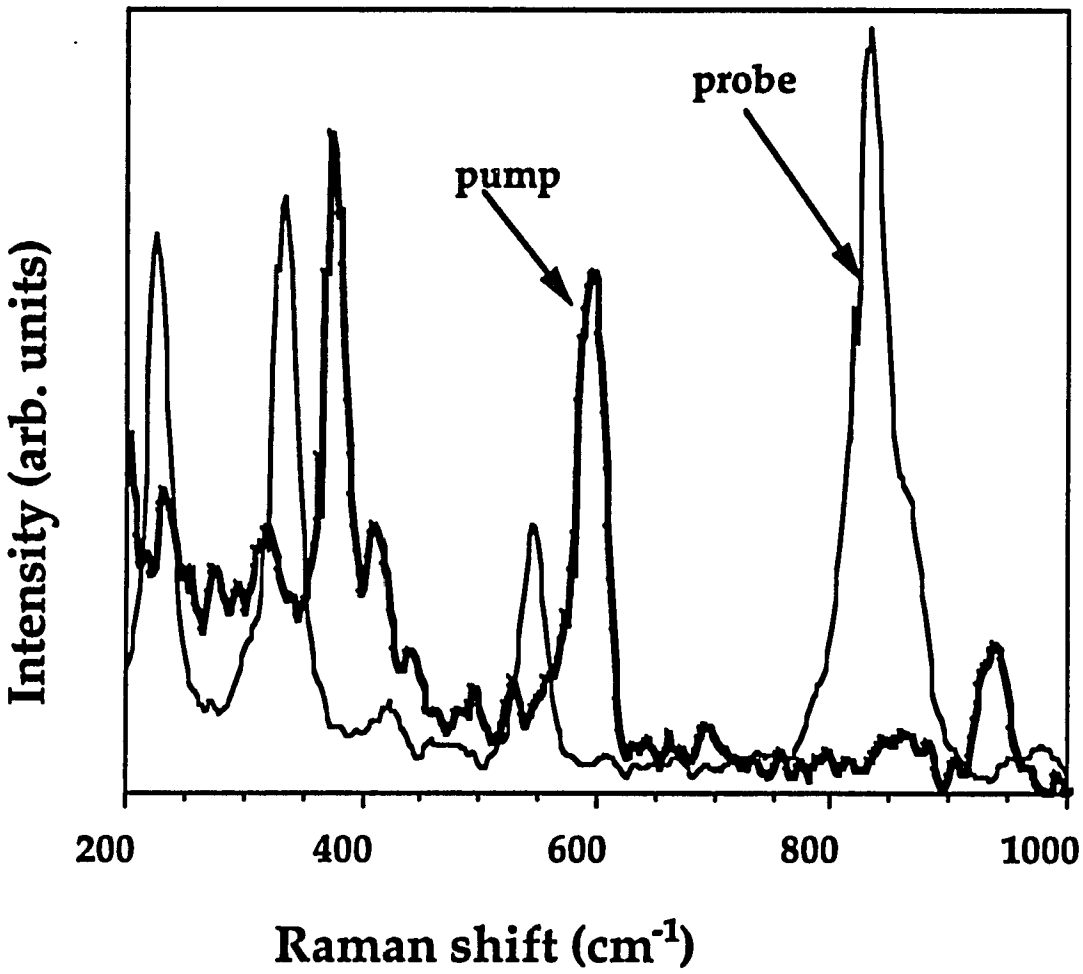

Figure 6.2: AntiStokes Raman spectrum of the pump and probe beams in the $P_{pump}//c$, $P_{probe}//b$ and $P_{scatt.}//b$ axis of the crystal scattering configuration. $\lambda_{pump}=\lambda_{probe}=590$ nm

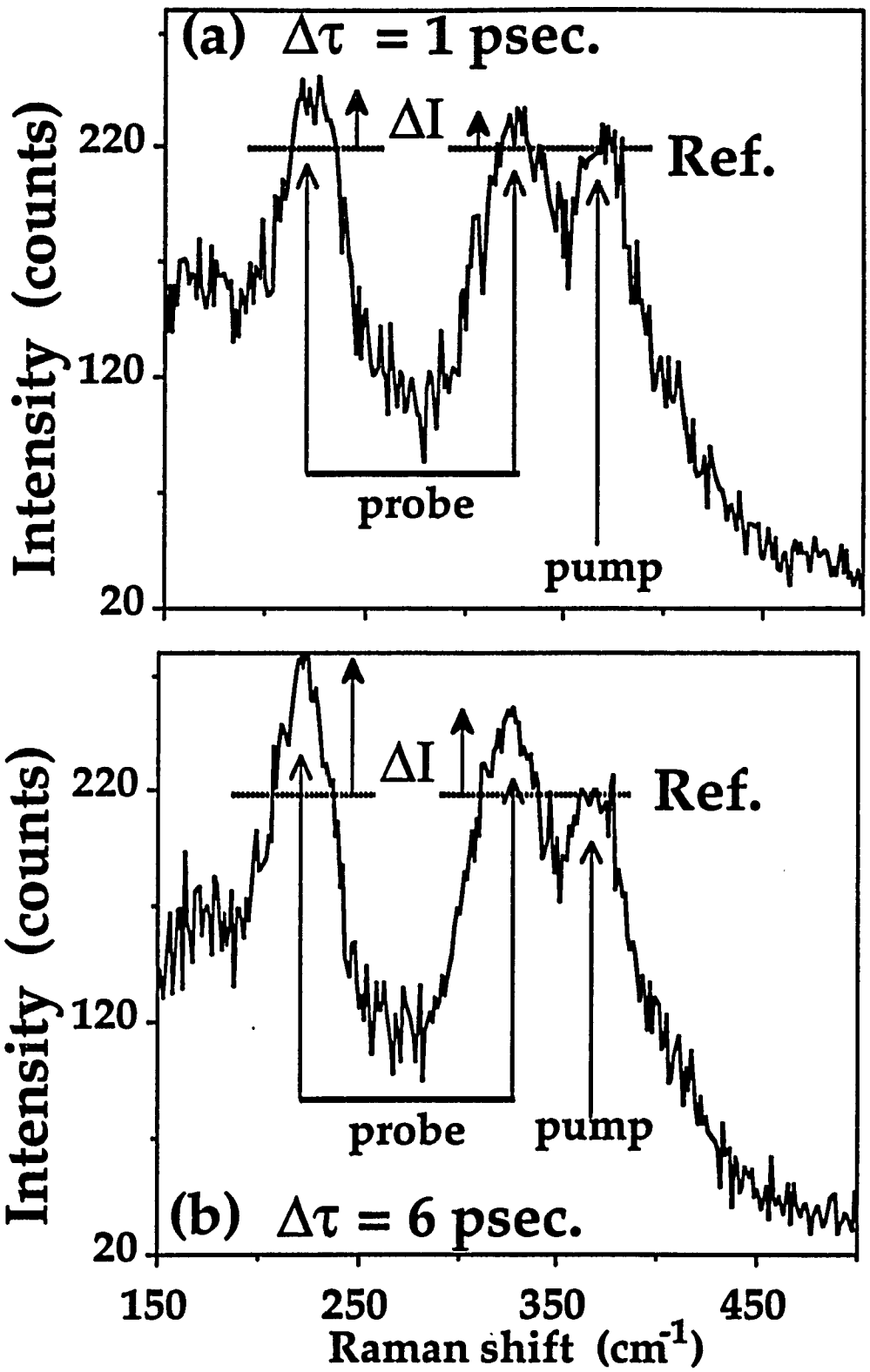

Figure 6.3 AntiStokes Raman spectra for two different delay times, (a) $\Delta\tau$=1 psec and (b) $\Delta\tau$=6 psec. ΔI is the difference in intensity between the probe-excited Raman lines at 335 cm^{-1} and 225 cm^{-1} and the pump -excited reference line (indicated by broken lines) at 375 cm^{-1}. $P_{pump}//c$, $P_{probe}//b$, $P_{scatt.}//b$-axis.

independent from the pump-probe delay time for positive delay times ($\Delta\tau>0$). On the other hand, the 335 cm^{-1} and 225 cm^{-1} lines arise from the probe beam and are expected to carry the Raman signal from the nonequilibrium phonon population generated by the nonradiative decay following the photoexcitation of the Cr ions by the pump pulse. Using the 370 cm^{-1} line as a reference, the change in the phonon population is estimated from the intensity of the phonon lines, at various delays between the pump and probe laser pulses. The 370 cm^{-1} Raman line is only due to the pump beam and its intensity is independent of the (positive) delay time. Therefore, it is a reliable reference parameter in this experiment.

The salient feature shown in fig. [6.3] is the difference in the intensity, denoted by ΔI, between the reference 370 cm^{-1} line and the lines from the probe beam at delays of 1 and 6 ps. Fig. [6.4] displays the time dependence of the ratio of the intensities of the probe associated Raman lines over the reference Raman line of the pump. The ratio is obtained using the integrated peak intensities (over a spectral width of 26 cm^{-1}) after subtraction of the luminescence background in this spectral region. Both Raman lines exhibit approximately the same increase and subsequent decrease in intensity with time. The rise time of the curve is related to the phonon emission time while the decay portion is related to phonon lifetimes. The 225 cm^{-1} mode profile rises to a maximum nonequilibrium population in 10 ± 1.5 ps and decays with time constant of 13.8 ± 3 ps. The 335 cm^{-1} mode profile peaks at 8 ± 1 ps and has a decay time of 10.3 ± 3 ps. These results directly show the time dependence of the nonequilibrium phonon population of different modes involved in the nonradiative decay of the impurity Cr ions in a forsterite crystal.

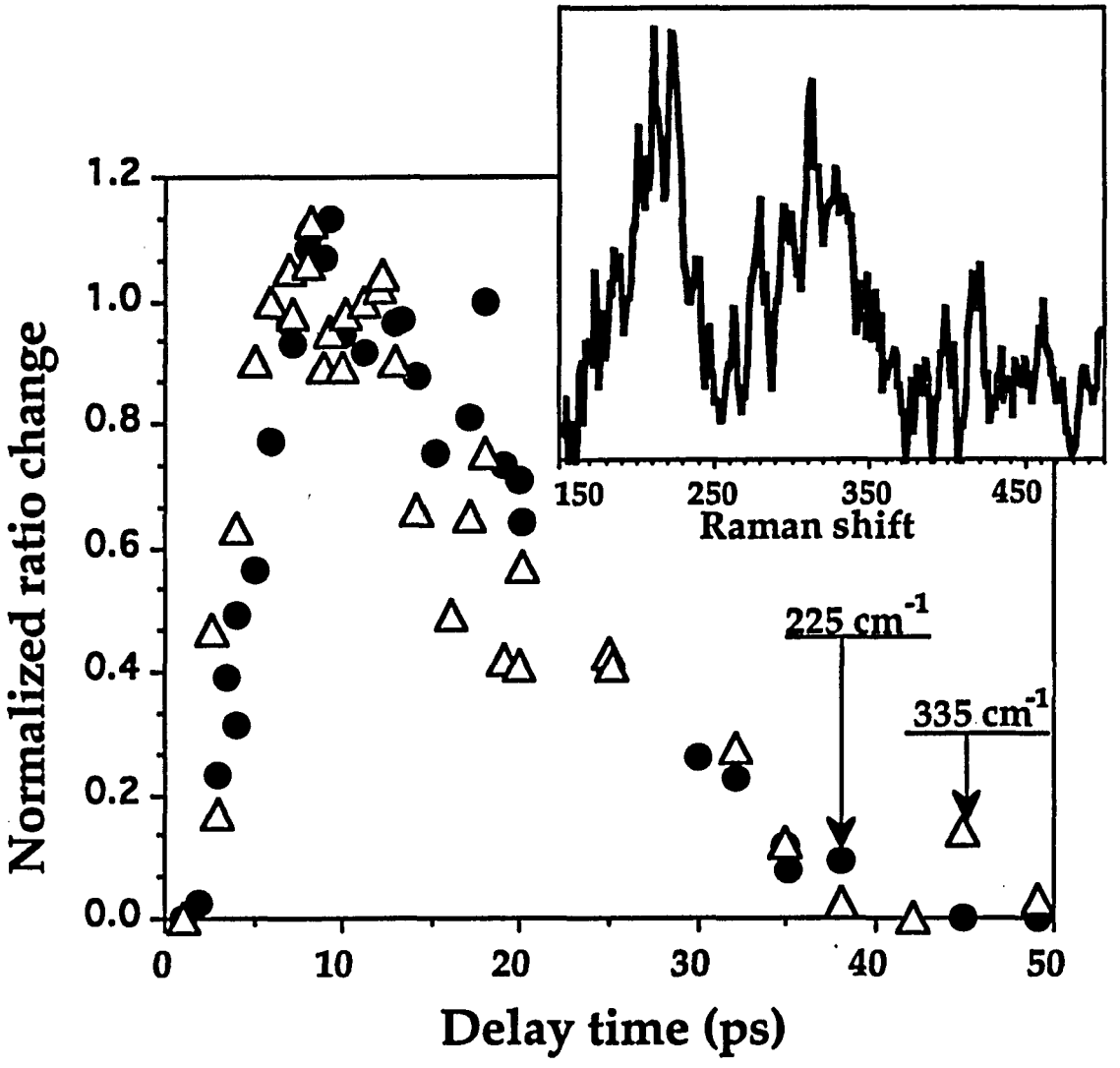

Figure 6.4: Temporal behavior of the intensity of the 225 cm^{-1} (circles) and 335 cm^{-1} (triangles) phonon modes as a function of pump-probe delay time. Insert shows the difference spectrum obtained after subtraction of the 1 ps delay time antiStokes Raman spectrum from the 6 ps spectrum.

The insert in fig. [6.4] was obtained by subtracting the antiStokes Raman spectra at 6 ps and 1 ps delay time. The peaks are centered at ≈218 and ≈330 cm^{-1} and are due to the increased intensity of the 225 and 335 cm^{-1} Raman lines at 6 ps delay time.

In the experimental data I include data points for only positive delay times ($\Delta\tau$) within $\Delta\tau$=1 and $\Delta\tau$=50 ps. The reason is that for $\Delta\tau$<0 the pump beam is probing the phonon population generated by the probe beam. In the next section we show that the 370 cm^{-1} mode participates in the nonradiative relaxation and therefore, its intensity may increase at negative delay due to the phonons generated by the probe pulse. In this case, although no nonequilibrium phonons are detected by the probe lines, the ratio of the intensity of the probe over the pump Raman lines will not give the correct measure of the ratio in the absence of nonequilibrium phonons. We also did not measure the intensities at delays -1<$\Delta\tau$<1 because of the fear for interference between the spatially and temporally overlapping pump and probe pulses in the crystal which can affect the ratio. For these reasons we don't know exactly the baseline (although we can estimate it) which in different time resolved experiments is obtained at negative delay times. Arbitrarily, we used zero for $\Delta\tau$=1 ps.

Measuring the spectrum between 300 and 900 cm^{-1}, the intensity of the higher energy antiStokes phonon lines was investigated using the same scattering geometry. From fig. [6.2] we see that the 335, 545 and 827 cm^{-1} Raman lines are due to the probe beam while the 370 and 590 cm^{-1} lines are from the pump beam. The spectrum is shown in fig. [6.5] for two different delay times (1 ps and 6 ps). As we see, only the intensity of the 335 cm^{-1} line changes (denoted by ΔI) but no significant change is observed in the intensity of the 545 and 827 cm^{-1} modes. This clearly shows that the 545 and

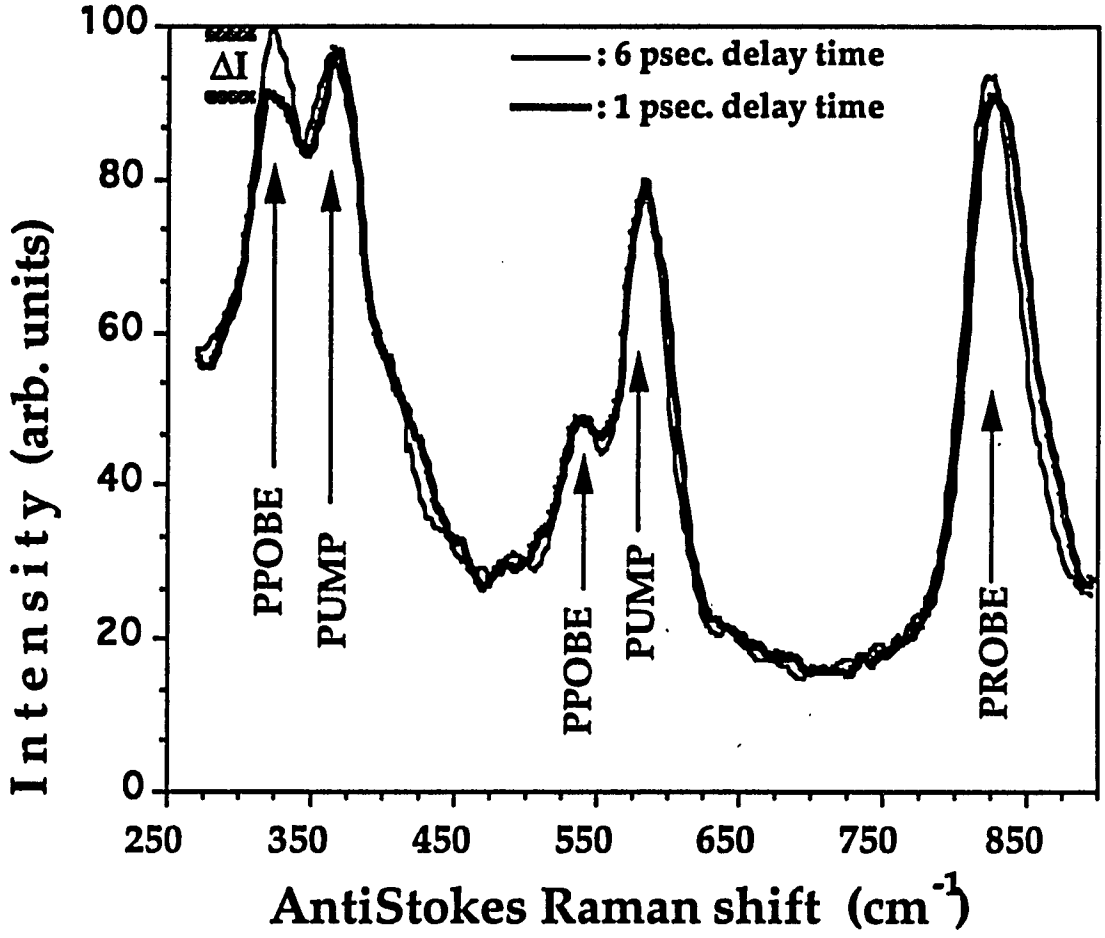

Figure 6.5: AntiStokes Raman spectrum at 1 psec (thick line) and 6 psec (thin line) pump-probe delay time in the Ppump//c, Pprobe//b and Pscatt.//b crystal axis scattering configuration. ΔI is the difference in intensity of the 335 cm^{-1} line at 1 and 6 ps delay time.

827 cm^{-1} phonon modes do not participate in the nonradiative relaxation of forsterite, at least to the degree that the 225 and 335 cm^{-1} modes participate. It also rules out the possibility that the change in the intensity of the probe beam associated Raman spectrum is due to induced transparency from the pump beam because in this case, the intensity of all modes should change.

The experiment was also performed with the sample held at liquid nitrogen temperature. At this low temperature, no Raman lines due to the pump beam were observed because the thermal population of these modes (370 cm^{-1} or higher) is very small. The absence of a reference line resulted in an enhanced experimental error in our measurements because the fluctuation of the laser beam power on the sample can not be taken into account. An additional problem was the stronger noise level due to backscattering from more optical elements in the scattered light collection path and the modified microscope objective. Data shown in fig. [6.6] , represent the integrated intensities of the 225 and 335 cm^{-1} lines at various pump-probe delay times. Although there is a significant fluctuation of the experimental data, it is clear that maximum intensity is obtained at ≈20 ps delay time. At room temperature, the maximum intensity occurs at ≈9 ps delay time. This indicates that the relaxation times at low temperature are longer compared to the relaxation at room temperature.

In order to expand our time resolved investigation into other modes, we repeated the experiment for two additional pump-probe-scattered light polarization configurations and with the sample held at room temperature. These configurations covered most of the Raman phonon modes observed in the backscattering geometry. The second configuration is $P_{pump}//c$, $P_{probe}//b$ and $P_{scatt.}//c$ axis of the crystal where the Raman lines due to the probe beam are at 370, 609, and 856 cm^{-1}. The pump and probe Raman lines

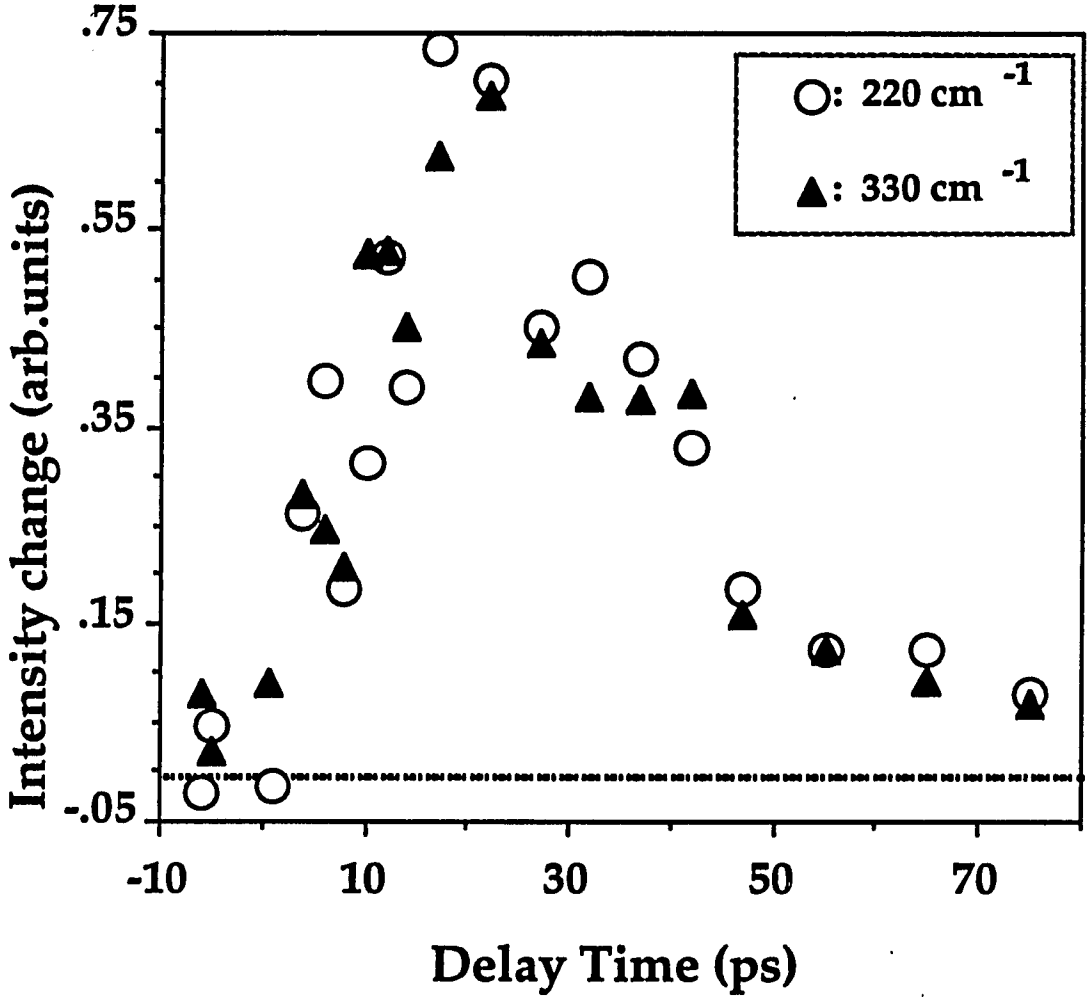

Figure 6.6: The intensity of the 225 (circles) and 335 cm^{-1} (triangles) antiStokes Raman lines as a function of the delay time at liquid nitrogen temperature.

are shown in fig. [6.7] under 590 nm, 10 ps pulsewidth laser excitation. Using this configuration ($P_{pump}//c$, $P_{probe}//b$, and $P_{scatt.}//c$) we detected changes in the intensity of the 370 cm^{-1} Raman line of the probe beam. The reference line were the overlapping 300 and 335 cm^{-1} modes (due to the spectrally broad laser pulses) arising from the pump beam. Spectra for two delay times (1 and 10 ps) is shown in fig. [6.8]. The time dependence of the ratio of the intensity of the 370 cm^{-1} over the reference Raman lines is shown in fig. [6.9]. The maximum intensity is observed at 9±1.5 ps and the population decays in 12.2±3.4 ps. The insert in fig. [6.9] was obtained by subtracting the antiStokes Raman spectra at 10 ps and 1 ps delay times. The peak is centered at ≈365 cm^{-1} and is due to the increased intensity of the 370 cm^{-1} Raman lines at 10 ps pump-probe delay time.

The third scattering configuration (see fig. [6.10]) is $P_{pump}//c$, $P_{probe}//a$, and $P_{scatt.}//a$ axis. The probe beam Raman lines to be examined are due to the 300, 502, 609, 770, 826 and 856 cm^{-1} modes. Two of these modes, the 502 and 770 cm^{-1} modes are not mentioned in table [4.3] as lattice modes although the rest of the probe beam lines are given having A_g symmetry. In addition, fig [6.10] shows that the pump beam Raman spectrum contains a peak at 745 cm^{-1} that is also not listed in table [4.3]. These three modes that are clearly observed in the Cr^{4+}-doped forsterite are not observed when the undoped or the Cr^{3+}-doped forsterite crystal is used. Therefore, we have three peaks located at 502, 745 and 770 cm^{-1} that appear only on the Cr^{4+}-doped crystal.

To understand the nature of these three modes the following experiment was performed. Using the same scattering geometry with the one used when the peaks appear ($P_{pump}//c$, $P_{probe}//a$, and $P_{scatt.}//a$ axis), the antiStokes Raman spectra were obtained for various laser wavelengths.

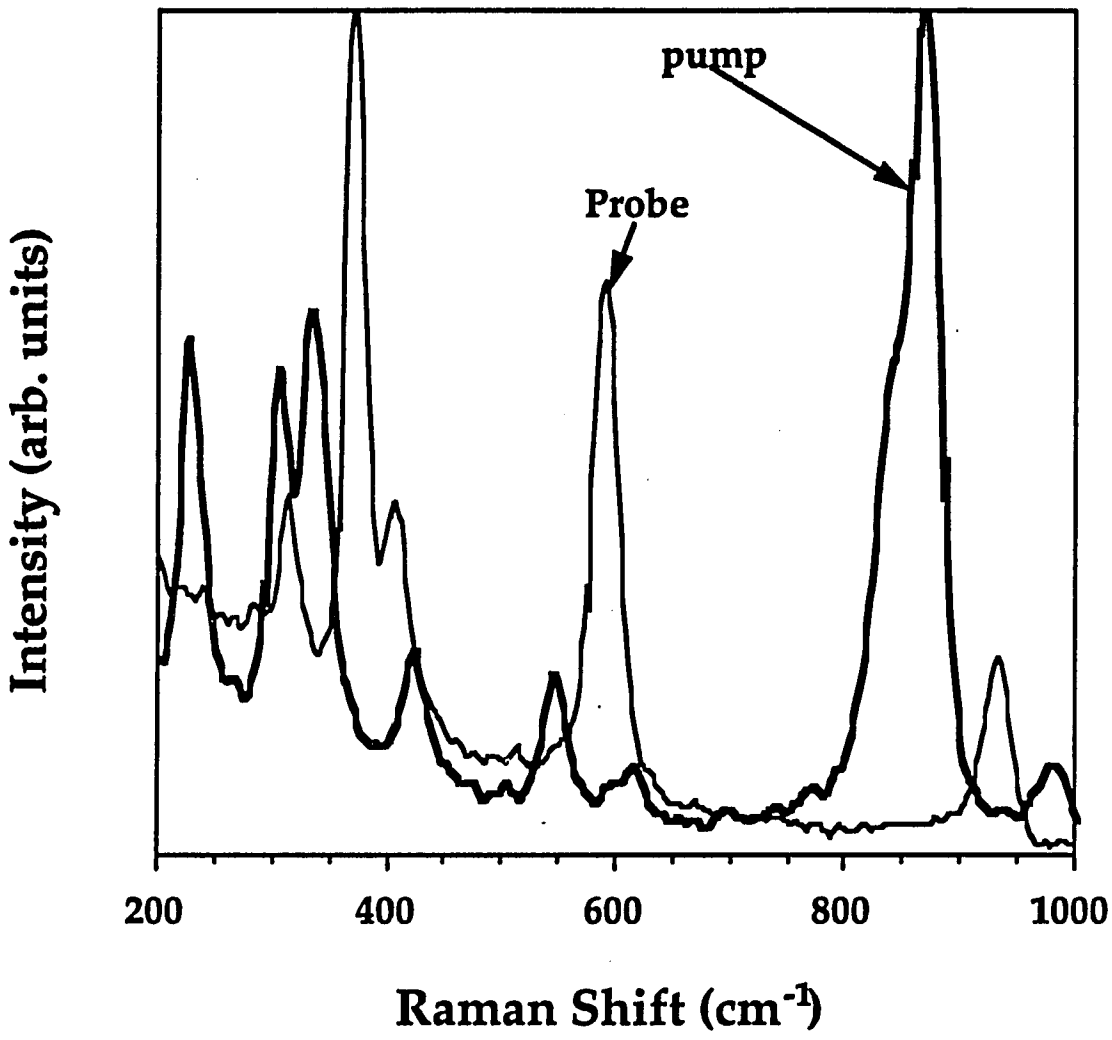

Figure 6.7: AntiStokes Raman spectrum of the pump and probe beams in the $P_{pump}//c$, $P_{probe}//b$ and $P_{scatt.}//c$ axis of the crystal scattering configuration. $\lambda_{pump}=\lambda_{probe}=590$ nm

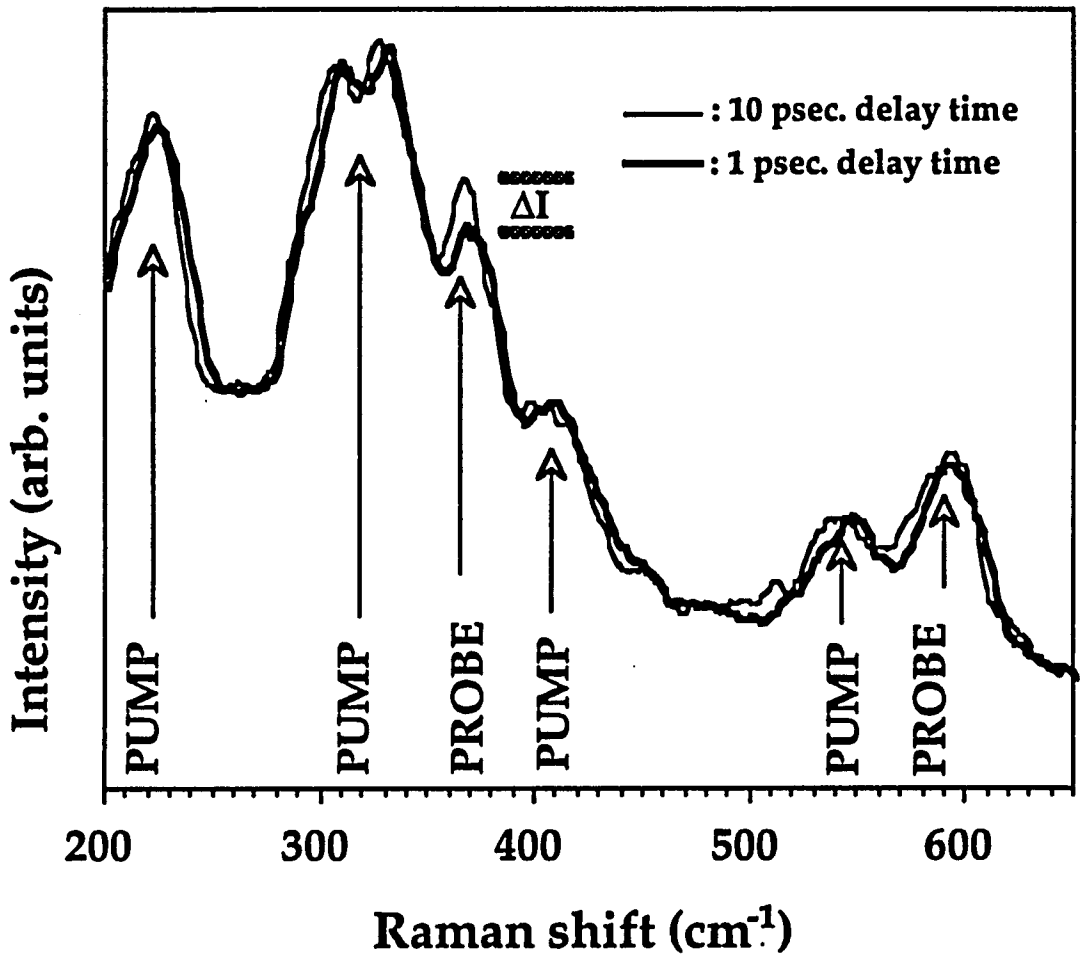

Figure 6.8: AntiStokes Raman spectrum at 1 psec (thick line) and 10 psec (thin line) pump-probe delay time in the Ppump//c, Pprobe//b and Pscatt.//c crystal axis scattering configuration. ΔI denotes the change in intensity of the 370 cm $^{-1}$line at 1 and 10 ps delay times.

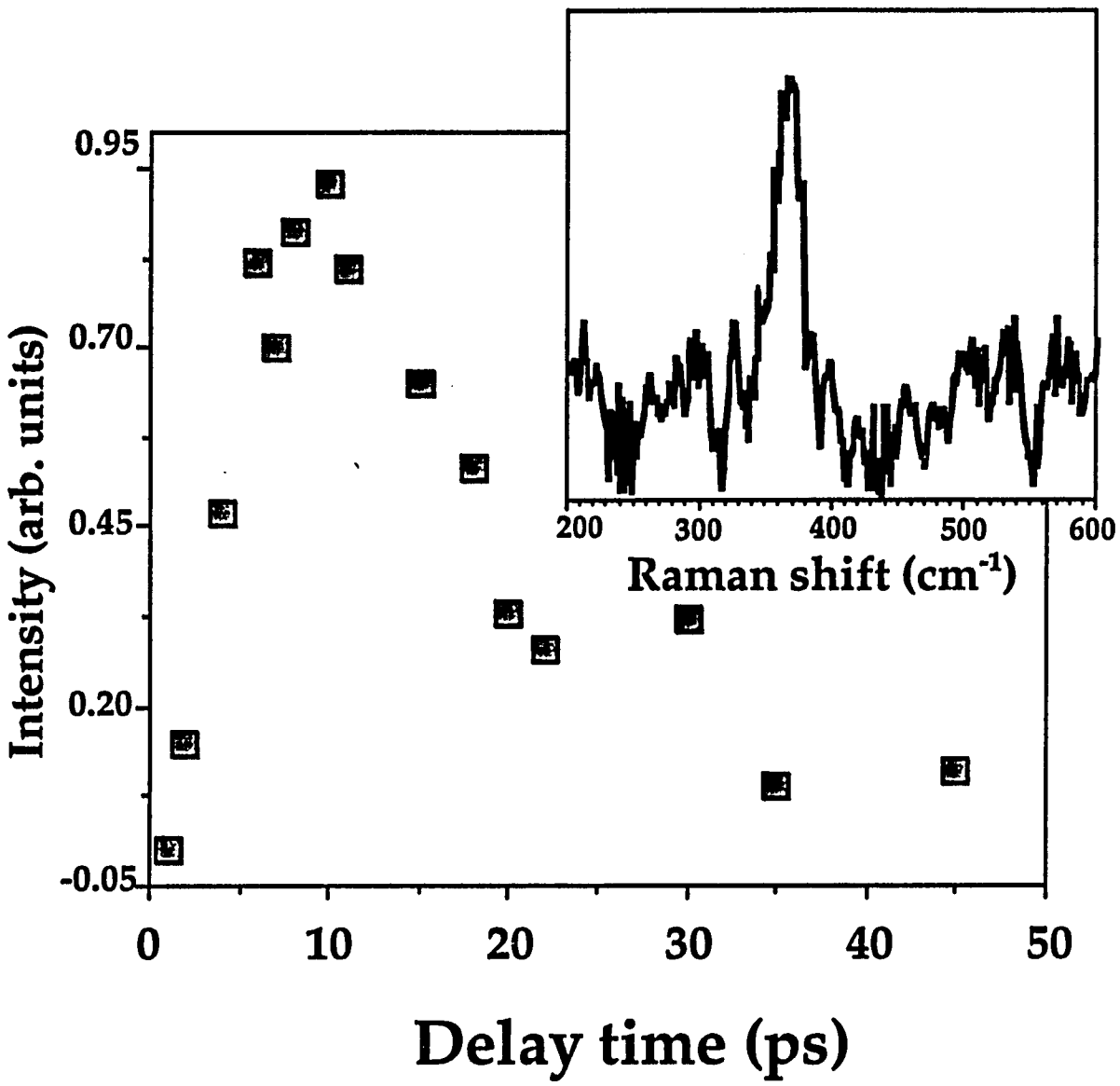

Figure 6.9: Temporal behavior of the intensity of the 370 cm^{-1} phonon modes as a function of pump-probe delay time. Insert shows the difference spectrum obtained after subtraction of the 1 ps delay time antiStokes Raman spectrum from the 10 ps spectrum.

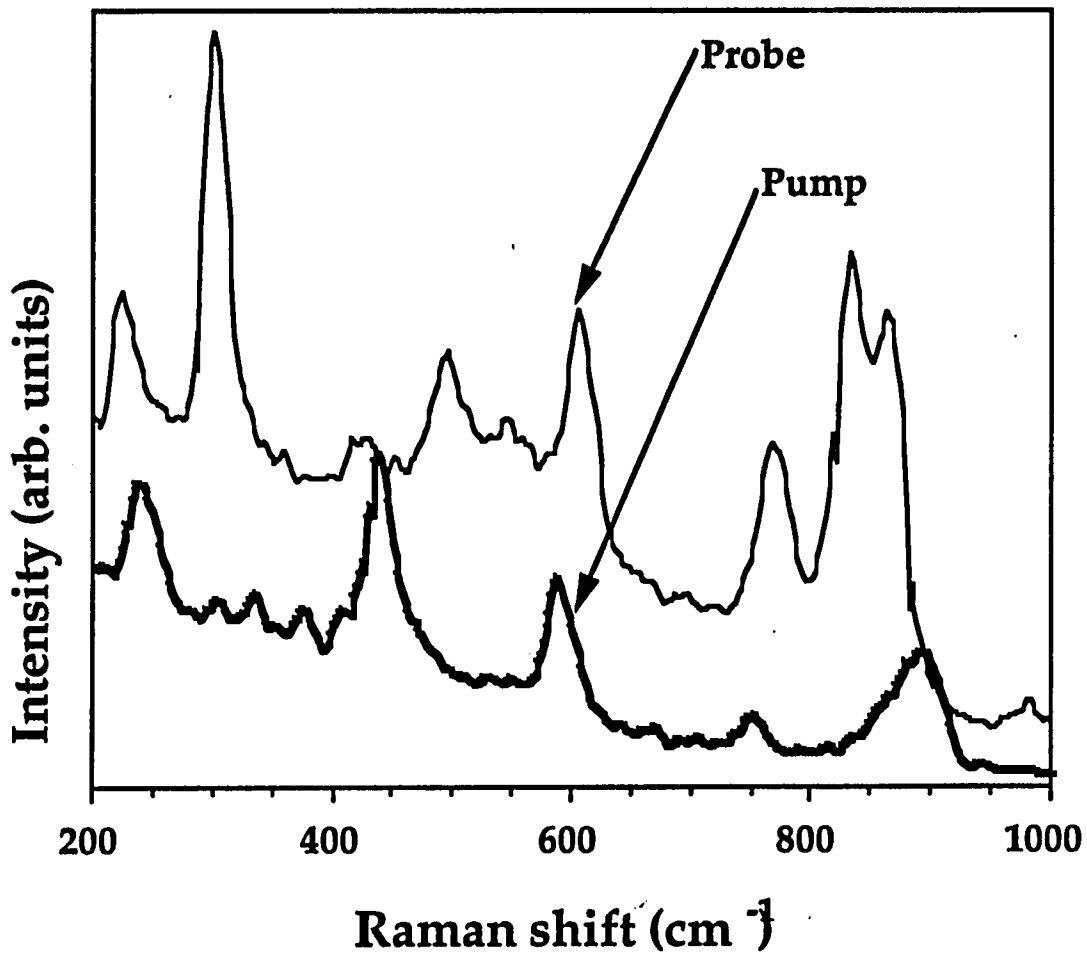

Figure 6.10: AntiStokes Raman spectrum of the pump and probe beams in the $P_{pump}//c$, $P_{probe}//a$ and $P_{scatt.}//a$ axis of the crystal scattering configuration. $\lambda_{pump}=\lambda_{probe}=590$ nm

More specifically, fig. [6.11] shows traces of antiStokes Raman spectra for 532, 575, 590, 609, 617 and 632 nm excitation wavelengths. The polarization of the laser beam and the scattered radiation is parallel to the a-axis of the crystal. The Raman lines at 856, 826, 609 and 424 cm^{-1} are lattice phonon modes and are observed in all spectra. In addition to the lattice modes, the two peaks at 502 and 770 cm^{-1} (marked with dashed lines) were observed only for certain excitation wavelengths. Similarly, antiStokes Raman spectra obtained under laser polarization parallel to the c-axis and scattered radiation polarization parallel to the a-axis for different laser wavelengths (see fig. [6.12]) show that the 745 cm^{-1} mode appears only under certain laser wavelengths.

Apparently what we see is resonantly enhanced Raman scattering from localized modes of the Cr^{4+} ions in forsterite. Fig. [6.13] shows the normalized scattering intensity of the 502 and 770 cm^{-1} local modes as a function of the scattered photon wavelength. In the same figure, the E//a excitation spectrum of Cr^{4+}-doped forsterite is shown (which is the same with the polarization of the laser beam for which the Raman spectrum contains the 502 and 770 cm^{-1} modes). We see that the resonant enhancement profile coincides with the absorption spectrum of the Cr^{4+} ions for the same incident photon polarization. In a similar way, fig [6.14] shows that the normalized scattering intensity of the 745 cm^{-1} local mode (observed when E_{pump}//c and $E_{scatt.}$//a-axis) as a function of the scattered photon wavelength has similar profile with the excitation spectrum for E//c. From the above characteristics and in accordance with the discussion in section 3.3.2 (about the Cr^{4+} vibrational modes) and section 3.3.5 (about resonant Raman scattering) we can conclude that the 502, 745 and 770 cm^{-1} modes are associated with vibration of the Cr^{4+} ions. These Cr^{4+} ions

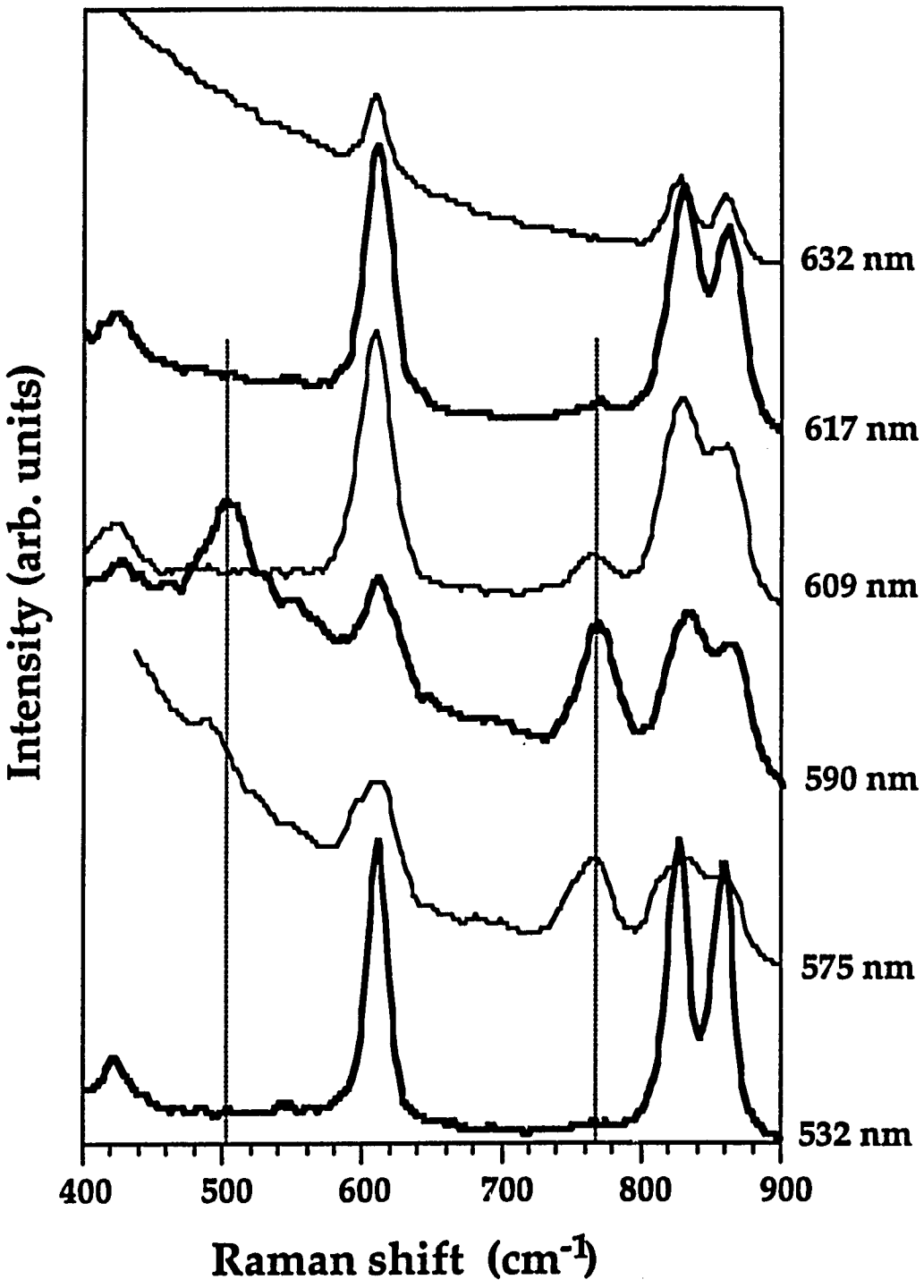

Figure 6.11: AntiStokes Raman spectra for different laser excitation wavelengths. The two local modes are located at 502 and 770 cm^{-1}. The laser polarization is E//a and the scattered light polarization P//a-axis

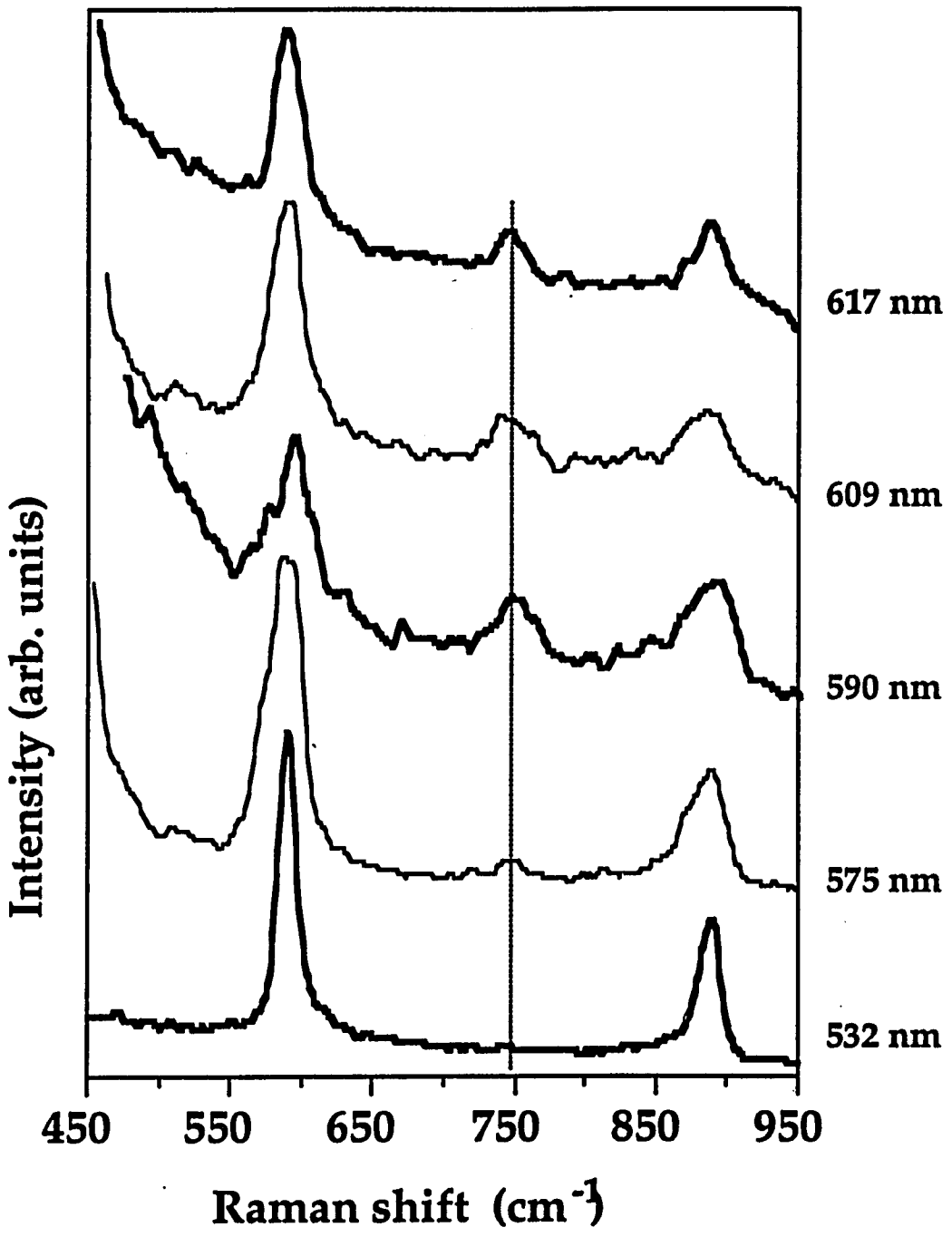

Figure 6.12. AntiStokes Raman spectra for different laser excitation wavelengths. The local mode is located at 745 cm^{-1}. The laser polarization is E//c and the scattered light polarization P//a-axis

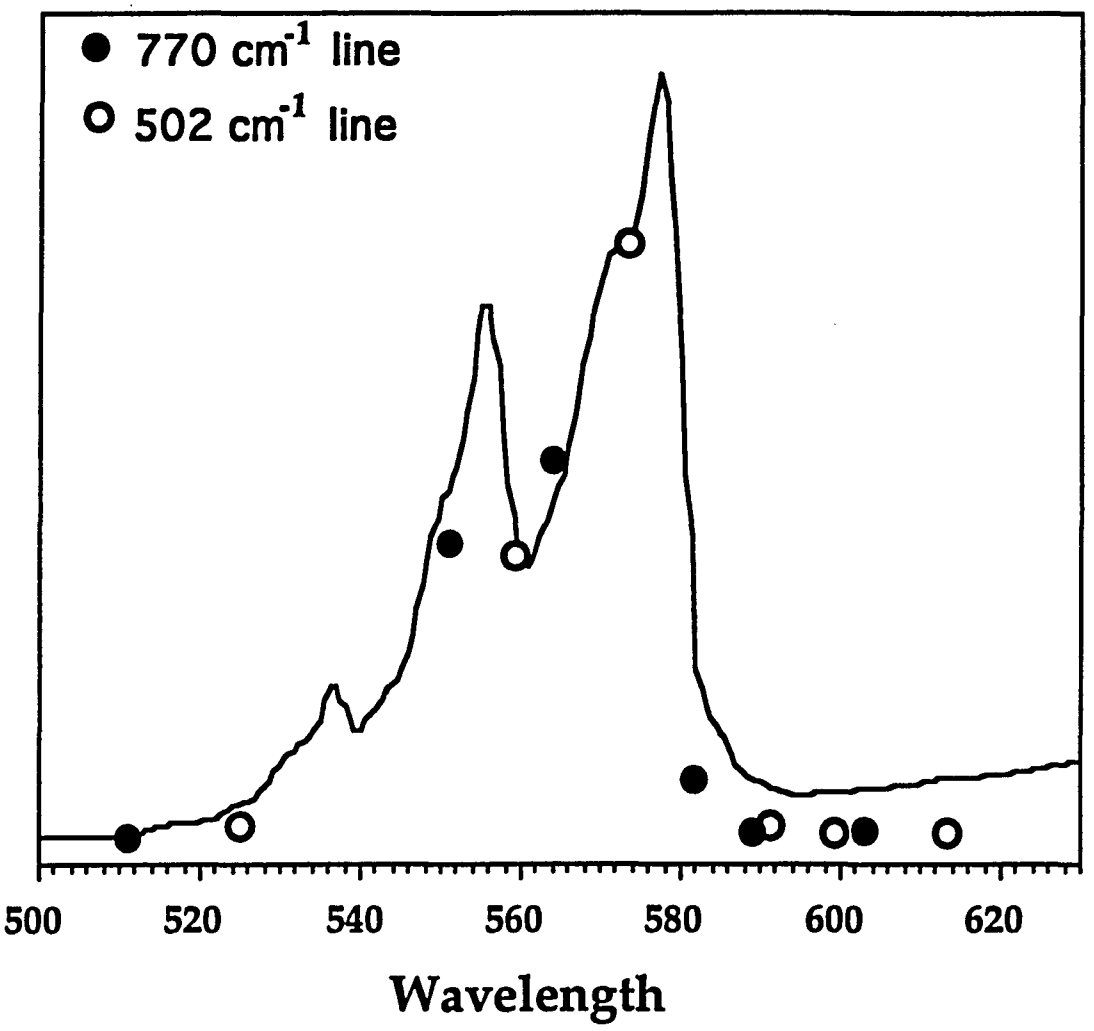

Figure 6.13: The position and the relative intensity of the 770 and 502 cm^{-1} resonant Raman lines is shown with respect to the excitation spectrum of forsterite for E//a. The incident laser beam polarization is E//a-axis.

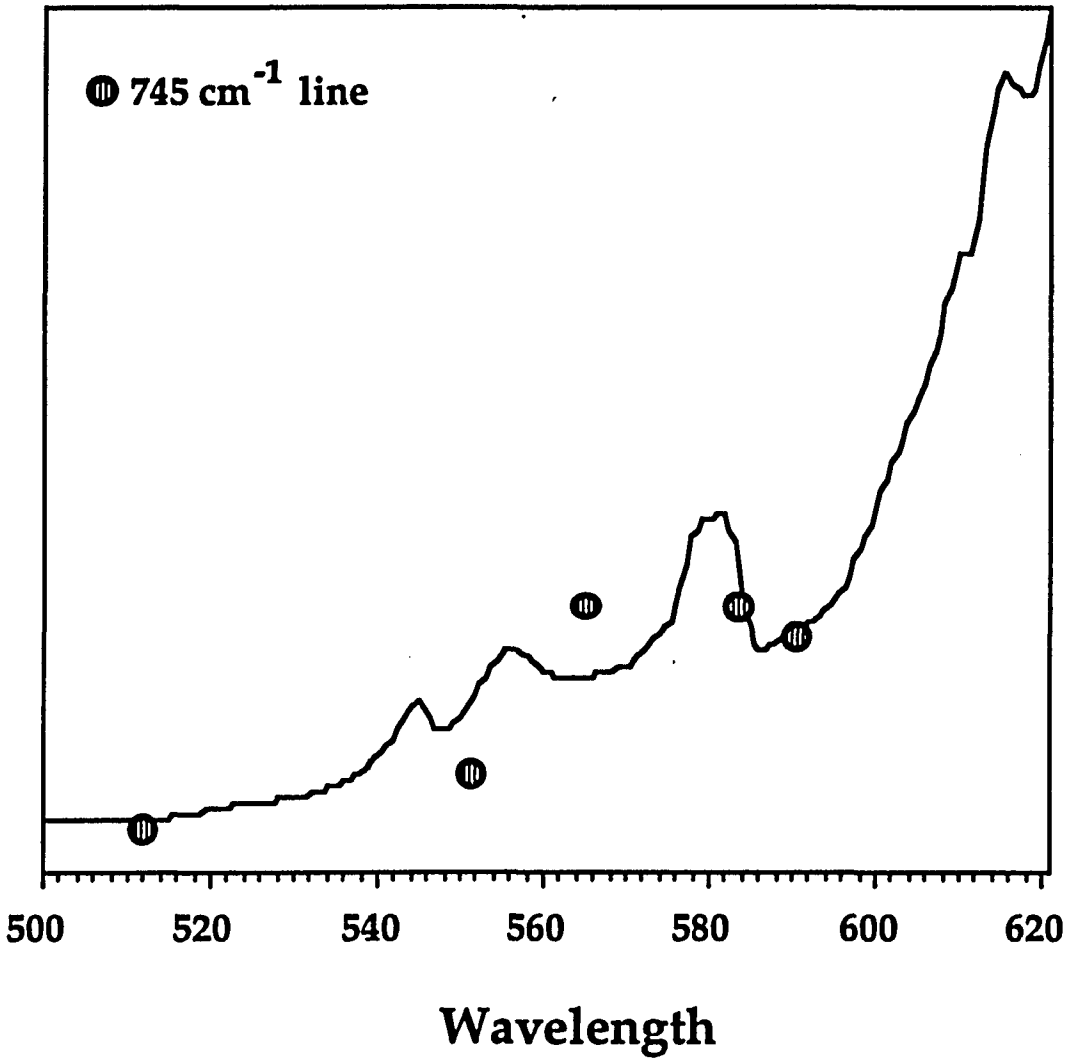

Figure 6.14: The position and the relative intensity of the 745 cm^{-1} resonant Raman line is shown with respect to the excitation spectrum of forsterite for E//c. The incident laser beam polarization is E//c-axis.

Raman scattering components are resonantly enhanced due to the absorption band which assures the resonant conditions described by eq. 3.109. Figs. [6.13] and [6.14] reveal that the resonant enhancement of the antiStokes Raman lines of the localized Cr^{4+} ion modes occurs when the scattered photon is at resonance with the absorption band (and not the incident photon). Similar resonant behavior has been reported in semiconductors.[14]

Using the third configuration ($P_{pump}//c$, $P_{probe}//a$ and $P_{scatt.}//a$-axis) in which the 502 and 770 cm^{-1} local modes are part of the probe beam spectrum, we did not observe any detectable changes in the intensity of the probe antiStokes Raman lines. In fig. [6.15] the antiStokes Raman spectra for three pump-probe delay times are shown. The two Cr^{4+}-ion associated Raman lines do not exhibit any detectable change in intensity. Fig [6.15a] shows that the two modes do not show increase in intensity in the 1 ps time scale that it could be the case if the Cr^{4+}-ion local modes have a faster rise time due to their direct coupling with the Cr^{4+} ions. On the other hand, fig. [6.15b] shows that there is no detectable change in the 10 ps time scale (as we have seen with the 225, 335 and 370 cm^{-1} modes). These measurements indicate that neither the Cr^{4+}-ion modes (502 and 770 cm^{-1}) nor the rest of the lattice modes arising from the probe beam in this configuration (300, 605, 826 and 856 cm^{-1}) participate in the nonradiative relaxation of the Cr ions in forsterite.

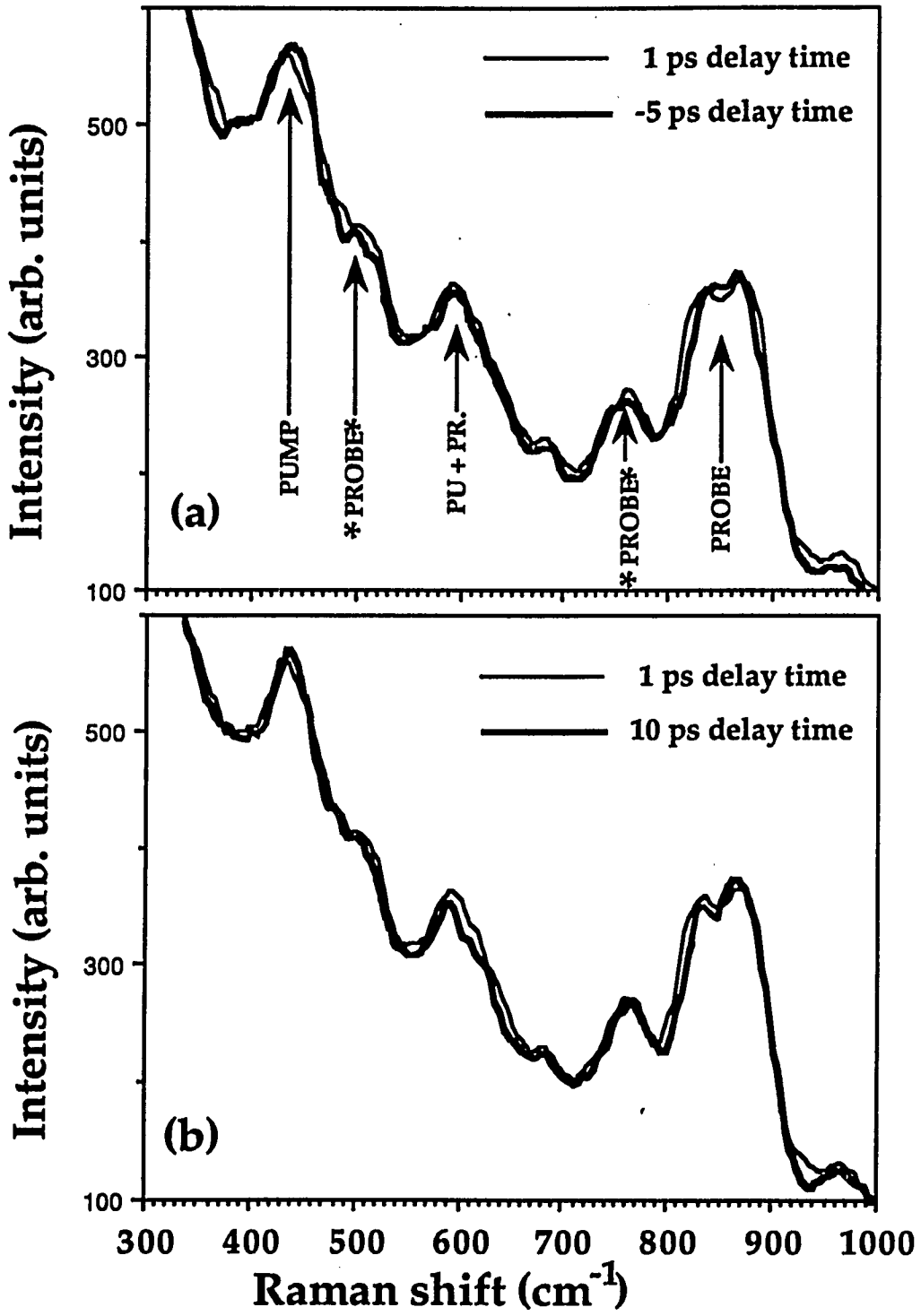

Figure 6.15: AntiStokes Raman spectrum at (a): -5 psec (thick line) and 1 psec (thin line) pump-probe delay time and (b): 10 psec (thick line) and 1 psec (thin line) pump-probe delay time in the Ppump//c, Pprobe//a and Pscatt.//a crystal axis scattering configuration. The two probe modes associated with the Cr ions are shown with an asterisk.

6.4 Modeling and rate equations.

The nonradiative relaxation process was discussed in section 3.2.5 where quantum mechanics was used to describe the transfer of energy from the hot ion into the lattice. In this section I will use rate equation analysis to describe the same process in order to obtain solvable expression that can be used to fit the experimental data and estimate the relaxation parameters.

The electron-lattice system dynamics is described using the following model. The 590 nm laser light excites the Cr ions to the $^3T_1$ electronic state at 2.1 eV above the ground state. The excited ions are sitting in an intermediate state which has a very short lifetime (t_d). This assumption is made in order to approximate the presence of the electronic bottleneck at 2.1 ± .15 eV shown in the up-converted hot luminescence spectra. Assuming t_d=0, we can always eliminate the presence of the intermediate state in our calculations. The energy released from the relaxation of this intermediate state [$dE_d/dt \approx (t_d)^{-1} V I_{pump}$] is the source of energy for the electronic system (E_e) which is transferred into the lattice system through emission of phonons (see figure on next page). Each vibrational mode participating in the nonradiative relaxation absorbs energy ($E(q_i)$) from the electronic system at a rate k_i and decays at a rate λ_i due to its finite lifetime. The nonradiative relaxation rate (k) of the electronic system (see fig. [6.16]) is the sum of the rates for energy transfer to the different participating phonon modes (k_i).

The rate equation describing the electronic system is:

$$\frac{dE_e}{dt} = -k E_e + \frac{dE_d}{dt} . \qquad (6.1)$$

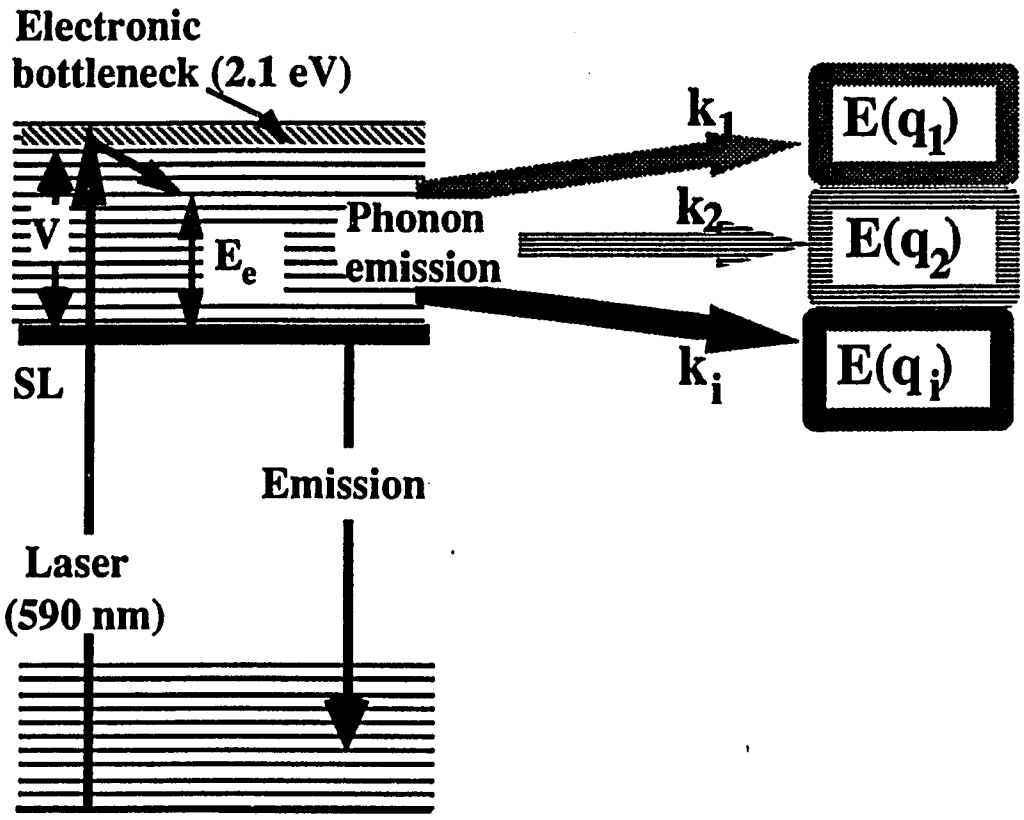

Figure 6.16: This schematic depicts the processes taken into account in the rate equation model. More details are given in the text.

The participating in the relaxation process phonon rate equation is:

$$\frac{dE(q_i)}{dt} = k_i E_e - \lambda_i E(q_i) \qquad (6.2)$$

where $E(q_i)$ is the energy of the (q_i) mode provided by the nonradiatively relaxing ion. The interaction of an isolated ion with the crystalline environment is interpreted as being due to the modulation of the crystalline electric field. As a first order approximation, rethermalization of the ion due to the increased lattice phonon population is negligible because the dominant effect in this time domain is the transfer of energy from the

hot point-like electronic system to the cold lattice environment and $E_e >> h\omega_{ph}$. In this analysis, the energy exchange between zero k-vector nonequilibrium phonons of different optical phonon modes should be insignificant and it is not taken into account. The energy exchange between the observed zero k-vector phonons and phonons of other modes or within the same mode but different k-vector will affect only the lifetime of the observed phonon population. Since $E(q_{i)} = N(q_i)h\omega_i$ the phonon population in turn is described by:

$$\frac{dN(q_i)}{dt} = \frac{k_i E_e}{h\omega_i} - \lambda_i N(q_i). \qquad (6.3)$$

The nonradiative relaxation time (k^{-1}), the phonon lifetime (λ_i^{-1}) and the lifetime of the electronic bottleneck (t_d) can be estimated from numerical fitting of eqs. 6.1 and 6.3 to the experimental phonon dynamics data.

The shape of the curves is determined by the nonradiative relaxation rate k, the intermediate state lifetime t_d, and the phonon lifetime λ_i^{-1}. The first two (k and t_d) should be the same for all participating modes since they describe the relaxation of the electronic system; and therefore, the phonon lifetime is the only independent parameter. The energy transfer rate k_i from the electronic system to a participating mode will affect the generated nonequilibrium phonon population of this mode and not the temporal behavior. The rise portion of the curve is greatly influenced by the relaxation characteristics of the electronic system (k^{-1} and t_d) while the behavior of the decaying part is dictated by the phonon lifetime (λ_i^{-1}). This behavior is depicted in fig. [6.17]. Fig. [6.17a] shows the dynamics of the nonequilibrium phonon population when the nonradiative relaxation time and the phonon lifetime are kept constant (k^{-1}=6 and λ_i^{-1}=15 ps) while the

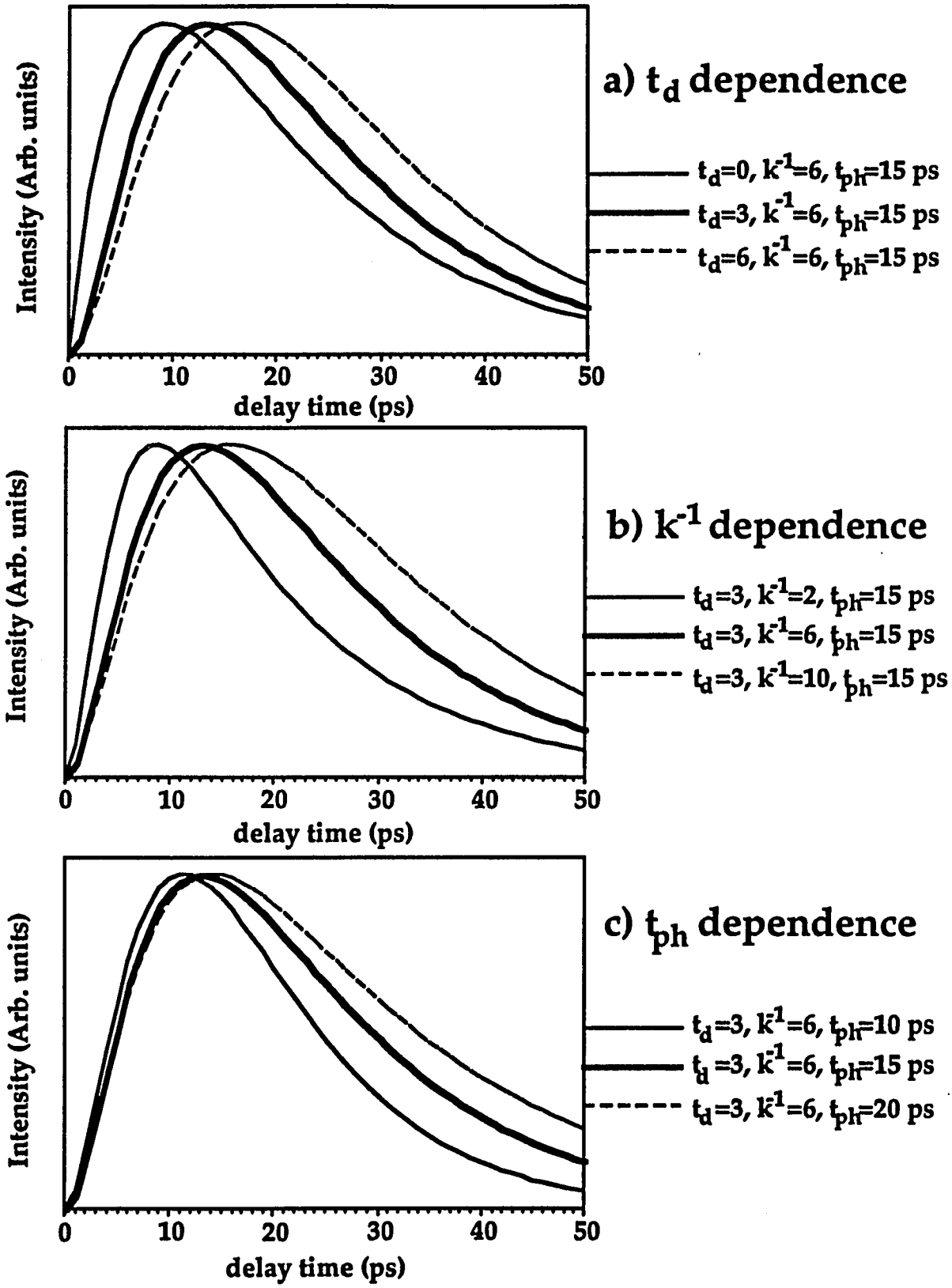

Figure 6.17: The dependence of the relaxation dynamics of the nonequilibrium phonon population on the a) lifetime of the intermediate state (bottleneck), b) nonradiative relaxation time and c) phonon lifetime. The model is described in the text and eqs. 1 and 3.

intermediate state lifetime (t_d =0, 3 and 6 ps) is the variable parameter. We see that when t_d=0, the rise portion of the curve is sharp while for increasing t_d the rise time becomes longer and the curve for small delay times ($\Delta\tau < t_d$) acquires parabolic shape. The peak position of the curve for different values of t_d is shifting as it is expected since the relaxation of the electronic system is delayed. The decay portion of the curve is almost identical and independent of relatively small changes of t_d. When the nonradiative relaxation time (k^{-1}) is the independent parameter (see fig. [6.17b] where t_d=3, $\lambda_i^{-1}=t_{ph}$=15 and k^{-1}=2, 6 and 10 ps), the early and the later parts of the curves do not change very much. However, varying the nonradiative relaxation time, the position of maximum intensity changes while the peak portion of the profile becomes wider for longer k^{-1}. When the phonon lifetime is the independent parameter, we see in fig. [6.17c] that the rise portion of the curve remains almost unchanged for different phonon lifetimes (t_d=3, k^{-1}=6 and t_{ph}=10, 15 and 20 ps) while the decay part is very different. In addition, for longer phonon lifetime the curve reaches maximum intensity at longer delay time. I have discussed in a previous section (see eq. 3.91) that the change on the average phonon occupation number of the phonon modes participating in the nonradiative relaxation result in a stronger antiStokes Raman scattering of these modes. The intensity of the antiStokes lines have linear dependence on the phonon occupation number and therefore, the profile of the chance of the intensity of the Raman lines is identical to the profile of the effective phonon occupation number. The rate eqs. 6.1 and 6.3 which describe the generated nonequilibrium phonon population were used to fit the experimentally obtained profiles of the change of the antiStokes Raman lines and estimate the nonradiative relaxation parameters.

Fitting of the experimental data for the 225 and 335 cm^{-1} modes at room temperature using eqs. 6.1 and 6.3 is displayed in fig. [6.18]. Curves from this model shown in figs. [6.18a] and [6.18b] with a thick line describe the data points very well. Using nonlinear least squares fitting, the estimated relaxation parameters are t_d=3±1.6 ps lifetime for the initially populated intermediate state, k^{-1}=2.8±1.6 ps for the nonradiative relaxation time, and the phonon lifetimes are λ^{-1}_{225} =15.7±2.8 ps and λ^{-1}_{335} =10.4±2.8 ps for the 225 cm^{-1} mode and the 335 cm^{-1} mode, respectively. The different lifetimes of the two modes explain the different formation times of the nonequilibrium phonon populations. The mode with the longer lifetime will reach the maximum population at a later time than the mode with the shorter lifetime. When no intermediate state is taken in to account (t_d=0), the parameters for the best fit (shown in figs. [6.18a] and [6.18b] with thin line) are k^{-1}=8.5 ± 1.6 ps for the nonradiative relaxation time, λ^{-1}_{225} =13.7 ± 2.8 ps and λ^{-1}_{335} =9.7 ± 2.8 ps. In the early part of the temporal profile the data points are below the fitting curve while in the maximum position the data points are above the curve. We could have achieved a better fitting of the experimental data using the simple dual relaxation model (t_d=0) by shifting the "zero" delay time by ≈2 ps. This shift is unrealistic since our zero delay time is known to within ± 150 fs. This suggests that the model we have used assuming the intermediate state just below the excitation level that delays the nonradiative relaxation by few ps is closer to the reality. Another possibility is that the observed modes do not participate in the early part of the nonradiative relaxation due to different selection rules at different parts of the electronic excited state.

The experimental data when the sample was held at liquid nitrogen temperature show a slower nonradiative relaxation. The fitting shown in

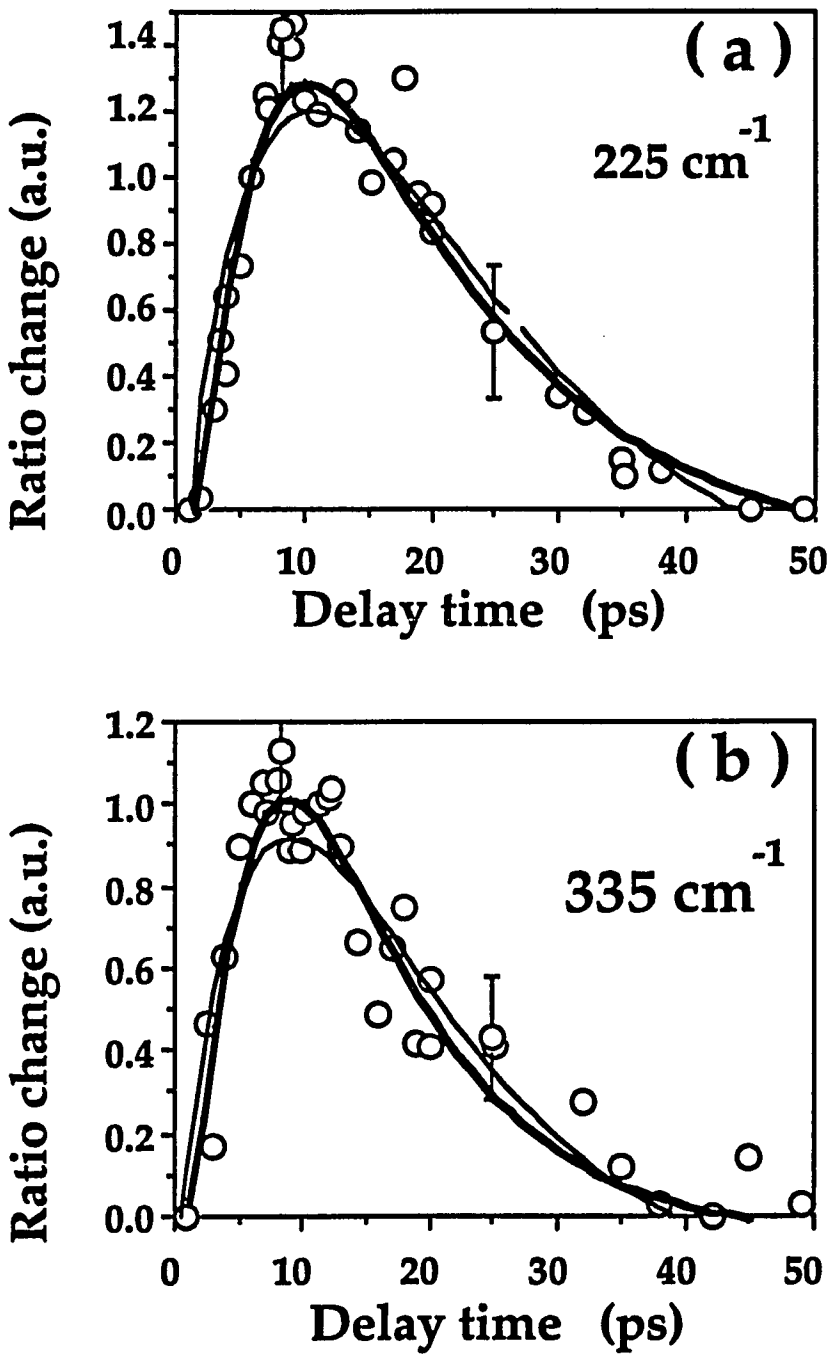

Figure 6.18: Fitting of the room temperature experimental data of the 225 and 335 cm^{-1} phonon modes. The thick line represents the best fit when an initially populated intermediate state is involved. The thin line is the best fit without the assumption of the intermediate state.

fig. [6.19] with thick line was obtained using eqs. 6.1 and 6.3. The fitting parameters are t_d=5±3.1 ps lifetime for the initially populated intermediate state, k^{-1}=8±3.1 ps for the nonradiative relaxation time, and the phonon lifetimes are λ^{-1}_{phonon} =22±4.9 ps. The thin line in fig. [5.16] represents the best fitting using the no intermediate state approximation (t_d=0). For this case, the relaxation parameters are k^{-1}=15±2.9 ps and λ^{-1}_{phonon} =20±4.6 ps. Due to the fluctuation of the data, the experimental error on the estimated parameters is large. However, there is no question that all relaxation parameters are longer at low temperatures.

Fig. [6.20] shows best fitting of the experimentally measured change of the intensity of the 370 cm^{-1} Raman line as a function of the delay time. Using eqs. 5.1 and 5.3, best fit is shown with thick line and the estimated parameters are: intermediate state lifetime t_d=3±1.7 ps, nonradiative relaxation time k^{-1}=2.8±1.7 ps and the phonon mode lifetime λ^{-1}_{370} =12.1±3.1 ps. When we used the dual relaxation model (t_d=0), the estimated nonradiative relaxation time k^{-1}=8.5±1.8 ps and the phonon lifetime λ^{-1}_{370} =11.6±3.2 ps. Best fit for this model is shown in fig. [6.20] as the thin line curve. From the two fitting curves of the intensity change of the 370 cm^{-1} line, the thin line explains the date reasonably well while the thick line fits the data exceptionally well indicating the advantage of the model we have adapted.

The estimated relaxation parameters for the three modes participating in the nonradiative relaxation are summarized in table 6.1. From the fitting to the experimental data using the rate eqs 6.1 and 6.3, it appears that the best fitting is obtained using the model that includes the presence of the electronic bottleneck immediately after excitation (thick curve in figs. [6.18], [6.19] and [6.20]).

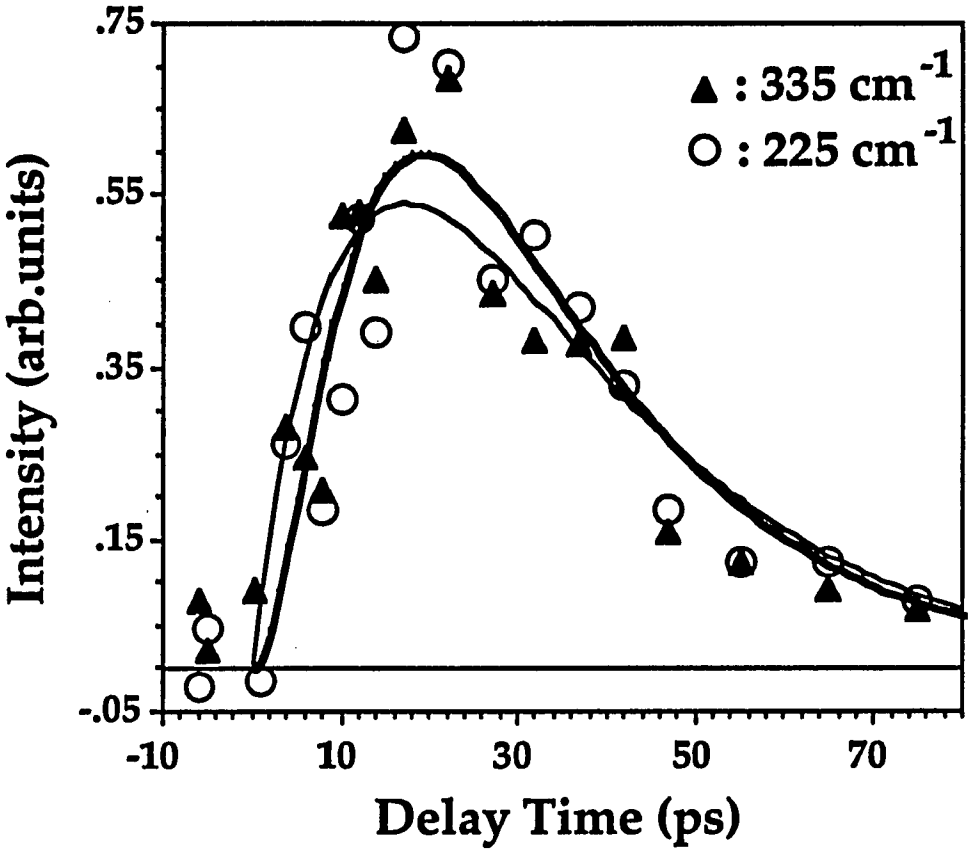

Figure 6.19: Best fit of the liquid nitrogen temperature experimental data of the 225 (circles) and 335 cm^{-1} (triangles) antiStokes Raman lines as a function of the delay time. The thick line is obtained assuming the presence of the intermediate state (td=5ps) while the thin line is the best fit when no intermediate state is taken into account (td=0).

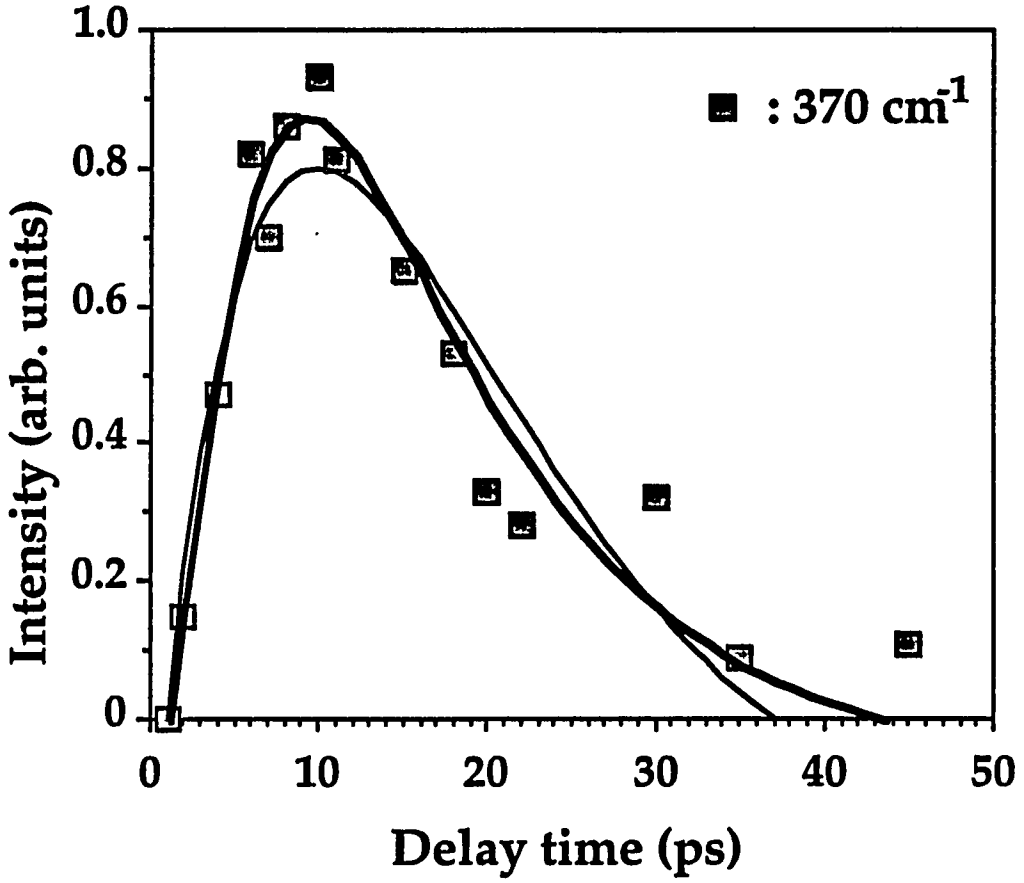

Figure 6.20: The fitting curves of the time resolved intensity dependence of the 370 cm^{-1} Raman mode. The thick line was obtained using eqs. 1 and 3 and the thin line using td=0.

Phonon mode / Temperature	Estimated relaxation parameters assuming the bottleneck (intermediate state) at 2.1 eV	Estimated relaxation parameters assuming no intermediate state at 2.1 eV (t_d=0)
225 cm^{-1} / T=293 K	t_d = 3 ± 1.6 ps k^{-1} = 2.8 ± 1.6 ps t_{phonon} = 15.7 ± 2.8 ps	k^{-1} = 8.5 ± 1.6 ps t_{phonon} = 13.7 ± 2.8 ps
225 cm^{-1} / T=80 K	t_d = 5 ± 3.1 ps k^{-1} = 8 ± 3.1 ps t_{phonon} = 22 ± 4.9 ps	k^{-1} = 15 ± 2.9 ps t_{phonon} = 20 ± 4.6 ps
335 cm^{-1} / T=293 K	t_d = 3 ± 1.6 ps k^{-1} = 2.8 ± 1.6 ps t_{phonon} = 10.4 ± 2.8 ps	k^{-1} = 8.5 ± 1.6 ps t_{phonon} = 9.7 ± 2.8 ps
335 cm^{-1} / T=80 K	t_d = 5 ± 3.1 ps k^{-1} = 8 ± 3.1 ps t_{phonon} = 22 ± 4.9 ps	k^{-1} = 15 ± 2.9 ps t_{phonon} = 20 ± 4.6 ps
370 cm^{-1} / T=293 K	t_d = 3 ± 1.6 ps k^{-1} = 2.8 ± 1.6 ps t_{phonon} = 12.1 ± 3.1 ps	k^{-1} = 8.5 ± 1.6 ps t_{phonon} = 11.6 ± 3.2 ps

Table 6.1: The nonradiative relaxation parameters estimated using the rate equations 1 and 3 and the experimental data of the intensity ratio of the 225, 335 and 370 cm^{-1} antiStokes phonon lines. t_d: lifetime of the initially populated intermediate state (bottleneck at 2.1 eV), k^{-1}: nonradiative relaxation time of the electronic system (k: rate for energy transfer from the ion into the lattice), t_{phonon}: lifetime of the nonequilibrium phonon.

6.5 Discussion.

In the difference spectra (inserts in figs. [6.4] and [6.8]), the peaks are slightly shifted with respect to peaks observed in the antiStokes Raman spectra. More specifically, in fig. [6.4] the peaks are located at ≈218 and ≈330 cm^{-1} instead of 225 and 335 cm^{-1} respectively. In fig. [6.8] the peak in the difference spectrum is at ≈365 cm^{-1} instead of 370 cm^{-1}. This displacement of the nonequilibrium phonon modes towards lower frequencies can be explained in terms of the discussion in section 3.3.2. The Cr^{4+} ions in forsterite are substituting Si in tetrahedrally coordinated sites. The Cr ions are heavier than the Si ions that they replace. Therefore, vibration of the lattice involving the heavier impurity center posses a lower vibrational frequency than the equivalent pure lattice vibrations. The phonons generated during the transfer of energy from the Cr ions are coupled to the Cr ions and their frequency is lowered with respect to the thermal lattice modes.

The three Cr^{4+}-ion associated modes (502, 745 and 770 cm^{-1}) are very different from any of the Raman active lattice modes. The high energy of these modes indicates that they are internal modes of the -(CrO_4) tetrahedron. Because the internal modes of forsterite involve vibrations of the Si ion with the four oxygen ions, replacing a Si ion that has atomic weight of 28 with a Cr ion that has atomic weight of 52 will produce a much heavier unit which has significantly lower modes of vibration. Since all observed local modes posses A_g symmetry, it is possible that the 745 and 770 cm^{-1} Cr^{4+}-modes are deduced from the "strong" lattice modes of the same symmetry (see table 4.3) at 826 or 856 cm^{-1} while the 502 cm^{-1} Cr^{4+}-mode is deduced from the 609 cm^{-1} lattice mode.

The ion responsible for lasing action in forsterite is the tetravalent chromium ion. The Cr^{4+} ions replace Si in the Mg_2SiO_4 host in tetrahedrally coordinated sites. The 225 cm^{-1} mode is a translational mode of the -SiO_4 tetrahedral. The 335 cm^{-1} mode consists of two modes ≈10 cm^{-1} apart which are not spectrally resolvable due to the wide spectral width of our laser; one mode is a rotational mode of the -SiO_4 tetrahedral while the other is a translational mode of Mg ions. Both modes have A_g symmetry. The 370 cm^{-1} mode that is also active is a rotational mode of the -SiO_4 tetrahedral having B_{2g} symmetry. On the other hand, the inactive modes are internal modes of the -SiO_4 as well as lattice modes of A_g or B_{2g} symmetry . This suggests that symmetry is not a dominated factor in governing which phonon modes participate in the nonradiative decay.

These experiments definitely shows that more than one phonon mode is involved in the nonradiative relaxation processes of the photoexcited Cr ion in a forsterite crystal. Moreover, the behavior of the three observed active phonon modes is similar. If the similar temporal behavior of the participating modes in the nonradiative processes in ionic crystals is a common characteristic, the widely used one phonon model will not lead to very different results. A phonon with a frequency which is the average over the active modes involved in the nonradiative decay will also have the same temporal behavior and probably, this is why the one phonon model is successful in many cases.

From the change in intensity of the 335 cm^{-1} and 225 cm^{-1} anti-Stokes Raman lines we can obtain an approximate value of the ratio of energy transferred to these two modes. The increase of the anti-Stokes Raman signal is proportional to the increase of the effective phonon occupation

number ($\Delta N(q_i)$). The ratio of the Raman line intensities at the maximum and minimum position of the temporal profile becomes:

$$\frac{I(q_i)_{max}}{I(q_i)_{min}} \approx \frac{N(q_i)+\Delta N(q_i)}{N(q_i)} \quad \text{or} \quad \frac{\Delta N(q_i)}{N(q_i)} \approx \frac{I(q_i)_{max} - I(q_i)_{min}}{I(q_i)_{min}} \tag{6.4}$$

where $N(q_i)$ is the thermal phonon occupation number of the (q_i) mode at room temperature and $I(q_i)_{max}$ ($I(q_i)_{min}$) the maximum (minimum) intensity of the anti-Stokes Raman line of the probe beam. From eq. 6.4 we obtain:

$$\frac{\Delta N(q_{225})}{\Delta N(q_{335})} \approx 2.4 \quad \text{or} \quad \frac{h\omega_{225}\,\Delta N(q_{225})}{h\omega_{335}\,\Delta N(q_{335})} \approx 1.6 \tag{6.5}$$

The later is the ratio of the energy that is transferred into the two participating modes. It follows that the relation between the energy transfer rates from the electronic system is approximately $k_{225} \approx 1.6\ k_{335}$. This method cannot be used for the case of the 370 cm^{-1} mode because the pump over the probe beam power was 1/1 instead of 1/3 used for the 225 and 335 cm^{-1} modes. However, the change of the intensity of the 370 cm^{-1} mode is slightly smaller than the change of the 335 cm^{-1} mode. If we take into account that the pump beam is more intense in the case of the 370 cm^{-1} mode and that the same $\Delta N(q)$ for both modes cause a larger increase in the intensity of the 370 cm^{-1} mode (due to the smaller thermal occupation number), we can conclude that the 370 cm^{-1} phonons emitted are at most as many as the 335 cm^{-1} phonons. All the above discussion is valid under the condition that the resonant enhancement of the antiStokes signal from the nonequilibrium phonons is the same in all modes.

The estimated phonon lifetimes of the 225 and 335 cm^{-1} phonon modes show that at liquid nitrogen the lifetime of the generated phonons is longer that at room temperature as it was expected. The optical phonons are splitting in lower energy phonons due to the anharmonic interactions within the lattice. Theoretical considerations,[15] Raman phonon mode linewidth measurements[16,17] and time resolved experiments[2,4] have shown that the phonon lifetimes are longer at lower temperatures. The theoretical expression for the phonon lifetime as a function of temperature under the assumption that the initial phonon splits into two lower energy phonons is given by eq. 3.38. The ratio of the phonon lifetimes at room temperature and liquid nitrogen temperatures leads to

$$\frac{\tau(T=78\ K)}{\tau(T=292\ K)} = \frac{\left(1+n_1(T=292\ K)+n_2(T=292\ K)\right)}{\left(1+n_1(T=78\ K)+n_2(T=78\ K)\right)} \qquad (6.6)$$

where $n_1(T)$ and $n_2(T)$ are the occupation number of the emitted lower-in-energy phonons and are given by:

$$n_i(T) = \left[\exp\left(\frac{h\omega_{phonon}}{k_B T_{eff.}}\right) - 1\right]^{-1} \qquad (6.7)$$

Fig. [6.21] shows the ratio of the phonon lifetimes given by eq. 6.6 for the 225 and 335 cm^{-1} (figs. [6.21a] and [6.21b] respectively) as a function of the energy of the emitted phonon ω_1. The energy of the second phonon is $\omega_2=\omega_{initial}-\omega_1$. The estimated phonon lifetimes from our experimental data are given in Table 6.1. For the 225 cm^{-1} mode we estimate a ratio of 1.40 when the electronic bottleneck (intermediate state) is taken into account and 1.46 when we use the dual relaxation model (t_d=0). For the 335 cm-1 mode the estimated ratio is 2.11 and 2.06 for the two relaxation models. The estimated values from the first model are shown in fig. [6.21] with a thick

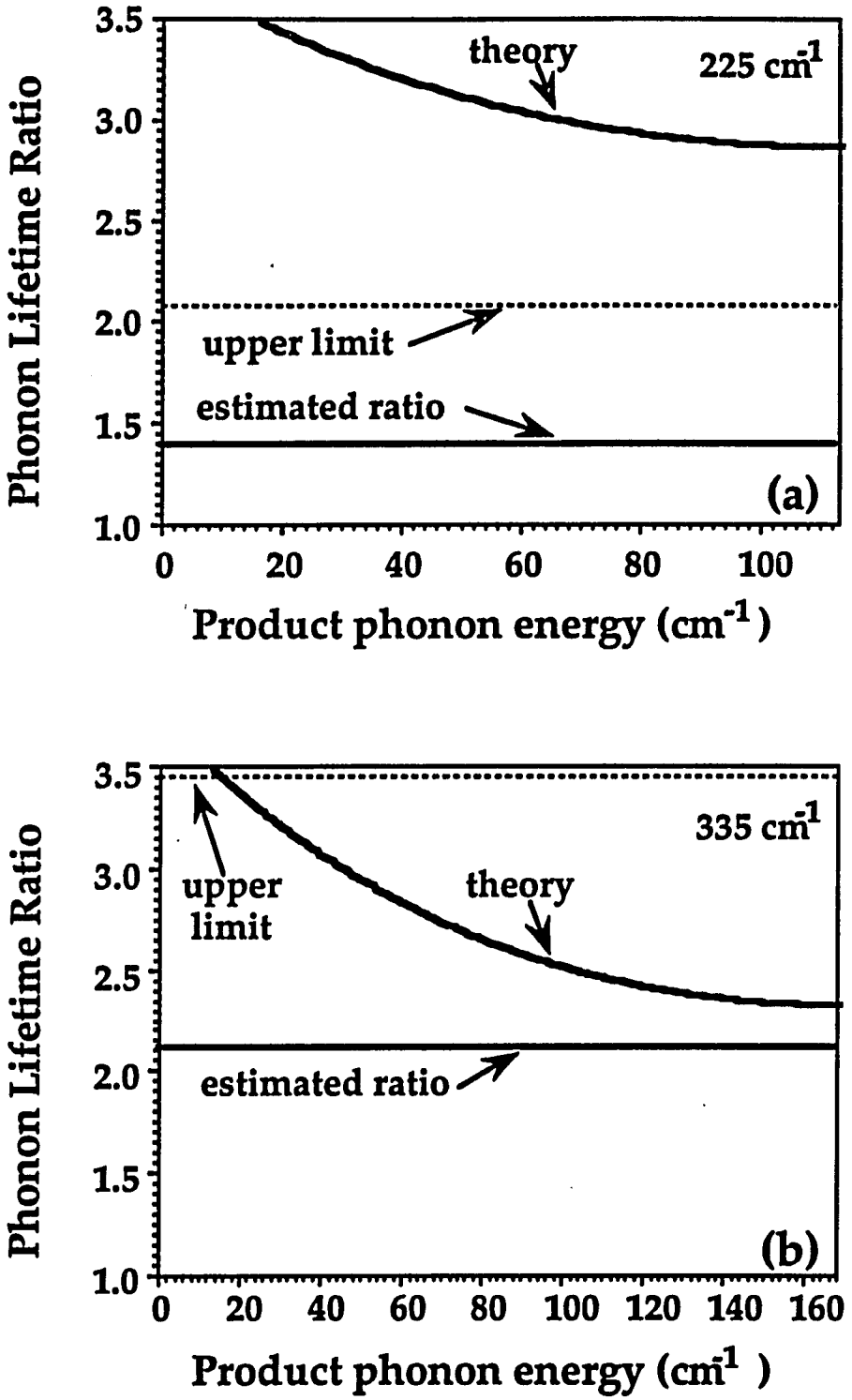

Figure 6.21: The ratio of the phonon lifetimes at liquid nitrogen and room temperature as a function of product phonon energy for (a) the 225 and (b) the 335 cm^{-1} modes. The curve represent the theoretically expected value under the assumption that the initial phonon breaks into two product phonons. The thick line is the experimentally estimated ratio while the broken line is the upper limit introduced by the experimental error in the estimation of the phonon lifetimes.

line while with broken line is the upper limit of ratio introduced by the experimental error in the estimation of the phonon lifetimes.

I would expect the thick line (experimentally estimated value) to cross the theoretical curve and from the crossing point to be able to estimate the frequencies of the phonons emitted from the breakdown of the 225 or 335 cm^{-1} nonequilibrium phonons. However, the estimated values from the experimental data are lower than the expected value from the theoretical expression especially for the 225 cm^{-1} mode, where the divergence is large and even the upper limit is far from the lowest expected value. A possible explanation for this disagreement between the theory and the experimental emerges if we consider the "heating" of the nonequilibrium phonon modes following the excitation of the impurity ion.

The temperature dependence of the phonon occupation number (eq. 6.7) assumes thermal equilibrium and that the temperature of the phonon mode is the same with the lattice temperature. But this is not the case for the phonons associated with the relaxation of the impurity ion in a crystal. A large amount of energy is dissipating from the ion into the surrounding lattice by the emission of nonequilibrium phonons in addition to the already existing thermal phonons and subsequently, the effective temperature of the participating phonon modes increases. When the 225 and 335 cm^{-1} phonons split into two new phonons, the temperature of the resulted phonon modes increases. The effective temperature of each phonon mode is different because it depends on the number of phonons emitted and on the frequency of the phonon mode. All this is happening in the immediate neighborhood of the excited ion picoseconds after photoexcitation. As more phonons of certain type are emitted the effective

temperature of this mode becomes higher. That makes the relative difference of the effective temperatures when the experiment is performed at room and liquid nitrogen temperature smaller that the relative difference of the lattice temperature. As the relative difference in temperature becomes smaller, the curves obtained by eq. 6.6 and shown in fig. [6.21] slide to lower values (the limit is 1 when the temperatures become the same). Therefore, what we experimentally measure is the result when we replace the T=292 and T=78 K in eq. 6.6 with the effective phonon mode temperatures and the resulting value will be smaller than what we estimated previously. This model also explains why the estimated values for the 225 cm^{-1} mode diverge with the experimentally observed value much more than the estimated and measured values for the 335 cm^{-1} mode. From eq. 6.5 we see that for every 335 cm^{-1} phonon emitted, there are 2.4 phonons of the 225 cm^{-1} mode emitted. This means that overall there are more 225 cm^{-1} phonons generated during the nonradiative relaxation of the Cr^{4+} ions than 335 cm^{-1} phonons. When these nonequilibrium phonons split into lower-in-energy phonons, there are more phonons of the type emitted from the breakdown of the 225 cm^{-1} nonequilibrium phonons than the type of phonons due to the breakdown of the 335 cm^{-1} phonons. The presence of more phonons of the type produced from the splitting of the 225 cm^{-1} phonons raises their effective temperature more than the effective temperature of the subproducts of the 335 cm^{-1} mode. Consequently, the relative difference of the effective temperature when the sample is at room or liquid nitrogen temperature is smaller for the phonons associated with the splitting of the 225 cm^{-1} phonons than for the phonons associated with the splitting of the 335 cm^{-1} phonons. Hence, the experimentally measured

ratio of the phonon lifetimes for the 225 cm^{-1} phonons diverges more than the experimentally measured value of the ratio for the 335 cm^{-1} phonons.

The estimated nonradiative relaxation time (k^{-1}) of the 225 and 335 cm^{-1} phonon modes at 77 K is longer than the relaxation time at room temperature (see table 6.1). The problem of nonradiative relaxation is very complicated and it is very difficult to obtain an analytical solution. Assuming only one phonon mode involved in the nonradiative relaxation generating (p) phonons of equal energy, the temperature dependent nonradiative relaxation rate W(T) (=k) given by eq. 3.34 becomes

$$W(T) = W_0 \left(n(\omega,T)+1\right)^{V/\omega} \qquad (6.8)$$

where W_0 is the rate at T=0, ω the average energy of the emitted phonons, $n(\omega,T)$ is the phonon occupation number and V is the energy to be released by the ion ($V/\omega = p$). In ion doped dielectric crystals, from the overall radiative and nonradiative relaxation from the storage level to the ground state, the change in the nonradiative relaxation rate as a function of temperature has often be used to estimate the average phonon mode involved in the relaxation process (see section 3.2.5). In accordance with the results presented in sections 5.3 and 5.5, the nonradiative relaxation time represents the time that the electronic system needs to reach the bottom of the $^3T_1$ state (≈12850 cm^{-1}) from the end of the bottleneck (≈16150 cm^{-1}) in the model where an intermediate state is taken in to account or from the excitation level (590 nm) when we use the dual relaxation model (t_d=0). The energy available for phonon generation is ≈3300 cm^{-1} for the first case ($t_d \neq 0$) and ≈4100 cm^{-1} in the second (t_d=0). The ratio of the nonradiative relaxation rate W(T) (eq. 6.8) at room and liquid nitrogen temperatures becomes

$$\frac{k^{-1}(T=78)}{k^{-1}(T=292)} = \frac{W(T=292)}{W(T=78)} = \left(\frac{n(\omega, T=292)+1}{n(\omega, T=78)+1}\right)^{V/\omega} \qquad (6.9)$$

The above ratio as a function of the emitted phonon energy (ω) is shown in fig. [6.22] as a thick curve for the case that (a) the energy available is V=3300 cm^{-1}, representing the model where the electronic bottleneck is taken into account and (b) V=4100 cm^{-1}, representing the dual relaxation model (t_d=0). The thick line is the experimentally estimated ratio while the thick broken line is the upper limit of the ratio due to the experimental error. The crossing point between the theoretical curve and the experimentally estimated value provides the "average phonon energy" involved in the relaxation process. When the electronic bottleneck is taken into account (fig. [6.22a]) the suggested phonon has ω=415 cm^{-1} while the lowest limit is ω=325 cm^{-1}. When the dual relaxation modes is used (fig. [6.22b]) the average phonon energy is ω=518 cm^{-1} while the lowest limit due to the experimental error is ω=448 cm^{-1}. From our experimental results we have determined that the 225, 335, and 370 cm^{-1} phonon modes are involved in the nonradiative relaxation. Therefore, in order the average phonon (among the participating modes) to be ω=415 cm^{-1} or ω=518 cm^{-1} as we estimated above, phonon modes of higher energy should also participate. From the up-converted hot luminescence experiments we have measured a mode at ≈512 cm^{-1} participating in the relaxation. However, in order the average phonon to be ω=518 cm^{-1} as we estimated from fig. [6.22b], a large number of very high energy phonons (820 to 970 cm^{-1}) should be active something that is not very likely because: a) We have not observed any of these modes in the up-converted HL spectra. b) The thermal occupation number of these modes is small and if they are Raman active, any

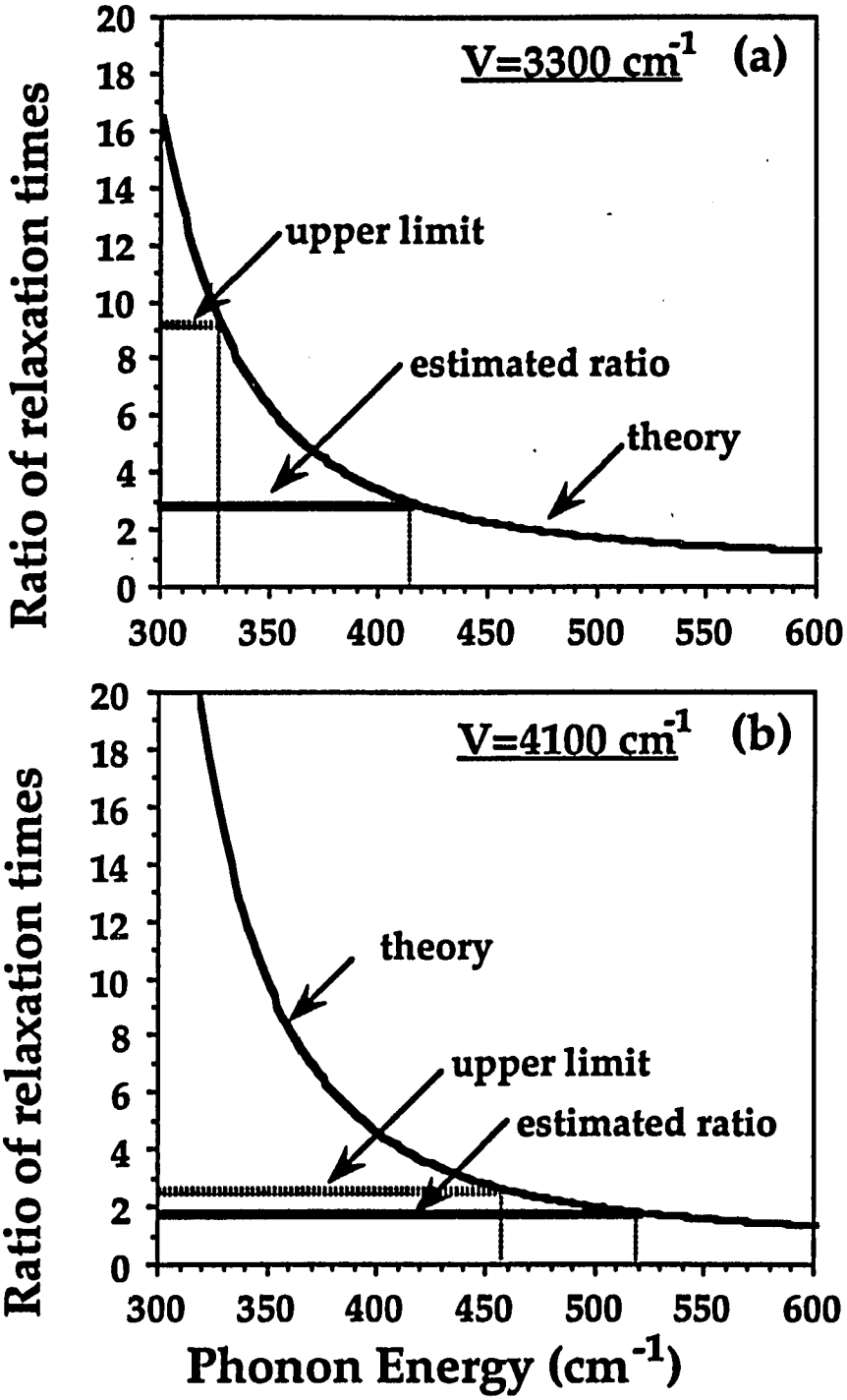

Figure 6.22: The ratio of the noradiative relaxation times at liquid nitrogen and room temperature as a function of the energy of the emitted phonons for (a): the energy transferred from the ion into the lattice is V=3300 cm^{-1} (when the bottleneck is taken in to account) and (b): the energy transferred is V=4100 cm^{-1} (applicable for the dual relaxation model). The curve is the theoretically estimated ratio under the assumption that only one mode is involved. The thick line is the experimentally estimated ratio while the thick broken line is the upper limit of the ratio due to the experimental error.

participation would have been observed as large change in the intensity of the antiStokes Raman lines (since that was possible for lower in energy modes). c) They consume so much energy that very little energy it would be left for the lower in energy modes. For these reasons, the result obtained from fig. [6.22b] predicting ω=518 cm^{-1} should be considered as not conceivable. This is another indication that the relaxation model that includes the electronic bottleneck is a better approximation.

Suppose that only the 225, 335, and 370 cm^{-1} phonon modes are involved in the nonradiative relaxation and that the available energy of 3300 cm^{-1} is distributed for the emission of seven (7) 225 cm^{-1} phonons, three (3) 335 cm^{-1} phonons and two (2) 370 cm^{-1} phonons. The 7/3/2 ratio for the number of phonons of different modes emitted was chosen in accordance to the discussion following eq. 6.5. In that case, using eq. 3.33 the ratio of the nonradiative relaxation times at room and liquid nitrogen temperatures becomes

$$\frac{k^{-1}(T=78)}{k^{-1}(T=292)} = \frac{W(T=292)}{W(T=78)} = \tag{6.10}$$

$$= \frac{\left(n(\omega=225, T=292)+1\right)^7 \left(n(\omega=335, T=292)+1\right)^3 \left(n(\omega=370, T=292)+1\right)^2}{\left(n(\omega=225, T=78)+1\right)^7 \left(n(\omega=335, T=78)+1\right)^3 \left(n(\omega=370, T=78)+1\right)^2} = 38$$

The estimated value of 38 for the ratio of the relaxation times from the theoretical equation is very different from the experimentally estimated ratio of 2.9. One explanation is that the ratio of 7/3/2 for the phonons of each mode emitted is not correct and there are other modes of higher energy involved. Another explanation can be the increase of the phonon mode temperature during the nonradiative relaxation. In semiconductors,

phonon mode temperatures of more than 1000 K have been measured during the nonradiative relaxation of hot electrons.[18,19] Assume that while the Cr ions in forsterite are nonradiatively relaxing, the average occupation number of the phonon modes involved increases by $\Delta n=2.8$ for the 225 cm^{-1} mode, $\Delta n=1.2$ for the 335 cm^{-1} mode and $\Delta n=0.8$ for the 370 cm^{-1} mode (the 7/3/2 ratio is preserved). In this case, the effective temperature (T_{eff}) of the modes when the sample is at room (liquid nitrogen) temperature becomes $^{225}T_{eff}=1200$ K (1070 K) for the 225 cm^{-1} mode, $^{335}T_{eff}=910$ K (790 K) for the 335 cm^{-1} mode and $^{370}T_{eff}=760$ K (655 K) for the 370 cm^{-1} mode. Using these parameters in eq. 6.10, the estimated ratio of the nonradiative relaxation times becomes 3.7 which is very close to the experimentally estimated value of 2.9. This shows that the "heating" of the phonon modes involved in the nonradiative relaxation can affect the relaxation rates. This is compensated in the single phonon mode model (eq. 6.8) by estimating an average phonon of higher energy than the real average of the participating modes.

Assume that the relaxation of the excited Cr^{4+} ions in forsterite involves the emission of seven 225 cm^{-1}, three 335 cm^{-1} and two 370 cm^{-1} phonons for a total of 12 phonons emitted. At room temperature, the estimated nonradiative relaxation time is 2.8 ps which implies that the average time for a phonon emission is 230 fs. At liquid nitrogen temperature, the estimated nonradiative relaxation time is 8 ps which means that the average time between the emission of two phonons is 665 fs. The later estimated value is identical with the estimated lifetime of the first vibronic level (660 fs) from the up-converted HL spectrum under 532 nm excitation.

In conclusion, the dynamics of the 225, 335, and 370 cm^{-1} phonon modes was time resolved at room and liquid nitrogen temperatures. The

modes exhibited time dependent changes while in a number of other modes we have not detected any changes. The low temperature relaxation parameters are significantly longer than at room temperature. The increase of the phonon mode temperature seems to play an important role in the relaxation characteristics. In our fitting model we included the presence of the bottleneck at 2.1 eV. This addition improves the fitting of the experimental data and provides an estimation of the lifetime of the bottleneck.

6.6 References.

1. R.R.Alfano and S.L.Shapiro, Phys. Rev. Lett., **26** 1247 (1971)
2. A. Laubereau,D.von der Linde and W. Kaiser, Phys. Rev. Lett., **27**, 802 (1971)
3. D.von der Linde, J.Kuhl and H.Klingenberg, Phys. Rev. Lett., **44** 1505 (1980)
4. J.A.Kash, J.C.Tsang and J.M.Hvam, Phys. Rev. Lett., **54** 2151 (1985)
5. C. L. Collins and P.Y.Yu, Phys, Rev. B. **30**, 4501 (1984)
6. R. G. Vebrich, V. Narayanamutri, and M. A. Chin, Phys. Rev. Lett., **45**, 1432 (1980)
7. P. Hu, V. Narayanamutri, and M. A. Chin, Phys. Rev. Lett., **46**, 192 (1981)
8. A. M. Stoneham, Philosophical magazine, **36** No 4 , 983 (1977)
9. R. S. Meltzer, J. E. Rives and G. S. Dixon, Phys. Rev. B, **28**, 4786 (1983)
10. R. J. G. Goossens, J. I. Dijkhuis, and H. W. de Wijn, Phys. Rev. B, **32**, 5163 (1985)
11. M. J. Van Dort, C. R. de Kok, J. I. Dijkhuis, and H. W. de Wijn, J. Lumin. **45**, 150 (1990)
12. D. M. Boye, J. E. Rives and R. S. Meltzer, J. Lumin. **45**, 147 (1990)
13. W. A. Tolbert, W. M. Dennis, and W. M. Yen, Phys. Rev. Lett., **65**, 607 (1990)
14. J. Shah, A. E. DiGiovanni, T. C. Damen, and B. I. Miller, Phys. Rev. B, **7**, 3481 (1973)
15. P. G. Klemens, Phys. Rev., **148**, 845 (1966).
16. K. Park, Phys. Lett., **22** (1), 39, (1966).

17. B. Kh. Bairamov, Yu. E. Kitaev, V. K. Negoduiko, and Z. M. Khashkhozhev, Sov. Phys. Solid State, **16**, 1323, (1975).

18. Dai-sik Kim and Peter Y. Yu, Phys. Rev. Lett., **64**, 946, (1990)

19. Dai-sik Kim and Peter Y. Yu, Appl. Phys. Lett., **56**, 1570, (1990)

Chapter 7

Conclusion.

In this thesis, the nonradiative relaxation processes in forsterite were investigated using time resolved Raman scattering and up-converted hot luminescence. The phonons emitted immediately after photoexcitation produce an increase in the occupation number of the participating phonon modes. During this cascade process, short-lived vibronic levels are populated giving rise to hot luminescence. Information on the time domain was obtained through the study of the temporal dynamics of the accepting phonon modes and by measuring the lifetime of parts of the up-converted luminescence. Information on the frequency domain concerning which are the accepting phonon modes was obtained from the energy separation of the peaks in the up-converted hot luminescence spectra and from the Raman lines showing time dependent changes in the pump-and-probe experiments. These two experimental techniques probe the same events and therefore they should provide compatible information. For this reason, I will briefly summarize the results obtained from each method.

The phonon modes involved in the vibrational relaxation in forsterite were determined by the up-converted HL experiments to be 218±20, 325±20, 365±20 and 513±12 cm^{-1}. On the other hand, in the difference spectra obtained after subtraction of the Raman spectra at different delay times, the nonequilibrium phonon peaks are located at ≈218, ≈330 and ≈365 cm^{-1}. We see that there is good agreement between the two experiments and only the 513 cm^{-1} mode was not indicated by the time resolved Raman experiments. According to table [4.3], the 513 cm^{-1} mode is only IR active

(B_{2u} symmetry) and therefore, the participation of this mode was impossible to be determined with the time resolved Raman experiment. From this point of view, in order to determine which are the participating phonon modes it is probably more preferable the up-converted hot luminescence experiment. The time resolved Raman experiments can only investigate Raman active phonon modes.

My analysis in chapter 5 indicates that the relaxation of the excited Cr^{4+} ions in forsterite involves the emission of ≈12 phonons. The estimated nonradiative relaxation time from the time resolved Raman scattering experiment is 2.8 ps at room temperature and 8 ps at liquid nitrogen temperature. This implies that the average time for a phonon emission is 230 fs and 665 fs at room and liquid nitrogen respectively. From the up-converted luminescence spectra I have also determined nonradiative relaxation times using the principle that the ratio of the intensities due to emission from different levels of the same electronic state should be equal to the ratio of their lifetimes. The best estimation was obtained under 532 nm excitation (fig. [5.20]) where the ratio of the intensities of the $^3T_1(t_2e) \rightarrow {}^3A_2$ emission and the emission of first vibronic level implies that the lifetime of the highest energy vibronic level is ≈ 660 fs. The later estimated value is identical with the estimated value of 665 fs from the time resolved experiment at liquid nitrogen temperature. Therefore, both techniques suggest that the average time for phonon emission outside the bottleneck is ≈ 660 fs.

The lifetime of the 2.1 eV bottleneck observed in the up-converted hot luminescence spectra was determined to be shorted than 10 ps at room and liquid nitrogen temperatures. The lifetime of this bottleneck was estimated by the time resolved Raman experiment to be 3±1.6 ps and 5±3.1

ps at room and liquid nitrogen temperature respectively. Therefore, there is agreement between the two experimental techniques.

These results show that the time resolved Raman experiments provide better time resolution than the streak camera measurements of the up-converted emission. The limitations in the time resolution are introduced by the apparatus used for each experiment. In the time resolved Raman experiments the limit is 450 fs which is the pulse duration of the laser. Using pulse compression techniques one can lower this limit but not significantly because the laser bandwidth in the spectral domain should be narrow enough to allow the separation between the different modes in the Raman spectrum. On the other hand, the limitation on the up-converted lifetime measurements arises from the time resolution of the streak camera which is ≈10 ps.

There are some point of interest that I would like to mention. In the time resolved Raman we have seen that symmetry does not seem to play an important role. Modes of certain symmetry participate and others of the same symmetry don't. This means that we should concentrate our attention to other criteria.

The other interesting point is that all the modes, as they were observed in the up-converted hot luminescence measurements, have frequencies almost identical to lattice modes of forsterite. There are no modes that can be interpreted as localized modes of the CrO_4 tetrahedron. On the resonant Raman scattering experiment we have seen that there are at least three local modes of the Cr ions (see figs. [6.11] and [6.12]) at 502, 745 and 770 cm^{-1}. The time resolved Raman experiment on these local modes have shown no participation of these modes in the nonradiative relaxation (see fig. [6.15]). The up-converted luminescence experiment under 1064 nm

two-step excitation (which probes the same part of the excited state that is probed with the Raman experiment under 590 nm - 2.1 eV excitation) have also shown no indication that these local modes participate. Therefore, we have to conclude that these local modes (502, 745 and 770 cm^{-1}) are not accepting modes in this part of the excited state (below 2.2 eV). On the other hand, the up-converted luminescence experiments under 580-760 nm excitation which are probing the 3.2-2.6 eV part of the excited state indicate that the first phonon emitted is 513 ± 12 cm^{-1}. This may suggest that the 502 cm^{-1} local mode participates in some way in the nonradiative relaxation in this part of the excited state but since there are IR-active lattice mode at 510 and 516 cm^{-1}, it is impossible at this point to be certain.

The absorption spectrum of the Cr^{4+}-doped forsterite of the $^3T_1$ electronic state (fig. [5.5]) shows that the spectrum in each polarization consists of three groups of absorption bands. I have discussed the features of these absorption spectra in section 4.2 where I indicated that the three bands are the zero, first and second order sidebands of a localized mode of average frequency ≈ 745 cm^{-1}. Apparently this is the same local mode with the 745 cm^{-1} local mode that I have measured in the resonant Raman scattering experiment. Therefore, the $^3T_1$ electronic state is coupled with a local mode during the absorption of light but this mode does not participate in the nonradiative relaxation. This may provide a clue to the question on which are the accepting phonon modes.

The up-converted hot luminescence and time resolved Raman scattering experiments have shown that the modes involved in the nonradiative relaxation of forsterite are the 218±20, 325±20, 365±20 and 513±12 cm^{-1} modes. These modes are slightly shifted towards lower frequencies with respect to the lattice modes as I have previously indicated

(section 6.5). The question is which are the selection criteria for the participating phonon modes. Unfortunately I have no definite answer to this question at this time. I believe more research is required experimental and theoretical. From the experimental point of view, other crystals should be studied in order to have a larger data base that will help to draw definite conclusions. However, the results obtained in forsterite may provide a preliminary description on the selection criteria of the participating phonon modes.

The vibrational state of an excited impurity ion immediately after photoexcitation can be conceived as a linear combination of the vibrational states associated with the excited ion. These phonon states can be either local modes (involving vibration of the Cr ions with its immediate neighbors) or quasi-lattice modes (involving lattice vibrations with the participation of the Cr ions) having frequencies slightly different from the pure lattice modes due to the presence of the heavier impurity ion. The nonradiative relaxation involves the transfer of energy from the ion into the lattice via the emission of lattice phonons. The link between the impurity ion and the lattice phonons is the impurity ion vibrations that can transfer their energy into the lattice vibrations. It is likely that the modes participating in the nonradiative relaxation are those that ensure some sort of resonance between the impurity ion associated modes and the lattice modes. Resonance occurs when a) the ion modes have similar energies to the lattice modes and the energy is transferred directly from the ion mode to the lattice mode and b) the sum of the energies of two lattice modes is close to the energy of a local mode and in that case, the energy is transferred via the generation of two lattice modes from the breakdown of the local mode. The first type of resonance is a first order process while the second type involves

the emission of two phonons and therefore it is a second order process. This means that if resonance of the first type exists between the ion and the lattice modes then it will dominate the process and almost all the energy will be transferred from the ion into the lattice through the ion modes that have energy similar to the lattice modes.

Fig. [7.1] depicts the processes taking place during the energy transfer from the ion into the lattice. The excess energy of the ion is transferred into the lattice through the impurity ion localized vibrations. The local modes of very different frequency than the lattice modes will not participate in the nonradiative relaxation because they are off resonance with the lattice modes. On the other hand, the lattice modes that are associated with the Cr ions (quasi-lattice modes) have frequencies very close to the "parent" lattice mode and they serve as the channel for energy transfer from the excited ion into the lattice.

This model explains why the phonon modes that participate (218±20, 325±20, 365±20 and 513±12 cm^{-1}) have frequencies very close to the lattice frequencies (225, 335, 370 and 510 or 516 cm^{-1}). The 745 and 770 cm^{-1} local modes of forsterite that have frequencies clearly different than the lattice modes (the nearest lattice modes are at 632 and 827 cm^{-1}) do not participate because they are out of resonance with the lattice modes. The 502 cm^{-1} local mode has two IR-active modes very close (510 and 516 cm^{-1}) and the up-converted HL spectra from the 3.2 to 2.6 eV part of the excited state show the emission of a 513±12 cm^{-1} phonon. Therefore, it is possible that the 502 cm^{-1} local mode participates in the vibrational relaxation in the 3.2 to 2.6 eV part of the excited state by providing the channel for energy to be transferred from the excited ion into the 510 or 516 cm^{-1} IR-active lattice modes.

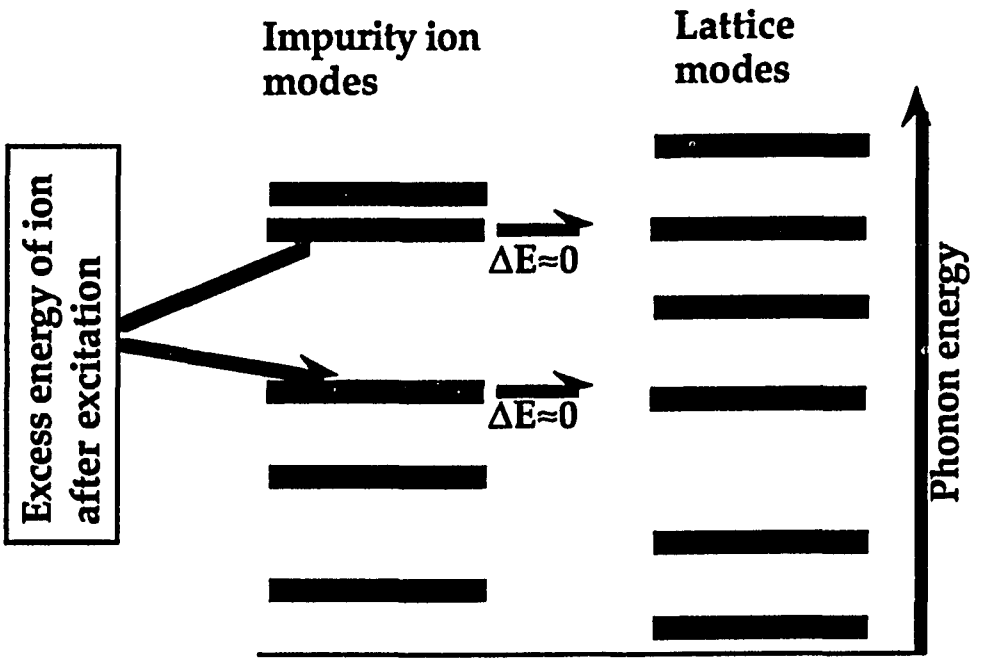

Figure 7.1: Schematic of the impurity ion and lattice phonon modes. The excess potential energy of the impurity ion is given into these lattice modes that are in resonance with the vibrational modes of the ion.

In binary liquids it has been shown that a normal vibrational mode of component A relaxes via energy transfer to a normal mode of component B.[1] Comparison between different mixing systems indicated the importance of near resonance between the modes of the two liquids. These experiments have demonstrated faster relaxation rates for the normal mode of component A when the modes of vibration of component B are in near resonance with the mode of component A. This behavior in liquids is similar to the model I have suggested above for the transfer of energy from the excited ion in a high vibrational state into the lattice through these lattice modes that ensure resonance with the localized vibrations of the impurity ion.

The up-converted HL experiments have shown that different phonon modes are involved in the vibrational relaxation at different parts of the excited state. Two step excitation with 617 nm pumping to reach 3.15 eV part of the excited state shows the emission of 513± 12 and 325 ± 12 cm^{-1} phonons. Pumping with 1064 nm to reach 2.3 eV, the phonons emitted are 323 ±20 and 218±20 cm^{-1}. This can be explained in terms of the different electron wavefunction for the impurity ion electron states at different parts of the excited state. The probability distribution for the outer electrons of the impurity ion depends on the electron wavefunction (electronic state). The impurity ions coupling with the surrounding lattice ligand ions depends on the electronic state. Through this electronic state dependent coupling, the ability of certain phonon modes to transfer energy from the excited ion into the lattice is enhanced while for other modes is suppressed. As a result, different phonon modes undertake the main load for energy transfer from the ion into the lattice at different parts of the excited state.

Understanding of the physics involved in the nonradiative relaxation will help design better lasers in the future. It is known that the same transition metal ion implanted in different host crystals can result in a crystal that may exhibit no emission at all or it may be an excellent laser crystal. The wide variety of resulting quantum efficiencies depends on the ion-lattice coupling strength which allows the photoexcited ions to relax to the ground state nonradiatively. If we know the details of the ion-lattice system we will be able to choose the impurity ion and the host crystal in order to produce crystals that have the desired properties such as mismatch between the localized and lattice modes.

The presence of the bottlenecks are also a point of interest. The population of the bottleneck occurs during the nonradiative relaxation and

it can be populated by direct one photon excitation or a two-step absorption of a photon from the storage level. The emission from the bottlenecks region is very weak but this is due to their short lifetime. A strong excitation pulse will produce a highly populated bottleneck that will remain populated for few picoseconds. During this period of time, the crystal may be used as amplifier of short light signals having frequencies equal to the emission frequency of the bottleneck. The bottlenecks can also be used as switches since they "open" only for few ps after photoexcitation and then "close". In addition one may thing of a laser cavity of appropriate design that uses a bottleneck as the lasing level for synchronously pumped operation. Immediately after excitation, the bottleneck is populated for few ps and becomes the lasing level. Few ps later the bottleneck is depopulated and the crystal becomes a saturable absorber that will help to generate ultrafast pulses. The pumping of such a bottleneck lasing level may be achieved through direct excitation or up-converted excitation. I believe that these possibilities must be investigated.

References.

1. A. Laubereau, L. Kirschner and W. Kaiser, Opt. Commun., 9, 182, (1973).

Chapter 8

Future direction.

Future work should have the following objectives: a) To increase the data base on which phonon modes are involved in the nonradiative relaxation of other crystals, b) To investigate for electronic bottlenecks in other materials and obtain information on their lifetimes c) Understand the physics involved in the nonradiative relaxation in order to formulate criteria for new laser crystals. The use of the up-converted hot luminescence and the time resolved Raman scattering techniques will allow the study of the nonradiative relaxation in other transition metal doped dielectric crystals.

A systematic study should involve the investigation of the nonradiative relaxation of the same transition metal ion in different host crystals and vice versa. Using the same impurity ion in different host crystals for which the electronic structure of the ion remains the same will provide information on the influence of the electronic states to the nonradiative relaxation. For example, we will see if the electronic bottlenecks of different crystals occur in a way that indicates they are due to the electronic structure of the impurity ion as we may expect. In addition, we will be able to see from the phonons participating in the nonradiative relaxation at different part of the excited state if the electronic state of the ion plays a role in the selection criteria and how. Using the same host crystal and different doping ions, we will be able to obtain information on the lattice modes that "tend" to participate in the nonradiative relaxation (if

there are any). This will provide very important knowledge which should allow a much better understanding of the nonradiative processes.

I would suggest the use of the up-converted technique for materials that have a long-lived storage level because this technique allows the investigation of a larger portion of the excited state. The use of the time resolved Raman technique is suggested for crystals that exhibit little or no emission which makes the use of the up-conversion technique impossible. Crystals that exhibit strong absorption but no emission are of particular interest from the point of view of physics involved because of their strong ion-lattice coupling.

I would also suggest the study of the electronic bottlenecks. I have briefly discussed possible applications in chapter 7. In forsterite, there are two electronic bottlenecks located at ≈2.1 and ≈2.45 eV emitting in the yellow-orange and green spectral region respectively. The 2.1 eV bottleneck can be reached with direct excitation by the 532 nm laser pulses of the YAG laser or by two-step excitation from the 1064 nm emission of the Nd:YAG laser. Therefore, pumping with 532 or 1064 nm laser pulses and probing with the 590 nm laser pulses of the dye laser at various pump-probe delay times we may be able to see gain in the intensity of the 590 nm pulses over the initial few ps following photoexcitation. The problem with forsterite is the presence of the Cr^{3+} ions which strongly absorb in the yellow spectral region. The Cr^{3+} ions may not allow observation of gain in forsterite but similar experiments in other materials will show if there is any possibility for practical applications of the electronic bottlenecks.

Appendix

Computer software.

The software developed for the Hamamatsu computer is presented in this section. The programs are written in "basic" language which contains additional commands for image processing. The first program is the **"HL.BAS"** and was used for the up-converted luminescence experiments. The second program is the **"RamInt.BAS"** and was used for the analysis of the time resolved Raman experiments at room temperature. The third program is the **"LT.BAS"** and was used for the low temperature Raman experiments.

1 HL.BAS

```
10 DIM WE(512), TE(512), RA(512), SMW(516), INST(30), SQ(512),
                                                    LLL(512), NBR(512)
20 GOPEN                    :'open the graphic plane overlay
30 GCLR                     :'clear the overlay planes formed before
50 INPUT "INPUT THE CENTRAL PIXEL NUMBER", CN
60 INPUT "INPUT THE WAVELENTH ON THE SPECTROMETER", WN
80 INPUT "    WHICH GRATING ( 3 / 4 / 5 )?====", GGN
81 IF GGN=4 THEN GN=21.3
82 IF GGN=5 THEN GN=33.3
83 IF GGN=3 THEN GN=10.6
84 IF GGN=3 OR GGN=4 OR GGN=5 THEN 120
85 GOTO 80
120 FOR I=0 TO 511
125 LLL(I)=((I-CN)/GN)+WN
126 NBR(I)=(1/LLL(I))*1E+7
130 RA(I)=1239790/LLL(I)
140 NEXT
150 WMCLR                   :'clear the window formed before
160 INPUT "    UPPER(5-----430) ==", W1 :'window
170 INPUT "    LOWER(10----440) ==", W2  :'size
180 WOPEN, X, W1, W2
190 INPUT "    CHANGE WINDOW SIZE?(Y/N)----", S$
200 IF S$="Y" OR S$="y" THEN 150
400 INPUT "WHICH IMAGE DISPLAY DO YOU WANT (1/2)====", IMN
```

```
410 IF IMN=2 THEN 460
420 IF IMN=1 THEN 440
430 GOTO 400
440 IOPEN 0
450 GOTO 470
460 IOPEN 1
470 WOPEN 1, X, W1, W2
480 IF IMN=1 THEN WSUM [0], 1 ELSE WSUM [1], 1
490 INPUT "DO YOU WANT TO SMOOTH THE PROFILE (Y/N) ? -" SM$
500 IF SM$="Y" OR SM$="y" THEN 630
510 MA=1            :'find the maximum intensity
520 MB=-1
530 FOR I=1 TO 511
540 IF MA<WD1(I) THEN MA=WD1(I)
550 IF MB>WD1(I) THEN MB=WD1(I)
560 NEXT
570 GCLR
580 FOR I=0 TO 511          :'draw a profile
590 LINE I+60, (MB/(MA-MB))*300+350-WD1(I)/(MA-MB)*300, I+1+60,
          (MB/(MA-MB))*300+350-WD1(I+1)/(MA-MB)*300
600 NEXT
610 GOTO 930
620 SM=1
630 RE=0
640 INPUT " SMOOTHING OVER  [ 2n+1 ] CHANELS, ENTER  n ==", RE
650 INPUT "    DO YOU WANT  INTEGRAL PROFILE (Y/N)?----", QPR$
660 PRINT "    PROCESSING OVER", 2*RE+1, "CHANELS"
670 FOR I=1 TO 511
680 SMW(I)=WD1(I)
690 NEXT
700 WQ=60+RE
710 WA=571-RE
720 FOR I=1 TO 1+RE
730 WD1(I)=0
740 NEXT
750 FOR I=511-RE TO 511
760 WD1(I)=0
770 NEXT
780 LINE WQ, 370, WA, 370
790 LINE WQ, 380, WA, 380
800 LINE WQ, 370, WQ, 380
810 LINE WA, 370, WA 380
820 FOR I=1+RE TO 511-RE
830 WQ=WQ+1
840 LINE WQ 370, WQ, 380
850 DF=0
860 FOR L=I-RE TO I+RE
870 DF=DF+SMW(L)
880 NEXT
890 IF QPR$="Y" OR QPR$="y" THEN 907
900 WD1(I)=DF/(2*RE+1)
904 GOTO 910
907 WD1(I)=DF
```

```
910 NEXT
920 GOTO 510
930 LINE 60, 40, 580, 40
940 LINE 60, 350, 580, 350
950 LINE 580, 40, 580, 350
960 LINE 60, 40, 60, 350
1000 LOCATE 5, 1
1010 OPRINT "COUNTS:"
1020 LOCATE 19, 1
1030 OPRINT "ENERGY:"
1040 LOCATE 5, 17
1050 OPRINT "CHANNEL:"
1055 LOCATE 19, 17
1056 OPRINT "WAVENUMBER:"
1060 IF AS$="Y" OR AS$="y" THEN 1080
1070 GOTO 1130
1080 OI=(MB/(MA-MB))*300+350
1090 LINE 60, OI, 580, OI
1100 AI=INT(14+12*(MB/(MA-MB)))
1110 LOCATE 3, AI
1120 OPRINT "0"
1130 FOR I=60 TO 350 STEP 20
1140 PSET 160, I
1150 PSET 260, I
1160 PSET 360, I
1170 PSET 460, I
1180 PSET 560, I
1190 NEXT
1200 FOR I=60 TO 580 STEP 20
1210 IF AS$="Y" OR AS$="y" THEN 1240
1220 PSET I, 250
1230 PSET I, 150
1240 PSET I, 50
1250 NEXT
1260 IF AS$="Y" OR AS$="y" THEN 1330
1270 LOCATE 3, 10
1280 OPRINT "1";
1290 LOCATE 3, 6
1300 OPRINT "2";
1310 LOCATE 3, 2
1320 OPRINT "3";
1330 LOCATE 2, 3
1340 OPRINT "I";
1350 LOCATE 2, 4
1360 OPRINT "N";
1370 LOCATE 2, 5
1380 OPRINT "T";
1390 LOCATE 2, 6
1400 OPRINT "E";
1410 LOCATE 2, 7
1420 OPRINT "N";
1430 LOCATE 2, 8
1440 OPRINT "S";
```

```
1450 LOCATE 2, 9
1460 OPRINT "I";
1470 LOCATE 2, 10
1480 OPRINT "T";
1490 LOCATE 2, 11
1500 OPRINT "Y";
1510 START=300
1520 DW=0
1530 DT=0
1540 DR=0
1550 LINE START, 41, START, 49   :'DISPLAY a cursor
1560 LINE  START, 49, (START-2), 45
1570 LINE  START, 49, (START+2), 45
1580 IIT=0
1590 ZX=-1
1600 GOTO 2130
1610 PRINT "********MOVE THE DOT LINE TO DETECT PEAK********"
1620 PRINT "*  C--LEFT  X--QUICK LEFT   B--RIGHT   N--QUICK RIGHT "
1630 PRINT "*      E---EXIT  P---PRINT OUT  I---INTEGRAL          *"
1640 PRINT "*****************************************************"
1650 V$=" "
1660 V$=INKEY$
1670 IF V$="E" OR V$="e" THEN 2280
1680 STRT=START
1690  IF V$="B" OR V$="b" THEN 1780 ELSE IF V$="X" OR V$="x"
       THEN 1720 ELSE IF V$="N" OR V$="n" THEN 1740 ELSE IF   V$="C"
OR V$="c" THEN 1760 ELSE IF V$="P" OR V$="p" THEN       1800 ELSE IF
V$="I" OR V$="i" THEN 1830
1700 START=START
1710 GOTO 1980
1720 START=START-10
1730 GOTO 1980
1740 START=START+10
1750 GOTO 1980
1760 START=START-1
1770 GOTO 1980
1780 START=START+1
1790 GOTO 1980
1800 INST(IIT+1)=START-60
1810 IIT=IIT+1
1820 GOTO 1610
1830 INTE=0
1840 IF ZX=-1 THEN 1860
1850 GOTO 1920
1860 INPUT "INTEGRATION OVER [ 2n+1 ] CHANELS. ENTER N=", ZX
1870 IF ZX<0 THEN 1890
1880 GOTO 1910
1890 PRINT "   ERROR !!!   REENTER"
1900 GOTO 1860
1910 PRINT "   INTEGRATION OVER", 2*ZX+1, "CHANELS IS
                                                    PERFORMED"
1920 FOR I=0 TO 2*ZX+1
1930  INTE=INTE+WD1(START-60+I-ZX)
```

```
1940 NEXT
1950 PRINT "AREA OF THE PEAK AT WAVE#",
                                    INT(RA(START-60)*10)/10, "IS", INTE
1960 PRINT "              "
1970 GOTO 1610
1980 IF START<70 THEN START=START+10
1990 IF START>570 THEN START=START-10
2000 LINE STRT, 41, STRT, 49, 0
2010 LINE STRT, 49, (STRT-2), 45,.0
2020 LINE STRT, 49, (STRT+2), 45, 0
2030 LINE START, 49, (START-2), 45
2040 LINE START, 49, (START+2), 45
2050 LINE START, 41, START, 49
2060 LOCATE 13, 1
2070 OPRINT WD1(START-60);
2080 LOCATE 27, 1
2090  OPRINT INT(RA(START-60))
2095 LOCATE 31, 17
2096 OPRINT INT(NBR(START-60))
2100 LOCATE 13, 17
2110 OPRINT (START-60)
2120 GOTO 1650
2130 LOCATE 1, 15
2140 OPRINT INT(RA(1));
2150 LOCATE 8, 15
2160 OPRINT INT(RA(100));
2170 LOCATE 14, 15
2180 OPRINT INT(RA(200));
2190 LOCATE 21, 15
2200 OPRINT INT(RA(300));
2210 LOCATE 27, 15
2220 OPRINT INT(RA(400));
2230 LOCATE 34, 15
2240 OPRINT INT(RA(500));
2270 GOTO 1610
2280 DR=0
2290 INPUT "    SAVE THIS PROFILE? (Y/N) ----", PR$
2300 IF PR$="Y" OR PR$="y" THEN 2320
2310 GOTO 2470
2320 INPUT "    DATA FILE NAME? ====", NE$
2330 OPEN "O", #2, NE$
2340 PRINT "ENTER THE DELAY TIME IN PICOSEC."
2350 INPUT T
2360 PRINT #2, T
2370 PRINT "ENTER  THE  TITLE"
2380 INPUT COM$
2390 PRINT #2, COM$
2400 PRINT #2, "Energy  (eV)"
2410 PRINT #2, "Counts"
2420 FOR I=1 TO 511
2430 PRINT #2, RA(I)
2440 PRINT #2, WD1(I)
2450 NEXT
```

```
2460 CLOSE
2470 IF IIT=0  THEN 2610
2480 INPUT "   PRINT OUT THE  MEASURED DATA? (Y/N)----", WIC$
2490 IF WIC$="N" OR WIC$="n" THEN 2790
2500 PRINT "PLEASE SET THE PRINTER AND PRESS Y IF READY"
2510 IF (INKEY$<>"Y") AND (INKEY$<>"y") THEN 2510
2520 RSPRINT "  RAMAN SHIFT AND INTENSITY"
2530 RSPRINT "                          "
2540 RSPRINT "-------------------------------------------------"
2550 RSPRINT "RAMAN SHIFT", "INTENSITY     "
2560 FOR I=1 TO IIT
2570  RSPRINT "-------------------------------------------------"
2580  RSPRINT RA(INST(I)), WD1(INST(I))
2590 NEXT
2600 RSPRINT "-------------------------------------------------"
2610 INPUT "   DO YOU WANT A PARTIAL INTEGRAL (Y/N)----", GH$
2620 IF GH$="n" OR GH$="N" THEN 2790
2630 IF GH$="Y" OR GH$="y" THEN 2650
2640 GOTO 2610
2650 INPUT "    ENTER (X1) IN PIXEL #----", XI1
2670 INPUT "    ENTER (X2) IN PIXEL #----", XI2
2675 INPUT "    ENTER (Y1) IN COUNTS----", YI1
2680 INPUT "    ENTER (Y2) IN COUNTS----", YI2
2690 LINE XI1+60, (MB/(MA-MB))*300+350-YI1/(MA-MB)*300, XI2+60,
                  (MB/(MA-MB))*300+350-YI2/(MA-MB)*300
2692 INPUT "    CONTINUE (Y/N)?----", DF$
2694 IF DF$="Y" OR DF$="y" THEN 2700
2696 LINE XI1+60, (MB/(MA-MB))*300+350-YI1/(MA-MB)*300, XI2+60,
                  (MB/(MA-MB))*300+350-YI2/(MA-MB)*300, 0
2698 GOTO 2675
2700 SINT=0
2710 SQA=(YI2-YI1)/(XI2-XI1)
2720 SQB=YI1-SQA*XI1
2730 FOR I=XI1 TO XI2
2740 SQ(I)=SQA*I+SQB
2750 SINT=SINT+WD1(I)-SQ(I)
2760 LINE I+60, (MB/(MA-MB))*300+350-SQ(I)/(MA-MB)*300, I+60,
          (MB/(MA-MB))*300+350-WD1(I)/(MA-MB)*300, 2770 NEXT
2778 PRINT "          \\\\\\\\\\\\\\\\\\\\\\\\\\\\\\\\\\\\\\\\"
2780 PRINT "   THE INTEGRAL IS  ", INT(SINT)
2782 PRINT "          ////////////////////////////// "
2785 INPUT "DO YOU WANT NEW INTEGRATION (Y/N)?", RQP$
2786 IF RQP$="Y" OR RQP$="y" THEN 2650
2794 PRINT " "
2795 PRINT "R E T U R N I N G   F O R   A   N E W   I M A G E"
2800 PRINT " "
 2810 GCLR
2820 WOPEN, X, W1, W2
2830 IMN=0
2840 SM$="A"
2850 A$=" "
2860 AS$="A"
2861 PR$="A"
```

```
2862 QPR$="A"
2864 RQP$="A"
2870 GOTO 400
```

2 RamInt.BAS

```
10 DIM WE(512), TE(512), RA(512), SMW(516), INST(30), SQ(512)
20 GOPEN                    :'open the graphic plane overlay
30 GCLR                     :'clear the overlay planes formed before
50 INPUT " INPUT THE CENTRAL PIXEL NUMBER=", CN
60 INPUT " INPUT THE WAVELENTH ON THE SPECTROMETER=", WN
80 INPUT "   WHICH GRATING ( 3 / 4 / 5 )?====", GGN
81 IF GGN=4 THEN GN=21.3
82 IF GGN=5 THEN GN=33.3
83 IF GGN=3 THEN GN=10.6
84 IF GGN=3 OR GGN=4 OR GGN=5 THEN 90
85 GOTO 80
90 INPUT "   INPUT THE LASER WAVELENGTH====", LW
120 FOR I=0 TO 511
130 RA(I)=(1/((I-CN)/GN+WN)-1/LW)*1E+7
140 NEXT
150 WMCLR                   :'clear the window formed before
160 INPUT "   UPPER(5-----430) ==", W1 :'window
170 INPUT "   LOWER(10----440) ==", W2  :'size
180 WOPEN, X, W1, W2
190 INPUT "   CHANGE WINDOW SIZE?(Y/N)----", S$
200 IF S$="Y" OR S$="y" THEN 150
210 INPUT "   ARE YOU GOING TO SUBSTRACT TWO
                                        HISTOGRAMS(Y/N)?----", AS$
220 IF AS$="Y" OR AS$="y" THEN 240
230 GOTO 400
240 INPUT "   SUBSTRACT: [S1]-[S2] WHICH DISPLAYED IMAGE IS
                                                    S1(1/2)=====", SN
250 IOPEN 0
260 WOPEN 1, X, W1, W2
270 WSUM [0], 1
280 IOPEN 1
290 WOPEN 2, X, W1, W2
300 WSUM [1], 2
310 IF SN=2 THEN 360
320 FOR I=0 TO 511
330 WD1(I)=WD1(I)-WD2(I)
340 NEXT
350 GOTO 490
360 FOR I=0 TO 511
370 WD1(I)=WD2(I)-WD1(I)
380 NEXT
390 GOTO 490
400 INPUT "   WHICH IMAGE DISPLAY DO YOU WANT (1/2)====", IMN
410 IF IMN=2 THEN 460
```

```
420 IF IMN=1 THEN 440
430 GOTO 400
440 IOPEN 0
450 GOTO 470
460 IOPEN 1
470 WOPEN 1, X, W1, W2
480 IF IMN=1 THEN WSUM [0], 1 ELSE WSUM [1], 1
490 INPUT "   DO YOU WANT TO SMOOTH THE PROFILE (Y/N) ? ----"
                                                              ,SM$
500 IF SM$="Y" OR SM$="y" THEN 630
510 MA=1            :'find the maximum intensity
520 MB=-1
530 FOR I=1 TO 511
540 IF MA<WD1(I) THEN MA=WD1(I)
550 IF MB>WD1(I) THEN MB=WD1(I)
560 NEXT
570 GCLR
580 FOR I=0 TO 511          :'draw a profile
590 LINE I+60, (MB/(MA-MB))*300+350-WD1(I)/(MA-MB)*300, I+1+60,
          (MB/(MA-MB))*300+350-WD1(I+1)/(MA-MB)*300
600 NEXT
610 GOTO 930
620 SM=1
630 RE=0
640 INPUT "   SMOOTHING OVER  [ 2n+1 ] CHANELS ENTER  n ===", RE
650 INPUT "    DO YOU WANT  INTEGRAL PROFILE (Y/N)?----", QPR$
660 PRINT "    PROCESSING OVER", 2*RE+1, "CHANELS"
670 FOR I=1 TO 511
680 SMW(I)=WD1(I)
690 NEXT
700 WQ=60+RE
710 WA=571-RE
720 FOR I=1 TO 1+RE
730 WD1(I)=0
740 NEXT
750 FOR I=511-RE TO 511
760 WD1(I)=0
770 NEXT
780 LINE WQ ,370, WA ,370
790 LINE WQ, 380, WA, 380
800 LINE WQ ,370, WQ, 380
810 LINE WA, 370, WA, 380
820 FOR I=1+RE TO 511-RE
830 WQ=WQ+1
840 LINE WQ, 370, WQ, 380
850 DF=0
860 FOR L=I-RE TO I+RE
870 DF=DF+SMW(L)
880 NEXT
890 IF QPR$="Y" OR QPR$="y" THEN 907
900 WD1(I)=DF/(2*RE+1)
904 GOTO 910
907 WD1(I)=DF
```

```
910 NEXT
920 GOTO 510
930 LINE 60, 40, 580, 40
940 LINE 60, 350, 580, 350
950 LINE 580, 40, 580, 350
960 LINE 60, 40, 60, 350
970 INPUT "   ENTER THE NAME OF PROFILE====", A$
980 LOCATE 5, 18
990 OPRINT A$
1000 LOCATE 5, 1
1010 OPRINT "COUNTS:"
1020 LOCATE 19, 1
1030 OPRINT "CURSOR:";
1040 LOCATE 5, 16
1050 OPRINT "CHANNEL:"
1060 IF AS$="Y" OR AS$="y" THEN 1080
1070 GOTO 1130
1080 OI=(MB/(MA-MB))*300+350
1090 LINE 60, OI, 580, OI
1100 AI=INT(14+12*(MB/(MA-MB)))
1110 LOCATE 3, AI
1120 OPRINT "0"
1130 FOR I=60 TO 350 STEP 20
1140 PSET 160, I
1150 PSET 260, I
1160 PSET 360, I
1170 PSET 460, I
1180 PSET 560, I
1190 NEXT
1200 FOR I=60 TO 580 STEP 20
1210 IF AS$="Y" OR AS$="y" THEN 1240
1220 PSET I, 250
1230 PSET I, 150
1240 PSET I, 50
1250 NEXT
1260 IF AS$="Y" OR AS$="y" THEN 1330
1270 LOCATE 3, 10
1280 OPRINT "1";
1290 LOCATE 3, 6
1300 OPRINT "2";
1310 LOCATE 3, 2
1320 OPRINT "3";
1330 LOCATE 2, 3
1340 OPRINT "I";
1350 LOCATE 2, 4
1360 OPRINT "N";
1370 LOCATE 2, 5
1380 OPRINT "T";
1390 LOCATE 2, 6
1400 OPRINT "E";
1410 LOCATE 2, 7
1420 OPRINT "N";
1430 LOCATE 2, 8
```

```
1440 OPRINT "S";
1450 LOCATE 2, 9
1460 OPRINT "I";
1470 LOCATE 2, 10
1480 OPRINT "T";
1490 LOCATE 2, 11
1500 OPRINT "Y";
1510 START=300
1520 DW=0
1530 DT=0
1540 DR=0
1550 LINE START, 41, START, 49   :'DISPLAY a cursor
1560 LINE  START, 49, (START-2), 45
1570 LINE  START, 49, (START+2), 45
1580 IIT=0
1590 ZX=-1
1600 GOTO 2130
1610 PRINT "****   **MOVE THE DOT LINE TO DETECT PEAK*********"
1620 PRINT "* C--LEFT  X--QUICK LEFT    B--RIGHT   N--QUICK RIGHT *"
1630 PRINT "*       E---EXIT  P---PRINT OUT  I---INTEGRAL          *"
1640 PRINT,"*************************************************************"
1650 V$=" "
1660 V$=INKEY$
1670 IF V$="E" OR V$="e" THEN 2280
1680 STRT=START
1690  IF V$="B" OR V$="b" THEN 1780 ELSE IF V$="X" OR V$="x" THEN
        1720 ELSE IF V$="N" OR V$="n" THEN 1740 ELSE IF V$="C" OR
        V$="c" THEN 1760 ELSE IF V$="P" OR V$="p" THEN 1800 ELSE IF
        V$="I" OR V$="i" THEN 1830
1700 START=START
1710 GOTO 1980
1720 START=START-10
1730 GOTO 1980
1740 START=START+10
1750 GOTO 1980
1760 START=START-1
1770 GOTO 1980
1780 START=START+1
1790 GOTO 1980
1800 INST(IIT+1)=START-60
1810 IIT=IIT+1
1820 GOTO 1610
1830 INTE=0
1840 IF ZX=-1 THEN 1860
1850 GOTO 1920
1860 INPUT "INTEGRATION OVER [ 2n+1] CHANELS. ENTER N===", ZX
1870 IF ZX<0 THEN 1890
1880 GOTO 1910
1890 PRINT "   ERROR !!!   REENTER"
1900 GOTO 1860
1910 PRINT "   INTEGRATION OVER", 2*ZX+1, "CHANELS WILL BE
                                                    PERFORMED"
1920 FOR I=0 TO 2*ZX+1
```

```
1930  INTE=INTE+WD1(START-60+I-ZX)
1940 NEXT
1950 PRINT "AREA OF THE PEAK AT WAVE#", INT(RA(START-
                                                    60)*10)/10, "IS", INTE
1960 PRINT "            "
1970 GOTO 1610
1980 IF START<70 THEN START=START+10
1990 IF START>570 THEN START=START-10
2000 LINE STRT, 41, STRT, 49, 0
2010 LINE STRT, 49, (STRT-2), 45, 0
2020 LINE STRT, 49, (STRT+2), 45, 0
2030 LINE START, 49, (START-2), 45
2040 LINE START, 49, (START+2), 45
2050 LINE START, 41, START, 49
2060 LOCATE 13, 1
2070 OPRINT WD1(START-60);
2080 LOCATE 27, 1
2090  OPRINT INT(RA(START-60))
2100 LOCATE 13, 16
2110 OPRINT (START-60)
2120 GOTO 1650
2130 LOCATE 1, 15
2140 OPRINT INT(RA(1));
2150 LOCATE 8, 15
2160 OPRINT INT(RA(100));
2170 LOCATE 14, 15
2180 OPRINT INT(RA(200));
2190 LOCATE 21, 15
2200 OPRINT INT(RA(300));
2210 LOCATE 27, 15
2220 OPRINT INT(RA(400));
2230 LOCATE 34, 15
2240 OPRINT INT(RA(500));
2250 LOCATE 21, 16
2260 OPRINT "RAMAN SHIFT (1/cm)";
2270 GOTO 1610
2280 DR=0
2290 INPUT "    SAVE THIS PROFILE? (Y/N) ----", PR$
2300 IF PR$="Y" OR PR$="y" THEN 2320
2310 GOTO 2470
2320 INPUT "    DATA FILE NAME? ====", NE$
2330 OPEN "O", #2, NE$
2340 PRINT "ENTER THE DELAY TIME IN PICOSEC."
2350 INPUT T
2360 PRINT #2, T
2370 PRINT "ENTER  THE  TITLE"
2380 INPUT COM$
2390 PRINT #2, COM$
2400 PRINT #2, "Raman shift"
2410 PRINT #2, "Counts"
2420 FOR I=1 TO 511
2430 PRINT #2, RA(I)
2440 PRINT #2, WD1(I)
```

```
2450 NEXT
2460 CLOSE
2470 IF IIT=0  THEN 2610
2480 INPUT "   PRINT OUT THE  MEASURED DATA IN SOME
                                                CHANNEL? (Y/N)----", WIC$
2490 IF WIC$="N" OR WIC$="n" THEN 2790
2500 PRINT "PLEASE SET THE PRINTER AND PRESS Y WHEN READY"
2510 IF (INKEY$<>"Y") AND (INKEY$<>"y") THEN 2510
2520 RSPRINT  RAMAN SHIFT AND INTENSITY IN SOME CHANNEL "
2530 RSPRINT "                                    "
2540 RSPRINT "-------------------------------------------------"
2550 RSPRINT "RAMAN SHIFT", "INTENSITY     "
2560 FOR I=1 TO IIT
2570  RSPRINT "-------------------------------------------------"
2580  RSPRINT RA(INST(I)), WD1(INST(I))
2590 NEXT
2600 RSPRINT "-------------------------------------------------"
2610 INPUT "   DO YOU WANT A PARTIAL INTEGRAL (Y/N)----", GH$
2620 IF GH$="n" OR GH$="N" THEN 2790
2630 IF GH$="Y" OR GH$="y" THEN 2650
2640 GOTO 2610
2650 INPUT "    ENTER (X1) IN PIXEL #----", XI1
2670 INPUT "    ENTER (X2) IN PIXEL #----", XI2
2675 INPUT "    ENTER (Y1) IN COUNTS----", YI1
2680 INPUT "    ENTER (Y2) IN COUNTS----", YI2
2690 LINE XI1+60, (MB/(MA-MB))*300+350-YI1/(MA-MB)*300, XI2+60,
                  (MB/(MA-MB))*300+350-YI2/(MA-MB)*300
2692 INPUT "    CONTINUE (Y/N)?----", DF$
2694 IF DF$="Y" OR DF$="y" THEN 2700
2696 LINE XI1+60, (MB/(MA-MB))*300+350-YI1/(MA-MB)*300, XI2+60,
                  (MB/(MA-MB))*300+350-YI2/(MA-MB)*300, 0
2698 GOTO 2675
2700 SINT=0
2710 SQA=(YI2-YI1)/(XI2-XI1)
2720 SQB=YI1-SQA*XI1
2730 FOR I=XI1 TO XI2
2740 SQ(I)=SQA*I+SQB
2750 SINT=SINT+WD1(I)-SQ(I)
2760 LINE I+60, (MB/(MA-MB))*300+350-SQ(I)/(MA-MB)*300, I+60,
                        (MB/(MA-MB))*300+350-WD1(I)/(MA-MB)*300
2770 NEXT
2778 PRINT "              \\\\\\\\\\\\\\\\\\\\\\\\\\\\\\\\"
2780 PRINT "    THE INTEGRAL IS   ", INT(SINT)
2782 PRINT "              ////////////////////////////// "
2785 INPUT "    DO YOU WANT ANOTHER INTEGRATION (Y/N)?----",
                                                          RQP$
2786 IF RQP$="Y" OR RQP$="y" THEN 2650
2790 INPUT "    DO YOU WANT TO DO SOMETHING ELSE(N/Y)----", EL$
2800 IF EL$="N" OR EL$="n" THEN 2880
2810 GCLR
2820 WOPEN, X, W1, W2
2830 IMN=0
2840 SM$="A"
```

```
2850 A$=" "
2860 AS$="A"
2861 PR$="A"
2862 QPR$="A"
2864 RQP$="A"
2870 GOTO 210
```

3 LT.BAS

```
10 DIM WE(512), TE(512), RA(512), SMW(516), WD2(516), INST(30),
                                                    WD1(512), SAV(512)
20 GOPEN                    :'open the graphic plane overlay
30 GCLR                    :'clear the overlay planes formed before
50 INPUT "INPUT THE CENTRAL PIXEL NUMBER", CN
60 INPUT "INPUT THE WAVELENTH ON THE SPECTROMETER", WN
80 INPUT "    INPUT THE CALIBRATION OF GRATING====", GN
90 INPUT "    INPUT THE LASER WAVELENGTH====", LW
120 FOR I=0 TO 511
130 RA(I)=-(1/((I-CN)/GN+WN)-1/LW)*1E+7
140 NEXT
150 GOTO 220
160 WMCLR                  :'clear the window formed before
170 INPUT "    UPPER(5-----430) ==", W1 :'window
180 INPUT "    LOWER(10----440) ==", W2  :'size
185 GOTO  ZX
190 INPUT "    CHANGE WINDOW SIZE?(Y/N)----", S$
200 IF S$="Y" OR S$="y" THEN 160
210 GOTO ZX+10
220 INPUT "WHICH IMAGE DISPLAY DO YOU WANT  (1/2) ? ==", TY
230 IF TY=1 THEN 260
240 IF TY=2 THEN 390
250 GOTO 220
260 IOPEN 0
270 PRINT "    OPEN THE WINDOW FOR THE SIGNAL"
280 ZX=300
290 GOTO 170
300 WOPEN 1, X, W1, W2
305 GOTO 190
310 WSUM [0], 1
320 PRINT "    OPEN THE WINDOW FOR THE REFERENCE SIGNAL"
330 ZX=360
340 GOTO 160
350 IOPEN 0
360 WOPEN 2, X, W1, W2
365 GOTO 190
370 WSUM [0], 2
380 GOTO 510
390 IOPEN 1
400 PRINT "    OPEN THE WINDOW FOR THE SIGNAL"
410 ZX=430
420 GOTO 170
```

```
430 WOPEN 1, X, W1, W2
435 GOTO 190
440 WSUM [1], 1
450 PRINT "   OPEN THE WINDOW FOR THE REFERENCE SIGNAL"
460 ZX=490
470 GOTO 160
480 IOPEN 1
490 WOPEN 2, X, W1, W2
495 GOTO 190
500 WSUM [1], 2
510 INPUT "   ENTER NORMALIZATION PARAMETER ===", NOR
513 INPUT "   ENTER CORRECTION NUMBER ====", XR
520 FOR I=10 TO 500
530 WD1(I)=WD1(I)-(NOR*WD2(I+XR))
540 NEXT
541 INPUT "ENTER X1 AND X2 FOR FLAT SPECTRA----", AAB, ABB
542 FOR I=AAB TO ABB
543 WD1(I)=0
544 NEXT
545 FOR I=1 TO 9
546 WD1(I)=0
547 NEXT
548 FOR I=501 TO I=511
549 WD1(I)=0
550 NEXT
551 FOR I=1 TO I=511
552 SAV(I)=WD1(I)
553 NEXT
554 FOR I=1 TO I=511
555 WD1(I)=SAV(I)
556 NEXT
557 INPUT "DO YOU WANT TO SMOOTH THE PROFILE  (Y/N)?-", SM$
560 IF SM$="Y" OR SM$="y" THEN 690
570 MA=1            :'find the maximum intensity
580 MB=-1
590 FOR I=1 TO 511
600 IF MA<WD1(I) THEN MA=WD1(I)
610 IF MB>WD1(I) THEN MB=WD1(I)
620 NEXT
630 GCLR
640 FOR I=0 TO 511          :'draw a profile
650 LINE I+60, (MB/(MA-MB))*300+350-WD1(I)/(MA-MB)*300, I+1+60,
              (MB/(MA-MB))*300+350-WD1(I+1)/(MA-MB)*300
660 NEXT
670 GOTO 970
680 SM=1
690 RE=1
700 INPUT " SMOOTHING OVER  [ 2n+1 ] CHANELS, ENTER  n ==", RE
710 PRINT "   SMOOTHING OVER", 2*RE+1, "CHANELS"
720 FOR I=1 TO 511
730 SMW(I)=WD1(I)
740 NEXT
750 WQ=60+RE
```

```
760 WA=571-RE
770 FOR I=1 TO 1+RE
780 WD1(I)=0
790 NEXT
800 FOR I=511-RE TO 511
810 WD1(I)=0
820 NEXT
830 LINE WQ, 370, WA, 370
840 LINE WQ, 380, WA, 380
850 LINE WQ, 370, WQ, 380
860 LINE WA, 370, WA, 380
870 FOR I=1+RE TO 511-RE
880 WQ=WQ+1
890 LINE WQ, 370, WQ, 380
900 DF=0
910 FOR L=I-RE TO I+RE
920 DF=DF+SMW(L)
930 NEXT
940 WD1(I)=DF
950 NEXT
960 GOTO 570
970 LINE 60, 40, 580, 40
980 LINE 60, 350, 580, 350
990 LINE 580, 40, 580, 350
1000 LINE 60, 40, 60, 350
1010 INPUT "   ENTER THE NAME OF PROFILE====", A$
1020 LOCATE 5, 18
1030 OPRINT A$
1040 LOCATE 5 1
1050 OPRINT "COUNTS:"
1060 LOCATE 19, 1
1070 OPRINT "CURSOR:";
1080 LOCATE 5, 16
1090 OPRINT "CHANNEL:"
1095 AS$="Y"
1100 IF AS$="Y" OR AS$="y" THEN 1120
1110 GOTO 1170
1120 OI=(MB/(MA-MB))*300+350
1130 LINE 60, OI, 580, OI
1140 AI=INT(14+12*(MB/(MA-MB)))
1150 LOCATE 3, AI
1160 OPRINT "0"
1170 FOR I=60 TO 350 STEP 20
1180 PSET 160, I
1190 PSET 260, I
1200 PSET 360, I
1210 PSET 460, I, 1220 PSET 560, I
1230 NEXT
1233 AS$="Y"
1240 FOR I=60 TO 580 STEP 20
1250 IF AS$="Y" OR AS$="y" THEN 1280
1260 PSET I, 250
1270 PSET I, 150
```

```
1280 PSET I, 50
1290 NEXT
1300 IF AS$="Y" OR AS$="y" THEN 1370
1310 LOCATE 3, 10
1320 OPRINT "1";
1330 LOCATE 3, 6
1340 OPRINT "2";
1350 LOCATE 3, 2
1360 OPRINT "3";
1370 LOCATE 2, 3
1380 OPRINT "I";
1390 LOCATE 2, 4
1400 OPRINT "N";
1410 LOCATE 2, 5
1420 OPRINT "T";
1430 LOCATE 2, 6
1440 OPRINT "E";
1450 LOCATE 2, 7
1460 OPRINT "N";
1470 LOCATE 2, 8
1480 OPRINT "S";
1490 LOCATE 2, 9
1500 OPRINT "I";
1510 LOCATE 2, 10
1520 OPRINT "T";
1530 LOCATE 2, 11
1540 OPRINT "Y";
1550 START=300
1560 DW=0
1570 DT=0
1580 DR=0
1590 LINE START, 41, START, 49   :'DISPLAY a cursor
1600 LINE  START, 49, (START-2), 45
1610 LINE  START, 49, (START+2), 45
1620 IIT=0
1630 ZX=-1
1640 GOTO 2170
1650 PRINT "********MOVE THE DOT LINE TO DETECT PEAK********"
1660 PRINT "*C--LEFT   X--QUICK LEFT   B--RIGHT  N--QUICK RIGHT *"
1670 PRINT "*      E---EXIT  P---PRINT OUT  I---INTEGRAL          *"
1680 PRINT "************************************************************"
1690 V$=" "
1700 V$=INKEY$
1710 IF V$="E" OR V$="e" THEN 2320
1720 STRT=START
1730  IF V$="B" OR V$="b" THEN 1820 ELSE IF V$="X" OR V$="x"
       THEN 1760 ELSE IF V$="N" OR V$="n" THEN 1780 ELSE IF   V$="C"
OR V$="c" THEN 1800 ELSE IF V$="P" OR V$="p" THEN       1840 ELSE IF
V$="I" OR V$="i" THEN 1870
1740 START=START
1750 GOTO 2020
1760 START=START-10
1770 GOTO 2020
```

```
1780 START=START+10
1790 GOTO 2020
1800 START=START-1
1810 GOTO 2020
1820 START=START+1
1830 GOTO 2020
1840 INST(IIT+1)=START-60
1850 IIT=IIT+1
1860 GOTO 1650
1870 INTE=0
1880 IF ZX=-1 THEN 1900
1890 GOTO 1960
1900 INPUT "INTEGRATION OVER [ 2n+1 ] CHANELS. ENTER N=", ZX
1910 IF ZX<0 THEN 1930
1920 GOTO 1950
1930 PRINT "   ERROR !!!   RENTER"
1940 GOTO 1900
1950 PRINT "   INTEGRATION OVER", 2*ZX+1, "CHANELS WILL BE
                                                    PERFORMED"
1960 FOR I=0 TO 2*ZX+1
1970  INTE=INTE+WD1(START-60+I-ZX)
1980 NEXT
1990 PRINT "AREA OF PEAK AT WAVE#", INT(RA(START-60)*10)/10,
                                                    "IS", INTE
2000 PRINT "            "
2010 GOTO 1650
2020 IF START<70 THEN START=START+10
2030 IF START>570 THEN START=START-10
2040 LINE STRT, 41, STRT, 49, 0
2050 LINE STRT, 49, (STRT-2), 45, 0
2060 LINE STRT, 49, (STRT+2), 45, 0
2070 LINE START, 49, (START-2) 45
2080 LINE START, 49,(START+2), 45
2090 LINE START, 41, START, 49
2100 LOCATE 13, 1
2110 OPRINT WD1(START-60);
2120 LOCATE 27, 1
2130  OPRINT INT(RA(START-60))
2140 LOCATE 13, 16
2150 OPRINT (START-60)
2160 GOTO 1690
2170 LOCATE 1, 15
2180 OPRINT INT(RA(1));
2190 LOCATE 8 15
2200 OPRINT INT(RA(100));
2210 LOCATE 14, 15
2220 OPRINT INT(RA(200));
2230 LOCATE 21, 15
2240 OPRINT INT(RA(300));
2250 LOCATE 27, 15
2260 OPRINT INT(RA(400));
2270 LOCATE 34, 15
2280 OPRINT INT(RA(500));
```

```
2290 LOCATE 21, 16
2300 OPRINT "RAMAN SHIFT (1/cm)";
2310 GOTO 1650
2320 DR=0
2330 INPUT "   SAVE THIS PROFILE? (Y/N) ----", PR$
2340 IF PR$="Y" OR PR$="y" THEN 2360
2350 GOTO 2510
2360 INPUT "   DATA FILE NAME? ====", NE$
2370 OPEN "O", #2, NE$
2380 PRINT "ENTER THE DELAY TIME IN PICOSEC."
2390 INPUT T
2400 PRINT #2, T
2410 PRINT "ENTER  THE  TITLE"
2420 INPUT COM$
2430 PRINT #2, COM$
2440 PRINT #2, "Raman shift"
2450 PRINT #2, "Counts"
2460 FOR I=1 TO 511
2470 PRINT #2, RA(I)
2480 PRINT #2, WD1(I)
2490 NEXT
2500 CLOSE
2510 IF IIT=0  THEN 2650
2520 INPUT "   PRINT OUT THE  MEASURED DATA? (Y/N)----", WIC$
2530 IF WIC$="N" OR WIC$="n" THEN 2650
2540 PRINT "PLEASE SET THE PRINTER AND PRESS Y TO READY"
2550 IF (INKEY$<>"Y") AND (INKEY$<>"y") THEN 2550
2560 RSPRINT "  RAMAN SHIFT AND INTENSITY "
2570 RSPRINT "                              "
2580 RSPRINT "-------------------------------------------------"
2590 RSPRINT "RAMAN SHIFT", "INTENSITY     "
2600 FOR I=1 TO IIT
2610  RSPRINT "-------------------------------------------------"
2620  RSPRINT RA(INST(I)), WD1(INST(I))
2630 NEXT
2640 RSPRINT "-------------------------------------------------"
2650 INPUT "   DO  YOU WANT SOMETHING ELSE ? (N/Y)----", VB$
2660 IF VB$="N" OR VB$="n" THEN 2800
2670 INPUT "   DO YOU WANT A NEW IMAGE ? (Y/N)----", RT$
2680 IF RT$="Y" OR RT$="y" THEN 220
2700 VB$="Y"
2710 RT$="N"
2720 GOTO 554
```

Bibliography.

Chapter 1.

1. L. F. Johnson, R. E. Dietz and H. J. Guggenheim, Phys. Rev. Lett. **11**, 318 (1963).

2. J. C. Walling, O. G. Peterson, H. P. Jenssen, R. C. Morris, and E. W. O'Dell, IEEE J. Quantum Electr. **QE-16**, 1302 (1980).

3. M. L. Shand and J. C. Walling, IEEE J. Quantum Electr. **QE-18**, 1829 (1982) ; J. Buchert, A. Katz, and R. R. Alfano, IEEE J. Quantum Electr. **QE-19**, 1477 (1983).

4. B. Struve, G. Huber, V. V. Laptev, I. A. Shcherbakov and E. V. Zharikov, Appl. Phys. B. **30**, 117 (1983).

5. P. F. Moulton, J. Opt. Soc. Am. **B3**, 125 (1986).

6. V. Petricevic, S. K. Gayen, R. R. Alfano, K. Yamagishi, H. Anzai, and Y. Yamaguchi, Appl. Phys. Lett. **52**, 1040 (1988); Appl. Phys. Lett. **53**, 2590 (1988).

8. L. A. Riseberg and H. W. Moos, Phys. Rev. **174**, 429 (1968).

9. N. Robertson and L. Friedman, Philosophical Magazine **33**, 753 (1976).

10. C. W. Struck and W. H. Fonger, J. Lumin. **10**, 1 (1975).

11. J. M. Wiesenfeld, L. F. Mollenauer and Erich Ippen, Phys. Rev. Lett. **47**, 1668 (1981).

12. S. K. Gayen, W. B. Wang, V. Petricevic, R. Dorsinville, and R. R. Alfano, Appl. Phys. Lett. **47** (5) 455 (1985).

13. S. K. Gayen, W. B. Wang, V. Petricevic, and R. R. Alfano, Appl. Phys. Lett. **49** (8) 437 (1986).

14. S. K. Gayen, W. B. Wang, V. Petricevic, S. G. Demos, and R. R. Alfano, J. Lumin. 47, 181 (1991).

15. A. M. Stoneham, Philosophical Magazine 36, 983 (1977).

16. B. Henderson and G. F. Imbusch, "Optical Spectroscopy of inorganic solids", (1989), ch. 5 and 9, John Wiley & Sons, New York.

Chapter 2.

1. "Ultrashort Pulse Measurements", D. J. Bradley and Geoffrey H. C. New, Proceedings of the IEEE, Vol. 62, No 3, (1974).

2. "Picosecond Laser Techniques and Design", A. G. Doukas, J. Buchert and R. R. Alfano, "Biological Events Probed by Ultrafast Laser Technology", Edited by R. R. Alfano, (1982).

3. "Ultrafast Laser Technology: The New Frontier in Optics", P. Delfeyett, S. K. Gayen and R.R. Alfano, Encyclopedia of Physical Science and Technology, Edited by R. A. Meyers, Academic Press, New York, (1987).

4. "Ultrafast Laser Technology", Roger Dorsinville, Proceedings of the IEEE, (1988).

5. "Picosecond laser Pulses", A. J. DeMaria, W.H. Glenn, M. J. Brienza and M. E. Mark, Proceedings of the IEEE, Vol. 57, No 1, (1969).

6. C. P. Ausschnitt, R. K. Jain and J. P. Heritage, IEEE J. Quantum Electron., Vol. QE-15, No 9, (1979).

Chapter 3.

1. K. Huang and A. Rhys, Proc. R. Soc., **204**, 406, (1951).

2. R. C. O'Rourke, Phys. Rev., **91**, 265, (1953).

3. L. A. Riseberg and H. W. Moos, Phys. Rev., **147**, 429, (1968).

4. H. W. Moos, J. Lumin., **1**, 106, (1970).

5. N. Robertson and L. Friedman, Philosophical Magazine **33**, 753 (1976).

6. N. Robertson and L. Friedman, Philosophical Magazine **36**, 1013 (1977).

7. C. W. Struck and W. H. Fonger, J. Lumin. **10**, 1 (1975).

8. H. Gummel and M. Lax, Ann. Phys. (N.Y.) **2**, 28 (1957).

9. H. L. Pryce, Phonons, edited by R. W. Stevenson (Plenum, New York, 1966), p. 403.

10. M. D. Sturge, Phys. Rev. B, **8**, 6, (1973).

11. G. Rickayzen, Proc. R. Soc., **241**, 480, (1957).

12. R. Englman and J. Jortner, Mol. Phys. **18**, 379, (1969).

13. P. T. Landsberg, Phys. Status Solidi, **41**, 457 (1970).

14. P. T. Landsberg, Phys. Status Solidi, **41**, 457 (1970).

15. F. K. Fong, S. L. Naberhuis and M. M. Miller, J. Chem. Phys. **56**, 4020, (1972).

16. J. Jortner, Mol. Phys. **32**, 379, (1976).

17. A. M. Stoneham, Philosophical Magazine **36**, 983 (1977).

18. For a general reviw and references, see R. Englman, Nonradiative decay of ions and Molecules in Solids, (North-Holland, Amstrerdam, 1979).

19. M. Lax, H. J. Carmichael and W. J. Shugard, Phys. Rev. B, **26**, 3547, (1982).

20. J.M. Wiesenfeld, Linn F. Mollenauer and Erich Ippen, Phys. Rev. Lett., **47**, 1668 (1981).

21. S. K. Gayen, W. B. Wang, V. Petricevic, R. Dorsinville, and R. R. Alfano, Appl. Phys. Lett. **47** (5) 455 (1985).

22. S. K. Gayen, W. B. Wang, V. Petricevic, and R. R. Alfano, Appl. Phys. Lett. **49** (8) 437 (1986).

23. S. K. Gayen, W. B. Wang, V. Petricevic, S. G. Demos, and R. R. Alfano, J. Lumin. **47**, 181 (1991).

24. A. M. Stoneham, Philosophical Magazine **36**, 983 (1977).

25. B. Henderson and G. F. Imbusch, "Optical Spectroscopy of inorganic solids", (1989), ch. 5 and 9, John Wiley & Sons, New York.

26. A. Laubereau,D.von der Linde and W. Kaiser, Phys. Rev. Lett., **27**, 802 (1971).

27. D.von der Linde, J.Kuhl and H.Klingenberg, Phys. Rev. Lett., **44** 1505 (1980)

28. J.A.Kash, J.C.Tsang and J.M.Hvam, Phys. Rev. Lett., **54** 2151 (1985)

29. K. T. Tsen, R. P. Joshi, D, K. Ferry and H. Morkoc,Phys. Rev. B, **39**, 2, 1446 (1973).

30. P. G. Klemens, Phys. Rev., **148**, 845 (1966).

31. R. G. Vebrich, V. Narayanamutri, and M. A. Chin, Phys. Rev. Lett., **45**, 1432 (1980)

32. P. Hu, V. Narayanamutri, and M. A. Chin, Phys. Rev. Lett., **46**, 192 (1981)

33. R. S. Meltzer, J. E. Rives and G. S. Dixon, Phys. Rev. B, **28**, 4786 (1983)

34. R. J. G. Goossens, J. I. Dijkhuis, and H. W. de Wijn, Phys. Rev. B, **32**, 5163 (1985)

35. M. J. Van Dort, C. R. de Kok, J. I. Dijkhuis, and H. W. de Wijn, J. Lumin. **45**, 150 (1990)

36. D. M. Boye, J. E. Rives and R. S. Meltzer, J. Lumin. **45**, 147 (1990)

37. W. A. Tolbert, W. M. Dennis, and W. M. Yen, Phys. Rev. Lett., **65**, 607 (1990)

38. Kazuaki Iishi, American Mineral., **63**, 1198-1208 (1978).

Chapter 4.

1. V. Petričević, S. K. Gayen, R. R. Alfano, K. Yamagishi, H. Anzai, and Y. Yamaguchi, Appl. Phys. Lett. **52**, 1040 (1988).

2. V. Petričević, S. K. Gayen, and R. R. Alfano, Appl. Phys. Lett. **53**, 2590 (1988).

3. H. R. Verdun, L. M. Thomas, D. M. Andrauskas, T. McCollum, and A. Pinto, Appl. Phys. Lett. **53**, 2593 (1988)

4. V. G. Barishevskii, M. V. Korzhik, A. E. Kimaev, M. G. Livshitz, V. B. Pavlenko, M. L. Meilman, and B. I. Minkov, Zh. Prikl. Spectrosk. (Moscow) **53**, 7 (1990).

5. A. Seas, V. Petričević, and R. R. Alfano, Opt. Lett. **16**, 937 (1992).

6. V. Petričević, S. K. Gayen, and R. R. Alfano, in *Tunable Solid-State Lasers*, Vol. 5 of the OSA Proceeding Series, M. L. Shand and H. P. Jenssen, eds. (Optical Society of America, Washington, D.C., 1989), pp. 77-84.

7. H. R. Verdun, L. M. Thomas, D. M. Andrauskas, T. McCollum, and A. Pinto, OSA Proceedings of the Advanced Solid-State Lasers, eds. M. L. Shand and H. P. Jenssen, Vol. 5, 85, (1989).

8. W. Jia, H. Liu, S. Jaffe, and W. M. Yen, Phys. Rev. B **43**, 5234 (1991).

9. R. Moncorge, G. Cormier, D. J. Simkin and J. A. Capobianco, J. Quantum Electr. **27**, 114 (1991).

10. K. R. Hoffman, J. Casas-Gonzales, S. M. Jacobsen, and W. M. Yen, Phys. Rev. B **44**, 125289 (1991).

11. H. Rager, Phys. Chem. Minerals **1**, 371 (1977).

12. L. V. Bershov, J. M. Gaite, S. S. Hafner, and H. Rager, Phys. Chem. Mineral **9**, 95 (1983).

13. V. Devarajan and E. Funck, J. Chem. Phys., **62**, No 9, 3406, (1975).

14. Kazuaki Iishi, American Mineral., **63**, 1198-1208 (1978).

15. N. Nishide, Y. Segewa, P. H. Kim, S. Namba, and A. Masuyama, Reza Kagaku Kenkyu **7**, 89 (1985).

16. M. Th. Paques-Ledent and P. Tarte, Spectroch. Acta **29A**, 1007, (1973).

17. A. Chopelas, American Mineral., **76**, 1101 (1991).

18. H. Rager and G. Weiser, Bull. Mineral. **104**, 603 (1981).

19. V. Petričević, unpublished data.

Chapter 5.

1. J. M. Wiesenfeld, Linn F. Mollenauer and Erich Ippen, Phys. Rev. Lett. **47**, 1668 (1981).

2. S. K. Gayen, W. B. Wang, V. Petricevic, R. Dorsinville, and R. R. Alfano, Appl. Phys. Lett. **47** (5) 455 (1985).

3. S. K. Gayen, W. B. Wang, V. Petricevic, and R. R. Alfano, Appl. Phys. Lett. **49** (8) 437 (1986).

4. S. K. Gayen, W. B. Wang, V. Petricevic, S. G. Demos, and R. R. Alfano, J. Lumin. **47**, 181 (1991).

5. A. M. Stoneham, Philosophical Magazine **36**, 983 (1977).

6. K. Peuker and E. D. Trifonov, Phys. Stat. Solidi **30**, 479 (1968).

7. V. Hizhnyakov and I. Tehver, Phys. Stat. Solidi **39**, 67 (1970).

8. Yuzo Mori, Ryo Hattori and Hiroshi Ohkura, J. Phys, Soc. Jap., **51**, 2713, (1982).

9. Y. Kondo, T. Noto, S. Sato and M. Hirai, J. Lumin., **38**, 164, (1987).

10. B. P Zacharchenya, V. D. Dymnikov, I. Ya. Karlik, D. N. Mirlin, L. P. Nikitin, V.I. Perel, and I.I. Reshina, J. Phys. Soc. Jap., **49**, Suppl. A., 573, (1980).

11. D. N. Mirlin, I. Ya. Karlik, L. P. Nikitin, I.I. Reshina, and V. F. Sapega, Solid State Comm., **37**, 757, (1981).

12. B. P Zacharchenya, J. Lumin., **24/25**, 669, (1981).

13. G. Fasol and H. P. Hughes, Phys. Rev.B, **33**, 2953, (1986).

14. C. L. Petersen and S. A. Lyon, Phys. Rev. Lett., 65, 760 , (1990).

15. P. Saari and K. Rebane, Solid State Comm., 7, 887, (1969).

16. Yihong Yang, Wolf von der Osten, and Fritz Luty, Phys. Rev. B, 32, 2724, (1985).

17. R. Moncorge, F. Auzel, and J. M. Breteau, Philosophical Magazine B 51, 489 (1985); R. Moncorge and T. Benyattou, Phys. Rev. B 37, 9186 (1988).

18. E. W. J. L. Oomen, J. Lumin., 50, 317, (1992).

19. A. Silversmith, W. Lenth and R. M. Macfarlane, Appl. Phys. Lett. 54, 2301, (1989).

20. G. Fasol, W. Hackenberg, H. P. Hughes, K. Ploog, E. Bauser, and H. Kano, Phys. Rev. B., 41, 1461, (1990)

21. K. R. Hoffman, S. M. Jacobsen, J. Casas-Gonzalez and W. M. Yen, Proceedings of the Advanced Solid-State Lasers Topical meting, Hilton Head, S.C., March 18-20, 1991

22. V. Petričević, S. K. Gayen, and R. R. Alfano, in *Tunable Solid-State Lasers*, Vol. 5 of the OSA Proceeding Series, M. L. Shand and H. P. Jenssen, eds. (Optical Society of America, Washington, D.C., 1989), pp. 77-84.

23. H. R. Verdun, L. M. Thomas, D. M. Andrauskas, T. McCollum, and A. Pinto, OSA Proceedings of the Advanced Solid-State Lasers, eds. M. L. Shand and H. P. Jenssen, Vol. 5, 85, (1989).

24. W. Jia, H. Liu, S. Jaffe, and W. M. Yen, Phys. Rev. B 43, 5234 (1991).

25. V. Devarajan and E. Funck, J. Chem. Phys., 62, No 9, 3406, (1975).

26. Kazuaki Iishi, American Mineral., 63, 1198-1208 (1978).

27. R. Pappalardo, D. L. Wood, and R. C. Linares, J. Chem. Phys., 35, No 4, 1460, (1961).

28. M. V. Iverson, J. C. Windscheif, and W. A. Sibley, Appl. Phys. Lett. **36**, 183, (1971).

29. W. E. Vehse, K. H. Lee, S. I. Yun and W. A. Sibley, J. Lumin., **10**, 163, (1975).

Chapter 6.

1. R.R.Alfano and S.L.Shapiro, Phys. Rev. Lett., **26** 1247 (1971)

2. A. Laubereau,D.von der Linde and W. Kaiser, Phys. Rev. Lett., **27**, 802 (1971)

3. D.von der Linde, J.Kuhl and H.Klingenberg, Phys. Rev. Lett., **44** 1505 (1980)

4. J.A.Kash, J.C.Tsang and J.M.Hvam, Phys. Rev. Lett., **54** 2151 (1985)

5. C. L. Collins and P.Y.Yu, Phys, Rev. B. **30**, 4501 (1984)

6. R. G. Vebrich, V. Narayanamutri, and M. A. Chin, Phys. Rev. Lett., **45**, 1432 (1980)

7. P. Hu, V. Narayanamutri, and M. A. Chin, Phys. Rev. Lett., **46**, 192 (1981)

8. A. M. Stoneham, Philosophical magazine, **36** No 4 , 983 (1977)

9. R. S. Meltzer, J. E. Rives and G. S. Dixon, Phys. Rev. B, **28**, 4786 (1983)

10. R. J. G. Goossens, J. I. Dijkhuis, and H. W. de Wijn, Phys. Rev. B, **32**, 5163 (1985)

11. M. J. Van Dort, C. R. de Kok, J. I. Dijkhuis, and H. W. de Wijn, J. Lumin. **45**, 150 (1990)

12. D. M. Boye, J. E. Rives and R. S. Meltzer, J. Lumin. **45**, 147 (1990)

13. W. A. Tolbert, W. M. Dennis, and W. M. Yen, Phys. Rev. Lett., **65**, 607 (1990)

14. J. Shah, A. E. DiGiovanni, T. C. Damen, and B. I. Miller, Phys. Rev. B, **7**, 3481 (1973)

15. P. G. Klemens, Phys. Rev., **148**, 845 (1966).

16. K. Park, Phys. Lett., **22** (1), 39, (1966).

17. B. Kh. Bairamov, Yu. E. Kitaev, V. K. Negoduiko, and Z. M. Khashkhozhev, Sov. Phys. Solid State, **16**, 1323, (1975).

18. Dai-sik Kim and Peter Y. Yu, Phys. Rev. Lett., **64**, 946, (1990)

19. Dai-sik Kim and Peter Y. Yu, Appl. Phys. Lett., **56**, 1570, (1990).

Chapter 7.

1. A. Laubereau, L. Kirschner and W. Kaiser, Opt. Commun., **9**, 182, (1973).